Universitat Autónoma de Barcelona

Institut de Física d'Altes Energies

Measurement of the electron-neutrino component of the T2K beam and search for electron-neutrino disappearance at the T2K Near Detector

Javier Caravaca Rodríguez

Memoria presentada para optar al grado de

DOCTOR EN FÍSICA

Supervisada por:

Dr. Federico Sánchez Nieto (Director)

Dr. Claudio Giganti (Co-director)

Dr. Enrique Fernandez Sánchez (Tutor)

y evaluada por:

Dr. Mauro Mezzeto (Presidente)

Dr. Ramón Miquel Pascual (Secretario)

Dr. Manuel Masip Mellado (Vocal)

Cerdanyola (Barcelona), 18 de Julio de 2014

A mi hermano y mis padres que, como el neutrino,
están ahí aunque casi nunca se vean.

Acknowledgments

First of all, I would like to thank the two people that have made possible this work. *Gracias* to Dr.Federico Sánchez for giving me the opportunity to work by his side in an always friendly environment, guiding my works and trusting on me. *Grazie mille* to Dr.Claudio Giganti for his help, for teaching me and having always an answer to my questions. What I have learnt with them in the last four years, thanks to their coordination and fruitful discussions, have been key to achieve the results presented in these pages.

I have been lucky to work within a group of smart and hard-working physicists, that have largely contribute to the whole analysis chain. I would like to explicitly thank to Davide Sgalaberna, the person with whom I developed most of the main part of the analyses, and Dr.Ben Smith, whose outstanding analysis framework and great job, specifically in the ν_e analysis, accelerated and improved my final results. I do not forget about Dr.Marco Zito, that gave me the first hints on the sterile neutrino searches and triggered the ν_e disappearance analysis. I thank also Dr.Costas Andreopoulos and Dr.Alex Himmel for reviewing intensively the sterile analysis, improving its quality and its scientific value.

Among the T2K Collaboration, many people have contribute to my work in the scientific plane as well as in the social plane. *Gràçies* Raquel, *grazie* Michela, Stefania, Enrico and Lorenzo, $\epsilon\upsilon\chi\alpha\rho\iota\sigma\tau\acute{\omega}$ Panos, *gamsa* Jiae, *gracias* Melody, Lorena, Anselmo, Michel and Sasha, *merci* Leïla and Benjamin, thanks Linda, Megan, Callum and Andy, *danke* Dennis and *arigató* Teppei and Ayako-chan. Thanks all of you for making Tokai enjoyable!

Gracias a mis compañeros de oficina en el IFAE y en especial el resto del grupo de neutrinos: Thorsten, Alfonso, John y Carlos. Debo nombrar especialmente a la administradora Cristina, cuya presteza y buen humor siempre hacen la burocracia menos tediosa.

Fuera del entorno científico, quisiera primero agradecer a mi amigo y antiguo compañero de piso Toño por todas las vivencias desde que llegué a Barcelona, a las personas que conocí en la Autónoma: Jorge, Santi, Ane, Andreu, Christopher y Anne, al resto de amigos de Barcelona en especial Geraldine, Juan, Erika y Marian, a mi equipo de waterpolo WAUB y a la banda de las clases de blues. Sin ellos no

habría mantenido la cordura durante el desempeño del presente trabajo.

Guardo un especial recuerdo de mi estancia en la *Cité Internationale Universitaire* de París, dónde conocí a muchas personas de las que no me olvido y que querría también agradecer: Rocío, Txell, Fran, Pierre, Paola, Elena, Limón, Fátima, Araceli, Gaizka, Ana, Mónica y Teresa.

Agradecer también a mis amigos de Cádiz que, aunque algunos lejos y otros no tanto, siempre estarán presentes allá dónde esté (algunos literalmente) y por ello os doy las gracias. Especialmente a Elena, Jose y Lidia. Durante la carrera conocí a muchas personas en Sevilla y Granada que hoy recuerdo. Agradezco en especial a Carmen todos los buenos momentos en Granada.

Por último, agradezco a mi familia estar siempre presente y apoyarme, a veces a disgusto, en mis trabajos y viajes. Gracias a vuestra confianza todo este trabajo ha sido posible.

Measurement of the electron-neutrino component of the T2K beam and search for electron-neutrino disappearance at the T2K Near Detector

Javier Caravaca Rodríguez

Institut de Física d'Altes Energies
Universitat Autónoma de Barcelona
Barcelona, Spain
2014

ABSTRACT

The T2K experiment is a long baseline neutrino experiment that has observed for first time the appearance of electron-neutrinos in a muon-neutrino beam. Thanks to this analysis, the last unknown neutrino mixing angle θ_{13} is measured with a good precision. The main background to this measurement is the contamination of electron-neutrinos produced in the neutrino beam together with the dominant muon-neutrino component. This is an irreducible component that needs to be measured and controlled. The prediction of this component at SuperKamiokande is based on the constrain of the neutrino flux and cross sections by a muon-neutrino selection at the T2K near detector ND280. To confirm this prediction, we measure the electron-neutrino event rates at ND280 before the oscillations occur, establishing that the electron-neutrino component is correctly reproduced by the simulation at the 10% level.

In addition, studying the electron-neutrino component is interesting to investigate the abnormal behaviour of some neutrino experiments. The reactor neutrino experiments as well as the results from the calibration of solar neutrinos detectors containing gallium, using radioactive sources, have observed a deficit of electron-neutrino at very short distances from the neutrino source. This depletion is not compatible with standard neutrino oscillation, but it can be explained by invoking a fourth neutrino with a mass of the order of $1\,\mathrm{eV}^2$. This neutrino does not feel any of the forces of the Standard Model, and hence is called *sterile neutrino*. Assuming that it mixes with the electron-neutrinos, it would be responsible of the short base-line electron-neutrino disappearance due to neutrino oscillation. The T2K near detector is located at a position short enough to study the light sterile neutrino oscillations. A oscillation model with an additional sterile neutrino apart from the three active species is tested, constraining to the oscillation parameters and comparing our results with the literature.

Medida de la componente de neutrinos electrónicos en el haz de T2K y búsqueda de desaparición de neutrinos electrónicos en el detector cercano de T2K

Javier Caravaca Rodríguez

Institut de Física d'Altes Energies
Universitat Autónoma de Barcelona
Barcelona, Spain
2014

RESUMEN

T2K es un experimento de oscilaciones de neutrinos de largo recorrido en el que por primera vez se ha observado la aparición de neutrinos electrónicos en un haz de neutrinos muónicos. Así pues, el único ángulo de mezcla que quedaba por conocer, θ_{13}, es medido con gran precisión. El *background* principal de esta medida es la contaminación de neutrinos electrónicos producida en el haz junto con la componente de neutrinos muónicos. Ésta es una componente irreducible que ha de ser medida y controlada.

La componente intrínseca de neutrinos electrónicos es medida antes de las oscilaciones en el detector cercano de T2K confirmando la predicción de la simulación con un precisión del 10%. Se establece que el *background* de neutrinos electrónicos está bien reproducido y que la principal medida del experimento T2K es exacta.

Por otro lado, estudiar la componente de neutrinos electrónicos es interesante para investigar el comportamiento anómalo de algunos experimentos. Estudios en reactores nucleares y resultados en la calibración de experimentos de neutrinos solares con Galio han observado un déficit de neutrinos electrónicos a cortas distancias de la fuente. Este déficit no es compatible con oscilaciones de neutrinos estándar, pero puede ser conciliado en el marco de las oscilaciones, mediante la introducción de un cuarto neutrino con una masa del orden de $1\,\mathrm{eV}^2$. Este nuevo neutrino no sentiría ninguna fuerza del Modelo Estándar y por ello es comúnmente llamado *neutrino estéril*. Asumiendo que se mezcla con los neutrinos de tipo electrónico, explicaría la desaparición a cortas distancias de los mismos. El detector cercano de T2K se encuentra a una distancia de la fuente óptima para el estudio de oscilaciones de neutrinos estériles ligeros. Investigamos el modelo más simple de neutrinos estériles con un sólo neutrino adicional, definiendo intervalos de confianza para los parámetros de oscilación y comparándolos con la literatura.

Table of Contents

List of Figures

List of Tables

Part I

Introduction

Outline of this thesis

This thesis describes the analysis of the electron-neutrino (ν_e) contamination in the T2K muon-neutrino (ν_μ) beam. The work is performed at the near detector of the T2K neutrino experiment (ND280) and it is intended to confirm the prediction of the ν_e component and, in addition, to study the short base-line anomalies observed in others neutrino experiments that lead to the idea of light sterile neutrinos.

In the first part, after an historical introduction to neutrinos in Chapter 1, the neutrino physics are presented, from its definition in the Standard Model until the future neutrino experiments. Special emphasis is given to the neutrino oscillation, as it defines the theoretical framework of the T2K experiment. Models with sterile neutrinos are presented in Chapter 2, as well as the experimental anomalies that motivatates its existence.

In the second part, the T2K experiment is described in Chapter 3, with special attention to the ν_e contamination in the neutrino beam, that is the target of the present work. The design of the whole experiment including accelerator facilities, near detectors and far detector are described in Chapter 4. The most updated oscillation results are presented in Chapter 5, with a special mention to the reduction of the uncertainties on the flux and cross sections predictions, using the ν_μ measurement at ND280.

The third part is main block, where the two complete analyses are presented. A selection of ν_e interactions at ND280 is performed in Chapter 6 together with a selection of two control samples described in Chapter 7. A complete study of the systematic uncertainties is provided in Chapter 8. The beam ν_e measurement is presented in Chapter 9 where we compare it with the prediction and discuss the level of compatibility. In Chapter 10, the ν_e disappearance due to light sterile neutrino oscillations is investigated using the simplest model, and the confidence contours provided by the data are calculated through frequentist techniques. Finally, in the last chapter [Chapter 11], we summarize our results and provide the outlook for both analyses.

I will use the natural units convention $\hbar = c = 1$ throughout the text. Nevertheless, I apologize as some figures present a different convention and some c factors are present.

Chapter 1

Neutrino physics

Neutrino physics is nowadays one of the most active fields in particle physics. The well established observation of the neutrino oscillation phenomenon by many experiments is not sustained considering massless neutrinos. The fact that neutrinos are massive is to date the only clear indication of physics beyond the Standard Model (SM). Neutrino oscillations also imply lepton flavour violation in the SM, that had never been observed before, although it is not a fundamental symmetry in the SM.

There are still many questions regarding the nature of the neutrinos that need to be addressed: absolute scale of neutrino masses, nature of neutrino mass (Dirac or Majorana), mass hierarchy, whether the CP symmetry is violated or not in the leptonic sector (CPV) or the number of neutrino families, are the main ones. Whereas collider experiments, as LHC, have not yet succeeded in finding new physics, many neutrino experiments are being built to study those remaining unknowns. Moreover, neutrinos provide interesting information about the Sun (solar neutrinos), the Earth (geoneutrinos and atmospheric neutrinos) and about the whole Universe through astrophysics or cosmology. In addition, they have interesting features that can be exploited for application in communications or controlling nuclear activities for instance.

1.1 Brief history of the neutrinos

At the end of the 19th century, it was observed that some elements can emit particles, which were called *alpha* and *beta*. The radioactivity had been discovered [20]. Lately, it was known that the beta emission were indeed electrons (e^-) emitted by the nucleus of radioactive elements. In the beta decay, an element turns into a lighter one trough the emission of an electron

$$ {}^{A}_{Z}X \rightarrow {}^{A}_{Z+1}X + e^- $$

According to this model, the energy of that electron must be peaked at the mass difference between the mother and the daughter elements

$$E_{e^-} = M_{ZX} - M_{Z+1X}$$

However, Chadwick in 1920 measured a continuous energy spectrum for the electron emitted in beta decays. At the beginning, the option of the violation of the energy conservation was considered by Bohr, but there was also the problem of the conservation of the angular momentum, that was violated by 1/2 in the beta processes.

In 1930, Pauli solved both problems proposing a new particle ν that carries part of the energy in the decay, with a mass smaller than the electron mass, neutral and with spin 1/2 [126]. He named it *neutron*, as the neutron (n) was not discovered until 1932 [30] by Chadwick. Enrico Fermi called this particle *neutrino* ("little neutron") in 1933, and also proposed the first model of beta decay called the Fermi interaction [85]

$$n \to p + e^- + \nu$$

being p the proton. Nowadays we know that that new particle is indeed an *anti-neutrino* $\bar{\nu}$.

The first idea for neutrino detection is due to Pontecorvo, who proposed to use the *inverse beta decay* (IBD) as a signature of the neutrino interaction [128]

$$\bar{\nu} + p \to n + e^+$$

where e^+ is the positron, the anti-particle of the electron. However, H. Bethe and R. Peierls estimated its cross-section using the theory of Fermi to be of the order of $10^{-44}\,\mathrm{cm}^2$ for neutrinos around an energy of 1 MeV [22]. It means that experiments need a very intense source of neutrinos and large target masses to detect some interactions.

At that moment, the best neutrino source candidate was the nuclear fission reactors. The first detection of the neutrino was achieved in 1956 with the experiment of C.L. Cowan and F. Reines using the nuclear reactor at Savanaah River Plant [76]. It was their second attempt after the unclear observation in the experiment at Handford 3 years before. They detected an increase in the event rate when the reactor was on with respect to when it was off. Those extra events could only come from neutrinos produced in

the reactor core. This is the first indirect observation of the neutrino. They measured a cross-section of $6 \times 10^{-44}\,\mathrm{cm}^2$, well compatible with the theoretical estimations from the studies of the β decay. This measurement paved the way to study the neutrino properties and further achievements were produced: the discovery of parity violation in processes involving neutrinos [142, 90] or the measurement of the neutrino helicity [98]. As conclusion the neutrinos were left-handed massless particles.

In 1960 appeared the first proposal to study the weak interaction with neutrinos produced in pion decays. The idea was to use accelerators to produce pion beams that eventually would decay into neutrinos [134]. There were suspects that the neutrinos coming from that source and the ones coming from beta decays were different:

$$\begin{aligned} &\pi \text{ decay:} && \pi^+ \to \mu^+ + \nu_1 \\ &\beta \text{ decay:} && {}^A_Z X \to {}^A_{Z+1} X + e^- + \nu_2 \end{aligned}$$

Indeed, two years later at Brookhaven, a new neutrino that produced "*mu-mesons*" instead of electrons was discovered [77]. It was the first experiment using a ν beam from π decays. At this point it was understood that the neutrino produced in the β decay was the *electron-neutrino* (ν_e) and the one from π decays the *muon-neutrino* (ν_μ). Later on, with the discovery of the last lepton τ in 1975 [127], the existence of a new neutrino *tau-neutrino* (ν_τ) was postulated. In 2000 it was detected by the first time in the DONUT experiment [61].

In 1973 a new neutrino interaction, the neutrino elastic scattering (ES), was discovered. A neutrino scatters with a nucleon or an electron transferring some momentum without producing new particles

$$\nu + (e^-, N) \to \nu + (e^-, N)$$

The first event of this type was seen at CERN bubble chamber experiment Gargamelle and it was an $\overline{\nu}_\mu$-electron scattering [102]. In these processes only one particle (either a lepton or a hadron) could be seen, being different from the IBD where the neutrino produces a charged lepton apart from hadrons. This new event belongs to the category called *neutral current* (NC) interactions while the IBD is a *charged current* (CC) interaction.

In a NC interaction the neutrino and the target (nucleon or lepton) are coupled with the Z^0 boson and it produces the same signature regardless the neutrino flavour. The number of neutrino species that

couples to the Z^0 boson was measured by the LEP experiment [10] to be

$$N_\nu = 2.984 \pm 0.008$$

establishing that the number of active neutrino species below $M_Z/2$, where $M_Z = 91\,\text{GeV}$ is the mass of the Z^0 boson, is three.

1.1.1 First neutrino oscillations observation

The history of the neutrino oscillation starts with the solar neutrino anomaly. After the discovery of the neutrinos and knowing that the Sun produces a huge neutrino flux, the scientific community started thinking in the possibility of detecting and studying them. According to the Solar Standard Model (SSM), the Sun produces only ν_e at different energies [Fig. 1.1] around the MeV, so they can be detected by IBD as proposed by Bruno Pontecorvo in 1946 [128] with the reaction

$$\nu_e + {}^{37}Cl \rightarrow {}^{37}Ar + e^-$$

The first experimental attempt is the Homestake Experiment [78] built in the Sixties. In 1968 they announced their first results showing a depletion of $\sim 2/3$ on the total neutrino flux. Over the whole period of 25 years they measured the total flux to be $2.56 \pm 0.16(\text{stat.}) \pm 0.16(\text{syst.})$ SNU[1] while the prediction is $7.6^{+1.3}_{-1.1}$ SNU [15]. This was called the *solar neutrino problem*.

Among some other exotic choices, there were two main solution trends: the prediction of the SSM was incorrect and it must be changed or the SSM is correct but neutrinos *oscillate* from the electron flavour to another flavour that do not produce IBD reactions. Provided the SSM was tested to be accurate, the latter was an elegant solution proposed by Pontecorvo in 1957 [100], based on the recent neutral kaons oscillations discovery [32]. At the beginning, he considered $\nu \rightleftarrows \bar{\nu}$ oscillations, but after the discovery of the ν_μ in 1962, he adapted his model to $\nu_e \rightleftarrows \nu_\mu$. In the same year and independently from Pontecorvo, the two neutrino mixing was proposed by Z. Maki, M. Nakagawa, S. Sakata [116] and the theory of the neutrino oscillation was further developed during the Seventies. For the investigation of the solar neutrino problem, matter effects were introduced in neutrino oscillation by Wolfenstein

[1] Solar Neutrino Unit: it corresponds to the neutrino flux that produces 10^{-36} captures per target per second

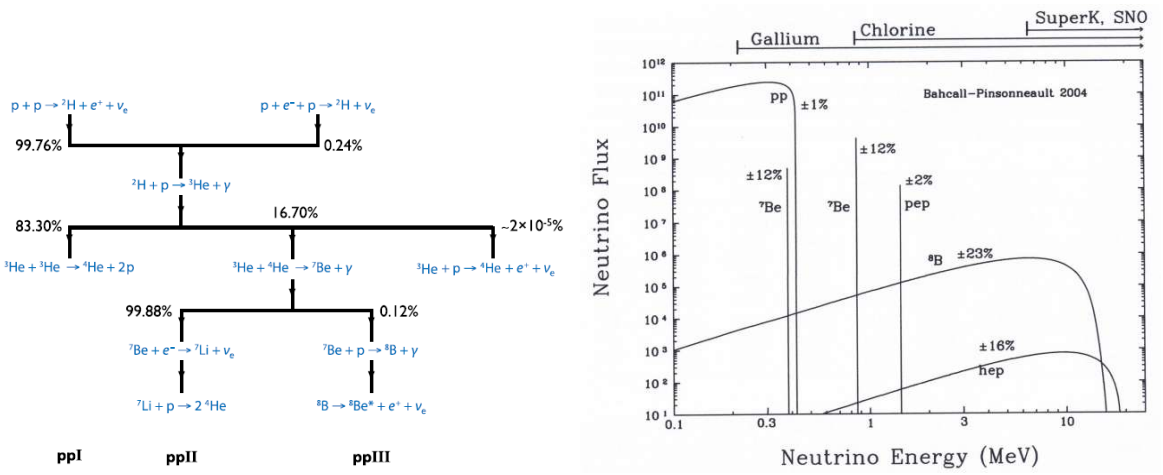

Fig. 1.1: Decay chain in the Sun (left) and solar neutrino energy spectrum for each branch (right). The two-body decays give definite energies unlike the three-body decays that provide a range of energies. Only ν_e flavour are produced in the Sun. Above the right figure we find the energy threshold for the different experiments.

(1978), Mikheyev and Smirnov (1985) in the so-called MWS effect [141]. During the following 30 years, some other experiments confirmed the result of the Homestake Experiment. For instance we name Gallex [107], Sage [44], Kamiokande [133] and SuperKamiokande [89], whose results are summarized in Fig. 1.2.

It was in 1998 when the SuperKamiokande detector reported a clear proof of the neutrino oscillations but in the atmospheric neutrino sector [143]. Finally, the solution to the solar neutrino problem was established by the Sudbury National Observatory (SNO) in 2001, that proved that solar ν_e oscillate to ν_μ and ν_τ but that the total neutrino flux, measured through NC, is conserved [130, 131].

1.2 Neutrinos in the Standard Model

The Standard Model of the fundamental particles is built to include the following features:

- there are three neutrino flavours.
- neutrinos interact only through the weak force in two different ways: one where the neutrino scatters with a fermion (lepton or nucleon) and then escapes from the interaction point with different kinematics (NC) and other where the neutrino produces a lepton of its same flavour (CC)

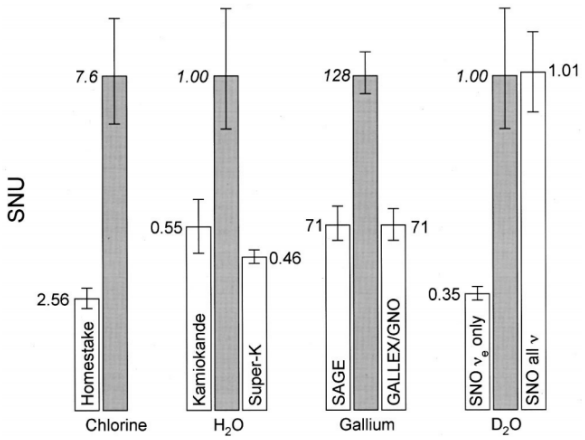

Fig. 1.2: Illustration of the solar neutrino problem and its solution: predictions and measurements for the solar neutrino flux in different experimental targets. There exist a general deficit in the measurements except for the SNO NC measurement.

- Neutrinos are found to be always left-handed and anti-neutrinos always right-handed
- Neutrinos are massless. This is not consistent with the observation of the neutrino oscillations since the SM was set up before the observation of that phenomenon.

The SM describes each elementary particle and their interactions. Years of developments have yielded to the final picture sketched in Fig. 1.3. There exist

- three charged leptons: electron (e), muon (μ), and tau (τ)
- three neutral leptons or neutrinos: electron-neutrino (ν_e), muon-neutrino (ν_μ) and tau-neutrino (ν_τ)
- six quarks: up (u), down (d), charm (c), strange (s), top (t) and bottom (b)
- four gauge bosons that carry the interaction information: gluons (g), photons (γ), $W^\pm$ and Z^0
- Higgs boson H: provides mass to the fermions

In addition, each particle in the leptonic and quark sectors have their corresponding anti-particles with same mass but opposite charges. The last piece of the SM, the Higgs boson, has been recently discovered at the LHC [60, 57] and it is the last of the multiples successes of the SM, that has become the most precise theory, and its predictions have been confirmed to date by the observations.

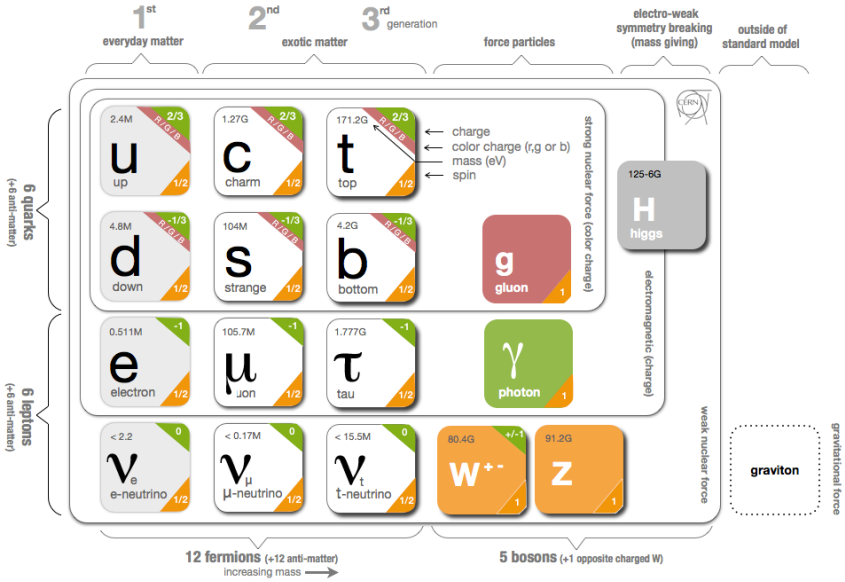

Fig. 1.3: Standard Model of the elementary particles.

Formally, the SM is described by the gauge theory based on the $SU(3)\times SU(2)_L\times SU(1)_Y$ gauge symmetry. Leptons, that are fermions of spin 1/2, are introduced through two fields: one SU(2) doublet left-handed L_L^l and one singlet right-handed l_R

$$L_L^l = \begin{pmatrix} l_L \\ \\ \nu_{Ll} \end{pmatrix} \qquad\qquad l_R$$

where l runs over the three families. Leptons are color-less and particularly neutrinos are charge-less as well, so that they only couple to the weak force described by the Lagrangian of the electroweak model

$$\mathcal{L} = \mathcal{L}_{CC} + \mathcal{L}_{NC} = \frac{g}{\sqrt{2}} \sum_l \bar{\nu}_{Ll}\gamma^\mu l_L W_\mu^+ + \text{h.c.} + \frac{g}{2\cos\theta_W} \sum_l \bar{\nu}_{Ll}\gamma^\mu \nu_{Ll} Z_\mu^0 \tag{1.1}$$

where g is the coupling constant, θ_W is the Weinberg angle and γ^μ are the Pauli matrices. $\mathcal{L}_{CC}$ gives the CC interactions driven by the gauge bosons $W^\pm$ and $\mathcal{L}_{NC}$ the NC interactions driven by Z^0. Unlike the quark sector, as neutrinos are mass-less, there is no flavour mixing, so the lepton number is conserved by families and neutrino oscillations are not allowed.

Including a bare mass term for the leptons in Eq. (1.1) violates gauge invariance. So they are built massless and they get their masses m_l by spontaneous symmetry breaking via the Higgs mechanism [56, 59]. To produce the mass term, the Higgs couples to the left and right-handed leptons by a Yukawa interaction

$$-\mathcal{L}_{Yukawa} = Y^l \bar{L}_L^l \phi l_R + \text{h.c.} \rightarrow \text{Symmetry breaking} \rightarrow m_l \bar{L}_L^l l_R$$

where Y^l is the Yukawa coupling, that is a free parameter in the theory. The mass becomes

$$m_l = \frac{v}{\sqrt{2}} Y^l \tag{1.2}$$

where $v \sim 246\,\text{GeV}$ is the vacuum expectation value of the Higgs field. We observe that we cannot get a mass term of this type if we do not have a corresponding right-handed lepton. The belief that neutrinos are massless was the reason not to include right-handed neutrinos in the SM.

Nevertheless, neutrino oscillations implies massive neutrinos and hence, physics beyond the SM. A mass term for them must be built. The simplest extension of the SM consists on including right-handed neutrinos ν_R so that they can acquire mass through the Higgs mechanism, as well as the others leptons. It generates the so-called Dirac mass term that after symmetry breaking has the form

$$\mathcal{L}_D = -m_D(\bar{\nu}_L \nu_R + \bar{\nu}_R \nu_L)$$

where $m_D = \frac{v}{\sqrt{2}} Y^\nu$ is the Dirac neutrino mass. To match the scale of the neutrino masses $\sim 0.1\,\text{eV}$, we need $Y^{\nu_l} \sim 10^{-11}$. Such a tiny Yukawa coupling is consider unnatural (the typical for the leptons ranges $Y^l \sim 10^{-6} - 10^{-3}$) and very unlikely.

Another way of including neutrino masses is through the Majorana mass term, that has the form:

$$\mathcal{L}_D = -\frac{1}{2} m_M (\bar{\nu}_L \nu_R^c + \bar{\nu}_R^c \nu_L) = -\frac{1}{2} m_M (\bar{\nu}_L C \bar{\nu}_L^T + \nu_L^T C \nu_L) = \frac{1}{2} m_M \bar{\nu}_M \nu_M$$

where $\nu_L^c \equiv C\bar{\nu}_L^T = \nu_R$ being C the charge-conjugation operator that inverts the charges of the neutrino state. ν_M is the Majorana field that fulfills

$$\nu_M \equiv \nu_L + \nu_R^c = \nu_M^c$$

So the neutrino becomes his own anti-particle. This term breaks gauge symmetries, so it is only possible for charge-less particles as the neutrinos, otherwise the charges would not be conserved. One advantage of this scenario is that we do not need an extra field (ν_R) as the left and right-handed states are just related by the operator C. On the other hand, this mass term violates lepton number by two units since the neutrino has lepton number 1 and the anti-neutrino -1.

An elegant model that explains the smallness of the neutrino masses arises mixing a Majorana term for ν_R with the Dirac term. If the mass m_R of ν_R is very large, $m_R \gg m_D$, we produce two neutrino mass states: one very heavy m_R, typically above the electroweak symmetry breaking scale so that cannot be observed, and another light state of the order of $\sim m_D^2/m_R$. This is the so-called *see-saw* mechanism [120].

1.2.1 ν interactions at T2K energies

Neutrino weak Charged Current (CC) and Neutral Current (NC) interactions are produced within the material of the detectors. Both neutrino-lepton and neutrino-nucleus interactions exist, but the cross-section of the former is $\sim 2 \times 10^3$ smaller than the latter at T2K energies, so, from now on, we will only consider neutrino interactions with nuclei. The CC *quasi-elastic* (CCQE) interaction is the one that dominates the T2K energy range ($\sim 0.5\,\text{GeV}$), where a neutrino ν_l interacts with a nucleon to create a charged lepton l and to change the nucleon:

$$\nu_l + n \rightarrow p + l^- \qquad \bar{\nu}_l + p \rightarrow n + l^+$$

Above the pion production threshold, neutrinos can produce a pion coherently (CCCoh) without breaking the nucleus:

$$\nu_l + A \rightarrow A + \pi^+ + l^-$$

At higher energies, the CC *resonant* interaction (CCRes) starts to dominate. In this reactions, a Δ resonance is produced and it decays to hadrons, usually pions and nucleons:

$$\nu_l + p \rightarrow l^- + \Delta^{++} \rightarrow p + \pi^+ + l^-$$

For very large energy, the neutrinos interact directly with the quark content of the nucleon, breaking it and producing more than one pion:

$$\nu_l + p \rightarrow p + N\pi + l^-$$

This is called CC *deep inelastic scattering* (CCDis). The energy threshold for a CC production is approximately the mass of the lepton in the case of ν_e and ν_μ and twice its mass in the ν_τ case. The predicted cross-sections for each of the interaction modes are shown in Fig. 1.4. The inclusive CC cross-section becomes linear above 1 GeV and around $0.7 \times 10^{-38} / E_\nu [cm^2 / \text{GeV}]$.

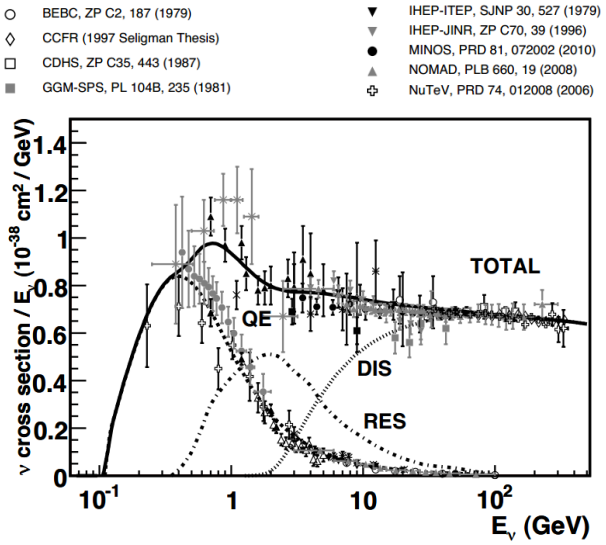

Fig. 1.4: Contributions of the different cross-sections to the total charged current cross-section (CC Inclusive) as function of energy. At low energy there is additional data: ▲ Baker *et al.*, 1982; ∗ Baranov *et al.*, 1979; ■ Ciampolillo *et al.*, 1979; ⋆ Nakajima

These interactions have their NC versions as well, where no lepton is produced and the neutrino only scatters with the nucleon, what is called, elastic scattering (ES) or produces charged or neutral pions. As the π^0 is an important background in the T2K ν_e analyses, we separate the NC producing a π^0 (NCπ^0) and the rest that does not create it (NCOther). A summary of all these processes is in Fig. 1.5 and a complete review of the neutrino cross-sections across the energy scales is reported in [88].

Neutrino interaction models predict cross-sections and kinematics of neutrinos scattering off bound or unbound nucleons. For bound nucleons within a nucleus, we call the neutrino-nucleon vertex the primary neutrino interaction vertex. The final state hadrons resulting from this interaction, for example

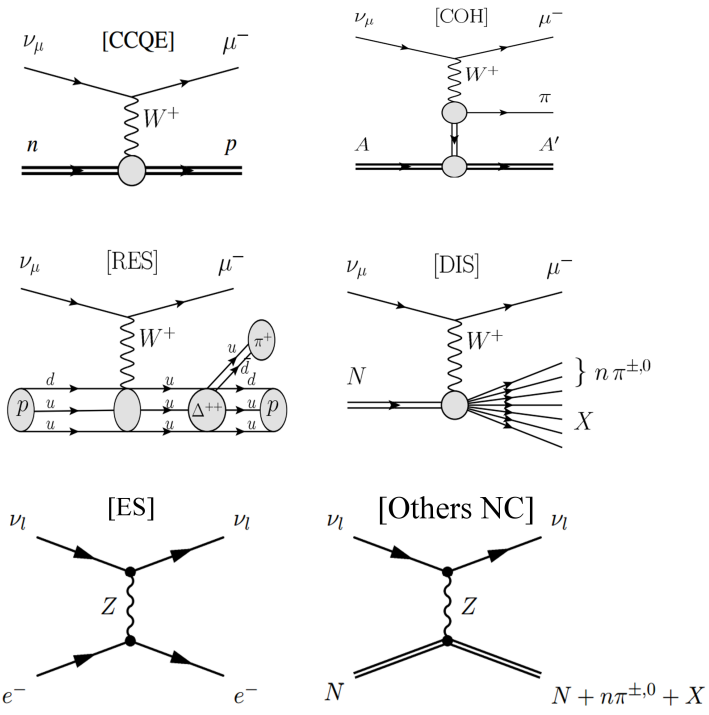

Fig. 1.5: Feynman diagrams for the typical neutrino interactions at T2K energies.

the proton from a CCQE interaction or the pion from a CCRes interaction, must propagate through the nuclear medium before observation. Since these particles interact via the strong force, there is a significant probability of re-interaction within the nucleus prior to escape. We refer to this re-interaction as a *final state interaction* (FSI). FSI affects the observable final state via particle absorption, scattering and particle production. This masks the interaction mode of the primary vertex, making direct measurements of pure CCQE, CCRes, etc. cross-sections difficult.

1.3 Neutrino oscillation theory

Neutrino oscillations are not possible in a model without neutrino masses. The unambiguous observation of the neutrino oscillation implies non-zero neutrino masses and hence, physics beyond the SM. In general, the flavour eigenstates $|\nu_\alpha\rangle$ ($\alpha = e, \mu, \tau, \dots$) will be related with the neutrino mass eigenstates

$|\nu_j\rangle$ $(j = 1, 2, 3, \dots)$ by linear combination

$$|\nu_\alpha\rangle = \sum_j U^*_{\alpha,j} |\nu_j\rangle \qquad\qquad |\nu_j\rangle = \sum_\alpha U_{\alpha,j} |\nu_\alpha\rangle$$

where $U_{\alpha,j}$ represent the terms of an unitary matrix U. In the standard three neutrino picture, this matrix is known as the **P**ontecorvo-**M**aki-**N**akaya-**S**akata (PMNS) matrix [116]. This expression is completely general for any number of neutrino flavour and mass eigenstates, so, to not lose generality, we consider the mixing of n neutrino with non-degenerate masses m_j.

If the mass eigenstates are different and non-degenerate, the flavour state $|\nu_\alpha\rangle$ will evolve in time following the time dependent Schrödinger equation. This phenomenon is known as neutrino oscillation and it is equivalent to the one observed in the quark sector driven by the **C**abbibo-**K**obayashi-**M**askawa (CKM) matrix [109]. After a time t, the probability that $|\nu_\alpha\rangle$ evolves to $|\nu_\beta\rangle$ is given, according to the quantum mechanics principles, by the scalar product

$$P_{\alpha\beta} = P(\nu_\alpha \to \nu_\beta) = |\langle \nu_\beta | \nu_\alpha(t) \rangle|^2 = |\sum_{j,k} U_{\beta,j} U^*_{\alpha,k} \langle \nu_j | T | \nu_k \rangle|^2$$

where T is the temporal evolution operator that has the form $T = e^{-i\mathcal{H}t}$, with $\mathcal{H}$ the Hamiltonian operator. In the approximation of the neutrino as a plane wave: $\mathcal{H}|\nu_j\rangle = E_j |\nu_j\rangle$, and the probability acquire the form

$$P_{\alpha\beta} = |\sum_k U_{\beta,k} U^*_{\alpha,k} e^{-iE_k t}|^2 = \sum_{j,k} U^*_{\alpha,j} U_{\beta,j} U_{\alpha,k} U^*_{\beta,k} e^{-i(E_j - E_k)t}$$

Provided that neutrinos are relativistic and are considered to have very small masses, they fulfill

$$E_j = \sqrt{m_j^2 + p_j^2} \approx p_j + m_j^2/2p_j \qquad\qquad p_j \approx E_j \approx E \qquad\qquad t \approx L$$

where p_j and E_j are the momentum and the energy for the eigenstate j, E is the energy associated to the neutrino flavour state and t and L are the time and the length traveled by the neutrino in the lab frame. Thus, we get

$$P_{\alpha\beta} = \sum_{j,k} U^*_{\alpha,j} U_{\beta,j} U_{\alpha,k} U^*_{\beta,k} e^{-i\frac{(m_j^2 - m_k^2)L}{2E}}$$

Developing last expression we get the general neutrino oscillation formula valid for n neutrino mass

states

$$P_{\alpha\beta} = \delta_{\alpha\beta} - 4\sum_{j>k} \Re(W^{jk}_{\alpha\beta}) \sin^2\left(\frac{\Delta_{jk}}{2}\right) \pm 2\sum_{j>k} \Im(W^{jk}_{\alpha\beta}) \sin(\Delta_{jk}) \tag{1.3}$$

where

$$W^{jk}_{\alpha\beta} = U^*_{\alpha,j} U_{\beta,j} U_{\alpha,k} U^*_{\beta,k} \qquad \Delta_{jk} = \frac{(m^2_j - m^2_k)L}{2E} \equiv \frac{\Delta m^2_{jk} L}{2E}$$

and we have used the unitary matrix condition

$$\sum_i = U^*_{\alpha,i} U_{\beta,i} = \sum_j U_{\alpha,j} U^*_{\beta,j} = \delta_{\alpha\beta} \tag{1.4}$$

The positive sign in the last term of Eq. (1.3) applies to neutrinos and the negative to anti-neutrinos. If this term is not null, the oscillations measured for neutrinos and anti-neutrinos are different and hence, this term is called the CP violation (CPV) term. In the neutrino disappearance case as $\alpha = \beta$, $W^{jk}_{\alpha\beta}$ is real and the CPV has no effect in the neutrino oscillation. The Eq. (1.3) has an oscillatory behaviour along the distance traveled by the neutrino, of period

$$L_T = \frac{4\pi E}{\Delta m^2_{jk}} \tag{1.5}$$

and an amplitude proportional to $W^{jk}_{\alpha\beta}$, combination of the matrix elements $U_{\alpha,i}$.

An unitary matrix, as the PMNS matrix, is the result of the product of $n(n-1)/2$ rotation matrices whose main block are

$$R = \begin{pmatrix} \cos\theta & \sin\theta e^{-i\delta} \\ -\sin\theta e^{-i\delta} & \cos\theta \end{pmatrix}$$

and a diagonal matrix containing n phases. Altogether, we have $n(n-1)/2$ mixing angles and $n(n+1)/2$ phases of which $2n-1$ can be absorbed redefining the wave function and hence, do not play any role in the oscillations. For the standard three neutrino case, we get 3 mixing angles θij and 1 complex phase δ. In neutrino experiments, the matrix elements are not measured directly, but it is assumed the

unitarity of the PMNS matrix and choose an appropriate parametrization. The most common is

$$U = \begin{pmatrix} 1 & 0 & 0 \\ 0 & c_{23} & s_{23} \\ 0 & -s_{23} & c_{23} \end{pmatrix} \begin{pmatrix} c_{13} & 0 & s_{13}e^{-i\delta} \\ 0 & 1 & 0 \\ -s_{13}e^{-i\delta} & 0 & c_{13} \end{pmatrix} \begin{pmatrix} c_{12} & s_{12} & 0 \\ -s_{12} & c_{12} & 0 \\ 0 & 0 & 1 \end{pmatrix}$$
$$= \begin{pmatrix} c_{12}c_{13} & s_{12}c_{13} & s_{13}e^{i\delta} \\ -s_{12}c_{23} - c_{12}s_{13}s_{23}e^{i\delta} & c_{12}c_{23} - s_{12}s_{13}s_{23}e^{i\delta} & c_{13}s_{23} \\ s_{12}s_{23} - c_{12}s_{13}c_{23}e^{i\delta} & -c_{12}s_{23} - s_{12}s_{13}c_{23}e^{i\delta} & c_{13}c_{23} \end{pmatrix} \tag{1.6}$$

where $c_{ij} \equiv \cos(\theta_{ij})$ and $s_{ij} \equiv \sin(\theta_{ij})$. If neutrinos are Majorana, there are some phases that cannot be absorbed by the neutrino mass eigenstates and they have to be taken into account. Nevertheless, the neutrino oscillation effect is the same regardless these phases, so there is no need to include them in this calculation.

1.3.1 Two neutrino approximation

The maximum of the neutrino oscillation effect is located at $L_T/2$ [Eq. (1.5)] from the neutrino source. As the mass eigenstates are separated by some orders of magnitude (see Section 1.4), an experiment in a given position is sensitive to only one Δm^2. In practice, we can neglect the terms in Eq. (1.3) where the dominant Δm^2 is not involved. It is equivalent to make the approximation of having only two effective neutrino mass eigenstates. In this case the PMNS matrix can be parametrized with only one mixing angle and none complex phases

$$U = \begin{pmatrix} \cos\theta & \sin\theta \\ -\sin\theta & \cos\theta \end{pmatrix}$$

and the complicated Eq. (1.3) becomes

$$P_{\alpha\beta} = \delta_{\alpha\beta} - |U_{\alpha 2}|^2 |U_{\beta 2}|^2 \sin^2\left(\frac{\Delta_{21}}{2}\right) \tag{1.7}$$
$$= \delta_{\alpha\beta} - (2\delta_{\alpha\beta} - 1)\sin^2(2\theta)\sin^2\left(1.27\Delta m^2[\,\mathrm{eV}^2]\frac{L[m]}{E[\,\mathrm{MeV}]}\right)$$

The oscillatory behaviour with respect to E/L can be appreciated in Fig. 1.6. The probability is exactly the same for neutrinos and for anti-neutrinos, as the term with $\mathrm{Im}(W^{jk}_{\alpha\beta})$ disappeared, so this

model cannot lead to CPV. The two neutrino approximation fits very well in most of the experimental situations, specially for the short base-line experiments were the standard oscillations are negligible.

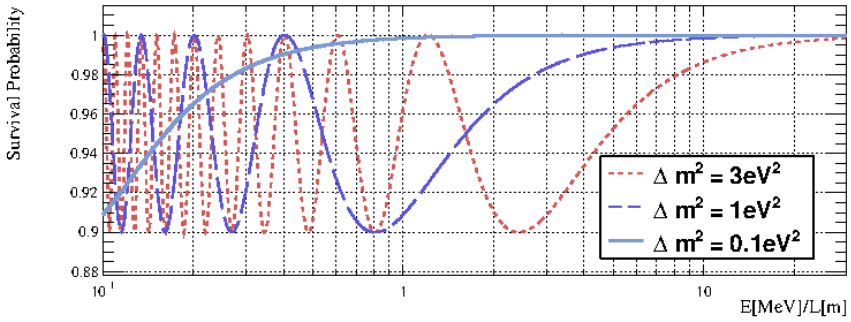

Fig. 1.6: Survival probability $P_{\alpha\alpha}$ as a function of the ratio E/L in the two neutrino approximation.

In practice, experiments do not have a monochromatic neutrino flux neither a perfect neutrino energy reconstruction, so what is measured is the average probability in an energy window given by

$$\langle P_{\alpha\beta} \rangle = \frac{\int dE \phi(E) \sigma(E) \epsilon(E) P_{\alpha\beta}(L/E)}{\int dE \phi(E) \sigma(E) \epsilon(E)} \tag{1.8}$$

where ϕ is the flux, σ is the neutrino cross-section for CC interactions and ϵ the efficiency of the neutrino interaction selection. The integral runs over the energy window. For $E/L \ll \Delta m^2$ we enter in the *fast oscillation regime*, where neutrinos of similar energy are in a different phase of the oscillation [Fig. 1.6]. In general, the neutrino energy is above the MeV scale, so experiments reach this regime for very long base-lines or when exploring large Δm^2. At this point the detector is not sensitive to the oscillatory behaviour and the probability becomes an averaged along the energy range and it approximates by

$$\langle P_{\alpha\beta} \rangle \approx \frac{\int dE P_{\alpha\beta}(L/E)}{\int dE} \approx \delta_{\alpha\beta} - (2\delta_{\alpha\beta} - 1)\frac{1}{2}\sin^2(2\theta) \tag{1.9}$$

So, for a very long base-line experiment we are not sensitive to Δm^2 and the oscillation effect is half of the maximum amplitude. The most sensitive position for an oscillation experiment is the first maximum, as the amplitude diminishes as we go further.

1.3.2 Matter effects

The presence of matter modifies the mixing angle and the oscillation wavelength. This occurs due to the coherent scattering of neutrinos with matter through the channels shown in Fig. 1.7. The NC

modes affect the same to all the neutrino families unlike the CC mode that only applies to ν_e since there are no μ or τ in stable matter. This is expressed by an effective potential V that affects to the ν_e and to be add to the Hamiltonian in vacuum

$$V = \pm\sqrt{2}G_F N_e$$

being G_F the Fermi constant and N_e the electron density in the medium. Positive sign applies to ν_e and negative to $\overline{\nu}_e$. When diagonalizing the total Hamiltonian, new effective oscillation parameters, θ_M for the mixing angle and Δm^2_M for the mass splitting are defined as

$$\frac{\Delta m^2}{4E_\nu} \equiv \Delta \to \Delta_M = \sqrt{(\Delta\cos 2\theta - V/2)^2 + (\Delta \sin 2\theta)^2}$$
$$\tan 2\theta \to \tan 2\theta_M = \frac{\Delta \sin 2\theta}{\Delta\cos 2\theta - V/2}$$

where θ and Δm^2 are the corresponding oscillation parameters in vacuum. If N_e changes smoothly (like within the Sun), the adiabatic condition applies and the mass eigenstates become also energy eigenstates, so that each of them evolve independently without mixing. However, the flavour composition depend on the density. For the so-called resonant density N_e^R that fulfills $V/2 = \Delta\cos 2\theta$, the eigenstates pass from being mainly ν_e to mainly ν_μ. This level crossing at the resonant point is called MSW effect [141]. The survival probability for a ν_e state in the adiabatic regime is

$$P_{ee} = \frac{1}{2}\left(1 + \cos 2\theta_M \cos 2\theta\right)$$

If $(\Delta m^2 \cos 2\theta)$ and $V/2$ have opposite signs, the level crossing does not occur, so the MSW effect only realizes for neutrinos if $\Delta m^2 > 0$ and for anti-neutrinos if $\Delta m^2 < 0$.

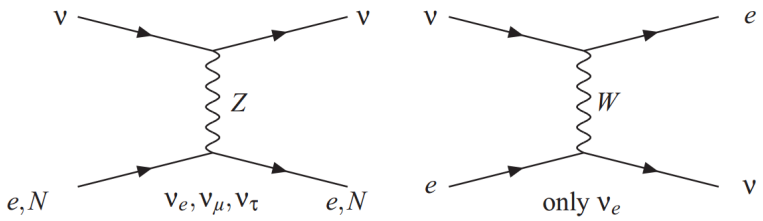

Fig. 1.7: Interactions of neutrinos with stable matter. The CC channel is only permitted for ν_e.

1.4 Neutrino oscillation measurements

Nowadays, the picture of the neutrino oscillation is almost complete. All the mixing angles and mass differences have been measured with a good precision. The first well established measurement was for θ_{23} in the atmospheric neutrinos studies of SuperKamiokande (SK) in 1998 [143] and only 14 years later the Daya Bay experiment [34] measured the last one: θ_{13}. A complete picture of the parameters for the neutrino oscillation is in Tab. 1.1.

This first reliable evidence of neutrino oscillations was revealed in the SK detector for atmospheric neutrinos. Cosmic rays interact with the atmosphere producing a shower of particles, like pions and kaons that decay producing four types of neutrinos: ν_μ, $\overline{\nu}_\mu$,ν_e and $\overline{\nu}_e$, in a approximate proportion of $2\nu_\mu$ per ν_e. A neutrino flux of typically $100\,\mathrm{m}^{-2}\mathrm{s}^{-1}\mathrm{sr}^{-1}\mathrm{GeV}^{-1}$ reaches the detector from every direction. For the ν_μ flux, SK showed an asymmetry on the number of events coming from above respect to the ones coming from below. This dependency on the zenith angle is due to the fact that neutrinos coming from above travel much less distance than the one coming from below, so the latter have time to oscillate. The neutrino survival probability is

$$P_{\mu\mu} = 1 - \sin^2(2\theta_{23}) \sin^2\left(1.27\Delta m^2_{31}[\,\mathrm{eV}^2]\frac{L[m]}{E[\,\mathrm{MeV}]}\right)$$

This effect was only seen for ν_μ's and not for ν_e's, so the hypothesis that the disappearance was due to interaction with the Earth was rejected. The neutrino oscillation model was confirmed [143] and the measured parameters were

$$\Delta m^2_{31} \sim 10^{-3}\,\mathrm{eV}^2 \qquad\qquad \sin^2(2\theta_{23}) > 0.82$$

Nowadays these parameters have been more precisely measured by accelerator experiments like K2K [63], MINOS [68] or T2K [54].

The second measurement was performed by the solar neutrino experiments and the reactor experiment KamLAND which study the *solar* parameters: Δm^2_{21} and θ_{12}. KamLAND is a 1kTon ultra-pure liquid scintillator detector located in Japan at $\sim 180\,\mathrm{km}$ average distance from 53 power reactors and that is very sensitive to the solar neutrino parameters [11]. As it is an experiment in vacuum, it is not sensitive to the sign of Δm^2, as both terms in Eq. (1.3) are symmetric under the permutation $i \leftrightarrow j$. On the other hand, solar experiments are sensitive to the sign of Δm^2 due to the strong matter effects, but

not to its absolute value. This is explained by two facts:

- Low neutrino energy: matter effects are negligible and the oscillations occur as in vacuum. They arrive to the Earth in the fast oscillation regime Eq. (1.9) so the detectors cannot observe any energy pattern, but just a depletion in the electron neutrino rate.

- High neutrino energy: The MSW effect realizes for neutrinos only if $\Delta m^2 > 0$ and the ν_e survival probability becomes independent from Δm^2

$$P_{ee} \simeq \sin^2 \theta_{12}$$

As the MSW effect is observed at high energy Fig. 1.2 by Homestake and SNO, Δm^2 must be positive. Hence, combining solar experiments with KamLAND we finally get:

$$\Delta m^2_{21} = 7.9^{+0.6}_{-0.5} \times 10^{-5}\,\text{eV}^2 \qquad\qquad \tan\theta_{12} = 0.40^{+0.10}_{-0.07}$$

The final important measurement concerning $\sin^2(2\theta_{13})$ was given by the T2K ν_e appearance analysis and by reactor experiments (Daya Bay [34, 35], Double Chooz [39] and RENO [36]) by observing $\overline{\nu}_e$ disappearance. In reactor experiments the $\overline{\nu}_e$ disappearance depends only on $\sin^2(2\theta_{13})$, the background is very small and the cross-section for IBD is very well known. This allows reactor experiments to perform a pure measurement of $\sin^2(2\theta_{13})$, while the accelerator ν_e appearance measurement depends also on the $\sin^2(2\theta_{23})$ and on the δ_{CP} phase. The most precise is the Daya Bay measurement [35]

$$\sin^2(2\theta_{13}) = 0.089 \pm 0.010(\text{stat}) \pm 0.005(\text{syst})$$

that exclude the non-oscillation hypothesis by 7.7σ, but the first evidence of a non-zero and a large $\sin^2(2\theta_{13})$ was given by T2K in 2011 [37].

A global fit in the general three neutrino picture has been done in [87], yielding the results showed in Tab. 1.1. The current picture of the neutrino oscillation theory is summarized in Fig. 1.8.

Parameter	best-fit
$\Delta m^2_{21}[\mathrm{eV}^2]$	$7.54^{+0.26}_{-0.22} \times 10^{-5}$
$\lvert\Delta m^2\rvert[\mathrm{eV}^2]$	$2.43^{+0.06}_{-0.10}(2.42^{+0.07}_{-0.11}) \times 10^{-3}$
$\sin^2(\theta_{12})$	$0.307^{+0.018}_{-0.16}$
$\sin^2(\theta_{23})$	$0.386^{+0.024}_{-0.21}(0.392^{+0.039}_{-0.22})$
$\sin^2(\theta_{13})$	$0.0241 \pm 0.0025(0.0244^{+0.0023}_{-0.0025})$

Table 1.1: Most updated measurements for the oscillation parameters in the complete three neutrino picture. They correspond to the best fit values after a global fit of all the available data for the neutrino oscillation experiments [87]. Δm^2 represents the mass difference from the third state to the mean of the first and second mass states. The results in brackets are for inverted hierarchy while the rest is for the normal one.

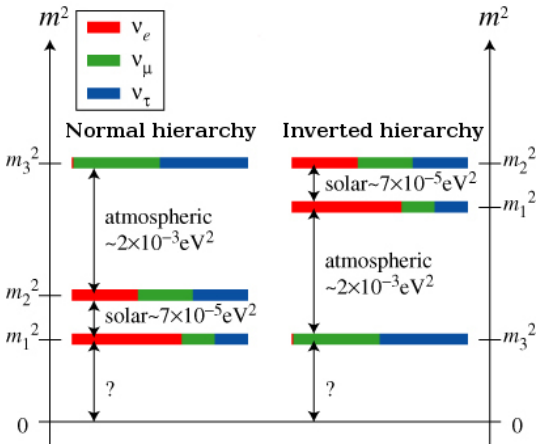

Fig. 1.8: Illustration of the mass eigenstate ordering. On the left there is the so-called normal hierarchy ($\Delta m^2_{31} > 0$) and on the right the inverted hierarchy ($\Delta m^2_{31} < 0$). Colors correspond to the mixing of the weak flavours with the mass eigenstates given by the PMNS matrix terms.

1.5 Future challenges for oscillation neutrino experiments

There are still some open questions concerning the art of the neutrino oscillations. Future experiment must reach enough precision to be sensitive to:

- Measure whether $\sin^2(2\theta_{23})$ is maximal or not: if θ_{23} is not maximal it is important to measure the octant of the angle.

- Mass hierarchy: the sign of the larger mass splitting is unknown yet. As Δm^2_{31} is slightly smaller in the inverted than in the normal hierarchy (see Fig. 1.8), we can measure it from very precise experiments in vacuum [114]. On the other hand, long base-line experiments with large matter effects is another technique to measure this unknown.

- CPV: this can be observed in beam accelerator-based neutrino oscillation experiments that operate with neutrinos and anti-neutrinos. As the value of $\sin^2(2\theta_{13})$ is large, beam experiments become a realistic choice for this measurement.

More intense beams and larger detectors is the proposal of the main next generation neutrino experiments. On the short term period, the NOνA experiment [69] is designed to be more sensitive to matter effects and hence measuring the mass hierarchy. In addition, together with the T2K data can constrain more the CPV phase in the near future. LBNE [64] and LBNO [65] are good candidates future long base-line experiments to measure both aspects: mass hierarchy and CPV. Specially sensitive to CPV is the Hyper-Kamiokande proposal [62]. It correspond to the next upgrade of the T2K experiment with a much larger far Cerenkov detector and an improved near detector.

Chapter 2

Sterile neutrinos

We have seen in the previous chapter that the three-flavour neutrino mixing is very well established and supported by many experimental data. Nevertheless, there are several experiments that observe an unexpected behaviour in their measurements of ν interaction rates that cannot be explained in the context of the PMNS matrix. They are essentially short base-line (SBL) experiments with an abnormal number of ν interaction that does not match the expectation. These experiments strongly depend on the ν flux prediction and cross-sections models and a solution to these anomalies could be corrections on those quantities due to systematic errors or backgrounds not properly accounted.

Another solution is proposing non-standard neutrino oscillations what implies new physics. In these experiments, the flight path of the neutrino is of the order of meters and in general the ratio L/E is very small. Provided that the standard mass differences are $\Delta m^2_{21} \sim 10^{-5}\,\mathrm{eV}^2$ and $\Delta m^2_{31} \sim 10^{-3}\,\mathrm{eV}^2$, the three-flavour oscillations in the regions explored by these experiments is negligible [Eq. (1.5)]. Then, to explain this in the oscillation scenario, we need to invoke an additional neutrino with a large $\Delta m^2 \sim 1\,\mathrm{eV}^2$. This neutrino cannot be couple to the Z^0 boson as we would see it in the Z^0 decay experiments [10]. Hence, it does not feel the weak interaction, so they are called *sterile* neutrinos. They would only reveal themselves by the mixing with the others *active* species.

Active and sterile neutrino mixing was originally proposed by Pontecorvo in one of its first models [129].

2.1 Sterile neutrino theory

A sterile neutrino is a right-handed neutrino that transforms as a singlet under SU(2). The SM does not include them, so we have to extend it to take them into account. As they are singlets they do not take part in the weak interactions except by mixing with active neutrinos.

To play a role in the oscillations, they must have a mass. A Majorana mass term can be built for

the right-handed neutrinos. This term is added to the Dirac mass term and Majorana mass term for left-handed neutrinos mentioned in Section 1.2. For simplicity, we study the case of one single neutrino generation (one active and one sterile), but the scenario can be extended easily for n neutrinos. The general neutrino mass term in the Lagrangian is then

$$-\mathcal{L}_M^\nu = m_D(\bar{\nu}_L\nu_R + \bar{\nu}_R\nu_L) + \frac{1}{2}m_L(\bar{\nu}_L C\bar{\nu}_L^T + \nu_L^T C\nu_L) + \frac{1}{2}m_R(\bar{\nu}_R C\bar{\nu}_R^T + \nu_R^T C\nu_R)$$

where we have sequentially: the Dirac mass term and the Majorana mass terms for the left-handed and right-handed neutrino fields. It can be written defining the mass matrix M:

$$-\mathcal{L}_M^\nu = \frac{1}{2}\begin{pmatrix} \bar{\nu}_L & \bar{\nu}_L^c \end{pmatrix} \underbrace{\begin{pmatrix} m_L & m_D \\ m_D & m_R \end{pmatrix}}_{M} \begin{pmatrix} \nu_R^c \\ \nu_R \end{pmatrix} + \text{h.c.} \tag{2.1}$$

This is the so-called Dirac-Majorana mass term and it has the same structure of a Majorana mass term. After diagonalizing the matrix M, it acquires the form

$$-\mathcal{L}_M^\nu = \frac{1}{2}\sum_{k=1,2} m_k\bar{\nu}_k\nu_k$$

where m_k are the mass eigenvalues and ν_k are the mass eigenstates that fulfill

$$\nu_k = \nu_L + \nu_R^c = \nu_k^c$$

They are two Majorana mass eigenstates, being the flavour eigenstates linear combination of them. It allows mixing between active and sterile neutrinos of the same chirality. It is interesting to highlight several special cases:

The pure Dirac case appears by imposing $m_L = m_R = 0$. For the case with 3 sterile neutrinos, they are identified as the right-handed component of the Dirac neutrino field, similar to the case discussed in Section 1.2.

For $m_D = 0$ we obtain the pure Majorana case where the sterile neutrino decouples and active and sterile neutrinos do not mix each other.

Considering a very heavy sterile neutrino $m_R \gg m_D$ we get the so-called *see-saw* mechanism, discussed in Section 1.2. The diagonalization of M yields one light neutrino mass eigenstate $\sim m_D^2/m_R$ and a

very heavy state of mass m_R. The light state is mainly active while the heavier one is mainly sterile. Both are pure Majorana particles. In this case, the SM is considered a good low energy theory as it is justified that we only find three active neutrinos, while the sterile neutrinos are out of scope.

Nevertheless, regardless a very heavy sterile neutrino could exist, we are interested in relatively light sterile neutrino, as they are the ones involved in the SBL anomalies (see Section 2.2). This scenario appears in the case of m_R below the symmetry breaking scale and hence, the SM is not a good effective theory anymore. Furthermore, to get a significant mixture of active and sterile states, we need small but non-zero Dirac and Majorana masses, being a strong challenge for a theory. On the other hand, neutrino oscillation are the same regardless the type of mass term taken into account (see Section 1.3). So the way the sterile neutrino is introduced in an extension of the SM does not affect to the neutrino oscillation effect.

2.1.1 Light sterile neutrino oscillations

In general, if we include n sterile right-handed neutrinos we have n new flavour states $|\nu_s\rangle_i$ and n new mass eigenstates $|\nu\rangle_{i+3}$ where i goes from 0 to n. The Fig. 2.1 illustrates this. The sterile and active states of same chirality can mix each other and lead to SBL oscillation if the new neutrino mass state is of $m \sim 1\,\text{eV}$. In this scenario the formula Eq. (1.3) is still valid and, in the following, we analyze two cases: models with only 1 or 2 sterile neutrinos.

The 3+1 neutrino model

The minimal extension of the neutrino standard model that we can built is adding to the active species one new state of mass m_4 that corresponds to a mostly sterile neutrino state s. Then, the PMNS matrix becomes a 4×4 matrix with new elements $U_{\alpha 4}$ and U_{si}, where $\alpha = e, \mu, \tau, s$ and $i = 1, \ldots, 4$. In the study of a $\Delta m^2 \sim 1\,\text{eV}^2$ at SBL, the standard oscillations are negligible, so we can consider the three active mass states as one effective state and approximate by the two neutrino model [Section 1.3.1]. The survival probability of a ν_e or a ν_μ is given by Eq. (1.3) and acquires the form:

$$P_{ee} \equiv P(\nu_e \to \nu_e) = 1 - 4|U_{e4}|^2(1 - |U_{e4}|^2)\sin^2\left(1.27\,\Delta\text{m}^2_{41}[\,\text{eV}^2]\frac{\text{L}[\,\text{m}]}{\text{E}[\,\text{MeV}]}\right) \tag{2.2}$$

$$P_{\mu\mu} \equiv P(\nu_\mu \to \nu_\mu) = 1 - 4|U_{\mu 4}|^2(1 - |U_{\mu 4}|^2)\sin^2\left(1.27\,\Delta\text{m}^2_{41}[\,\text{eV}^2]\frac{\text{L}[\,\text{m}]}{\text{E}\,\text{MeV}}\right) \tag{2.3}$$

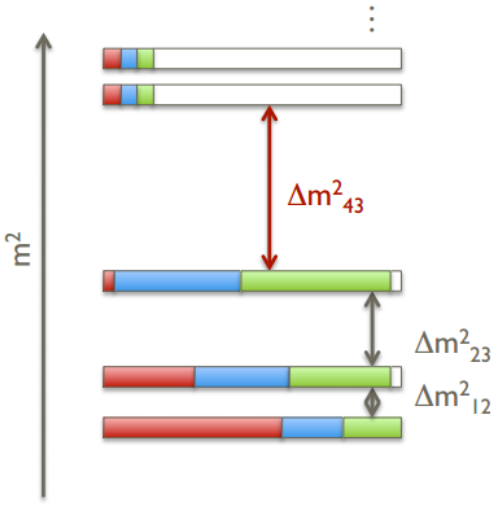

Fig. 2.1: Mass eigenstates in the 3+n neutrino model. The three states at the bottom correspond to the mostly active flavours. The colors indicate the mixing with the flavour eigenstates. A new sterile flavour ν_s (blank) has been added that mixes mildly with the three standard mass eigenstates and strongly with the new ones.

The ν_e and ν_μ disappearance probabilities are independent each other, since steriles can mix with one flavour and not with the other. For the case of oscillation between actives species we obtain:

$$P_{e\mu} \equiv P(\nu_\mu \to \nu_e) = P(\nu_e \to \nu_\mu) = 4|U_{e4}|^2|U_{\mu 4}|^2 \sin^2\left(1.27\,\Delta m^2_{41}[\,\mathrm{eV}^2]\frac{\mathrm{L[\,m]}}{\mathrm{E\,MeV}}\right) \tag{2.4}$$

where we have invoked the unitarity of the PMNS matrix [Eq. (1.4)].

From Eqs. (2.3) and (2.4), the maximum of the oscillations occur at the same L/E ratio and the period [Eq. (1.5)] is the same in the three cases. Like in the standard oscillations, we parametrize the new matrix defining 3 new mixing angles

$$\sin^2(2\theta_{ee}) = 4|U_{e4}|^2(1-|U_{e4}|^2)$$
$$\sin^2(2\theta_{\mu\mu}) = 4|U_{\mu 4}|^2(1-|U_{\mu 4}|^2)$$
$$\sin^2(2\theta_{e\mu}) = 4|U_{e4}|^2|U_{\mu 4}|^2$$

This is the most common convention and the one we adopt along this thesis. If $|U_{e4}|, |U_{\mu 4}|$ are small, at first order we have

$$\sin^2(2\theta_{e\mu}) \approx \frac{1}{4}\sin^2(2\theta_{ee})\sin^2(2\theta_{\mu\mu}) \tag{2.5}$$

This means that the appearance channel is coupled with the disappearance, so observing ν_e appearance implies both ν_e and ν_μ disappearance to exist. It is important to remark that CPV is not allowed in the two neutrino approximation, so in this model, neutrino and anti-neutrino behave in the same way.

The 3+2 and 1+3+1 model

Adding two sterile neutrinos introduces much more freedom in the model. The oscillation probabilities become more complicated and we will only treat these models qualitatively. One more sterile neutrino implies an extra Δm^2, but also the possibility of having a complex phase that would drive the CPV at the SBL experiments. These models allow different behaviour for neutrinos and anti-neutrinos.

We distinguish a model in which two steriles are heavier than the three standard states called 3+2 and another with one state heavier and one lighter, called 1+3+1. The latter model implies that the standard mass eigenstates have masses of the order of $\Delta m^2 \sim 1\,\mathrm{eV}^2$. The performances of these models on reproducing the neutrino experiments data are discussed in Section 2.2.4.

2.2 Experimental hints to sterile neutrinos

There are some oscillation experiments difficult to be reconcile with the standard three neutrino framework. These anomalies can be the smoking gun of the existence of sterile neutrinos.

The first experiment that found an abnormal neutrino rate was the LSND experiment in 1998. It reports an unexplained excess of ν_e event interactions at SBL compatible with $\nu_\mu \to \nu_e$ oscillation for a $\Delta m^2 \sim 1\,\mathrm{eV}^2$. Some other hints were found in calibration with intense radioactive sources of solar neutrino detectors with Gallium. The MiniBooNE experiment, designed to test LSND, found excesses of ν_e at low energies using neutrinos and anti-neutrinos. The most recent piece of the puzzle appeared in 2010 with a re-evaluation of the neutrino flux at nuclear power plants. The new flux over-predicts the observed neutrino rates leading to a general deficit of $\overline{\nu}_e$ measured in the reactors.

Together with these anomalies that can be considered evidences of sterile neutrinos, there are other experiments that, on the contrary, perfectly agree with the standard oscillations. Namely, the KARMEN experiment, the ν_μ disappearance searches at SciBooNE/MiniBooNE and the MINOS experiment.

We will start describing the SBL ν_e disappearance experiments in Section 2.2.1, stressing the anomalies

in reactors and Gallium experiments, followed by the ν_e appearance in Section 2.2.2, ν_μ disappearance in Section 2.2.3, a discussion about the global picture in Section 2.2.4 and a summary in Section 2.2.5.

2.2.1 $\nu_e \to \nu_s$: ν_e disappearance

We find two groups of anomalies known as the reactor anti-neutrino anomaly and the gallium anomaly. They both observe a deficit in the ν_e interaction rates near the neutrino source for neutrino energies of the order of the MeV. Interpreting this depletion as ν_e disappearance in the 3+1 model [Section 2.1.1], these experiments lead to measurements on $\sin^2(2\theta_{ee})$ and Δm^2_{41}.

The reactor anti-neutrino anomaly

Reactors are a powerful source of neutrinos. The β^- decay of a nuclei rich in neutrons provides a flux of $\sim 10^{20}\overline{\nu}_e/s$ at the core, with an energy of the order of 1 MeV. $\overline{\nu}_e$ are observed at detectors through IBD. An accurate theoretical prediction of this flux is very difficult as it needs precise core monitoring, knowledge of branching ratios of every decay chain and anti-neutrino cross-sections.

The thermal power is continuously monitored and the $\overline{\nu}_e$ flux is predicted from the fission rate. Each fission triggers a chain of, typically, 6 beta decays that produces 6 $\overline{\nu}_e$ per fission. However, in practice there are many decay branches with many nuclei of different charges. So the total $\overline{\nu}_e$ product is the sum of all of them. Finally the $\overline{\nu}_e$ flux is used to calculate the positron energy spectrum observed at detectors through IBD. The cross-section for this process has been measured to be consistent with the prediction at the 1.4% level [81] and it is:

$$\sigma = \frac{2\pi^2}{m_e^5 f_{p.s.} \tau_n} E_e p_e \times 10^{-42}\,\mathrm{cm}^2$$

where m_e, E_e and p_e are the mass, energy and momentum of the positron when the recoil of the neutron is neglected, $f_{p.s.} = 1.7152$ is the phase-space factor of the free neutron, including outer radiative corrections, and τ_n the neutron lifetime, precisely measured with an uncertainty of 0.2% [19].

A calculation of the $\overline{\nu}_e$ flux from first principles is very difficult and the errors reach the 10% level, so a data-driven prediction is needed. The first one was performed in the 1980s at the Grenoble reactor of ILL [84]. They measured the electron energy distribution (coming from the β^-) and inferred the $\overline{\nu}_e$ flux as both are directly related. The final errors were of the order of 5% and the prediction was in

agreement with following reactors: ILL-Grenoble [105], Goesgen [145], Rovno [8], Krasnoyarsk [113], Savannah River [99] and Bugey [82].

In 2010 the situation changes due to three factors:

- A more precise flux calculation was developed to be used in the Double Chooz experiment [39]. This new calculation is based on an *ab initio* approach where the total $\overline{\nu}_e$ flux is predicted from the sum of all beta-branches of all fission products modeled by a simulation. The final conclusion is that the flux is predicted to be 3% larger than the standard one [122].
- More precise techniques leads to better knowledge of the neutron life time whose measurement decreased in the past 30 years, increasing the predicted cross-section of the IBD by 1%.
- The long-lived isotopes accumulating in the reactors are taken into account increasing the flux by 1%.

All the reactor neutrino experiments need to be re-evaluated in this new scenario. Since in the past, experiments presented a good agreement, currently there appears a slight deficit mostly compatible within 1σ if the experiments are considered individually. However, the overall ratio, if all the experiments are combined, becomes 0.927 ± 0.023 (Fig. 2.2 [119]) (being 0.980 ± 0.024 with the old flux). Then, the significance of the deficit turns to be of 3.0σ. This the so-called *reactor anti-neutrino anomaly*.

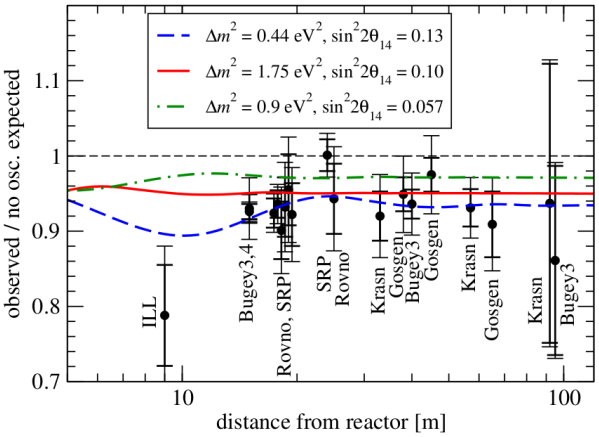

Fig. 2.2: Ratio between the measured and predicted $\overline{\nu}_e$ flux at the different reactors for experiment ordered by base-line distance . A deficit of 3σ is present in the global fit [122]. Three cases for ν_e disappearance due to sterile neutrino mixing are shown for illustration.

Two kinds of studies can be performed to measure the oscillation parameters: a rate only analysis and a rate plus $\overline{\nu}_e$ energy shape analysis. The first one is a simple counting experiment while the second

also includes the energy spectrum information. The study with rate and shape informations [110] is compatible with sterile oscillation with parameters $|\Delta m^2_{41}| = 1.75\,\mathrm{eV}^2$ and $\sin^2(2\theta_{ee}) = 0.10$, excluding the only active oscillation by 99.7%CL. The allowed regions in the oscillation parameter space for $\sin^2(2\theta_{ee})$ and Δm^2_{41} are given in Fig. 2.3.

A complete picture with all the reactor experiments at short and long base-lines (LBL) as a function of the distance is shown in Fig. 2.4.

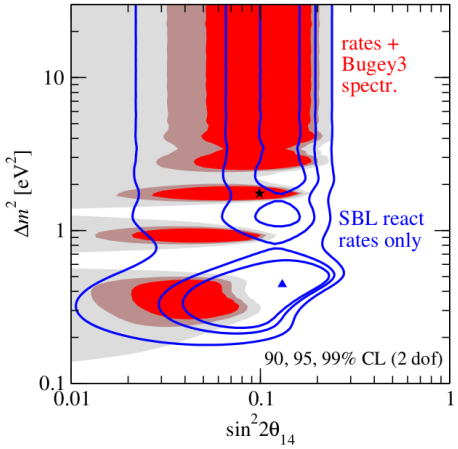

Fig. 2.3: Δm^2_{41}, $\sin^2(2\theta_{ee})$ plane of the new oscillation parameters for the hypothetical neutrino sterile in the reactor anomaly. The blue line represents the rate-only analysis, while the colored regions shows the result with also the $\overline{\nu}_e$ energy shape information.

The gallium anomaly

The GALLEX ([107], running during 1991-1997) and SAGE ([44, 45], running during 1989-2010) experiments were designed to study the solar neutrino problem. As Homestake, they detect neutrino interactions by IBD. The relevant feature of these experiments is the usage of ^{71}Ga instead of ^{37}Cl, whose threshold for IBD is much smaller (233 keV instead of 814 keV), allowing to investigate the whole neutrino energy range, especially the pp flux that is the most intense source [Fig. 1.1]. In addition, SAGE and GALLEX are very massive detectors of about 50 and 30 tonnes respectively.

They were calibrated using intense radioactive sources located inside the tanks. ^{51}Cr and ^{37}Ar were chosen and neutrinos were produced by electron capture:

$$e^- + {}^{51}Cr \rightarrow {}^{51}V + \nu_e$$
$$e^- + {}^{37}Ar \rightarrow {}^{37}Cl + \nu_e$$

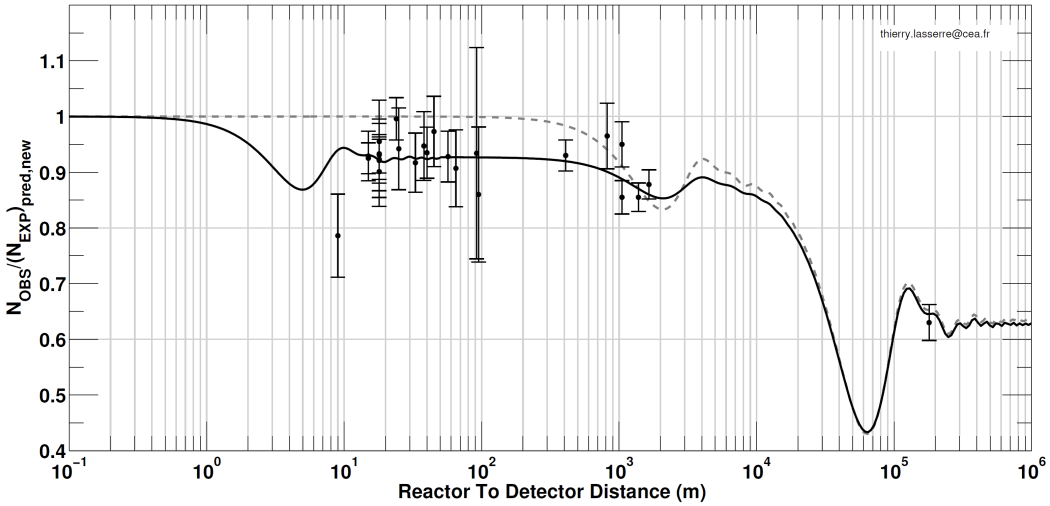

Fig. 2.4: Ratio of the $\overline{\nu}_e$ event with respect the prediction for reactor experiments at different baselines. For illustration, the 3+1 model is shown in black while the standard oscillation hypothesis is in dotted gray. The first dip and the ratio lower than 1 up to 1 km for the 3+1 model is due to the sterile neutrino oscillation. The 19 experiments that compose the reactor anomaly are the ones below 100 m. The second dip is driven by the atmospheric oscillations where detectors like Palo Verde [23], Chooz [58], Double Chooz [39] or Daya Bay [35] are located and the third dip is due to solar oscillations with the KamLAND [11] experiment exploring that region.

The dynamics of these interactions (energy of the ν_e, cross-sections and branching ratios) are known with high precision so that they are good candidates for detector calibration. The amount of radioactive material is the only parameter needed to calculate the ν_e flux. The ν_e are detected in the same way as the solar neutrinos using the reaction

$$\nu_e + {}^{71}Ga \rightarrow {}^{71}Ge + e^-$$

whose cross-section is very well known from measurements of electron capture in ${}^{71}Ge$. After the exposure of typically 1 month, the ${}^{71}Ge$ is chemically extracted and Germane is produced (GeH^4) to be used as a proportional counter to measure the amount of ${}^{71}Ge$. This technique is applied several times during the years of running. After the exposure, the amount of Ge was smaller than expected as shown in Fig. 2.5, where the gray band shows the best fit value that corresponds to a ratio with respect to the prediction of $R = 0.87 \pm 0.05$ [46]. The neutrino flight path is of the order 1 m so that we can explore regions of $\Delta m^2_{41} \sim 1\,\mathrm{eV}^2$. The best fit values for the 3+1 model for the gallium anomaly are

$$\sin^2(2\theta_{ee}) = 0.50,\ \Delta m^2_{41} = 2.24\,\mathrm{eV}^2$$

with a significance of 2.7σ, being the allowed parameter region in Fig. 2.6.

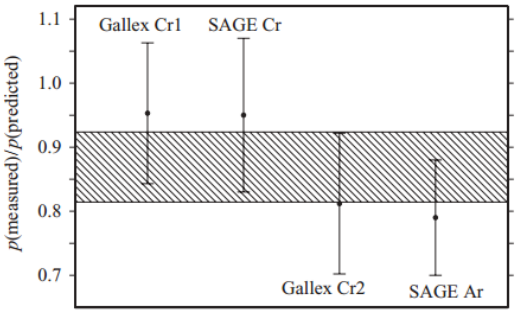

Fig. 2.5: Ratio for the measured and predicted production of ^{71}Ge by IBD from artificial sources inside the GALLEX and SAGE gallium detectors. The unexpected low interaction rates is the so-called *gallium anomaly*.

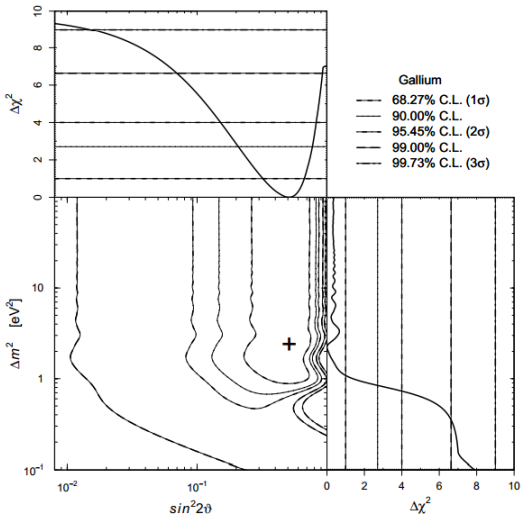

Fig. 2.6: Allowed regions for the oscillation parameters in the $\nu_e \to \nu_s$ hypothesis for the gallium anomaly, [97].

Other experiments

Solar neutrinos Experiments measuring the solar neutrino flux are Chlorine [33], GALLEX/GNO [108], SAGE [45], Super-Kamiokande I-IV [47], SNO [131] and Borexino [38]. Also the KamLAND [11] results are included in this set as it is a very long base-line neutrino experiment. Considering the 3+1 model, the survival probability of the ν_e becomes

$$P^{SUN}_{\nu_e \to \nu_e} \simeq P^{st}_{\nu_e \to \nu_e} \left(1 - 2(|U_{e3}|^2 |U_{e4}|^2)\right)$$

where $P^{st}_{\nu_e}$ is the ν_e survival probability with standard oscillations. Therefore U_{e3} and U_{e4} are highly degenerate as they have the same effect suppressing the survival probability. Nevertheless, in the presence of steriles there are corrections of $P^{st}_{\nu_e\to\nu_e}$ in the case that $|U_{e3}|^2 \neq 0$ or $|U_{e4}|^2 \neq 0$ as $|U_{e1}|^2 + |U_{e2}|^2 = 1 - (|U_{e3}|^2 + |U_{e4}|^2)$. In addition, as the sterile do not feel the NC potential, it leads to modifications of the probability if we include sterile species. Specifically, the SNO measurement on NC is able to measure the probability $1 - P^{SUN}_{\nu_e\to\nu_s}$ that breaks the degeneracy of U_{e3} and U_{e4}.

The allowed parameter region is just a straight vertical line as shown in Fig. 2.7 because this measurement is not sensitive to Δm^2 due to the fast oscillations. The contour at the 95%CL excludes partially the gallium anomaly.

Cross-section on carbon measurements KARMEN [91] and LSND [14] experiments measure the ν_e cross-section in carbon in function of the energy

$$\nu_e + {}^{12}C \to {}^{12}N_{gs} + e^-$$

As both measurements are consistent each other as well as with the prediction, they set some constraints to the ν_e disappearance channel. This analysis provides the confidence region shown in Fig. 2.7, that agrees with the solar results and excludes part of the gallium anomaly.

Long base-line reactor experiments Reactor experiments with a base-line of the order of $\sim 1\,\text{km}$ are included in this category. These experiments are Palo Verde [23], Chooz [58], Double Chooz [39], Daya Bay [35], RENO [36]. They are not sensitive to the sterile neutrino oscillation pattern as the neutrinos arrive in the fast oscillation regime. Then, they only measure an overall ratio on the number of events as in the solar case. To break the degeneracy of U_{e3} and U_{e4}, the precise measurement of $\sin^2(2\theta_{13})$ from Daya Bay and RENO is needed. The allowed region is shown in Fig. 2.7, excluding slightly more than the solar constraint.

2.2.2 $\nu_\mu \to \nu_e$: ν_e appearance

We study three neutrino beam experiments: LSND and MiniBooNE that present anomalies, and KARMEN that is compatible with the standard oscillations. They study the $\nu_\mu \to \nu_e$ oscillation and hence are sensitive to the parameter $\sin^2(2\theta_{e\mu})$ and Δm^2_{41}.

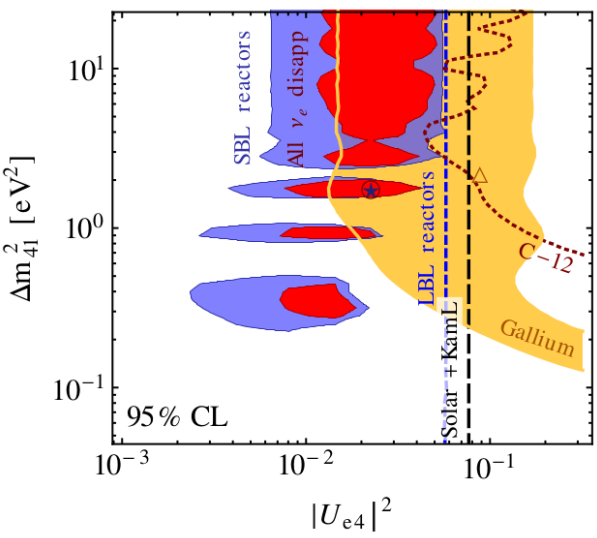

Fig. 2.7: Allowed regions at the 95%CL for the space of oscillation parameters. It shows the reactor anomaly, gallium anomaly, LBL reactor experiments and the solar neutrino results including KamLAND. The contour for the global analysis of the ν_e ($\overline{\nu}_e$) disappearance measurements discussed in Section 2.2.4 is provided as well.

The LSND experiment

The LSND experiment (1993 - 1998, [14]) in Los Alamos National Laboratory (LANL, US) searched for ν_e appearance in a $\sim 30\,\text{MeV}$ ν_μ beam at 30 m from the source. The ratio L/E is optimal for the study of $\Delta m^2_{41} \sim 1\,\text{eV}^2$.

Protons are accelerated up to 800 MeV thanks to the LAMPF accelerator and strike a 30 cm long water target producing π^+ that decay at rest producing ν_μ and μ. The background coming from $\mu^+ \to e^+ + \overline{\nu}_\mu + \nu_e$ is expected to be 10^{-3} of the ν_μ flux. The dominant ν_μ component travels 30 m until a 167t mineral oil Cerenkov detector that detects the $\overline{\nu}_e$ IBD. Thus, the detector is completely transparent to $\overline{\nu}_\mu$ and only $\overline{\nu}_e$ events can be detected. An excess of data is observed [4], compatible with $\overline{\nu}_e$ appearance in a $\overline{\nu}_\mu$ beam due to SBL oscillations. The allowed parameter space presented at Fig. 2.9 shows that the results are compatible at the 99%CL with

$$\Delta m^2_{41} > 1\,\text{eV}^2 \quad \sin^2(2\theta_{e\mu}) \sim 10^{-3} \tag{2.6}$$

The KARMEN experiment

The KARMEN experiment (1986 - 2002) uses the ISIS synchrotron at Rutherford Appleton Laboratory (RAL, UK) [91]. It presents many similarities with the LSND experiment. It looks for the same signal as LSND in the same neutrino energy range, through the same detection signature (IBD) and at almost the same distance (17.7 m).

The detector is a segmented liquid scintillator of 56t located at an angle of 100° from the beam direction. It compensates the smaller fiducial mass with a very good energy resolution and a smaller background than LSND (approximately a factor of two smaller). The final e^+ selection shows no discrepancies with the predicted backgrounds. They observe 15 events with respect to a prediction of 15.8 ± 0.5 for background only [12]. These results exclude the ν_e appearance due to oscillations to steriles at 90%CL as it is showed in Fig. 2.9, so it is strongly in tension with the LSND results.

The MiniBooNE experiment

The MiniBooNE experiment at Fermilab (US) collects data since 2002 in both neutrino [2] and anti-neutrino modes [3] using a beam with a mean energy of 0.7 GeV. The usage of magnetic horns allows to focus or defocus the mesons depending on their charge, and hence to enhance the neutrino beam with ν_μ or $\overline{\nu}_\mu$.

The neutrinos travel 540 m arriving to a spherical Cerenkov detector at $\sim$ 500 m filled with 800t of mineral oil (CH_2), and interact with the Carbon nuclei through CC interactions

$$\text{Neutrino mode:} \quad \nu_e + C \rightarrow C^* + p + e^-$$
$$\text{Anti-neutrino mode} \quad \overline{\nu}_e + C \rightarrow C^* + n + e^+$$

The selected events for both runs are shown in Fig. 2.8. They both show an unexpected excess at low energy that lead the allowed regions in the oscillation parameter space shown in Fig. 2.9.

2.2.3 $\nu_\mu \rightarrow \nu_s$: ν_μ disappearance

The ν_μ disappearance analyses at SBL are sensitive to the 3+1 model parameters $\sin^2(2\theta_{\mu\mu})$ and Δm^2_{41}. Up to date, none of the experiments has shown evidence of ν_μ or $\overline{\nu}_\mu$ disappearance, what

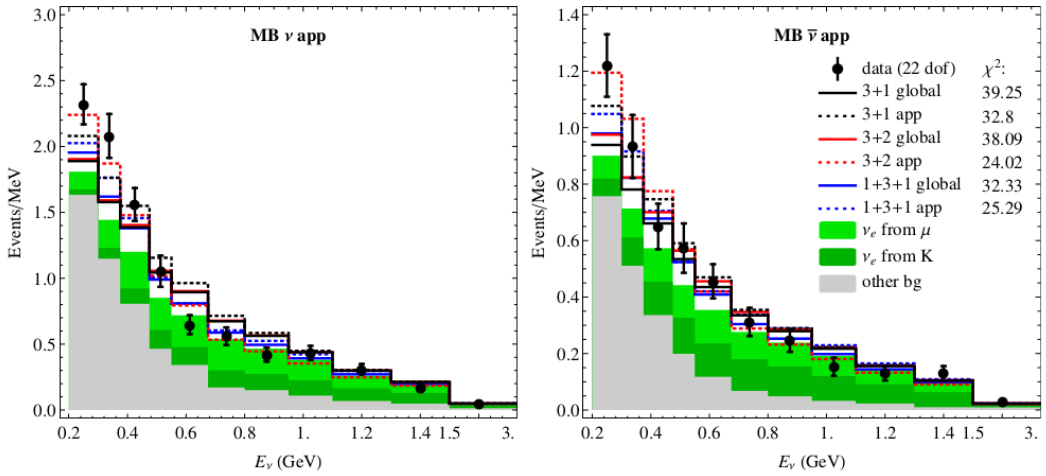

Fig. 2.8: Reconstructed neutrino energy of the final selected events for the ν_e on the left and $\overline{\nu}_e$ on the right at MiniBooNE.

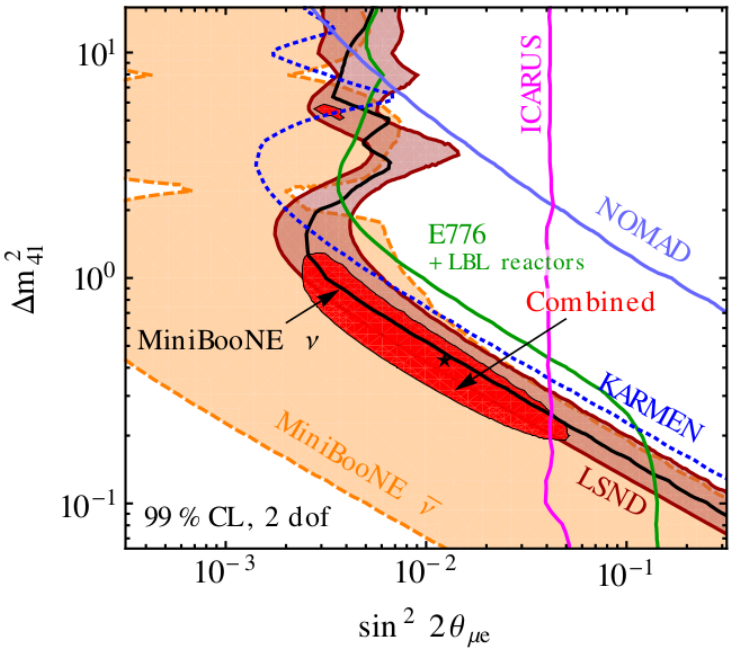

Fig. 2.9: Allowed oscillation parameter region for the LSND and MiniBooNE anomalies along with the not abnormal KARMEN experiment. Some other experiments as well as the result for a global fit of all of them are shown [110].

presents serious problem of consistency with the $\nu_\mu \rightarrow \nu_e$ appearance measurement for LSND and MiniBooNE, as discussed in Section 2.1.1.

MiniBooNE and SciBooNE

SciBooNE is a detector operated in the same beam line as MiniBooNE. It is located at 100 m from the source, closer than MiniBooNE (540 m), so it plays the role of near detector in the joint study. The SciBooNE detector is made of a fully active scintillator detector of 16t (SciBar), an electronic calorimeter and a muon range detector. In both experiments ν_e CC interactions are detected. The sample of stopped muons in SciBooNE is fitted together with the sample of muons detected at MiniBooNE.

A good agreement with the expectation is reported [115, 31]. The same analysis was performed for the $\overline{\nu}_\mu$ beam with equivalent results. Both analyses are compatible with the null oscillation hypothesis for ν_μ ($\overline{\nu}_\mu$) SBL disappearance, setting strong constrains to the ν_μ mixing with ν_s.

MINOS

The most stringent constraint at $\Delta m^2_{41} \sim 1\,\mathrm{eV}^2$ comes from the MINOS long base-line experiment [40]. MINOS is located at the NuMi beam line at Fermilab and count with a near detector (ND at 1.04 km) and a far detector (FD at 735 km). They measure the neutral current (NC) rate in both detectors.

The analysis uses a selection at the ND and the ratio of the data over the simulation is used to reweight the predicted number of ν_μ events at the FD that is compared with the data. The 3+1 model is tested with the assumption that no oscillation can be detected at the ND within the systematic uncertainties. This assumption is estimated to be correct between the range $0.3 < \Delta m^2_{41} < 2.5\,\mathrm{eV}^2$. As we are in the fast oscillation regime, we are not sensitive to the Δm^2_{41}, so MINOS set a constrain only in $\sin^2(2\theta_{\mu\mu})$ (green dashed region in Fig. 2.10). There are no evidences of disappearance and the results are compatible with SciBooNE and MiniBooNE ν_μ ($\overline{\nu}_\mu$) analyses.

CDHSW and CCFR

These are two SBL neutrino old experiments from 1984: the Cern Dortmund Heidelberg Saclay Warsaw (CDHSW) [83] and the Chicago Columbia Fermilab Rochester (CCFR) [136, 137]. The CDHSW (CCFR) have two detectors located in the beam line at 130 m ($\sim$ 800 m) and 885 m ($\sim$ 1200 m) from

the source for a neutrino energy peaked at 3 GeV (40 GeV to 230 GeV for ν_μ and 165 GeV for $\overline{\nu}_\mu$). We see that the CCFR energy range is much larger than all the other experiments so it explores mixing at $10\,\mathrm{eV}^2 > \Delta m^2 > 1000\,\mathrm{eV}^2$. A joint analysis of the near and the far detectors was performed for each of the experiments in order to minimize the systematic uncertainties. The results for both experiments is shown in Fig. 2.10. The constraint at high $\Delta\mathrm{m}^2_{41}$ comes from the CCFR experiment while the one at $\Delta\mathrm{m}^2_{41} \sim 5\,\mathrm{eV}^2$ from CDHSW.

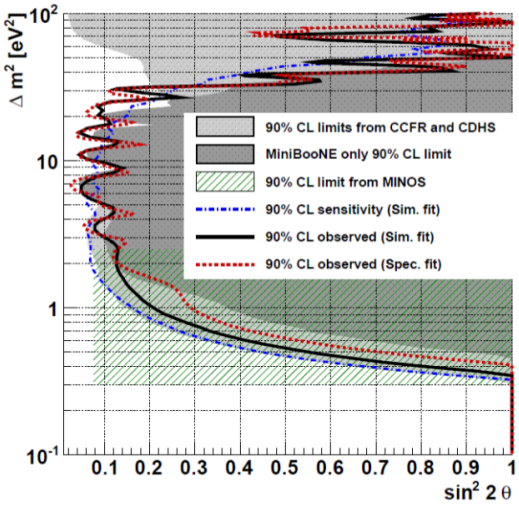

Fig. 2.10: Rejected oscillation parameter space for the null searches of ν_μ disappearance of SciBooNE/MiniBooNE, MINOS, CDHSW and CCFR.

2.2.4 Global fits

It is interesting to discuss the global picture in which joint fits of different analysis are worked out. The results we presented above can be classified in:

- Disappearance experiments: $\nu_e(\overline{\nu}_e) \to \nu_s$ and $\nu_\mu(\overline{\nu}_\mu) \to \nu_s$ channels, they are only sensitive to one of the mixing matrix element ($\sin^2(2\theta_{ee})$ or $\sin^2(2\theta_{\mu\mu})$).
- ν_e appearance experiments: sensitive to both mixing angles through Eq. (2.5).

The $\nu_e(\overline{\nu}_e)$ disappearance experiments are essentially compatible among them. If we fit both reactor and gallium anomalies we are able to reject the non oscillation hypothesis by 99.9%CL (3.6σ) [110]. The LBL and solar experiments are slightly in tension with the gallium anomaly, so including them in the joint fit makes broader the confidence intervals. The final allowed parameter space for the global fit on

Model	χ^2	*Goodness-of-fit*
3+1	712/(689-9)	1.2×10^{-4}
3+2	701/(689-14)	0.34×10^{-4}
1+3+1	694/(689-14)	21.0×10^{-4}

Table 2.1: χ^2 values for the global fits. The *goodness-of-fit* shows the consistency between the appearance versus the disappearance experiments.

the ν_e disappearance data is in Fig. 2.7 and its best fit point sits in $\sin^2(2\theta_{ee}) = 0.09,\ \Delta m^2_{41} = 1.78\,\mathrm{eV}^2$ rejecting the null hypothesis by 99.8%CL.

ν_e disappearance is sensitive to $\sin^2(2\theta_{ee})$ while ν_μ disappearance is sensitive to $\sin^2(2\theta_{\mu\mu})$. It means that a combination of both channels is sensitive to the ν_e appearance parameter $\sin^2(2\theta_{e\mu})$ since the mixing angles are related through Eq. (2.5). A combined analysis of disappearance and appearance data shows that the experiments are strongly in tension [110]. The three different sterile neutrino models described in Section 2.1.1 (3+1, 3+2, 1+3+1) are used to fit the data and their allowed parameter spaces are shown in Fig. 2.11. We observe that any of the models is able to reconcile appearance and disappearance experiments. Tab. 2.1 quantify the tension between both data sets showing the *goodness-of-fit*. The poor values indicate that the probability that both experimental sets agree is below 0.2%. The 1+3+1 is slightly favoured respect to the others and the 3+2 is the model giving the worst agreement with the data. On the other hand, the 1+3+1 model implies a sum of the active neutrino masses of about $\sim 3\,\mathrm{eV}^2$, what might be in tension with recent cosmological results [70].

ν_e disappearance measurements are not in direct conflict with other data, as the mixing angles that drive the oscillations are different. The tension is mainly driven by the fact that the ν_e appearance detected at MiniBooNE and LSND predicts ν_μ disappearance, which has not been observed.

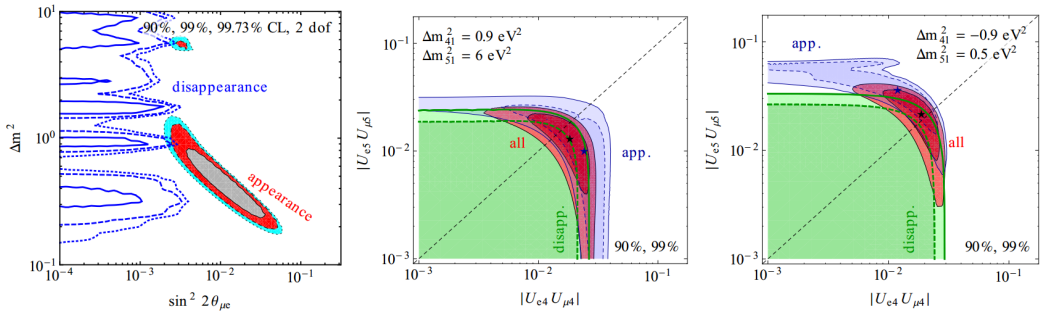

Fig. 2.11: Left: allowed regions for the oscillation parameter space $\sin^2\theta_{\mu e}$ and Δm^2 in the 3+1 model. Middle: 3+2 model. Right: 1+3+1 model. Figures show contours for the disappearance experiments only, appearance experiments only and global fits.

Experiment	Channel	Result
Reactor anomaly	$\nu_e \to \nu_e$	$\sin^2(2\theta_{ee}) = 0.10$ and $\|\Delta m^2_{41}\| = 1.75\,\mathrm{eV}^2$ (3.0σ)
Gallium anomaly		$\sin^2(2\theta_{ee}) = 0.50$ and $\Delta m^2_{41} = 2.24\,\mathrm{eV}^2 (2.7\sigma)$
Reactor + Gallium		$\sin^2(2\theta_{ee}) = 0.17 \pm 0.04$ and $\|\Delta m^2_{41}\| > 1.5\,\mathrm{eV}^2$ (3.6σ)
Solar + KamLAND		$\sin^2(2\theta_{ee}) < 0.1$ (95%CL)
LSND	$\nu_\mu \to \nu_e$	$\Delta m^2_{41} > 1\,\mathrm{eV}^2, \sin^2(2\theta_{e\mu}) \sim 10^{-3}$(90%CL)
KARMEN		$\Delta m^2_{41} < 1\,\mathrm{eV}^2$(90%CL)
NOMAD		$\sin^2(2\theta_{e\mu}) < 10^{-3}$ and $\Delta m^2_{41} < 0.2\,\mathrm{eV}^2$ $(90\%CL)$
MiniBooNE (ν mode)		$\Delta m^2_{41} < 1\,\mathrm{eV}^2$(90%CL)
MiniBooNE ($\bar{\nu}$ mode)		$\sin^2(2\theta_{e\mu}) \sim 10^{-3}$ and $\Delta m^2_{41} > 1\,\mathrm{eV}^2$ $(90\%CL)$
MiniBooNE + SciBooNE	$\nu_\mu \to \nu_\mu$	$\sin^2(2\theta_{\mu\mu}) < 0.05\,\mathrm{eV}^2$ at $\Delta m^2_{41} \sim 10\,\mathrm{eV}^2$ $(90\%CL)$
MINOS		$\sin^2(2\theta_{\mu\mu}) < 0.05\,\mathrm{eV}^2$ at $\Delta m^2_{41} \sim 1\,\mathrm{eV}^2$ $(90\%CL)$
CDSHW		$\sin^2(2\theta_{\mu\mu}) < 0.05\,\mathrm{eV}^2$ at $\Delta m^2_{41} \sim 10\,\mathrm{eV}^2$ $(90\%CL)$
CCFR		$\sin^2(2\theta_{\mu\mu}) < 0.05\,\mathrm{eV}^2$ at $\Delta m^2_{41} \sim 100\,\mathrm{eV}^2$ $(90\%CL)$

Table 2.2: Summary of the SBL neutrino interaction rate measurements. Anomalies and results compatible with standard oscillations are presented together.

2.2.5 Summary

We have described the anomalies that motivate the introduction of sterile neutrinos. They are difficult to fit in the scenario of the standard neutrino oscillations. Nevertheless, even introducing one sterile neutrino at $\Delta m^2_{41} \sim 1\,\mathrm{eV}^2$ there are still some tensions between experiments. A summary table with all the experiment discussed in this section (anomalous and standard ones) together with the impact in a 3+1 neutrino model is provided in Tab. 2.2.

Part II

The T2K experiment

T2K overview

The T2K (Tokai to Kamioka) experiment is a long baseline neutrino oscillation experiment located in Japan that started taking data in March 2010 and continues its operations since then [5]. It produces a neutrino beam using the Japan Proton Accelerator Research Complex (J-PARC) on the east coast of Japan (Tokai village) pointing to the Kamioka laboratory (West Japan) where the far detector (SuperKamiokande) stands. The neutrinos travel for 295 km with a mean energy of $\sim$ 600 MeV, so its design is optimized to study neutrino oscillations at the *atmospheric* mass difference Δm^2_{23}. Near detectors (ND280 and INGRID) placed at 280 m from the hadron production point provide valuable information of the neutrino beam before they oscillate. In short, the experimental overview [Fig. 2.12] is:

- We produce a $> 90\%$ muon neutrino beam with a narrow energy distribution at the maximum of the oscillations thanks to the off-axis setup. T2K is using near and far detectors not collinear with the beam-line, but displaced by a small angle (off-axis). Protons are accelerated to 30 GeV and strike a Carbon target to produce hadrons (pions and kaons) that decay mainly into ν_μ;
- Neutrino interactions are measured before the neutrino oscillation using near detectors placed at 280 m from the source to reduce the flux and cross-section systematic uncertainties at the far detector. The near detectors also measure neutrino cross-sections and participate in sterile neutrino searches;
- Observe neutrino interactions at the far detector, where the neutrino beam composition is significantly affected by the oscillations. Comparing the observed neutrino spectrum with the expected one allows to measure precisely the oscillation parameters $\sin^2(2\theta_{13})$ through ν_e appearance, and $\sin^2(\theta_{23})$ and Δm^2_{23} through ν_μ disappearance.

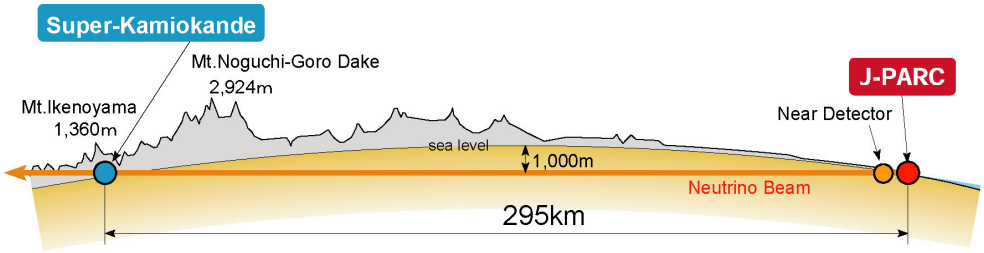

Fig. 2.12: Sketch of the T2K experiment.

Chapter 3

The T2K neutrino beam

Muon neutrinos are produced through the decays of hadrons coming from high energy proton-Carbon interactions. A horn system focuses hadrons of a positive (negative) charge, that decay into neutrinos (anti-neutrinos) and reduces the contamination of anti-neutrinos (neutrinos). To enhance ν_μ's of definite energy at the oscillation maximum, the off-axis technique is applied.

3.1 The neutrino beam-line

The J-PARC facilities provide the intense neutrino beam that is studied firstly at the near detectors hall, located inside J-PARC, and then at SK. The production of the neutrino beam is sketched in Fig. 3.1 and is summarized as follows:

1. The J-PARC complex accelerates protons up to 30 GeV and injects them in the neutrino beam-line, where they are bent towards the direction of SK;
2. The protons hit a graphite target producing hadrons, mainly pions and kaons;
3. The hadrons of a specific charge are collimated using a system of three magnetic horns while the opposite charged hadrons are defocused. They enter in a $\sim$ 96 m Helium tunnel where decay to neutrinos and other particles like muons;
4. A beam dump stops most of the particles that are not neutrinos.

3.1.1 The J-PARC accelerator

It consists of three accelerators: a linear accelerator (LINAC), a rapid-cycling synchrotron (RCS) and the 1567.5 m circumference main ring (MR) synchrotron. A picture of J-PARC with its accelerators is

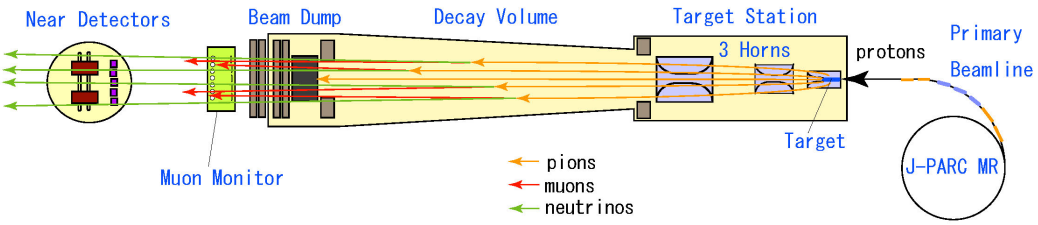

Fig. 3.1: Sketch of the neutrino beam production.

in Fig. 3.2. It injects $\sim 3 \times 10^{14}$ protons per spill of 5.6μs in the target station, with a maximum power of 750kW.

An H^- beam is accelerated up to 400 MeV (181 MeV at present) by the LINAC, and is converted to an H^+ beam by charge-stripping foils at the RCS injection. The beam is accelerated up to 3 GeV by the RCS with a 25Hz cycle. The proton beam injected into the MR is accelerated up to 30 GeV. The number of bunches in the MR is eight (six before June 2010, corresponding to the first T2K run). There are two extraction points in the MR: slow extraction for the hadron beam-line and fast extraction for the neutrino beam-line. In the fast extraction mode, that is the one used by the neutrino facility, the eight circulating proton bunches are extracted within a single turn by a set of five kicker magnets [75]. A precise measurement of the extracted proton beam timing is crucial to discriminate various backgrounds in the neutrino detectors, like the cosmic rays.

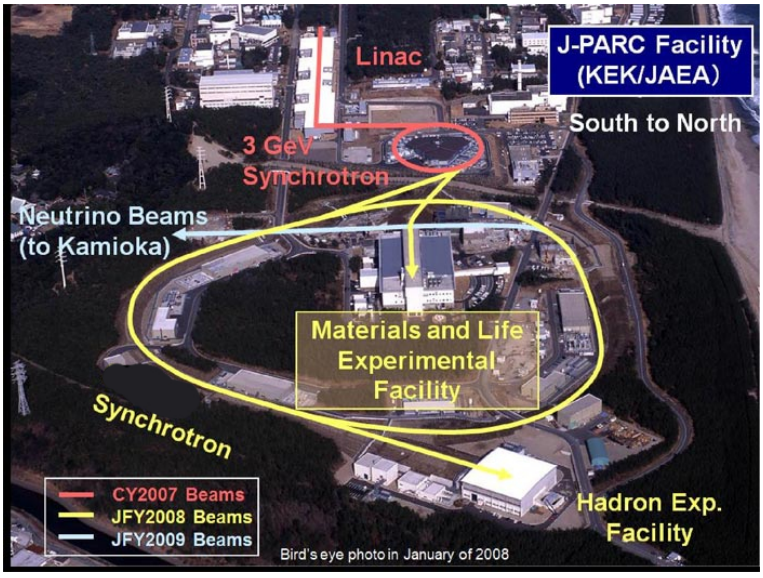

Fig. 3.2: Aerial view of the J-PARC complex.

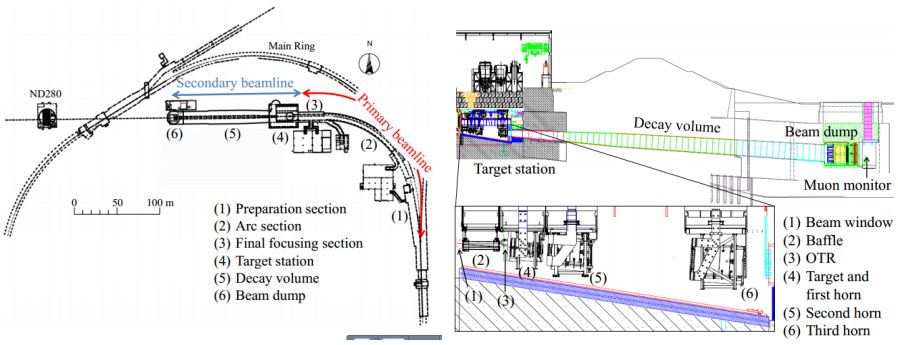

Fig. 3.3: Sketch of the beam line (left) and detail of the secondary beam-line (right).

3.1.2 The primary beam-line

At this stage the extracted proton beam is transported to line it up in the direction of the secondary beam-line and bent to point to SK.

In the preparation section (first 54 m), the extracted proton beam is tuned with a series of 11 normal conducting magnets (four steering, two dipole and five quadrupole magnets) so that the beam can be accepted by the next section called arc section. This runs over the next 147 m and the beam is bent toward the direction of Kamioka by 80.7°, with a 104 m radius of curvature, using 14 doublets of superconducting combined function magnets. There are also three pairs of horizontal and vertical superconducting steering magnets to correct the beam orbit. The downstream part is the focusing section, where ten normal conducting magnets (four steering, two dipole and four quadrupole magnets) guide and focus the beam onto the target, while directing the beam downward by 3.637° with respect to the horizontal.

The intensity, position and profile of the proton beam in the primary sections are precisely monitored by the proton beam monitor (five current transformers, 21 electrostatic monitors, 19 segmented secondary emission monitors and 50 beam loss monitors). A well-tuned proton beam is essential for stable neutrino beam production, and to minimize beam loss in order to achieve high-power beam operation.

3.1.3 The secondary beam-line

The secondary beam-line [Fig. 3.3] consists of three sections: the target station, decay volume and beam dump. The target station contains: a baffle which is a collimator to protect the magnetic horns;

an optical transition radiation monitor to monitor the proton beam profile just upstream of the target; the target to generate secondary pions; and three magnetic horns provided with 250 kA (designed for up to 320 kA) current pulse to focus the pions; all these components are located inside a helium vessel. The produced pions enter the decay volume and decay mainly into muons and muon neutrinos. All the hadrons, as well as muons below 5 GeV, are stopped by the beam dump while the neutrinos pass through the beam dump. Most of the muons above 5 GeV pass through the beam dump and are monitored in the MUMON to characterize the neutrino beam.

The target The target core is a 1.9 interaction length (91.4 cm long), 2.6 cm diameter and 1.8 g/ cm^3 graphite rod. If a material significantly denser than graphite were used for the target core, it would be melted by the pulsed beam heat load. The core and a surrounding 2 mm thick graphite tube are sealed inside a titanium case which is 0.3 mm thick. The target assembly is installed inside the bore of the first horn inner conductor and it is cooled by helium gas flowing through the gaps at a flow speed of $\sim$ 250 m/s. When the 750 kW proton beam interacts with the target, the temperature at the center is expected to reach 700°C (assuming that the radiation damage reduces the thermal conductivity of the material by a factor of four).

The horns The T2K beam-line uses three horns of different sizes located in the target station. Each magnetic horn consists of two coaxial (inner and outer) conductors which encompass a closed volume [139, 125]. A toroidal magnetic field is generated in that volume. The field varies as $1/r$, where r is the distance from the horn axis. The first horn collects the hadrons that are generated at the target installed in its inner conductor. The second and third horns focus the pions. When the horn is run with a operation current of 320 kA, the maximum field is 2.1 T and the neutrino flux at SK is increased by a factor of 16 (compared to horns at 0 kA) at the spectrum peak energy (0.6 GeV). They are optimized to maximize the neutrino flux; the inside diameter is as small as possible to achieve the maximum magnetic field, and the conductor is as thin as possible to minimize pion absorption while still being tolerant of the Lorentz force, created from the 320 kA current and the magnetic field, and the thermal shock from the beam.

The decay volume The decay volume is a $\sim$ 96 m long steel tunnel filled with Helium to reduce the pion absorption. The cross-section is 1.4 m wide and 1.7 m high at the upstream end, and 3.0 m wide and 5.0 m high at the downstream end. It is wider at the end of the tunnel to increase the acceptance

of higher angle particles. The decay volume walls and concrete are cooled down to below 100°C using water in order to dissipate the heat produced by the hits of the pions.

The beam dump and the muon monitor The beam dump sits at the end of the decay volume. The distance between the center of the target and the upstream surface of the beam dump along the neutrino beam direction is 109 m. The beam dump core is made of 75 tons of graphite (1.7 g/cm^3), and is 3.174 m long, 1.94 m wide and 4.69 m high. It is contained in the helium vessel. Fifteen iron plates are placed outside the vessel and two inside, at the downstream end of the graphite core, to give a total iron thickness of 2.40 m. Only muons above ~ 5 GeV can go through the beam dump to reach the downstream muon pit.

The neutrino beam intensity and direction can be monitored on a bunch-by-bunch basis by measuring the distribution profile of muons, because muons are mainly produced along with neutrinos from the pion two-body decay. The neutrino beam direction is determined to be the direction from the target to the center of the muon profile. The muon monitor (MUMON, [117, 118]) is located just behind the beam dump. The muon monitor is designed to measure the neutrino beam direction with a precision better than 0.25mrad, which corresponds to a 3 cm precision of the muon profile center. It is also required to monitor the stability of the neutrino beam intensity with a precision better than 3%. A detector made of nuclear emulsion was installed just downstream of the muon monitor to measure the absolute flux and momentum distribution of muons.

3.2 The off-axis technique

One of the most important features of the T2K beam is that the direction of the proton beam and the axis of the target and horns is 2.5° away from the direction to the far detector. This is called off-axis technique and it was first proposed by the BNL experiment E889 [18]. It allows to produce a narrow band beam at the oscillation maximum with the following advantages:

1. Improves the sensitivity to the oscillation parameters. The off-axis configuration produces an energy peak at the first oscillation maximum at the far detector with a larger neutrino flux than the on-axis setup [Fig. 3.4]. It increases the number of neutrinos that oscillate, enhancing the ν_μ disappearance and ν_e appearance.

2. At $\sim 600\,\text{MeV}$ the dominant interaction is the CCQE interaction [Fig. 1.4]. As it is better known, this interaction has less uncertainties and hence, reduces the cross-section systematic errors that affect the oscillation measurements.

3. Minimizes the background for ν_e appearance analysis. It reduces the beam ν_e contamination in the analysis region around the $\sim 600\,\text{MeV}$. This is because the ν_e's come from three body decays that behave differently than the two-body decays when the off-axis technique is applied.

This technique is useful only in the case we know the relevant Δm^2 precisely, as in the current situation.

The source of a neutrino beam is mainly pions decay. A charged pion decays $\sim 100\%$ to a muon and a muon neutrino:

$$\pi^+ \to \nu_\mu + \mu^+ \qquad \pi^- \to \overline{\nu}_\mu + \mu^-$$

This is a two-body decay that yields an energy for the outgoing neutrino of [111]

$$E_\nu = \frac{(1 - m_\mu^2/m_\pi^2)E_\pi}{1 + \gamma^2 \tan\theta^2}$$

where E_ν, E_π are the energy of the neutrino and the pion, m_π, m_μ are the pion and muon rest masses, $\gamma = E_\pi/m_\pi$ and θ is the off-axis angle. For the neutrinos collinear with the pions ($\theta = 0$), the neutrino energy is strictly proportional to the energy of the pion. For neutrinos with an angle different from zero the relation becomes more complex as can be seen in Fig. 3.5, where the dependency with E_π is weaker with respect to the on-axis neutrinos. It means that the pions of a broad energy band contribute to almost the same neutrino energy and hence, we have more intensity in the energy region of interest.

3.3 The neutrino beam composition

When the protons hit the Carbon target, charged pions and kaons are produced. They decay to neutrinos according to the branching ratios given in Tab. 3.1. We observe that most of the decays yield ν_μ that will be the dominant beam component. The 94.4% comes directly from secondaries or tertiary charged pions while the 5.4% comes from charged kaons. The remainder is a negligible component

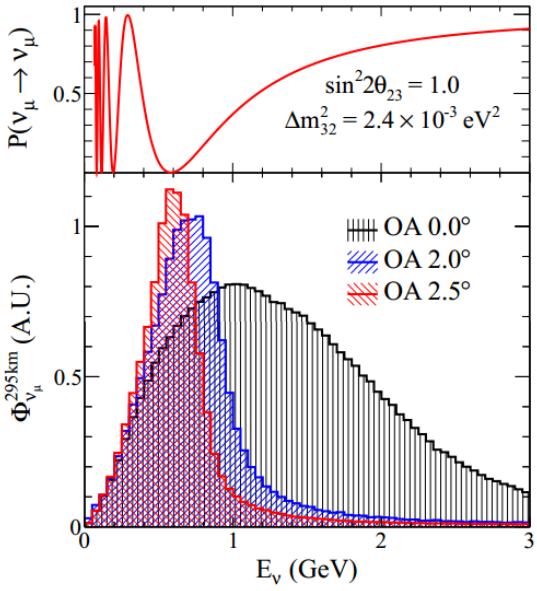

Fig. 3.4: Effect of the off-axis angle in the neutrino beam flux. The curves are normalized by area, but still the off-axis configurations have more neutrinos at the oscillation maximum than the on-axis in absolute numbers.

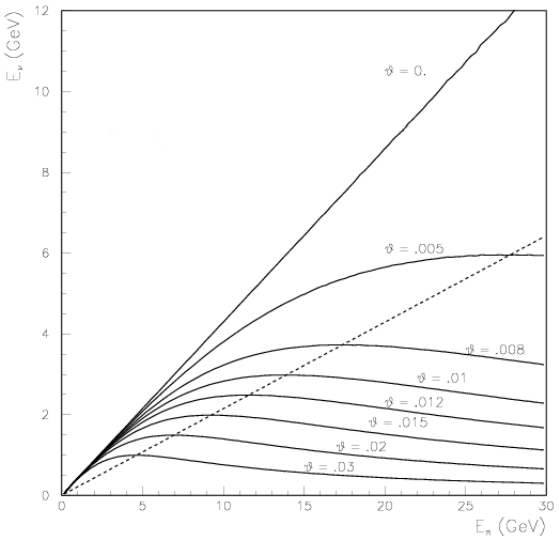

Fig. 3.5: Energy of the neutrino versus the energy of the pions for different off-axis angles.

from neutral kaons. The pion component dominates the neutrino source at the peak while the kaons form the high energy tail of the neutrino flux. Nevertheless, the beam is not made of pure ν_μ as some negative mesons are not sufficiently defocused by the horns and they decay mainly in $\overline{\nu}_\mu$ according to the conjugated channels of Tab. 3.1. They form the second component in the neutrino flux of about the 6.2% of the total flux. Finally, a 1.1% of ν_e and a negligible 0.1% of $\overline{\nu}_e$ are expected. The Fig. 3.6 shows the predicted neutrino flux at SK and ND280 divided by neutrino flavour.

Particle (GeV)	Decay channel	Branching ratio (%)
π^+	$\rightarrow \mu^+\nu_\mu$	99.9877
	$\rightarrow e^+\nu_e$	1.23×10^{-4}
K^+	$\rightarrow \mu^+\nu_\mu$	63.55
	$\rightarrow \pi^0\mu^+\nu_\mu$	3.353
	$\rightarrow \pi^0 e^+\nu_e$	5.07
K^0_L	$\rightarrow \pi^-\mu^+\nu_\mu$	27.04
	$\rightarrow \pi^-e^+\nu_e$	40.55

Table 3.1: Branching ratios for the meson decays that yield neutrinos.

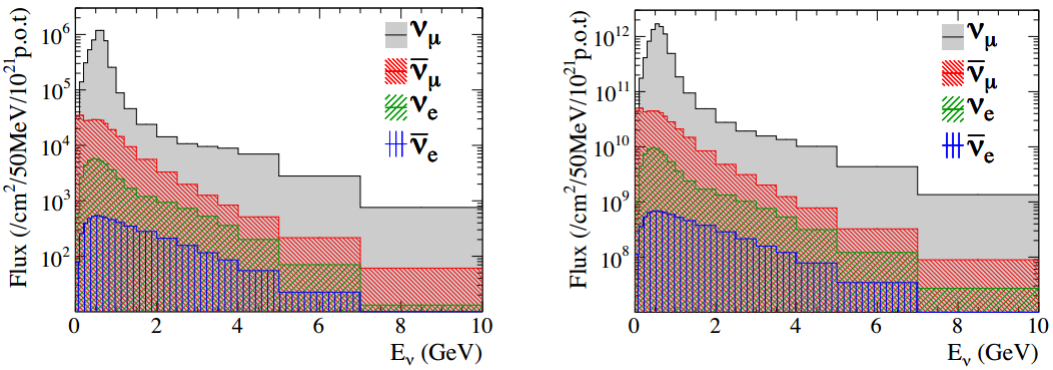

Fig. 3.6: Neutrino flux distributions in neutrino energy predicted at SK (left) and ND280 (right). The colors show the contributions for the different neutrino families.

3.3.1 The ν_e contamination

The ν_e contamination is the main background for the ν_e appearance analysis at SK [Section 5.2] and it has three sources:

- Direct pion and kaon decays: In Tab. 3.1 we see that some channels provide ν_e. As the branching ratio for the pions is very small, this component is negligible while the ν_e coming from kaon is large;

- Muon decay in flight: a residual of muons is produced after $\pi^{\pm}$ and $K^{\pm}$ decays Tab. 3.1. Some of them decay according to:

$$\mu^+ \to e^+ \nu_e \overline{\nu}_\mu \qquad \mu^- \to e^- \overline{\nu}_e \nu_\mu \qquad (\sim 100\%)$$

  before being stopped by the beam dump.

The muons that are stopped at the beam dump decays also in neutrino, but since they decay at rest they provide a low energy isotropic ν_e flux that is negligible at ND280 and SK distances. Some muons overcome the beam dump decaying also to ν_e, but again it becomes a negligible low energy component.

The ν_e fluxes at SK and ND280 divided by neutrino parent is in Fig. 3.7. As the ν_e's from muons come from a sequential decay of pion or kaons to muons and then to ν_e, they populate the low energy region of the spectrum below 1 GeV. On the other hand, the ν_e coming from kaons are more energetic and they populate the high energy tail above 1 GeV.

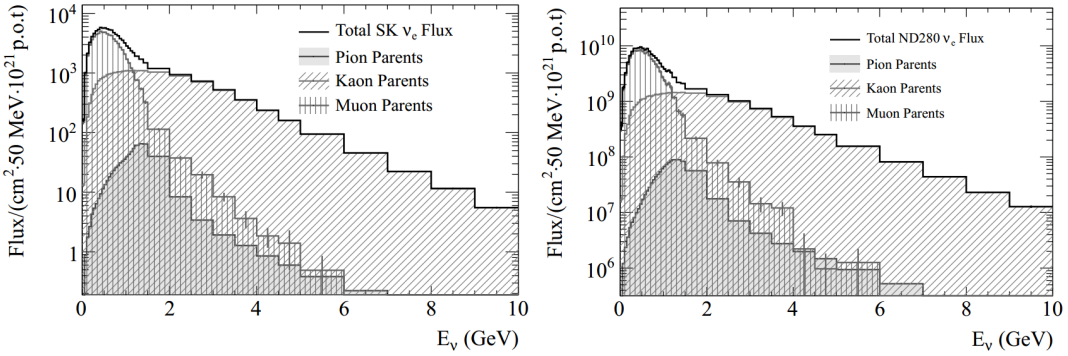

Fig. 3.7: Electron neutrino flux component predicted at SK (left) and ND280 (right).

3.4 Neutrino flux prediction

The neutrino flux at INGRID, ND280 and SK is predicted by a Monte-Carlo simulation based on experimental data. The full secondary beam-line is simulated by the beam Monte-Carlo developed by the T2K collaboration. The interactions inside the graphite target and the baffle are simulated by `FLUKA` [86] and the kinematic information for particles emitted from the target is transferred to a program called `JNUBEAM` that simulates the neutrino production from the hadron decays. `JNUBEAM` is a `GEANT3`-based Monte-Carlo [24] that propagates the outgoing hadrons through the secondary beam-line

until the detectors, including hadron secondary interactions outside the target (mainly in the aluminum of the primary horn) using the GCALOR software [146].

The uncertainties in the flux prediction are large mainly because of the poor knowledge of the hadron production. Then, to reduce the flux errors, the hadron production is constrained using external data. In order to do this, the FLUKA simulation is tuned by the results of the NA61/SHINE experiment [Section 3.4.1]. A small component of the flux uncertainty comes from errors in the beam alignment that are small thanks to the INGRID monitoring. A summary of the final flux uncertainties is in Fig. 3.9 and for a more detailed explanations see [6].

In a second step, the neutrino flux is also measured along with the neutrino cross-section using the ν_μ event rates at ND280 Section 5.1. This reduces the error in the neutrino flux from 20% to not more than 10%.

3.4.1 The NA61/SHINE experiment

The NA61/SHINE [7] (SPS Heavy Ion and Neutrino Experiment) is a multi-purpose facility to study hadron production in hadron-proton, hadron-nucleus and nucleus-nucleus collisions at the CERN Super Proton Synchrotron (SPS). It performs a precise hadron production measurement at the same proton energy using a thin target and a T2K replica target to improve the knowledge of the initial neutrino beam flux. The layout of the NA61/SHINE detector is sketched in Fig. 3.8 and it consists on a large acceptance hadron spectrometer with excellent capabilities in charged particle momentum measurements and identification by a set of six Time Projection Chambers as well as Time-of-Flight detectors [7].

The phase space of interest for T2K purpose is fully covered by the NA61/SHINE experiment. It provides results for the pion [43, 41] and the kaon [42] interaction cross-sections, so that the neutrino flux at T2K is tuned accordingly. This data driven prediction reduces the neutrino flux errors to $10\% - 15\%$ as can be seen in Fig. 3.9, where the largest contribution comes from the hadro-production. Furthermore, the uncertainty on the ratio of the flux predictions at the far and the near detectors is less than 2% around the peak.

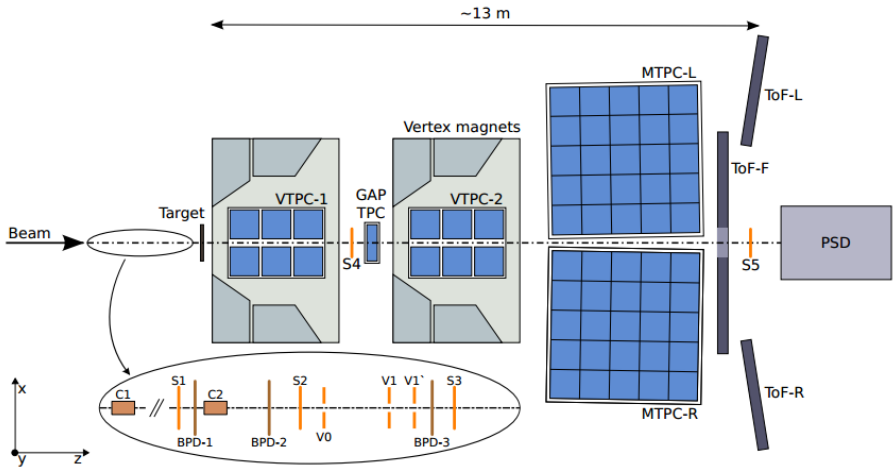

Fig. 3.8: Sketch of the NA61/SHINE detectors

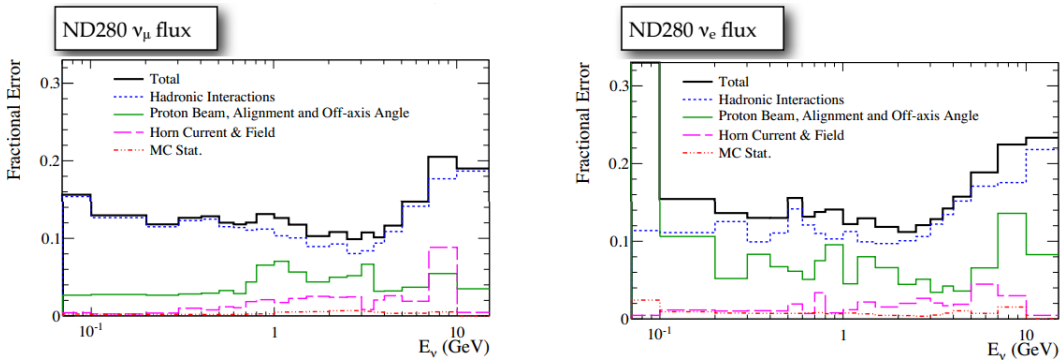

Fig. 3.9: Neutrino flux errors at ND280 as a function of the neutrino energy evaluated with the NA61 experiment and the beam monitor, divided by neutrino flavours. The errors are broken down by components where the largest one is clearly the hadro-production.

Chapter 4

The T2K Detectors

4.1 The near detectors

The Near Detector Complex is installed at a distance of 280 m from the target. It is formed by the main off-axis detector (ND280) that is a magnetized tracking detector with very good particle identification capabilities, and the scintillator on-axis detector (INGRID) that accounts mainly on beam alignment measurements. The design of the complex is shown in Fig. 4.1.

4.1.1 On-axis detector: INGRID

The Interactive Neutrino GRID (INGRID) is a scintillator neutrino detector located on-axis at 280 m and designed to monitor the neutrino beam direction and intensity by means of neutrino interactions in Iron. Using the number of observed neutrino events in each module, the beam center is measured to a precision better than 10 cm that corresponds to 0.4mrad precision.

Design

It consists on 14 identical modules arranged as a cross of two identical groups along the horizontal and vertical axis, and two additional separate modules located at off-axis directions outside the main cross, as shown in Fig. 4.1. Each INGRID module is a cube of 124 cm^3 made of a sandwich of 9 Iron plates and 11 scintillator layers surrounded by veto scintillator planes that track interactions outside the module. The Iron plates serves as neutrino interaction target (7.1t per module) and the scintillator layers and the veto planes are made of 24 and 22 doped polystyrene scintillator bars, respectively.

In addition, an extra module different from the others called the Proton Module, has been added in order to detect protons together with muons produced in ν_μ CC neutrino interactions. It lacks on Iron plates and has a finer segmentation for the scintillator planes, so the tracking capabilities are improved.

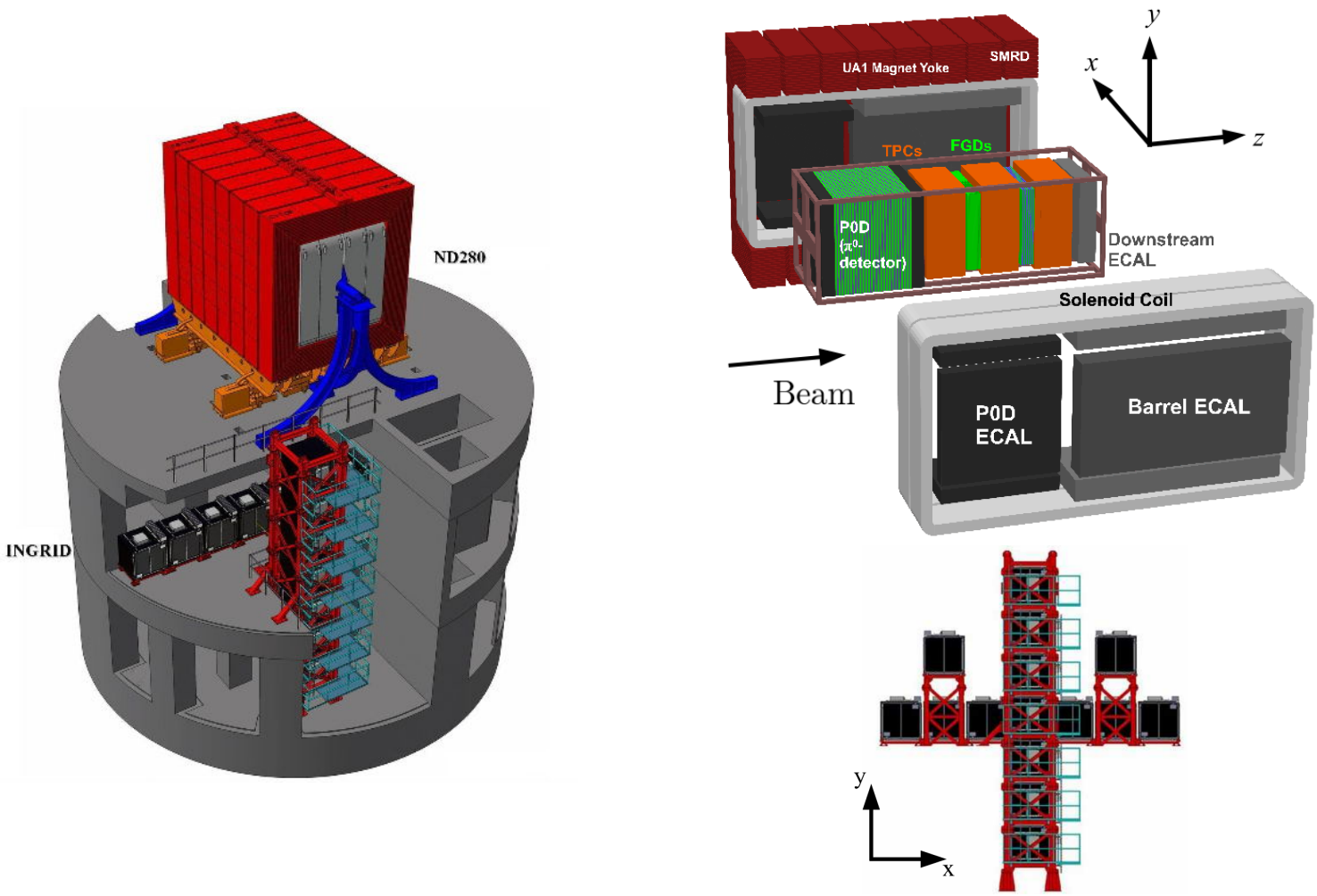

Fig. 4.1: Near detectors at 280 m from the neutrino source. At the top is ND280 in an off-axis position while at the bottom is the on-axis INGRID detector.

Readout and tracking

In the INGRID modules the charge is readout by the Hamamatsu Multi-Pixel Photon Counter (MPPC, [144, 121]), photosensors ([132]) attached to the wavelength-shifting (WLS) fibers that collect the light within the scintillator bars an derive it to the MPPC. It provides the position and the timing of the charge deposit and the tracking to the particles produced in the neutrino interactions.

4.1.2 Off-axis detector: ND280

The off-axis near detector of T2K has the important role of characterizing the neutrino spectra that arrives to SK measuring neutrino interaction rates before the oscillation. It was built to fulfill several requirements:

- it must provide information to determine the expected ν spectra at SK detector.
- the ν_e contamination of the beam must be measured as a function of neutrino energy
- it must have the capability to reconstruct neutral current single π^0 events to control the second most important background of ν_e appearance at SK.

ND280 consists on a combination of different detectors placed inside a magnet. It is constituted by the following elements shown in Fig. 4.1:

- the refurbished UA1/NOMAD magnet instrumented with scintillator to perform as a muon range detector (SMRD). Inside its cavity, a metal frame container, called the "basket" sits.
- The basket is surrounded by an electromagnetic calorimeter (ECAL) divided in 13 separated pieces.
- Inside the basket is placed the π^0 scintillator detector (P0D) and the section called the *tracker*, made of a sandwich of gaseous detectors (Time Projection Chamber, TPC) and the active targets (Fine Grained detectors, FGD).

A display of a charged particle crossing the entire ND280 is shown in Fig. 4.2.

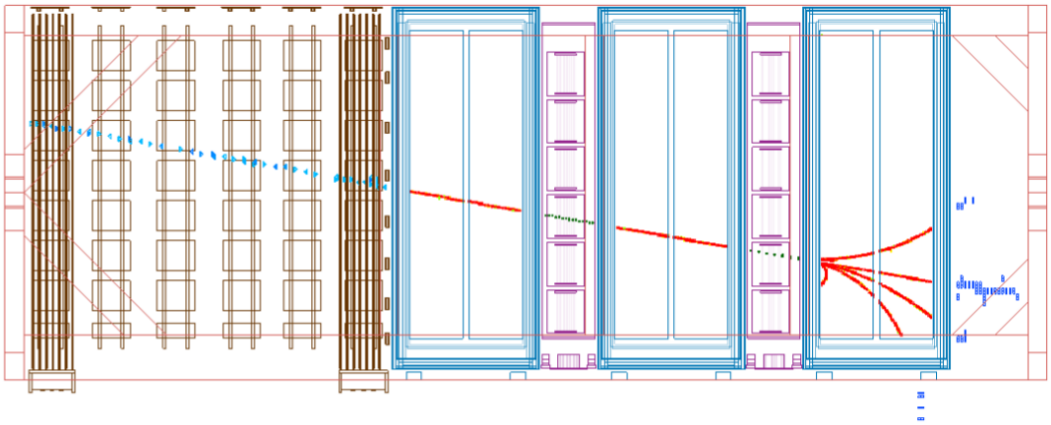

Fig. 4.2: Typical event display in ND280.

The UA1 magnet

ND280 uses the same magnet used at CERN for UA1 [1] and NOMAD [13] experiments, providing a dipole magnetic field of 0.2T. It creates a magnetic field orthogonal to the beam direction bending particles upside or downside depending on their charge. It enables the measurement of the momentum and the sign of the charge of the particles produced in neutrino interactions.

Design The magnet consists on water-cooled aluminum coils, which create the horizontally oriented dipole field, and a flux return yoke. The dimensions of the inner volume of the magnet are 7.0 m × 3.5 m × 3.6 m. The external dimensions are 7.6 m × 5.6 m × 6.1 m and the total weight of the yoke is 850 tons. The coils are made of aluminum bars with 5.45 cm x 5.45 cm square cross-sections, with a central 23 mm diameter bore for water to flow. When the magnet is in an open position, the inner volume is accessible, allowing access to the detectors.

Side Muon Range Detector (SMRD)

The SMRD performs multiple functions. Firstly, it records muons escaping with high angles with respect to the beam direction measuring their momenta. Secondly, it triggers on cosmic ray muons that enter or penetrate the ND280 detector. Finally, it helps identify beam-related event interactions in the surrounding cavity walls and the iron of the magnet.

Design The SMRD consists of a total of 440 scintillator modules which are inserted in the 1.7 cm air gaps between 4.8 cm thick steel plates which make up the UA1 magnet flux return yokes. Each yoke consists of 16 steel plates and hence has 15 air gaps in the radial direction. For every yoke, there are three layers of scintillator modules on the top and bottom. All of the SMRD modules populate the innermost gaps so as to be able to detect particles escaping the inner detectors.

π^0 detector (P0D)

The primary aim of the P0D is to control the second more important background for the ν_e appearance analysis at SK: the π^0 production. It aims to measure the NC process

$$\nu_\mu + N \rightarrow \nu_\mu + N + \pi^0 + X$$

on a water (H_2O) target and so, under the same conditions that in SK. The idea is having a fillable detector that allows to perform neutrino interaction rates measurement with and without water, so that it allows to extract a pure neutrino cross-section on water analysis by a subtraction method.

Design The 2103 mm × 2239 mm × 2400 mm scintillator P0D detector consists on 40 scintillator modules formed by 134 vertical and 126 horizontal polystyrene scintillator bars, each of one instrumented with a WLS fiber inside (Kuraray double-clad Y11 of 1 mm diameter) and attached to a MPPC at one end. The modules are interleaved with fillable water target bags and lead and brass sheets. This arrangement forms a neutrino target where the P0D operates with the water target bags filled or emptied. The mass of the detector with and without water is 16.1 tons and 13.3 tons respectively.

Fine Grained Detector (FGDs)

ND280 is equipped with two scintillators FGD that provide the target mass for neutrino interactions in the tracker part combined with tracking performances for particles exiting the interaction vertex. They are located in between the TPCs and the combination allows a precise track reconstruction of particles. The upstream FGD is fully active extruded polystyrene scintillator while the second one alternates scintillator with water layers in order to allow cross-section measurements in water.

Design Each FGD is 2300 mm width 2400 mm height 365 mm depth and contains 1.1 tons of target material. The first FGD consists on 5,760 scintillator bars, arranged into 30 layers of 192 bars each, with each layer oriented alternately in the x and y directions perpendicular to the neutrino beam to allow 3D hit reconstruction. The second FGD is a water-rich detector consisting of seven XY modules of plastic scintillator alternating with six 2.5 cm thick layers of water (for a total of 2,688 active scintillator bars and 15 cm total thickness of water). Each scintillator bar has a reflective coating containing TiO_2 and a WLS fiber going down a hole in its center with one end connected to an MPPC.

Time Projection Chambers (TPCs)

The TPCs are the most important device in ND280. They provide:

- precise tracking: the charged particles are very well tracked and they cross the light gaseous material without scatter;
- momentum and charge measurement: thanks to the magnetic field inside the basket, the particles are curved with a radius that is proportional to the momentum of the track. Measuring the radius allows to measure the momentum and the charge;
- particle identification: the ionization produced by the charged particles that cross the gas is drifted and collected on the TPC readout system (MicroMegas [95]). The combined measurement of the deposited energy and the momentum of the particle provides a powerful tool for its identification.

Their goal is to measure the neutrino event rates as a function of the neutrino energy and to allow ND280 to measure the ν_e contamination and neutrino cross-sections for different topologies. Its layout is in Fig. 4.3.

Design Each TPC [21] consists of a copper-clad inner box (x = 1808 mm × y = 2230 mm × z = 854 mm) that holds Ar:CF_4:iC_4H_{10} (95:3:2) gas, contained within an Aluminum outer box that holds CO_2 as an insulating gas as showed in Fig. 4.3. On the central cathode, a $25kV$ voltage is applied producing an electric field in the gas volume that drift the electrons on the readout planes installed on the two sides of each TPC. Each TPC has two readout planes where the deposited charge is amplified and read using 12 Bulk MicroMegas modules ([95]) per readout plane. The modules are arranged in two vertical columns that are offset so that the small inactive regions between modules are not aligned to

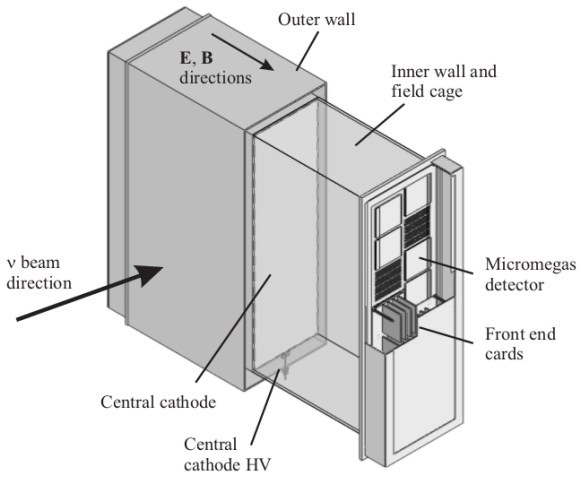

Fig. 4.3: Time Projection Chamber layout.

allow at least partial reconstruction of horizontal tracks entering in a dead zone. The Bulk MicroMegas Detector are planes of $342 \times 359\,\mathrm{mm}^2$ segmented in 36×48 (1728) pads of $6.85 \times 9.65\,\mathrm{mm}^2$ providing a $3\,\mathrm{m}^2$ active region per TPC and a resolution of typically 0.7 mm per column.

The TPC principle The cornerstone of the ν_e analysis is the powerful particle identification in the TPC. A general gaseous detector works in the following way:

1. The charged particle ionize the gas producing ions and electrons.
2. The electric field inside the TPC drifts the electrons to the readout plane where the ionization is amplified and the deposited charge is measured.
3. The curvature of the track due to the magnetic field is reconstructed what provides a measurement of the momentum.
4. As the speed of the electrons is constant and depends on the gas composition, a measurement of the arrival time of the electrons allows a three-dimensional reconstruction.

The detection of the drifted electrons and the measurement of the ionization is performed by Micro Mesh Gaseous detectors modules (MicroMegas, [95]) attached to the walls opposite to the cathode. They amplify the deposited charge applying a strong electric field of $\sim$ 40kV/cm in a thin region of about 100μm. A mesh that separate the drift region from the amplification region provides this high

potential. When a drifted electron crosses the mesh, it gets accelerated triggering a shower that is detected by the read out pads in the MicroMegas. Clusters are formed consisting of neighbouring pads within a column (row) for roughly horizontal (vertical) tracks.

TPC momentum measurement A magnetic field exists inside the ND280 tracker region allowing the measurement of the momentum. Neutrino energy estimation in CCQE events is limited at about the 10% level due to the Fermi motion of the struck nucleons. Thus, the TPC goal is to achieve a resolution in the momentum of $\delta p_\perp / p_\perp < 0.1 p_\perp [\,\mathrm{GeV}]$ (where $p_\perp$ is the component of the momentum perpendicular to magnetic field direction). This requirement is fulfilled as the precision on the momentum measurement is $\sim 10\%$ for tracks of momentum $\sim 1\,\mathrm{GeV}$.

TPC particle identification The particle identification (PID) is based on a combination of precise measurements of the momentum and the ionization energy. The ionization energy depends on the relativistic $\beta\gamma$ factor through the well known Bethe-Bloch formula Fig. 4.4:

$$-\frac{dE}{dx} \propto \beta\gamma = \frac{p}{m} \tag{4.1}$$

where p is the momentum and m the mass at rest of the particle. So measuring the momentum and comparing the expected energy loss at that momentum for each particle hypothesis with the measured one, allows the identification of the particles. This is illustrated in Fig. 4.5 where we show the dependency of the ionization as a function of the momentum for several particle hypotheses (lines). The deposited energy of electrons in 1atm Argon gas is roughly 40% larger than for muons over the momentum range of interest. Then to distinguish electrons from muons the requirement in the ionization resolution needs to be better than 10%.

The resolution on the deposited energy is computed by taking the mean value of the charge deposited by the particle crossing the gas. As the ionization is affected by long tails (Landau tails) the resolution substantially improves if we cancel those tails. This is what is called the truncated mean method. This method is optimized and the truncated mean of the energy loss C_T is defined as the mean of the 70% of the MicroMegas columns with less charge.

To discriminate among the different particles we define the pulls δ_α for each particle hypothesis $\alpha =$

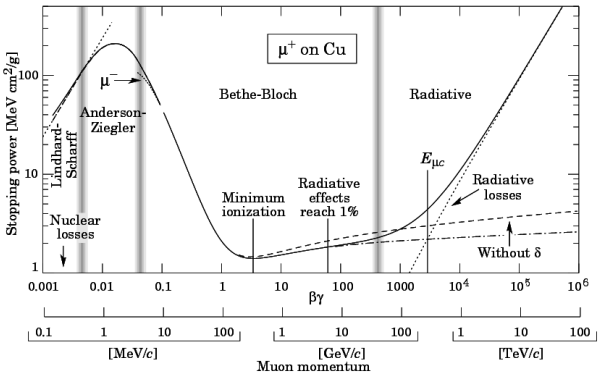

Fig. 4.4: Deposited energy in function of the $\beta\gamma$. It shows the case of the positive muons in Copper.

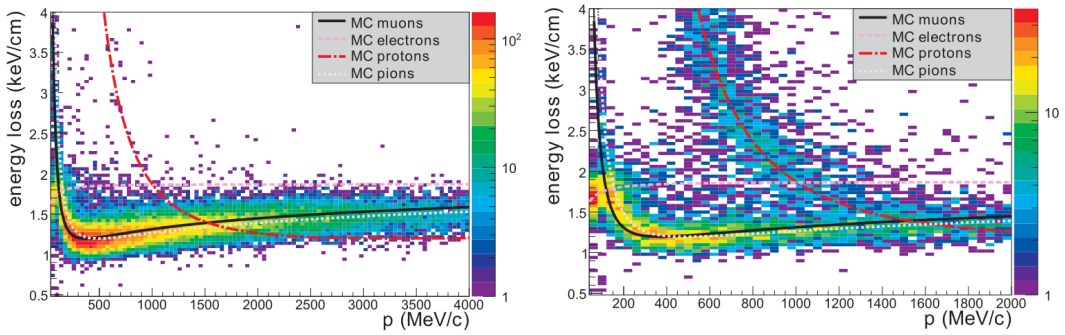

Fig. 4.5: Energy loss calculated using the truncated mean method C_T versus the momentum of the negative (left) or positive (right) particle measured by the TPC. The different curves represent the prediction for different hypothesis and the colored histograms correspond to the data.

$e, \mu, p, \cdots$ as

$$\delta_\alpha = \frac{C_T^{meas} - C_T^\alpha}{\sigma^\alpha} \tag{4.2}$$

where C_T^{meas} is the measured C_T and C_T^α and σ^α are the predicted C_T and its resolution for the hypothesis α. The distribution of the pulls in the electron and muon hypotheses are shown in Fig. 4.6, where we observe that electrons and muons are clearly distinguishable. The C_T resolution is about 7.8% for minimum ionizing particles (below the requirement). This allows muons to be distinguished from electrons in the TPCs being the muon misidentification probability well below 1% for any momentum range.

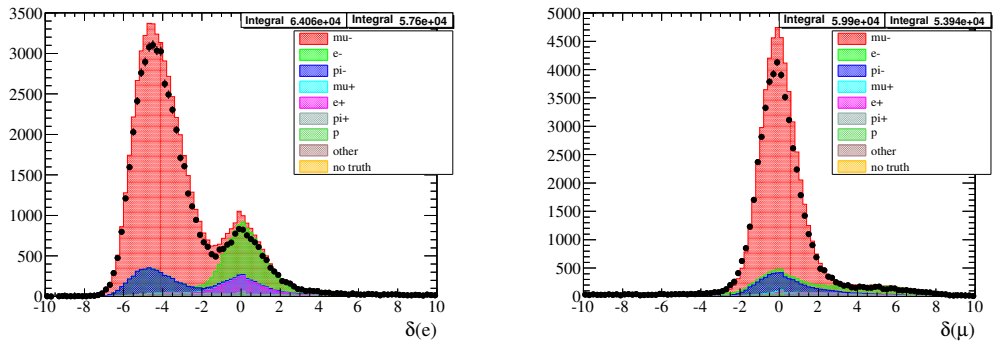

Fig. 4.6: Pulls δ_α in the electron (left) and muon (right) hypotheses for Monte-Carlo (color) and data (dots) for the total data exposure.

Electromagnetic Calorimeters (ECal)

The ECal is made of 13 modules surrounding the whole surface of the inner detectors (P0D, TPCs and FGDs) providing full coverage for all particles exiting the inner detector volume. Its role is reconstructing particles produced in neutrino interactions at high angle, providing particle identification (track vs. shower separation) and detecting the photons that do not convert in the tracker. The ECal performs a key function in the ν_e analysis as it provides complementary PID capabilities to the ones of the TPC, allowing a better distinction of electrons and muons.

Design The ECal is made of 13 independent modules of three different types arranged as in Fig. 4.1: six Barrel-ECal (BrECal) modules surround the tracker volume on its four sides parallel to the z (beam) axis; one downstream module (DsECal) covers the downstream exit of the tracker volume; and six P0D-ECal modules surround the P0D detector volume on its four sides parallel to the z axis.

Each module is instrumented with polystyrene scintillator bars of 4.0 cm × 1.0 cm of cross-section with a WLS going through it and a MPPC in one or both ends. The DsECal module consists of 34 layers (50 2.04 m bars each) with lead sheets of 1.75 mm thickness, BrECal modules have 31 layers each with the same lead sheets, the P0DECal modules are made of 6 active scintillator layers separated by five layers of 4 mm thick lead converter. Consecutive layers have their bars at 90° to allow three-dimensional reconstruction of electromagnetic clusters and charged particle tracks.

The BrECal and P0DECal modules were constructed in 2009-10 and were installed in ND280 in July-October 2010, so the T2K first data run lacks on this detectors.

The ECal particle identification The general principle of an electromagnetic calorimeter is that muons pass through the material as minimum ionizing particles (MIP) and hence, they are reconstructed as tracks. On the other hand, electrons and photons shower when they cross an ECal module releasing most of their energy, thus they are reconstructed as electromagnetic showers. The MIPs are distinguished from the showers using the following features:

- Circularity: distribution of the hits in the cluster and how round it is. Being the short and thick electron/photon-like and large and thin MIPs.
- QRMS: standard deviation of the hit charges in the cluster. Showers tend to be more spread than MIPs.
- Truncated Max ratio: ratio between the highest and the lowest charge collected by an ECal layer. The highest and the lowest charge hits are remove before computing the total charge per layer in order to reduce the noise and the number of saturated channels.
- Front Back Ratio: total charge in the back quarter divided by the one in the front quarter. As a typical shower deposits most of the charge at the first $\sim 1/4$ of the path, this number helps to disentangle between shower-like and MIP-like events.

For each ECal cluster a log-likelihood ratio is built with these four observables and summing the likelihood for both the shower and MIP hypothesis. The discriminator (called MipEM) is set to be < 0 for MIP-like and > 0 for shower-like clusters as it is illustrated in Fig. 4.7. Another ECal observable that we use to exploit the ECal PID is the total energy deposition (EMEnergy). A MIP deposits typically 300 MeV crossing the whole ECal independently of the momentum, while electrons release their whole energy. If the particle has higher momentum than 300 MeV, the EMEnergy is a very good discriminant between muons and electrons.

4.2 The far detector: SuperKamiokande

The world's largest water Cerenkov detector, SuperKamiokande [48], is used as far detector in the T2K experiment. It is located 1 km deep (2700 m.w.e.[1]) and 295 km west from J-PARC and it is used to measure neutrino interactions after the oscillations. Since its construction in 1996 as a neutrino

[1] meters-water-equivalent: equivalent depth in water regarding the absorption of the cosmic rays by the medium

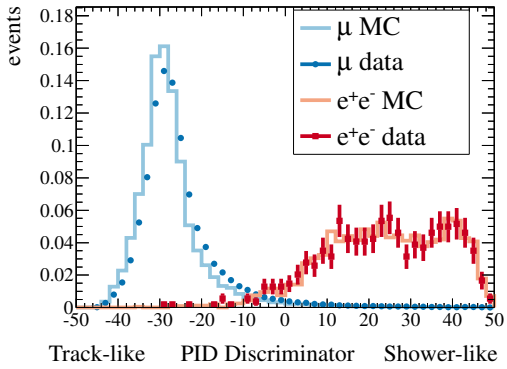

Fig. 4.7: MipEM (ECal discriminant) distribution for muons and electron particle guns for Monte-Carlo (lines) and through-going muons and photon conversions for data (dots). This variable is set to be > 0 for shower-like and < 0 for MIP-like clusters.

observatory and to look for proton decay [135, 104, 123], the famous detector has achieved lots of neutrino measurements over the running periods called SK-I SK-II, SK-III and the last SK-IV still in progress. Among them, the most important one are the measurements on the flux of the solar neutrinos [89] and the historical atmospheric neutrinos oscillation observation in 1998 [143]. Because of its long-running operation, the behavior of SK is well understood and the calibration of the energy scale is known to the percent level.

Design

SK is a cylindric Cerenkov detector filled with 50kt of ultra-pure water surrounded by 13,000 *photo-multipliers tubes* (PMT) to catch the dim Cerenkov light produced by the leptons traveling faster than light in the water [106]. It consists of two major volumes separated by a stainless steel vessel: the inner detector (ID) of 33.8 m in diameter and 36.2 m in height and with 11,129 50 cm PMTs on its walls; and the outer detector (OD) that is concentric to the ID, houses a space of 2 m between the ID and the outer walls and has 1,885 outward-facing 20 cm PMTs. To optically separate both spaces, a stainless steel scaffold of 50 cm covered by plastic sheets stands in the middle. A drawing of SK is in Fig. 4.8.

The 50 cm PMTs (Hamamatsu R3600, [138]) in the ID provide 40% surface coverage and an accurate timing response as well as a large photosensitive area that converts the Cerenkov light in an electron flux. These features make this device able to reconstruct vertex point interactions for the large flux of the neutrino beam. A schematic view of the ID PMTs is in Fig. 4.9.

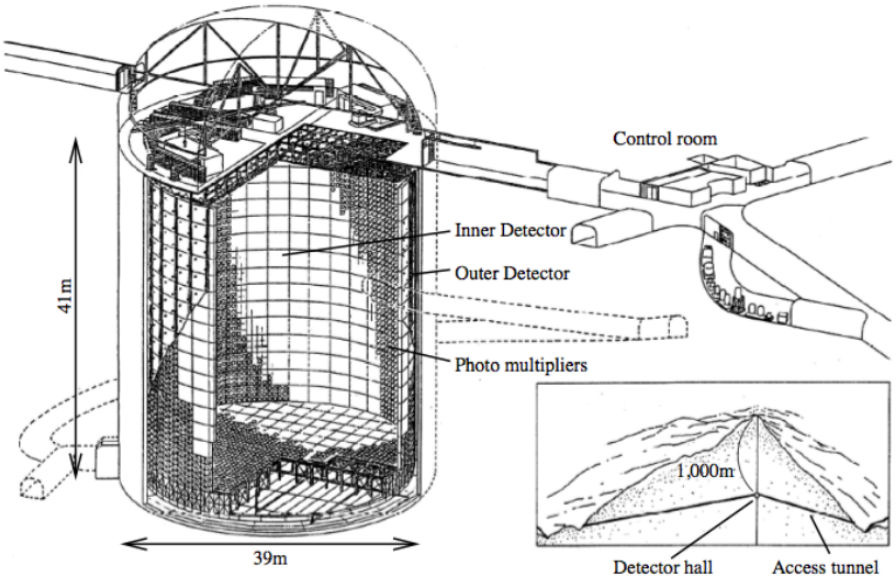

Fig. 4.8: SuperKamiokande, far detector of the T2K experiment. In the drawing, features and parts of this Cerenkov detector can be distinguished as well as an scheme of its location down the mount Ikenoyama.

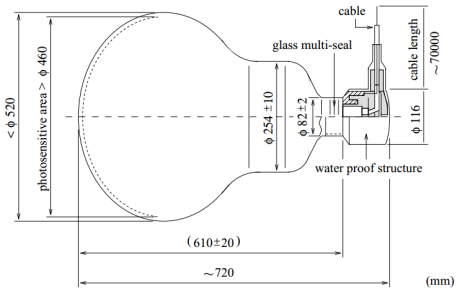

Fig. 4.9: Scheme of a 50 cm PMTs (Hamamatsu R3600, [138]) used in SK ID reconstruction.

Reconstruction and particle identification

The principle of a neutrino Cerenkov detector is the following:

- a neutrino interacts with a nuclei in the water producing a lepton,
- if the lepton travels faster than light in the water, a shock light wave is produced and the particle emits light in a direction θ with respect to the lepton direction such that

$$\cos\theta = 1/\beta n$$

where β is the speed of the lepton in units of c and n the refraction coefficient of the medium (water in this case). This is called the Cerenkov effect [106].

- the light forms a cone whose axis is collinear with the path of the lepton. It arrives to the ID walls where the PMTs collect its light detecting a light ring.

The Cerenkov angle is maximal for very fast particles and it becomes narrower as the energy of the particle is smaller. It is not produced for particles with an energy below the Cerenkov threshold E_{min} that for water is:

$$E_{min} \sim \frac{4}{\sqrt{5}} m \tag{4.3}$$

where m is the mass of the particle.

Thanks to this technique, many features of the out-coming lepton can be measured: the position and time of the interaction or the energy and direction of the lepton. In addition, looking at the characteristics of the rings we can perform a primary particle identification. The idea is that the muon, heavier and resilient to change its momentum, travels very straight. On the other hand, electrons are lighter and use to scatter on the water or to produce electromagnetic showers at the T2K energies. This results in a very sharp reconstructed Cerenkov ring for the muons and a fuzzy ring for the electrons as can be appreciated in Fig. 4.10.

In addition, SK is able to disentangle between electrons and π^0. The π^0 decays immediately in two photons that leave two electron-like Cerenkov rings instead of only one as for the ν_e CC interaction. However, the reconstruction of both rings is very hard in the case that photons are emitted almost collinear (the two rings overlap) or one of the photons is very low energetic (the ring is very small). A new reconstruction algorithm developed in 2013 permits to reduce the π^0 background in the ν_e appearance analysis a factor of 4 with respect to the previous analyses.

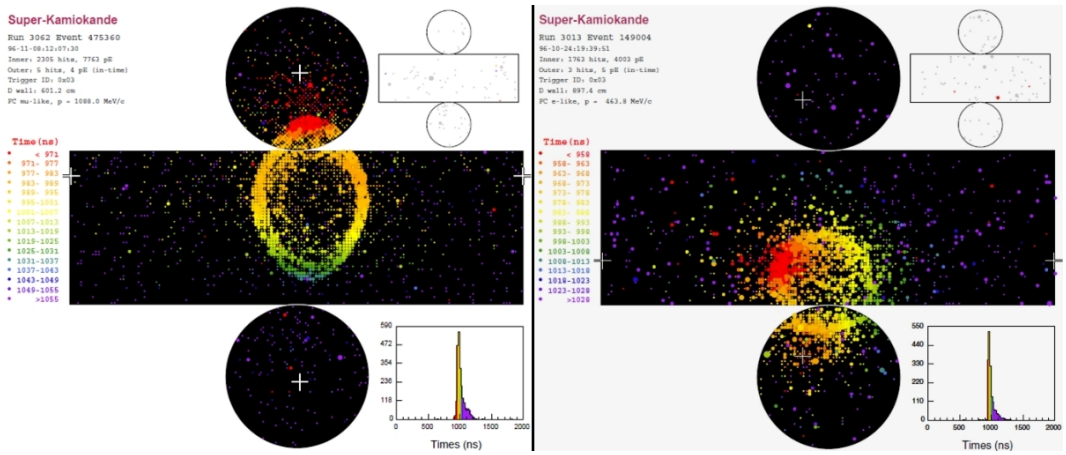

Fig. 4.10: Cerenkov light ring reconstructed at SK. The left plot corresponds to a muon-like event and the right one to an electron-like event.

Chapter 5

T2K oscillation results

The main analysis of T2K is the search for ν_e appearance and ν_μ disappearance at SK. In order to measure the oscillation parameters accurately, the neutrino flux and the neutrino cross-section need to be constrained at the $\sim 10\%$ level. The neutrino flux is monitored at ND280 where a study of the ν_μ interactions is done to measure and further constrain the uncertainties in the flux and cross-section.

5.1 ν_μ CC analysis at ND280

A measurement *in situ* of the neutrino flux as a function of the neutrino energy is performed studying the ν_μ CC interaction rates at ND280. The neutrino interaction rates depend on the flux but also on the neutrino cross-section, so that this analysis places further constraints in both: the T2K flux and the cross-section models. This technique reduces the flux and cross-section uncertainties as well as introduces a correlation among them. With the ND280 ν_μ analysis we decrease the systematic errors in the ν_μ component, but also in the ν_e component due to two reasons:

- The ν_μ and ν_e fluxes are very correlated: kaon decays produce both, ν_μ and ν_e. In addition, the muons that contribute to the ν_e component at low energy, come from the same pion decays that produce the main ν_μ component.
- The ν_μ and ν_e cross-sections are very similar: at first order they are the same and only differences of about 3% arise mainly from Final State Interaction and radiative corrections differences [79]. Hence, constraining cross-section models for ν_μ also does it for ν_e.

ν_μ CC interactions at ND280 are selected and classified in three different samples. The idea is to look for muons produced in the upstream FGD and reconstructed in the TPCs, and characterize the event attending to the other tracks emitted in the neutrino interaction. For the last step it is important the proper identification of the π^+. This is done by reconstructing them in the TPC or by looking for time

delayed energy depositions in the FGD due to the decay of the π^+ in a muon and then in an electron (called Michel electron). In short, the selection is:

- Select the highest momentum negative track in the event starting inside the FGD and with at least one TPC segment.
- Apply the TPC particle identification to select muons and reject electrons, pions and protons
- Classify topologically the event:
  1. CC-0π: events without reconstructed pions or electrons in the tracker;
  2. CC-1π^+: events with a reconstructed π^+ in the tracker and without π^- or electrons;
  3. CC-Other: the rest of the events.

After the data reduction we select 25589 events in total while 29477 are predicted by the simulation. Tab. 5.1 shows the number of events entering in each sample for data and Monte-Carlo. The momentum and angular distributions [Fig. 5.1] are fit to measure the flux and cross-section. The distributions before and after the fit are shown in Fig. 5.2. The uncertainties in the flux prediction are reduced from 20% to $\sim$ 10% and the flux and cross-section errors in the prediction of the number of neutrino interactions at SK become the 6%. The impact of this measurement on the SK analyses are shown below and for further details and the effect in our analysis we refer to Chapter 8.

Selection	Data	Monte-Carlo	Prediction after ν_μ fit
ν_μ-0π	17369	19980	17352
ν_μ-1π^+	4047	4953	4110
ν_μ-Other	4173	4545	4119
Total	25589	29477	25581

Table 5.1: Number of selected events in the ND280 CCν_μ samples for data and Monte-Carlo.

5.2 ν_e appearance

The measurement of the $\sin^2(2\theta_{13})$ mixing angle through ν_e appearance was the main purpose of the T2K experiment. The last of the mixing element remained unknown until 2011 [34], due to its small value. In 2011, the T2K collaboration published the first indication of electron neutrino appearance from a muon neutrino beam at 2.5σ significance based on a data set corresponding to 1.43×10^{20} POT

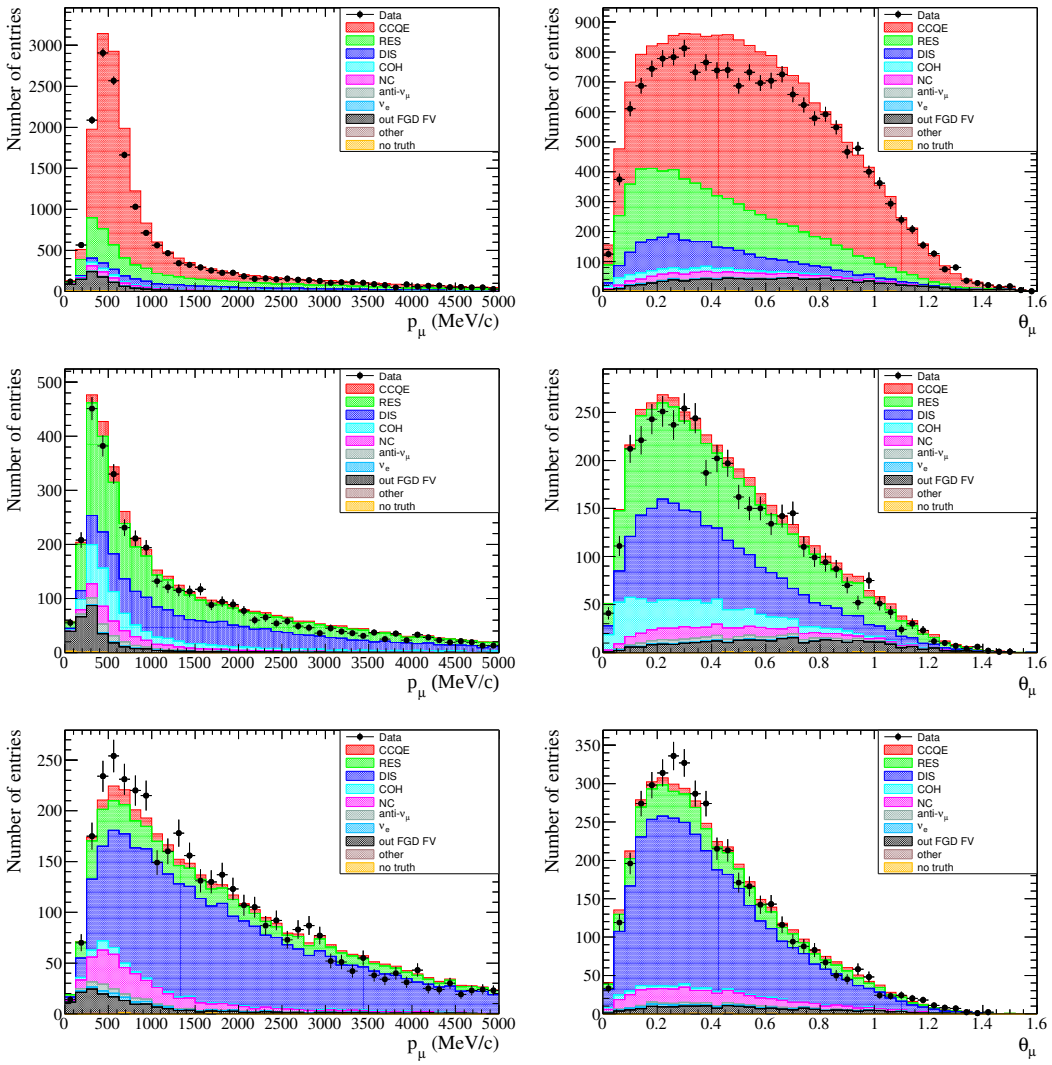

Fig. 5.1: Momentum (left) and angular (right) distributions for the ν_μ selection at ND280 before the fit for data and Monte-Carlo separated by neutrino interaction modes. From top to bottom: CC-0π, CC-1π^+ and CC-Other

[50]. This result was followed by the publication of further evidence for electron neutrino appearance at 3.1σ in early 2013 [51]. Here we present the first significant observation of ν_e appearance in a ν_μ beam described in [55].

After traveling 295 km to SK, the ν_μ oscillate into ν_e with a probability given by Eq. (1.3) that after

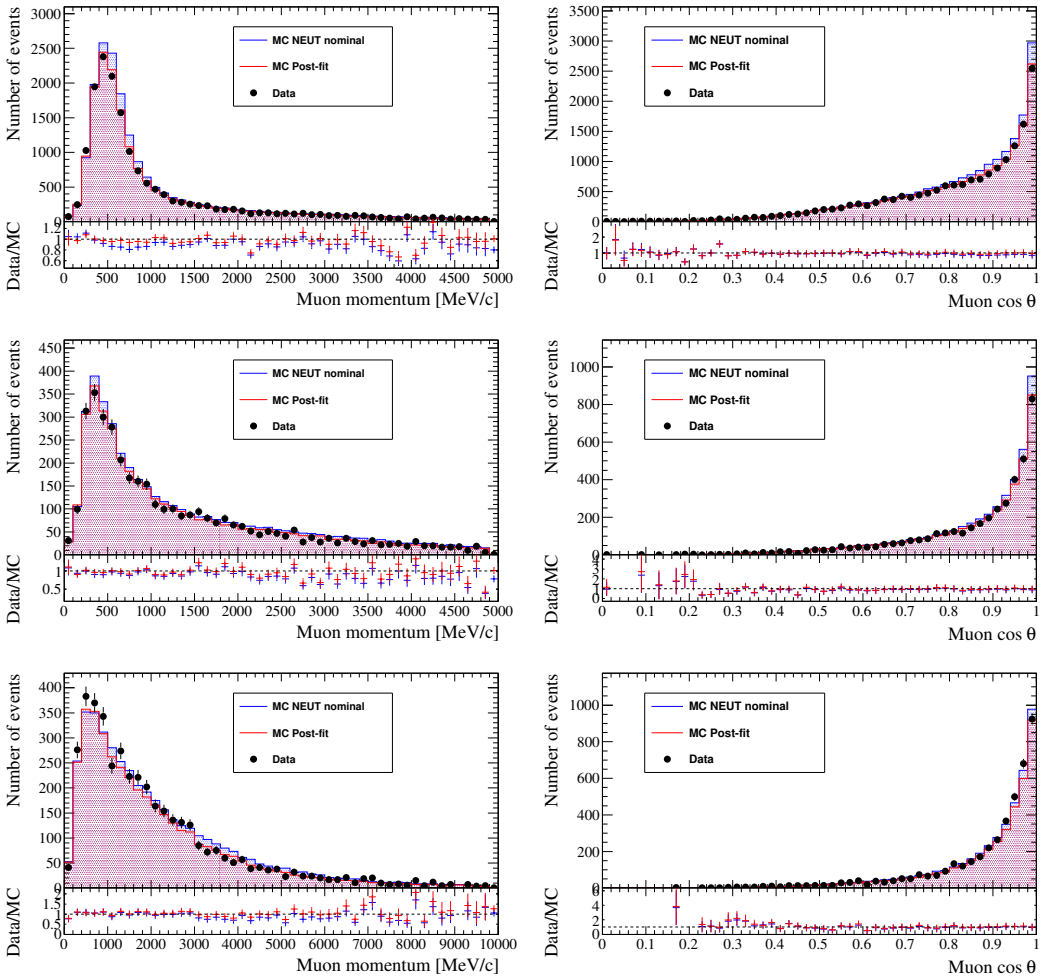

Fig. 5.2: Momentum (left) and angular distributions (right) for the muons selected at ND280. The selection is divided by topology in (from top to bottom): CC-0π, CC-1π^+ and CC-Other. The colored histograms show the expected distributions before and after the ν_μ fit.

developing it, acquires the form:

$$
\begin{aligned}
P(\nu_\mu \to \nu_e) = & \sin^2\theta_{23}\sin^2(2\theta_{13})\sin^2\frac{\Delta m^2_{31}L}{4E} \\
& - \frac{\sin 2\theta_{12}\sin 2\theta_{23}}{2\sin\theta_{13}}\sin\frac{\Delta m^2_{21}L}{4E}\sin^2(2\theta_{13})\sin^2\frac{\Delta m^2_{31}L}{4E}\sin\delta_{CP} \\
& + \text{CP term, solar term, matter effect term}
\end{aligned}
$$

where we observe that this channel is sensitive to $\sin^2(2\theta_{13})$ and CPV. A good measurement implies a precise knowledge of the rest of the parameters in the PMNS matrix.

To look for the ν_e appearance, we select ν_eCC events at SK looking for electrons using the power of the particle identification [Section 4.2]. Although the main ν_μCC interactions are rejected, a sizable background of π^0 produced in ν_μNCπ^0 interactions dominates (9.0 events and 3.9 for the rest of the background). Thanks to a new algorithm implemented in 2013, we are able to distinguish between ν_eCC events and π^0 events removing $\sim 80\%$ of the ν_μNCπ^0 events with a reduction in the ν_e efficiency of only 2% [Fig. 5.3]. The last analysis of SK reveals 28 ν_e-like events from which only 4.92 ± 0.55 are expected without oscillations. Now, the main background for this channel is the irreducible ν_e intrinsic component of the beam that we pointed out in Section 3.3.1. 3.2 events are expected to come from ν_e background, while only 1.1 NC interactions. Measuring this component to check our prediction is key to rely on the final results for $\sin^2(2\theta_{13})$. The only way to control the ν_e contamination is measuring it before the neutrino oscillation at the ND280 near detector.

The data reduction for the selection chain is shown in Tab. 5.2. The reconstructed neutrino energy distribution E_ν^{Rec} for the final ν_e events is shown in Fig. 5.4 along with the small expected background. It is also shown the reduction of the systematic errors thanks to the ν_μ ND280 flux and cross-section measurements. The best fit value $\sin^2(2\theta_{13}) = 0.140^{+0.038}_{-0.032}$ is measured assuming $|\Delta m^2_{32}| = 2.4 \times 10^{-3}\,\text{eV}^2$, $\sin^2\theta_{23} = 0.5$ and $\delta_{CP} = 0$ for normal hierarchy, and $\sin^2(2\theta_{13}) = 0.170^{+0.045}_{-0.037}$ for the inverted hierarchy, giving a significance of 7.3σ with respect to the null hypothesis.

The last unknown element in the PMNS matrix, δ_{CP}, can only be measured in the $\nu_\mu \to \nu_e$ channel by comparing neutrino and anti-neutrino channels (as established in Section 1.3). Currently, comparing our present measurement of $\sin^2(2\theta_{13})$ with the one given by the reactor experiments, that are only sensitive to $\sin^2(2\theta_{13})$, allows to constrain δ_{CP}. The value $\sin^2(2\theta_{13}) = 0.098 \pm 0.013$ [101] is obtained from reactors and δ_{CP} values outside the region 0.19π and 0.80π for the normal hierarchy and between -0.97π and 0.04π for the inverted hierarchy are excluded at the 90%CL [Fig. 5.5].

Selection	Data	$\nu_\mu \to \nu_e$	$\nu_\mu + \overline{\nu}_\mu$CC	$\nu_e + \overline{\nu}_e$CC	NC	Total MC
Fiducial volume	377	26.2	247.8	15.4	83.0	372.4
Single ring	193	22.7	142.4	9.8	23.5	198.4
e-like ring	60	22.4	5.6	9.7	16.3	54.2
$p_e > 100\,\text{MeV}$	57	22.0	3.7	9.7	14.0	49.4
No decay-e	44	19.6	0.7	7.9	11.8	40.0
E_ν^{Rec}	39	18.8	0.2	3.7	9.0	31.7
Non π^0-like	28	17.3	0.1	3.2	1.0	21.6

Table 5.2: Expected number signal and background events passing each cut of the ν_e selection at SK assuming $\sin^2(2\theta_{13}) = 0.1$, $\sin^2(\theta_{23}) = 0.5$, $\Delta m^2_{32} = 2.4 \times 10^{-3}\,\text{eV}^2$, $\delta_{CP} = 0$ compared to the data.

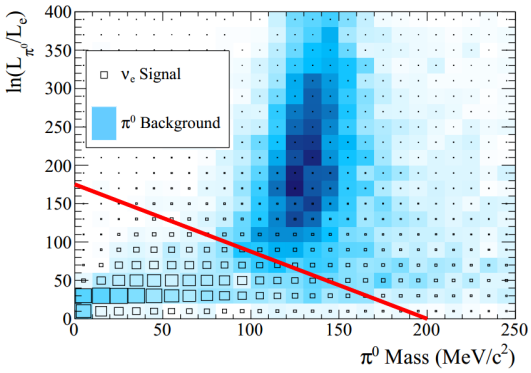

Fig. 5.3: Criteria to discriminate π^0 events from ν_e CC events at SK. The X axis corresponds to the reconstructed π^0 mass making the hypothesis of two electron-like rings. The Y axis represents the likelihood ratio between the π^0 and the electron hypothesis. The events above the red line are rejected, corresponding with the peak of the π^0 background (blue).

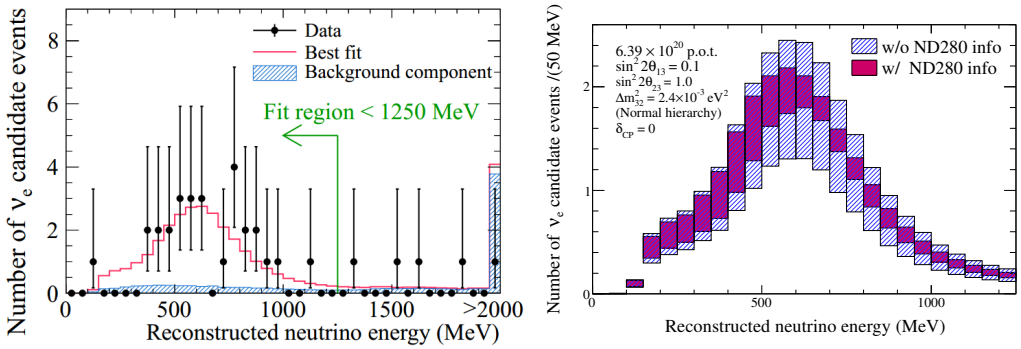

Fig. 5.4: Reconstructed neutrino energy distribution for ν_e events at SK. **Left:** In blue is shown the expected events while the dots represent the data. A clear excess due to the $\nu_\mu \rightarrow \nu_e$ is observed. **Right:** effect of the ND280 ν_μ constrain of the systematic errors.

5.3 ν_μ disappearance

The most precise measurement on $\sin^2(\theta_{23})$ is set by the T2K ν_μ disappearance analysis. The ν_μ survival probability is

$$P(\nu_\mu \rightarrow \nu_\mu) \simeq 1 - 4\cos^2\theta_{13}\sin^2\theta_{23}\sin^2\left(1.267\frac{\Delta m^2[\mathrm{eV}^2]L[\mathrm{km}]}{E_\nu[\mathrm{GeV}]}\right) - 4\cos^4\theta_{13}\sin^4\theta_{23}\sin^2\left(1.267\frac{\Delta m^2[\mathrm{eV}^2]L[\mathrm{km}]}{E_\nu[\mathrm{GeV}]}\right)$$

where Δm^2 is the relevant mass splitting according to the hierarchy (Δm^2_{32} for the normal and Δm^2_{13} for the inverted). The first term dominates since $\sin^2(2\theta_{13}) \ll 1$. A precise measurement of $\sin^2(\theta_{23})$ is

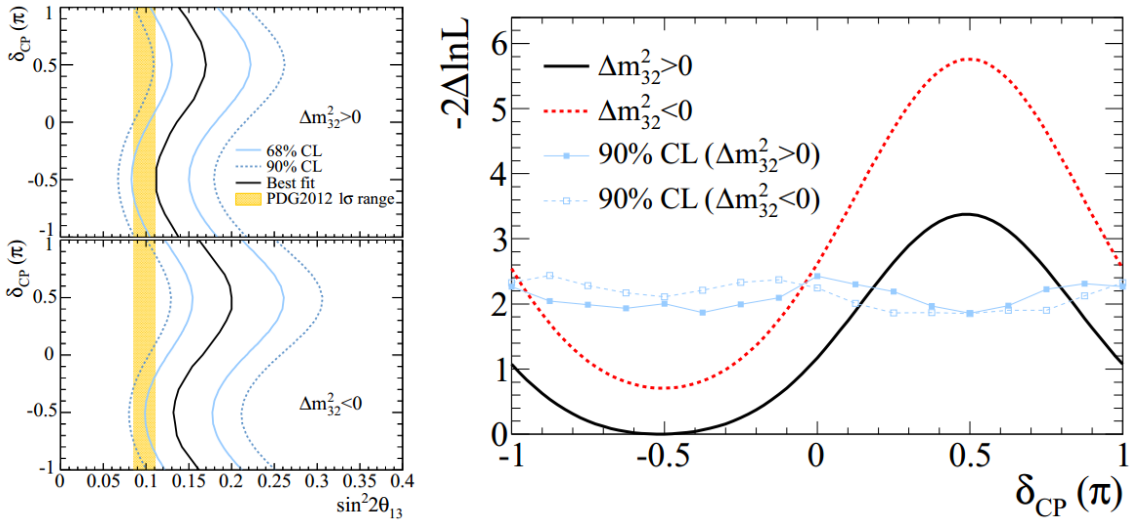

Fig. 5.5: **Left**: allowed regions for the $\sin^2(2\theta_{13})$ as a function of δ_{CP} for normal (top) and inverted (bottom) hierarchy. The shaded region shows the $\sin^2(2\theta_{13})$ constrain from [101]. **Right**: $-2\Delta \ln L$ value as a function of the δ_{CP} for the analysis of T2K ν_e data plus the reactor measurement from the PDG2012 [101]. Critical values (horizontal lines) are calculated with the Feldman-Cousin method [92] and the points of the curves above those lines are exclude at 90%CL.

interesting for constraining models on neutrino mass generation and determining if $\sin^2(\theta_{23})$ is larger or smaller than $\pi/4$ (the octant of $\sin^2(\theta_{23})$). After a publication with the first results [52], the results for an analysis with the entire data set [54] is presented here.

We select 120 ν_μ events after the selection criteria that enhance the ν_μ CCQE component. 446.0 ± 22.5 events are expected if oscillation does not occur. The events are distributed in reconstructed neutrino energy as it is shown in Fig. 5.7. The best fit value sits in the point $\sin^2(\theta_{23}) = 0.514^{+0.055}_{-0.056}$ and $\Delta m^2_{32} = 2.51 \pm 0.10 \times 10^{-3}\,\mathrm{eV}^2$ for the normal hierarchy and $\sin^2(\theta_{23}) = 0.511 \pm 0.055$ and $\Delta m^2_{13} = 2.48 \pm 0.10 \times 10^{-3}\,\mathrm{eV}^2$ for the inverted one. The rest of the parameters are treated as nuisance parameters within the constraints: $\sin^2\theta_{13} = 0.0251 \pm 0.0035$, $\sin^2\theta_{12} = 0.312 \pm 0.016$, $\Delta m^2_{21} = 7.50 \pm 0.20 \times 10^{-5}\,\mathrm{eV}^2$ and δ_{CP} constrained to the physical boundaries $[-\pi, \pi]$. Matter effects are included as well with a value of the Earth density of $\rho = 2.6 g/\,\mathrm{cm}^3$. The confidence contours on the parameter plane based on the Feldman-Cousin technique [92] are shown in Fig. 5.7, being the measured value compatible with maximal mixing.

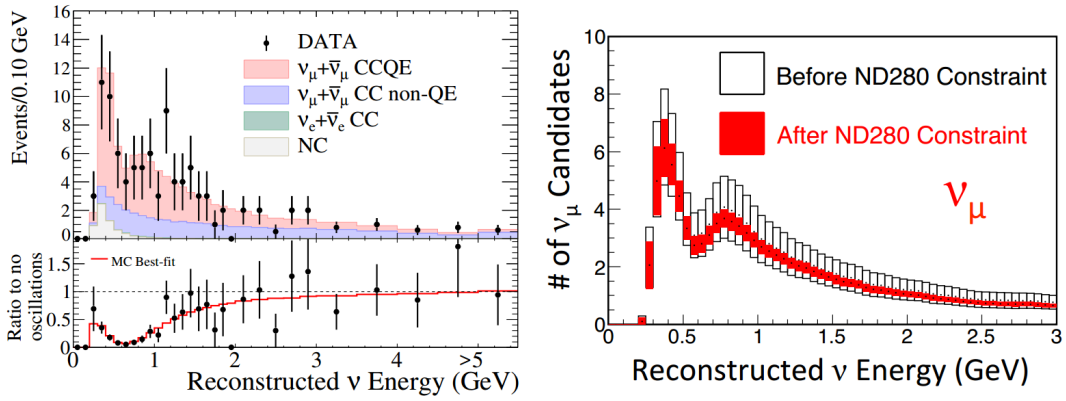

Fig. 5.6: Reconstructed neutrino energy distribution for ν_μ events at SK. **Left**: The Monte-Carlo (colored histograms) shows the best fit on the data (dots). At the bottom there is the ratio with respect to the non oscillation hypothesis. The disappearance of ν_μ events is evident. **Right**: reduction of the systematic uncertainties due to the ND280 ν_μ fit.

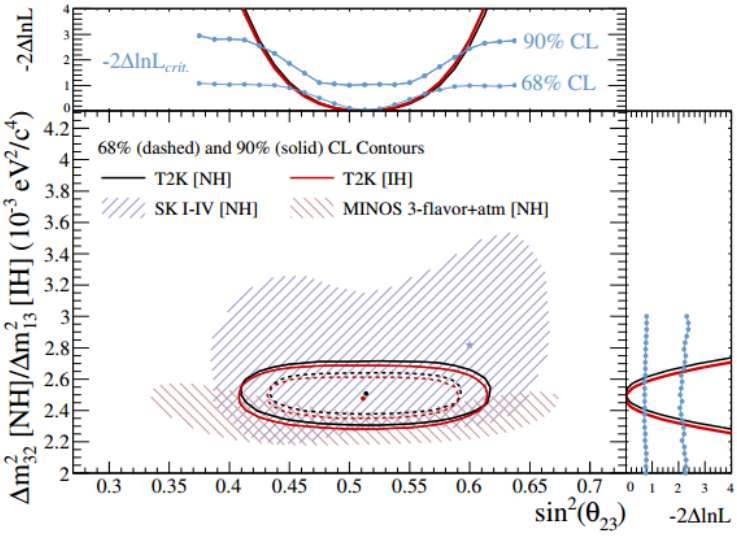

Fig. 5.7: Confidence intervals in $\sin^2(\theta_{23})$ and Δm^2 from the latest T2K ν_μ disappearance data at SK. The T2K results are shown for normal (black) and inverted (red) hierarchies together with the SK atmospheric neutrino data and MINOS measurements.

5.4 Others and future measurements

δ_{CP}

Data of anti-neutrino is being collected this year (2014) enabling the neutrino-antineutrino comparison in the ν_e appearance channel. A combined analysis of T2K and the NOνA experiment that is starting

the data taking this year, can constrain further the δ_{CP} [17].

Neutrino cross-sections

Using the large statistics at ND280 together with its capabilities, precise cross-section measurements in function of the neutrino energy can be performed. [53] describes the measurement of the inclusive ν_μ CC cross-section on the Carbon of the upstream FGD. 4485 ν_μ CC events are selected at ND280 measuring a flux-averaged total cross-section of

$$\sigma(\nu_\mu \text{CC}) = (6.91 \pm 0.13 \text{ stats. } \pm 0.84 \text{ systs. }) \times 10^{39}\,\text{cm}^2\text{nucleon}^{-1}$$

for a neutrino mean energy of 0.85 GeV, agreeing the prediction of the neutrino event generator NEUT [103].

A similar analysis with ν_e events to measure ν_eCC interactions in Carbon has been performed and will be published soon, reporting a measured cross-section compatible with the prediction. This analysis is described in the T2K internal paper [26] and corresponds to the first measurement of the ν_e cross-section at the T2K energies in Carbon. Neutrino NC cross-section on Oxygen is measured at SK [49]. The Oxygen nuclei gets excited due to the NC *quasi-elastic* (NCQE) interaction:

$$\nu + {}^{16}O \rightarrow \nu + n + {}^{15}O^*$$

Afterwards, the Oxygen de-excites emitting a photon that can be detected at SK. This process is dominant at T2K energies and the expected cross-section is $2.01 \times 10^{-38}\,\text{cm}^2$ while the measured one is

$$\sigma(NCQE) = 1.35^{+0.59}_{-0.29} \times 10^{-38}\,\text{cm}^2$$

consistent at the 90%CL with the expectation.

The anti-neutrino T2K data being collected at this moment (2014) will allow future measurements of anti-neutrino cross-sections in Carbon and Oxygen.

Part III

ND280 ν_e analyses

Analyses overview

In this part we present two different analyses performed in the tracker of ND280:

- Measurement of the ν_e interaction rates and comparison with the predicted by the ND280 ν_μCC analysis
- Search of ν_e disappearance at SBL due to oscillations to light sterile neutrinos

Both analyses are based on a ν_e selection using the ND280 tracker described in Chapter 6. The cornerstone of the selection is the PID capabilities of the TPCs and ECALs, that can reduce the dominant muon component of the beam below 1%. At low momentum, photon conversion becomes the dominant background, so a sample rich in pairs electron-positron coming from photons is selected in Chapter 7 to control it. The second most important background are the misidentified muons, that are measured in Chapter 7.

The measurement of the ν_μ CC interaction rates at ND280 described in Section 5.1 allows to reduce the flux and the cross-section uncertainties in the ν_e interaction rate prediction. This is possible since the ν_μ and ν_e fluxes are highly correlated and also their cross-sections are similar (see Section 5.1). A complete study of the set of systematic errors that applies to the analyses is presented in Chapter 8.

The maximum likelihood method is performed to measure the ν_e beam component and estimate the compatibility with the Monte-Carlo prediction in Chapter 9. It describes the work published in [74].

The second analysis is presented in Chapter 10, where the likelihood ratio technique is applied to calculate the sensitivity of ND280 to ν_e disappearance in the 3+1 model [Section 2.1.1] and the confidence intervals in the oscillation parameter space using the total amount of available data. A paper on this second analysis is being written and will be published as soon as it gets the approval of the T2K collaboration (we refer to the T2K internal note, [28]).

A diagram of the analysis flow is shown in Fig. 5.8 to clarify the overall technique.

General information

Data set In both analyses the whole data collected by ND280 between January 2010 and May 2013 are used. It corresponds to an exposure of 5.9×10^{20} protons on target (POT). The data are subdivided into different run periods as shown in Tab. 5.3. A small fraction of Run III data ($\sim 15\%$) was collected with magnetic horns operating at 205 kA instead of the nominal 250 kA.

Monte-Carlo The simulated data used in this analysis corresponds to more than ten times the POT of the data [Tab. 5.3]. The whole ND280 detector is simulated in a code where the various experimental conditions of the different data taking periods are reproduced. Run I lacks on BrECAL, there are data runs with or without water in the P0D detector layers and we ignore the right-side BrECal entirely for Runs III and IV as some channels were broken during the 2011 earthquake.

The neutrino interaction generator that we use by default in this analysis is NEUT 5.1.4. [103]. After NEUT triggers a neutrino interaction in ND280, the final state particles are propagated through the detector and their energy deposit simulated using `GEANT4` [9]. The response of the active detectors including the electronics are simulated by the `elecSim` package [71] developed by the T2K collaboration.

Analysis framework In general for data and Monte-Carlo, `ROOT` [25] is used as framework and it provides the data storage that is arranged using the `Tree` format.

The selection was developed using the `highland` (`high` level `a`nalysis at the `n`ear `d`etector) framework [72], which provides a set of common tools for every ND280 analysis. The framework benefits from the global reconstruction provided by the `oaAnalysis` package [73].

The detector systematic errors estimation is done also within the `highland` framework, while the propagation is performed directly in the ν_e analysis framework. The package called `T2KReweight` calculates the effect of the flux and cross-section variations on the selected sample, providing the framework for the propagation of the systematic uncertainties coming from the flux and cross-section.

The fitting code used for the ν_e analyses has been developed by a part of the ND280 ν_e group and profits on the `highland` outputs and the `T2KReweight` tool.

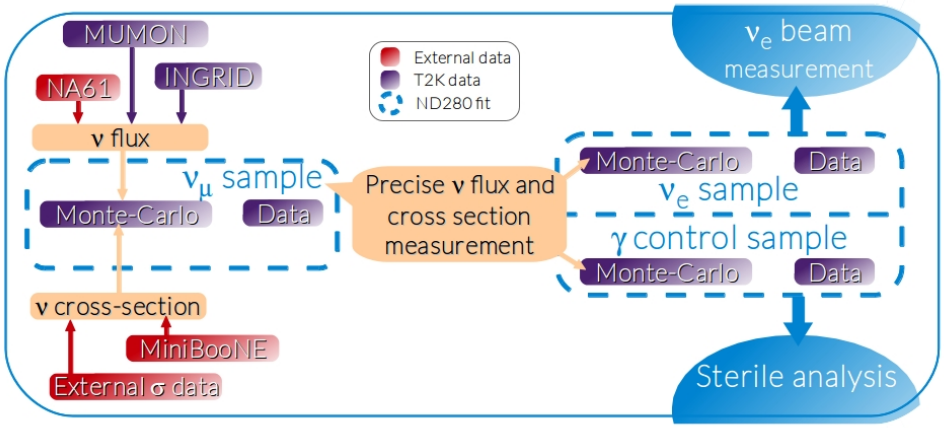

Fig. 5.8: Sketch of the analysis flow.

T2K run	Dates	Data POT	MC POT
Run I	Jan. 2010 – Jun. 2010	1.7×10^{19}	1.7×10^{20}
Run II	Nov. 2010 – Mar. 2011	7.9×10^{19}	7.9×10^{20}
Run III	Mar. 2012 – Jun. 2012	15.6×10^{19}	16.0×10^{20}
Run IV	Jan. 2013 – May. 2013	33.8×10^{19}	33.5×10^{20}
Total	Jan. 2010 – May. 2013	59.00×10^{19}	59.02×10^{20}

Table 5.3: Definition of T2K runs and the amount of data and Monte-Carlo POT used in the analysis.

Chapter 6

ν_e CC event selection

The selection of ν_e charged current (ν_eCC) interactions in ND280 is difficult due to the small fraction of ν_e that we have in the T2K beam. This component is expected to be of the order of 1.2% of the total neutrino flux and to select it we have to reject the large amount of ν_μ interactions producing muons in the final state. We define our signal as ν_eCC interaction in the FGD that creates an electron. We classify the ν_e interactions in CC quasi-elastic (ν_eCCQE) or CC non-quasi-elastic (ν_eCCnonQE) as follows:

$$\begin{aligned} \nu_e\text{CCQE}: &\quad \nu_e + n(^{12}C,^{16}O) \rightarrow e^- + p \\ \nu_e\text{CCnonQE}: &\quad \nu_e + n(^{12}C,^{16}O) \rightarrow e^- + p + (\pi^\pm, \pi^0, \gamma, \ldots) \end{aligned}$$

where neutrino interactions on Carbon occurs in both FGD's while interactions on Oxygen only happens in the water layers of FGD2. We aim to identify the electrons on these interactions and detect the other particles to characterize the event. A fundamental tool for this analysis is the particle identification (PID): combining the TPC and the ECAL PID capabilities we reject more than 99.8% of the μ coming from ν_μ interactions.

Nevertheless ν_μ interactions can also generate photons in ND280, through π^0 production, that can convert inside the FGD producing electrons entering the TPC and mimic in some cases a ν_e interaction. As we will show, this electromagnetic process is the main source of background for our analysis, larger than the few muons that are misidentified as electrons. An important point to stress is that for these two backgrounds we do not simply rely on the Monte-Carlo but we measure and control them using the data. Other backgrounds coming from misidentified pions and protons that are selected in the analysis are small as it will be shown in the next sections.

In summary we define the following categories to differentiate the contributions of signal and background in our selection:

- *Signal*: ν_eCCQE interactions
- *Signal*: ν_eCCnonQE interactions
- *Background*: electrons coming from photon conversion
- *Background*: misidentified muons
- *Background*: any other case

We have developed and optimized a criteria to select ν_eCCQE and ν_eCCnonQE interactions candidates with a good purity and high statistic for the current data exposure. We distinguish four stages with different aims:

1. *Quality cuts:* select a lepton created within a time window compatible with the one of the bunches of the neutrino beam and inside the FGD to reject cosmic events and interaction outside Carbon;
2. *Electron identification:* require the lepton to be compatible with an electron to reject the dominant component of ν_μ CC interactions;
3. *Backgrounds suppression:* reject as much as possible the large component of low energy electrons produced by photon conversions due to ν_μ interactions inside or outside the FGD;
4. *ν_eCCQE/$\nu_e$nonCCQE separation:* classify events according to their topology and further reject some background events.

A sketch of the whole selection criteria flow is shown in Fig. 6.1 and details are given in the following subsections. We stress that the Monte-Carlo that we show in this section correspond with the *nominal* Monte-Carlo, *i.e.* the prediction *before* the ν_μ ND280 measurement of the flux and cross-section.

6.1 Quality cuts

Beam trigger

We analyze only events associated to the beam trigger, *i.e.* compatible with one of the 8 (6 for Run I) bunches of the beam spill. We accept events within 4σ ($\sigma = 15$ns) from the center of each bunch. In this way the background coming from the cosmic neutrinos is largely reduced.

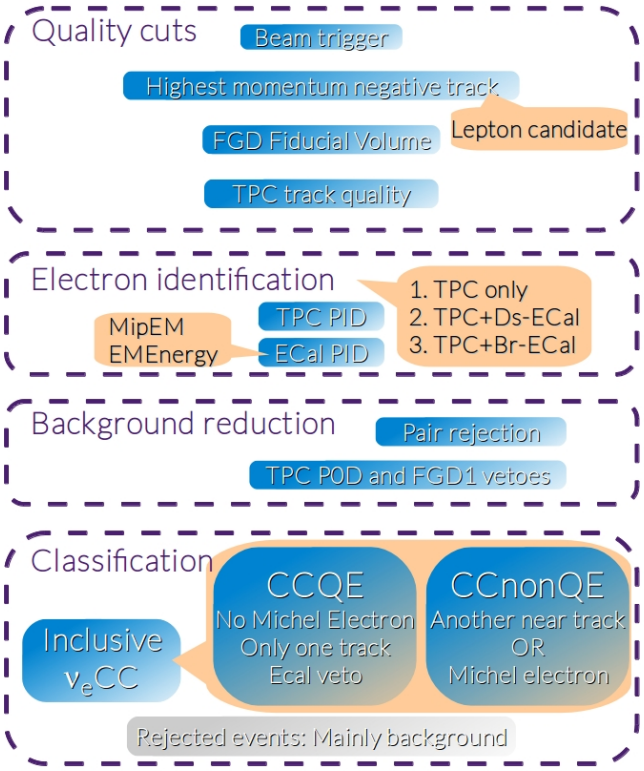

Fig. 6.1: Sketch of the selection flow applied for the ν_eCCQE and ν_eCCnonQE samples.

Electron candidate selection

In a CC interaction, most of the energy is carried by the lepton, so we choose the highest momentum forward-going track reconstructed in a TPC (if any) as the most probable candidate to be a lepton. We do not use the upstream TPC as we look for interactions in the FGD's and the lepton is usually produced forward-going. As we want to select ν events and get rid of the $\bar{\nu}$, we only look for the most energetic track among the negative tracks. This track has at least a TPC segment connected to an FGD segment. Since at very low momentum the selection is completely dominated by low energetic photon conversions, we remove the tracks with momentum lower than 200 MeV. This is what we call the *electron candidate*.

Fiducial volume

We define a fiducial volume (FV) inside both FGD as shown in Fig. 6.2, where we require the electron candidate to start. This is aimed to:

- reject the copious background of muons produced in a ν_μ interaction in the sand or the concrete walls of the ND280 pit (called in jargon *sand muons* or *through-going muons*);
- reject neutrino interactions inside ND280 but outside the FGD, as the interaction type is very difficult to address;
- reduce neutrino interactions in other materials but Carbon and Oxygen (water).

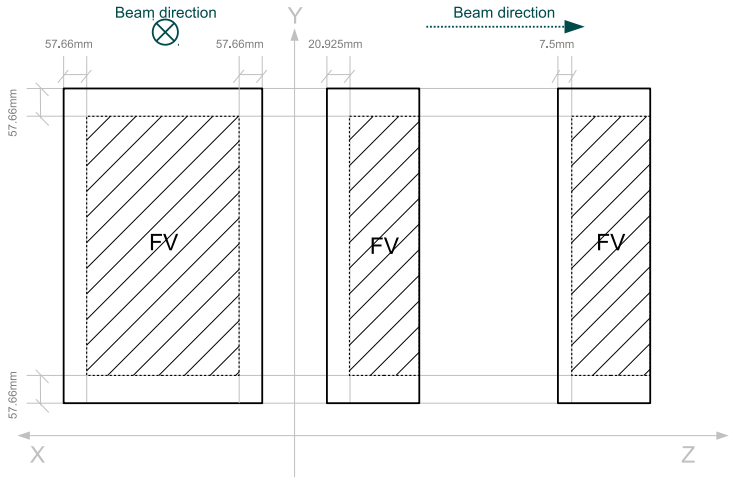

Fig. 6.2: Definition of the FGD fiducial volume.

TPC track Quality

A good TPC track quality ensures the smallest muon contamination. It is demonstrated that the PID performances of the TPC become sensibly worse when reducing the number of clusters that are used to calculate the energy deposition (that goes from 7% with 72 cluster, to 12% to 24 clusters [93], [94]). In our analysis we want to keep a high quality as we need to get rid of the dominant muon background, so we require the electron candidate to have more than 35 clusters in the TPC.

The momentum of the electron candidate after these first basic cuts is shown in Fig. 6.3. We are dominated by muons and there are other backgrounds at low momentum.

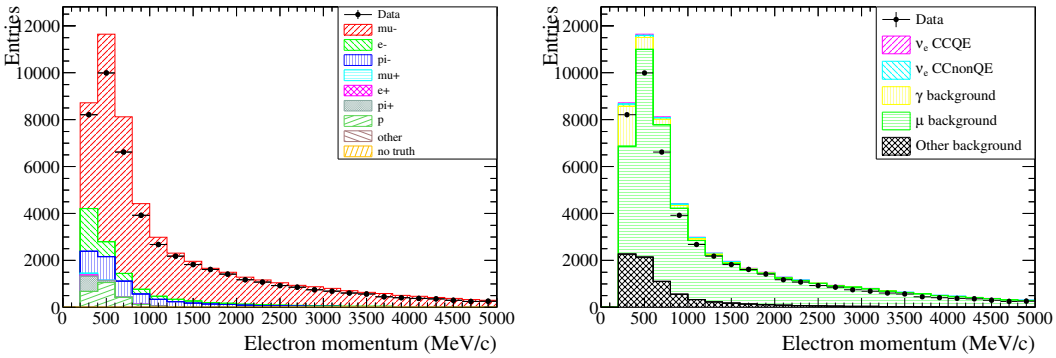

Fig. 6.3: Momentum of the electron candidate, after the first four cuts. The left plot shows the Monte-Carlo broken down by the particle type, and the right plot broken down by signal and background categories.

6.2 The particle identification

To select electrons, we use a combination of the PID capabilities of the TPCs and the ECals [Section 4.1.2]. The electron efficiency and purity are largely enhanced if the ECal is used combined with the TPC. Nevertheless, this is not always possible since sometimes the electron candidate is not reconstructed in an ECal module, so we can only use TPC information. As the ability of the ECal to discriminate between muons and electrons degrades for low momentum particles, we ignore any ECal information if the momentum of the track, as it enters the ECal, is less than 300 MeV and only the TPC is used in those cases.

We have optimized the PID criteria attending to whether the ECal is used or not, which ECal module is used and the energy of the particle. We distinguish three different PID paths: only TPC, TPC with DsECal and TPC with BrECal. In Tab. 6.1 is shown the fraction of events, efficiency and purity per case and in Fig. 6.4, the momentum distribution broken down in each case. At high momentum most of the tracks enter the DsECal since the angular acceptance and the reconstruction efficiency is larger, whilst at low momentum there is a larger variety of paths taken.

	FGD1 vertices			FGD2 vertices		
Category	events (%)	eff. (%)	pur. (%)	events (%)	eff. (%)	pur. (%)
TPC only	45.4	56.6	92.6	34.1	53.1	90.9
TPC+DsECal	32.0	82.6	97.2	59.0	89.1	93.8
TPC+BrECal	22.6	86.1	91.4	6.9	88.6	86.5

Table 6.1: Fraction of electrons entering each PID branch. The efficiency of selecting ν_eCC interactions occurring in the FGD is shown as well as the electron purity per branch.

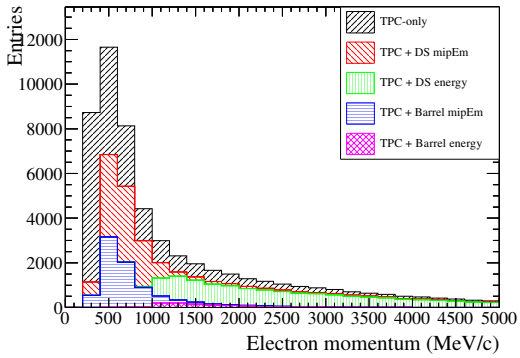

Fig. 6.4: Momentum of the tracks after the quality cuts divided in the different PID criteria.

Using only the TPCs

In this category we find low momentum tracks that do not reach the ECals or tracks whose TPC and ECal matching failed. In this case we can only use the TPC PID information. We require the track to be electron-like, not muon-like, and not pion-like. In order to do this we define the electron pull δ_e, muon pull δ_μ and pion pull δ_π [Eq. (4.2)] and apply the following cuts to the most upstream TPC segment of the reconstructed track:

$$-1 < \delta_e < 2 \qquad |\delta_\mu| > -2.5 \qquad |\delta_\pi| > -2$$

These cuts are shown sequentially in Fig. 6.5.

Using the Downstream ECal

For tracks reconstructed in the DsECal, we use a combination of the most upstream TPC and DsECal informations and develop the following criteria attending to the ECal PID variables in Section 4.1.2:

- $-2 < \delta_e < 2.5$
- mipEm > 0 if the momentum of the track as it enters the ECal is less than 1 GeV
- EMEnergy > 1100 MeV if the momentum of the track is greater than 1 GeV

We have loosen the electron pull cut and require only compatibility with an electron. We do not use the TPC discriminant δ_μ nor δ_π since it is more efficient to use the ECal capabilities instead of the TPC to reject non-electron-like particles. These cuts are shown sequentially in Fig. 6.6.

Using the Barrel ECal

For tracks with a BrECal segment, we use the same selection criteria as for tracks that enter the DsECal. There are much less clusters reconstructed in the BrECal than the DsECal since the acceptance is lower at high angles: the electron candidate is typically produced very straight, so it crosses the DsECal more likely than the BrECal, and only the low energetic electrons are bended crossing the BrECals. The cuts are shown sequentially in Fig. 6.7.

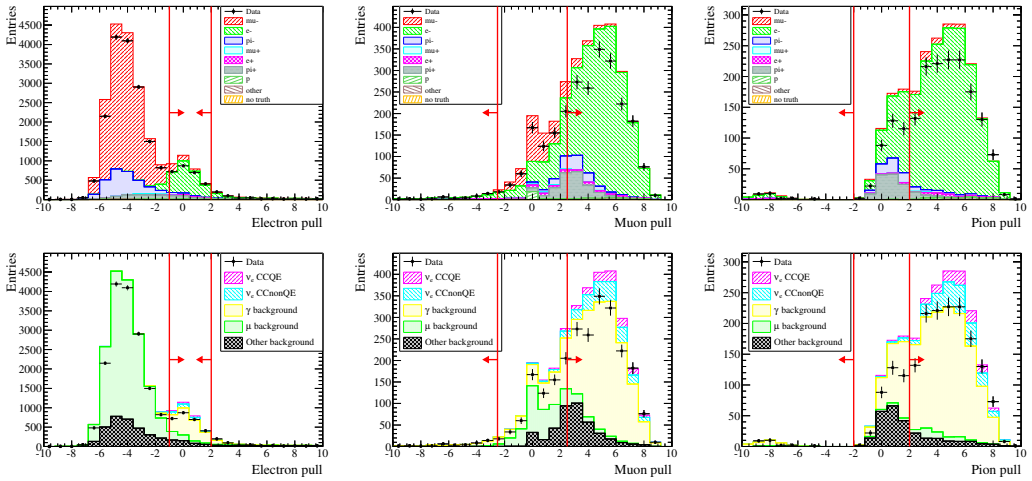

Fig. 6.5: PID criteria for tracks using only a TPC: δ_e (left), δ_μ (middle) and δ_π (right). From left to right the cuts are applied sequentially. Top (bottom) figures show the Monte-Carlo broken down by particle type (signal/background categories).

Overall PID

After applying the whole PID selection, we have the sample shown in Fig. 6.8. We find that 99.8% of muons are rejected by the selection obtaining a sample 91.7% pure in electrons. However, the majority of these electrons come from photon conversions, rather than ν_e interactions, as shown in Tab. 6.2.

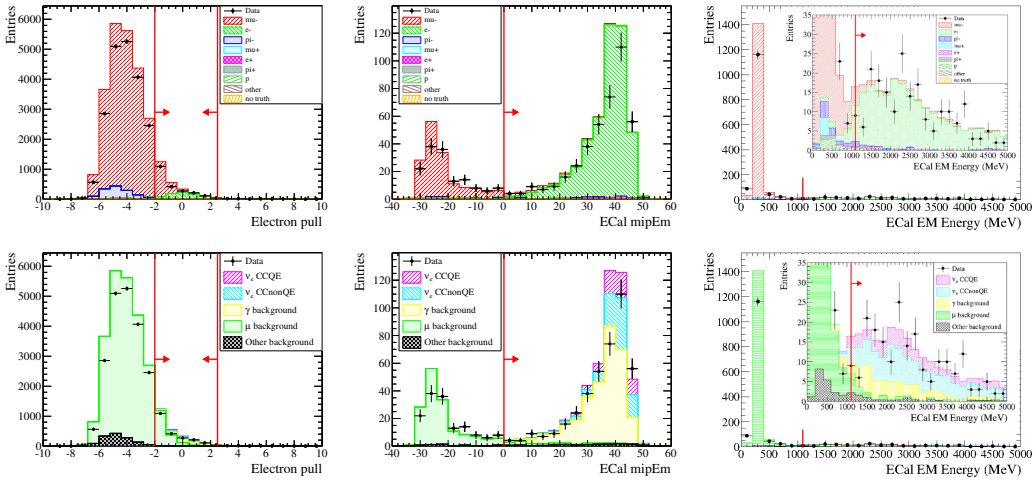

Fig. 6.6: PID criteria for tracks using TPC and DsECal: δ_e (left), mipEm (middle) and EMEnergy (right). From left to right the cuts are applied sequentially. Top (bottom) figures show the Monte-Carlo broken down by particle type (signal/background categories).

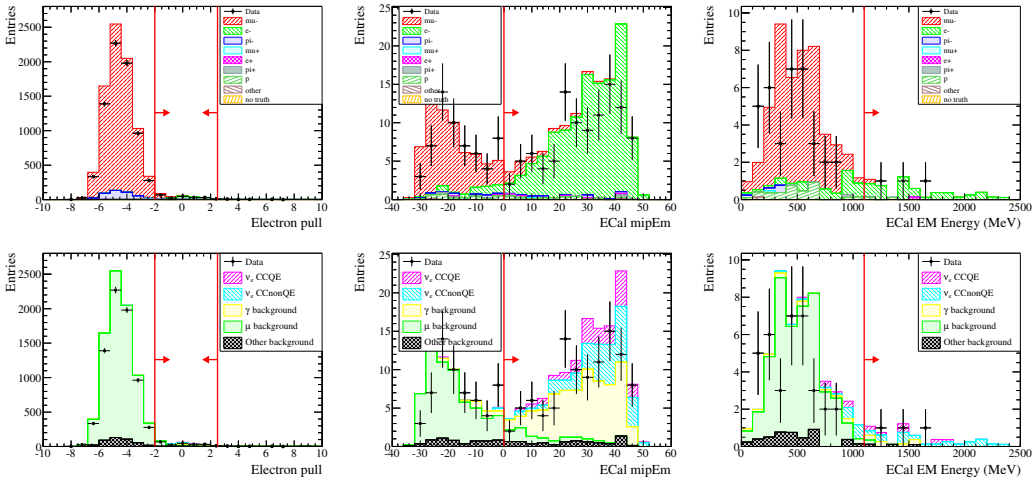

Fig. 6.7: PID criteria for tracks using TPC and BrECal: δ_e (left), mipEm (middle) and EMEnergy (right). From left to right the cuts are applied sequentially. Top (bottom) figures show the Monte-Carlo broken down by particle type (signal/background categories).

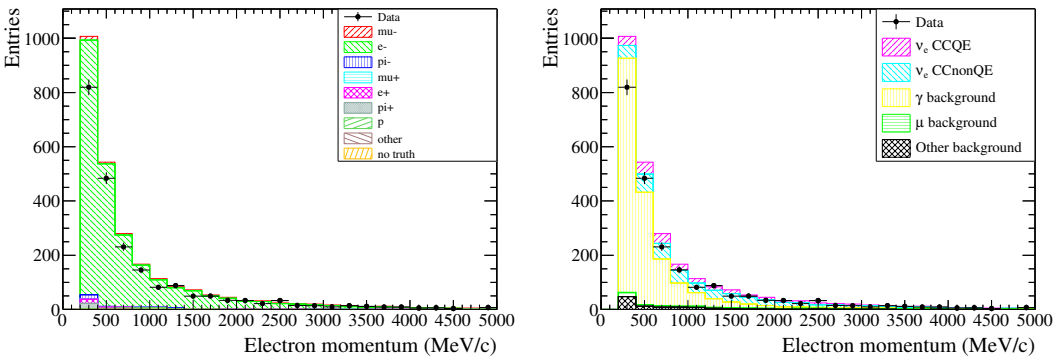

Fig. 6.8: Momentum of the electron candidate passing the full PID selection.

Category	Purity (%)	MC expected events
ν_e CCQE	9.6	253.5
ν_e CCnonQE	17.9	474.2
γ background	64.7	1710.8
μ background	3.3	88.4
Other	4.4	115.5

Table 6.2: Composition of the ν_e selection after the PID selection.

6.3 Background suppression

To achieve a clean sample of ν_e interactions we need to reduce the backgrounds that dominate the selection. Specifically, the photon conversion is abundant due to production of π^0 in ν_μ CCDIS and NC interactions and we have developed a criteria to reduce its contamination below the 50%. One way to reduce this background is applying vetoes to reject events with activity upstream to the electron candidate. The majority of the ν_e interactions produce particles in the direction of the ν_e, so if we detect other tracks upstream to the electron candidate, it is probably a background event coming from a γ conversion. Another way is reconstructing directly the γ conversion if the positron is detected.

Upstream TPC veto

We remove the events with activity in the upstream TPC. We localize the starting point of the second highest momentum particle in the event and calculate the distance with the electron candidate. The

difference between the z coordinates of their starting points is:

$$\Delta z_{TPC} = z_2 - z_1$$

and its distribution Δz is shown in Fig. 6.9 where we see that at low values we have mostly background events. Then, we accept the events with

$$\Delta z_{TPC} > 150\,\text{mm}$$

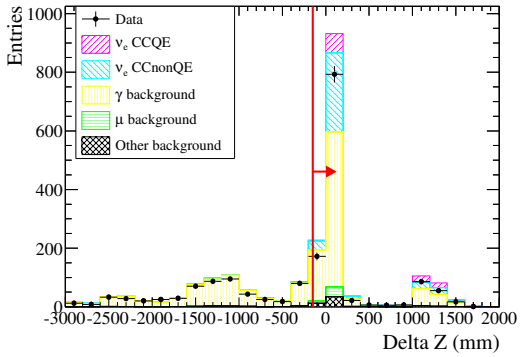

Fig. 6.9: Upstream TPC veto. Δz defined as the distance between the starting point of the electron candidate and the second highest momentum track in the event.

e^+e^- pair rejection

This cut aims to directly reduce the dominant photon conversion component. It is very effective in the case in which both the e^+ and the e^- produced by the photon reach the TPC. We have developed an algorithm to reject these events in which we look for a secondary track in the same event that fulfills the following conditions:

- It starts inside the FV;
- It is close to the electron candidate: the distance between their starting points must be smaller than 10 cm;
- It has charge opposite to the one of electron candidate;

- It has a TPC PID compatible with an electron ($|\delta(e)| < 3$).

Using the kinematic information of the electron candidate and the secondary track, the invariant mass m_{inv} is reconstructed under the hypothesis of a photon conversion:

$$m_{inv} = \sqrt{2m_e^2 + 2\left(E_+^2 E_-^2 - p_+^2 p_-^2\right)} \tag{6.1}$$

where $p_\pm$ is the measured momentum of each track and $E_\pm^2 = m_e^2 + {p_\pm}^2$ is the energy of each track assuming an electron. The distribution of m_{inv} is shown in Fig. 6.10 where we observe that the majority of the γ background is concentrated at low m_{inv} as if they come from a γ conversion has to be compatible with zero. We accept the event only if

$$m_{inv} > 100\,\text{MeV}$$

and the momentum of the electron candidate passing this cut is shown in Fig. 6.10.

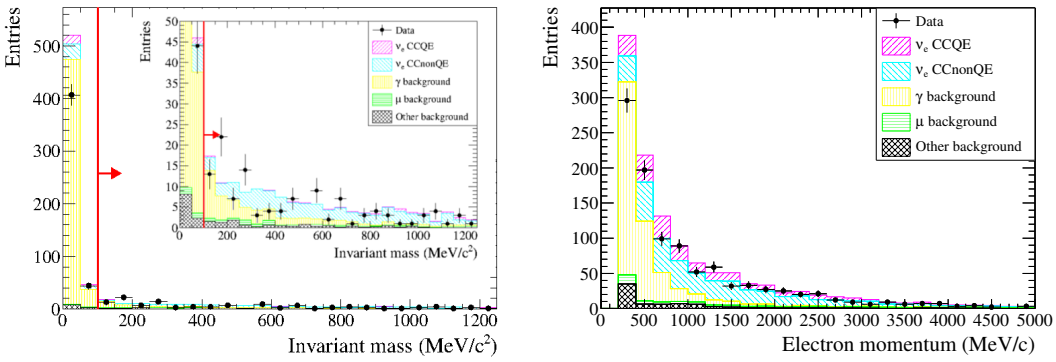

Fig. 6.10: Pair rejection. Left: m_{inv} distribution for the selected pair; right: momentum distribution of the electron candidate passing this cut.

P0D, FGD and ECal vetoes

We further reject activity upstream to the electron candidate to reduce the backgrounds. If the electron candidate starts in the upstream FGD we require that there are no other reconstructed objects in the P0D in the same event. On the contrary, if it starts in the downstream FGD, we also require no tracks reconstructed in the upstream FGD. The number of P0D and FGD objects in each event are shown in Fig. 6.11.

We keep rejecting upstream activity looking now at the ECal. The cut is similar to the TPC veto but applied to ECal objects reconstructed in the same event. If there are ECal objects in the same event, we calculate the distance between the cluster and the starting position of the electron candidate Δz_{ECal}. The low values are populated with photon conversions as shown in Fig. 6.11. The two peaks in the figure correspond to the distance between the DsECal and each of the FGDs. We only accept events that fulfill

$$\Delta z_{ECal} > 150\,\text{mm}$$

After applying the vetoes we have an inclusive ν_eCC selection with a purity of 59% [Tab. 6.3]. The γ background has been reduced from 64.7% to 29.3% and it is not the dominant component of the selection anymore, although it is still the most important background. The momentum distribution of the selected electrons at this point is in Fig. 6.11.

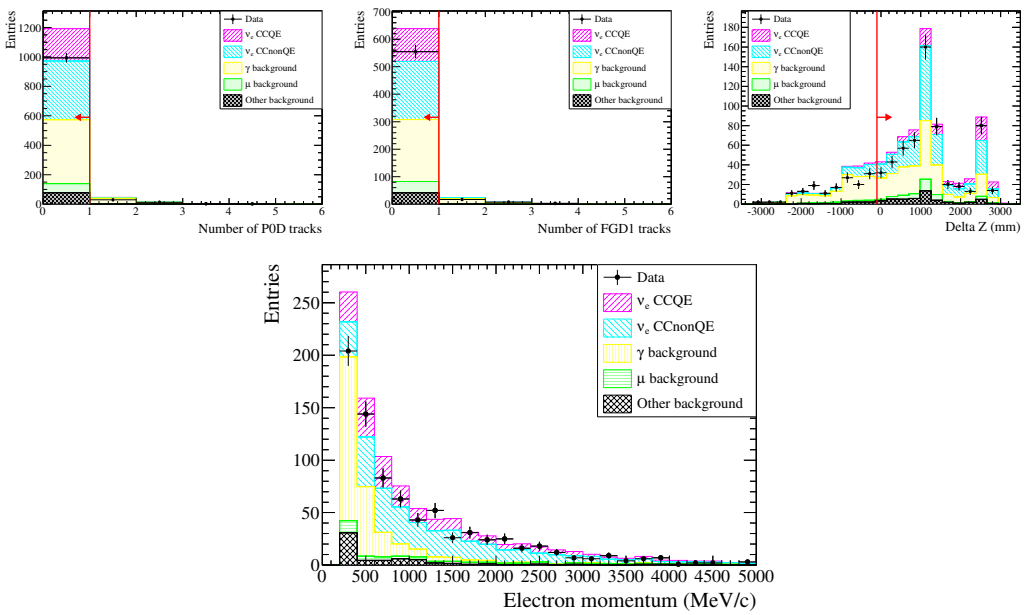

Fig. 6.11: P0D, FGD and ECal vetoes. Left: number of reconstructed segments in the P0D in the same event; middle: number of tracks in the upstream FGD in the same event; right: z distance between the electron candidate and the most upstream ECal object; and bottom: momentum of the candidates passing this cut.

Category	Purity (%)	MC expected events
ν_e CCQE	22.0	213.0
ν_e CCnonQE	36.5	354.1
γ background	29.3	284.5
μ background	5.4	52.7
Other	6.9	67.1

Table 6.3: Composition of the ν_eCC selection up to the final vetoes before the topological classification.

6.4 CCQE and CCnonQE classification

The following sections describe the criteria we apply to classify the events and enhance the ν_eCCQE and ν_eCCnonQE interactions. Notice that some events in the inclusive ν_eCC selection are not selected in any of the two categories, but most of them are background events, so the ν_e purity increases by applying the following cuts.

6.4.1 CCQE selection

ν_eCCQE events are characterized by having no other particles ejected from the nucleus except the electron and the proton. The proton is usually a low momentum particle that is often not reconstructed. For this reason, requiring a single reconstructed track is the best way to select a clean sample of ν_eCCQE interactions. All the conditions we apply to the events are aim to reject other activity than the one produced by the electron candidate. We require to the event:

- no Michel electron in the FGD,
- no other tracks in the Tracker,
- no other ECal activity.

We remark that in this category the ν_eCCnonQE is also background by definition.

Michel Electron tagging

When a muon stops in an FGD, it decays 100% of the times to an electron through

$$\mu \rightarrow e^- + \overline{\nu}_e + \nu_\mu$$

This electron release all its energy in the FGD providing a characteristic signature of a charge cluster delayed in time with respect to the electron candidate interaction. It is called Michel electron. The same occurs for the stopped pions in the FGD: they decay at rest to a muon and then to a Michel electron. So, a delayed cluster in the FGD is a sign that pions are produced and hence the event is a ν_eCCnonQE.

We look for Michel electrons only in the first FGD[1]. The number of Michel electron candidates in the event is shown in Fig. 6.12 where we see that most of the ν_eCCQE events have no Michel electrons, and the great part of the events that have at least one, belong to the background categories.

Track multiplicity in the Tracker

We require no other tracks within the same FGD where the electron candidate starts. For candidates starting in the upstream FGD we remove the events with more than one track in the FGD, no matter whether they are matched with a TPC track or not (TPC/FGD or FGD-only). The cut in the FGD-only multiplicity is only applied to the upstream FGD while the TPC/FGD cut is applied for both[2]. The number of tracks in the same event is shown in Fig. 6.12 for the two FGDs.

ECal activity

A ν_eCCQE interaction in the downstream FGD produces only one cluster in the DsECal related with the main electron candidate. If the interaction occurred in the upstream FGD, the electron can shower in the other FGD and produce more than one cluster in the DsECal. Provided this, we reject the events with more than one DsECal object only when the electron candidate starts in the downstream FGD. The number of DsECal objects that are not connected to the electron candidate is shown in Fig. 6.12.

6.4.2 CCnonQE selection

The ν_eCCnonQE events are characterized by having more than one particle exiting the nucleus, being pions the most common candidates. In order to identify this interaction, we look for extra activity not produced by the electron candidate. Specifically, we require

[1] Because the systematic error for the Michel tagging efficiency is only computed for this FGD

[2] Because the systematic errors for the FGD reconstruction is only calculated for tracks stopping in the upstream FGD. Moreover, it is only calculated for tracks with an angle $\cos(\theta) > 0.3$, so we only apply this criteria to tracks with this feature.

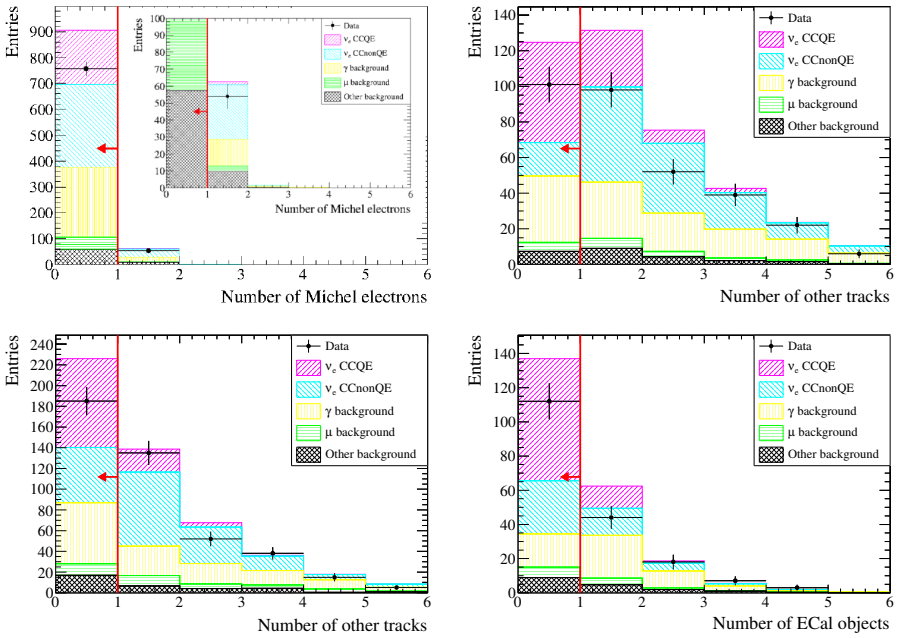

Fig. 6.12: ν_eCCQE cut chain shown sequentially. From left to right and top to bottom: number of Michel electron candidates in first FGD, number of other tracks in first FGD, number of other tracks in second FGD and number of DsECal objects not associated with the electron candidate.

- *either* a Michel electron in the event,

- *or* another track starting near the electron candidate

From Fig. 6.13 we observe that the majority of the events with some Michel electron are ν_eCCnonQE events, so we require the event to have at least one Michel electron candidate. For those cases in which we do not have a Michel electron, we search for secondary tracks. We use the inverse selection of Section 6.4.1, *i.e.* we require others FGD-only or FGD-TPC tracks. Then, the distance d between the electron candidate and the nearest secondary track is reconstructed [Fig. 6.13] and we accept only events that fulfill:

$$d < 50\,\text{mm}$$

This last condition serves to reduce the γ background in the ν_eCCnonQE selection.

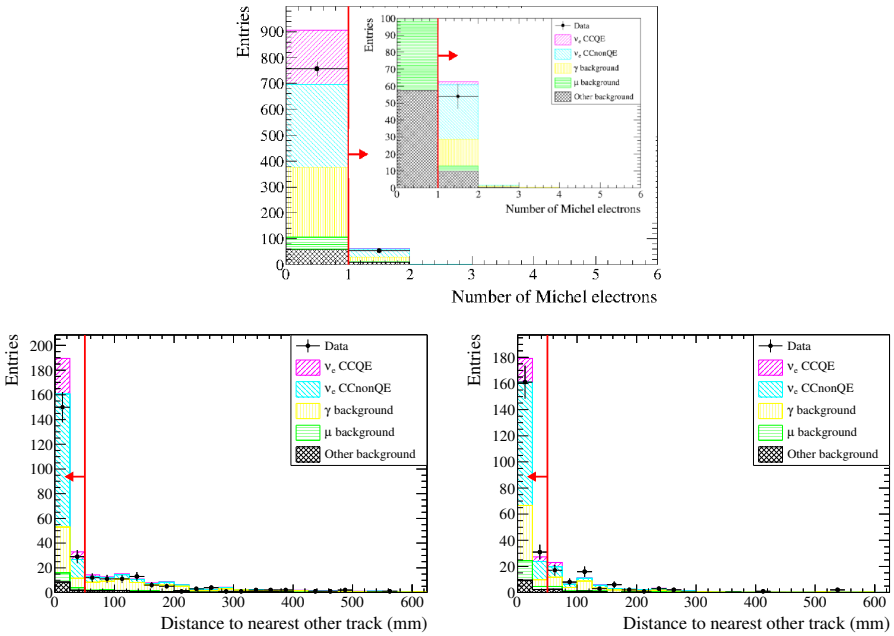

Fig. 6.13: ν_eCCnonQE cut chain shown sequentially. Number of Michel electrons in the event (top), distance between the electron candidate and its nearest track for upstream FGD events (left) and for downstream FGD events (right).

6.5 Final selection

After passing the criteria, we select 225 events in the ν_eCCQE and 392 in the ν_eCCnonQE distributed in momentum as shown Fig. 6.14. The ν_e purity is 68.3% for the ν_eCCQE selection, and 65.8% for the ν_eCCnonQE selection, with a purity for the relevant interaction mode in each selection of $\sim 50\%$. The fraction of each component is shown in Tab. 6.4. Regarding the purity depending on the ν_e parent particle, we observe that the ν_eCCQE selection has 21.7% of ν_e coming from μ decay, while the ν_eCCnonQE selection has only 8.1%. This is due to the $\nu_e(\mu)$ component populates the low energy region of the neutrino flux and hence, it produce more CCQE interactions than CCnonQE. This is an interesting feature as our selections allow to study the muon and kaon productions by separate. Regarding the backgrounds, we have a $\sim$ 30% contamination in each sample driven mainly by γ conversions ($\sim$ 20%).

The ν_eCCQE efficiency in the ν_eCCQE sample is 19.6%, and the ν_eCCnonQE efficiency in the ν_eCCnonQE sample is 19.6% as well. The combined ν_eCC efficiency adding both selections is 25.6%. In Fig. 6.15 we show the efficiency as a function of some Monte-Carlo observables like the neutrino energy, the electron

momentum and the electron polar angle $\cos(\theta)$. The low efficiency at low momentum and energy is due to the requirement that the particle needs to be reconstructed in the TPC, so it as to exit from the FGD where it was produced. The efficiency and purity of the selections at each stage of the process are shown in Fig. 6.16 and in Tab. 6.5 we show the reduction in the number of events with each cut in both data and Monte-Carlo. In general, the number of events surviving each cut as well as the distributions present a good agreement between data and Monte-Carlo.

Finally, we show in Fig. 6.17 the display of two signal events passing each selection criteria to illustrate the typical topology of the events we deal with.

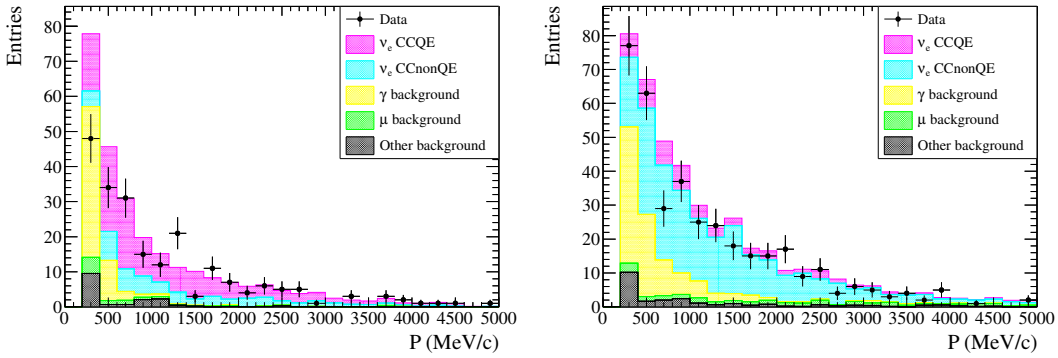

Fig. 6.14: Momentum of the electron candidate for the final ν_eCCQE (left) and ν_eCCnonQE (right) samples.

	ν_eCCQE selection		ν_eCCnonQE selection	
	Purity (%)	MC expected events	Purity (%)	MC expected events
ν_eCCQE	48.0	130.4	12.6	56.5
ν_eCCnonQE	19.5	53.0	53.2	238.6
ν_e from μ	21.7	59.0	8.1	36.2
ν_e from K	45.1	122.5	57.1	255.8
ν_e from other	0.7	2.0	0.7	3.2
γ background	21.8	59.4	22.1	98.9
μ background	4.2	11.5	6.1	27.4
Other background	6.4	17.4	6.0	26.9

Table 6.4: Composition of the final selected ν_e samples. The ν_e component is broken down by interaction type and by neutrino parent.

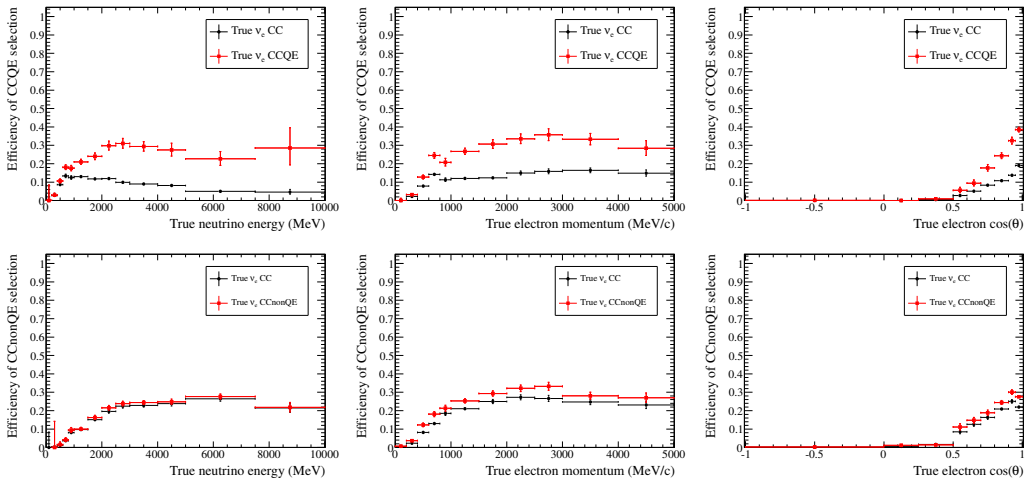

Fig. 6.15: ν_eCC and ν_eCCQE efficiencies for the ν_eCCQE selection (top) and ν_eCC and ν_eCCnonQE efficiencies for the ν_eCCnonQE selection (bottom) as a function of the Monte-Carlo neutrino energy (left), electron momentum (middle) and electron polar angle cos(θ) (right). The efficiency is relative to the number of events that have the highest momentum negative track starting in the FV.

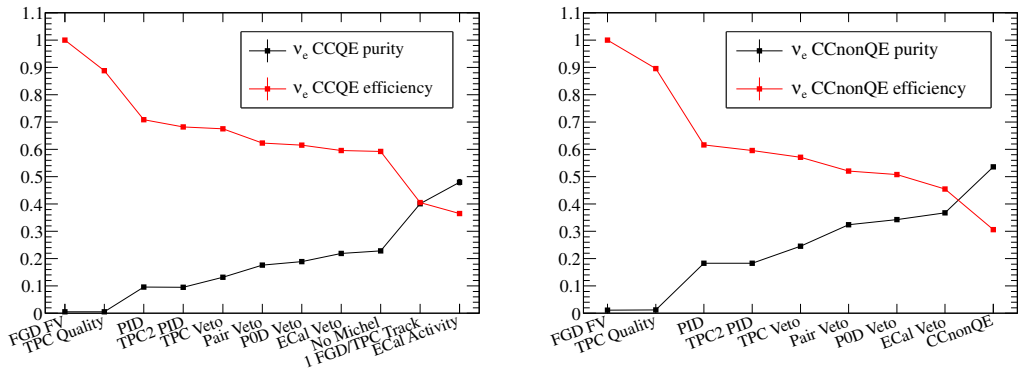

Fig. 6.16: ν_eCCQE efficiency and purity for the ν_eCCQE selection (left), and ν_eCCnonQE efficiency and purity for ν_eCCnonQE selection (right), as each cut is applied. The efficiency is relative to the number of events that have the highest momentum negative track starting in the FV.

6.5.1 Backgrounds

Photon conversion

Pair production from low energy photon conversions is the dominant background for the low energy part of of the spectrum in the ν_eCC selection. Those photons come from the unique decay channel of

	Events		Relative ratio (%)	
Cut	Data	MC	Data	MC
Good quality TPC track, $p > 200$ MeV/c	50469	57452.9	100.0	100.0
PID	2217	2642.3	4.4	4.6
PID in second TPC	2141	2559.4	96.6	96.9
TPC1 veto	1493	1829.4	69.7	71.5
Pair veto	1042	1262.6	69.8	69.0
P0D and FGD1 veto	972	1164.4	93.3	92.2
Upstream ECal veto	811	971.4	83.4	83.4
CCQE: No Michel electrons	769	927.9	94.8	95.5
CCQE: One track	292	360.9	38.0	38.9
CCQE: No ECal activity	225	271.9	75.0	75.3
$\rightarrow$ in FGD1	111	134	48.9	49.6
$\rightarrow$ in FGD2	114	136	52.6	52.3
CCnonQE	392	448.3	47.8	46.1
$\rightarrow$ in FGD1	199	241	50.5	53.9
$\rightarrow$ in FGD2	193	206	49.5	46.1

Table 6.5: Reduction in the number of events selected in data and Monte-Carlo. The Monte-Carlo numbers of events are scaled to the data POT.

the neutral pion π^0 produced in a neutrino interaction

$$\nu + X \rightarrow \nu + X' + \pi^0 \qquad \pi^0 \rightarrow \gamma\gamma$$

where one of the two γ converts inside the FGD and the electron is reconstructed in the TPC. If the positron is also reconstructed in the TPC, we are able to reject the event with the pair veto. Nonetheless, many times the positron is not detected being impossible to distinguish it from a ν_eCCQE interaction.

The π^0's come mainly from the dominant ν_μ component in the T2K flux through CCDIS or NCπ^0. The ν_μ can interact inside the FV (InFV) or outside (OOFV). Interactions OOFV are mostly produced in nuclei other that Carbon that are not as well controlled as the interactions InFV, because the ν_μ cross-section measurement [Section 5.1] lacks on this component. The OOFV component has two origins:

- γ conversions: corresponding to an OOFV ν_μ interaction that creates an electron or a positron in the FV (OOFV$e^+ - e^-$). It is the 33.1% of the total background;
- Misidentified particles: misidentified muons, protons or pions produced in a OOFV ν_μ interaction (OOFV Other). Being the 16.7% of the total background.

A control sample is needed to measure *in situ* the important photon background coming from inside

or outside the FV. It is developed and presented in the next chapter.

Misidentified muons

There are very few muons that are misidentified as electrons in our final selection ($\sim 5\%$ of the selected events). They are mainly at low energy, were it is produced the overlapping between the TPC deposited energy curves for muons and electrons [Fig. 4.4], and where the ECal is not good distinguishing between showers and tracks. A cross check with the data is needed to verify the prediction and it is presented in Chapter 7.

Other backgrounds

The remainder of the background comes from misidentified particles other than muons. They are mainly pions at low energy and very few protons at 1 GeV. Again the reason is the overlap of the dE/dx curves for pions and protons with electrons. This background is very small and we rely on the Monte-Carlo prediction as any difference has a negligible impact on the analysis.

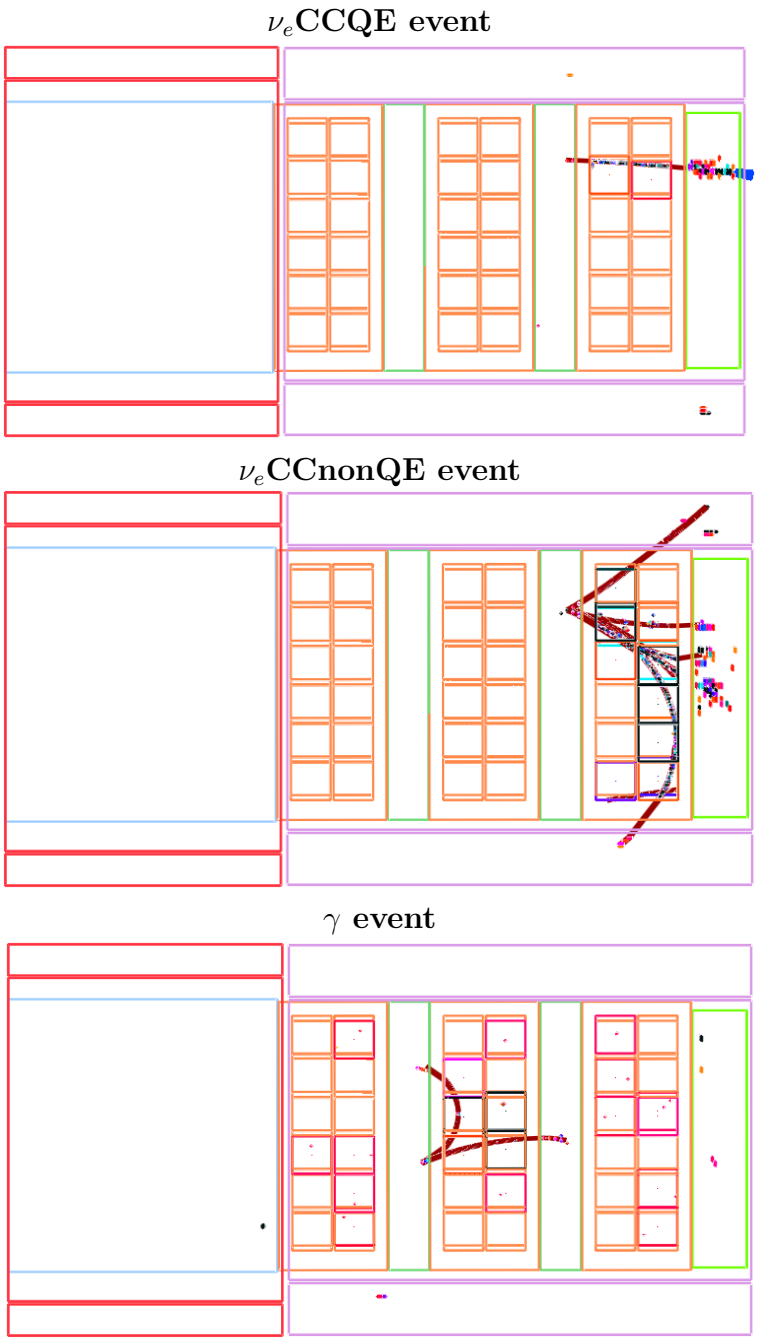

Fig. 6.17: Event displays of typical signal events passing the ν_eCCQE and ν_eCCnonQE selections presented in this chapter and a photon conversion event passing the γ selection described in the next chapter.

Chapter 7

Control samples

To further control the backgrounds we developed two analyses: one that selects photon conversions in the tracker and other that estimates the misidentified muons using a data-driven method. As the previous chapter, the studies are done using the nominal Monte-Carlo before the ν_μ ND280 measurement of the flux and cross section.

7.1 Photon control sample

The photon selection is intended to study and control the dominant background in the ν_eCC selection. This control sample is obtained selecting a clean sample of γ conversions inside the FGD. This will improve our knowledge of the γ background as it helps to constrain the uncertainties related to the π^0 production and interactions OOFV. The γ selection is based on the identification of an electron-positron pair when both particles enter in the TPC. We base our selection in searching for tracks with opposite charges and with an invariant mass compatible with zero. On the following we describe the selection cuts we developed to enhance the γ conversions:

Beam trigger

The event timing must be compatible with one of the 8 bunches (6 bunches for run I).

Primary track

The highest momentum negative track of the event is selected. This is the primary track of our event.

Fiducial volume

The primary track has to start within the FV. Up to here the selection criteria is the same than in the ν_eCC selection case.

TPC track quality

Require that the main track has more than 18 reconstructed clusters in the TPC. The TPC PID is not as important in this selection as in the ν_eCC sample, thus we relax the cut in the number of TPC reconstructed nodes for 35 to 18.

Secondary track

To reconstruct a photon conversion we require at least one secondary track with opposite charge with respect to the primary track, reconstructed in the TPC and starting in the FV. The number of secondary tracks for the events passing the last three cuts are shown in Fig. 7.1. The events with no secondary tracks are rejected. The track whose starting point is closest to the starting point of the primary is defined as the secondary track.

Distance

A pair e^--e^+ from a photon conversion must come from the same vertex, thus we require that the distance between the starting points of the primary and secondary tracks is smaller that 10 cm. The distribution of the distance is showed in Fig. 7.1. We observe that the majority of the e^- and e^+ are below this cut.

Invariant mass

At this point, our sample is mainly populated by muons and protons. As the invariant mass for a pair coming from a photon conversion must be null, we largely enhance our signal by reconstructing and requiring a low invariant mass for each event. We build the invariant mass m_{inv} using the kinematics of both tracks applying Eq. (6.1) and we require it to be smaller than 50 MeV. The m_{inv} distribution is shown in Fig. 7.1, where we observe that most of the e^- and e^+ have low m_{inv} while the other particles

are in the higher region. The e^- purity before this condition is applied is about 12% and becomes 90% after this condition, with an almost unchanged efficiency.

Electron PID

Finally, to further increase the e^- purity we apply the TPC PID to both tracks following the criteria:

$$|\delta_e^p| < 2 \qquad |\delta_e^s| < 3$$

where δ_e^p is the electron pull for the primary track [Fig. 7.1] and δ_e^s the one for the secondary track.

Final photon selection

We are able to select 990 events in the data with an e^-/e^+ purity of 98% and moreover, the 95% are coming from γ conversions. Only the 5% is coming from ν_eCC interactions. The momentum distribution of the primary track passing the whole criteria is in Fig. 7.2, and in Tab. 7.1 the fraction and the number of events of each component. This selection enhances the γ component that comes from neutrino interactions OOFV, with a 60.7% for γOOFV and 32.9% for γInFV. Thanks to this fact, we control the OOFV component in the ν_eCC selection that is the background that present more uncertainties. The e^-/e^+ efficiency and purity is shown in Fig. 7.3 for the criteria chain.

A large deficit of events is observed in the low momentum part. This comes from the large uncertainties associated with the π^0 production and the OOFV component, and we stress that the deficit is compatible within the final uncertainties presented in next chapter. A similar deficit is observed in the ν_eCCQE selection at low momentum [Fig. 6.14] where the γOOFV is dominant. This is an indication of the need of including this control sample in our analyses to increase the knowledge of the photon background and rely on the final measurements.

Apart from this main purpose, a clean sample of electrons is extremely useful for calibration, testing or systematic errors calculations. This sample can also be used to compute the TPC PID systematic error as the electron contain is very high even without applying the final PID cut. We refer to Appendix A.2 for that work. As final point and only for illustration purpose, we show in Fig. 6.17 a typical photon conversion event passing the selection criteria.

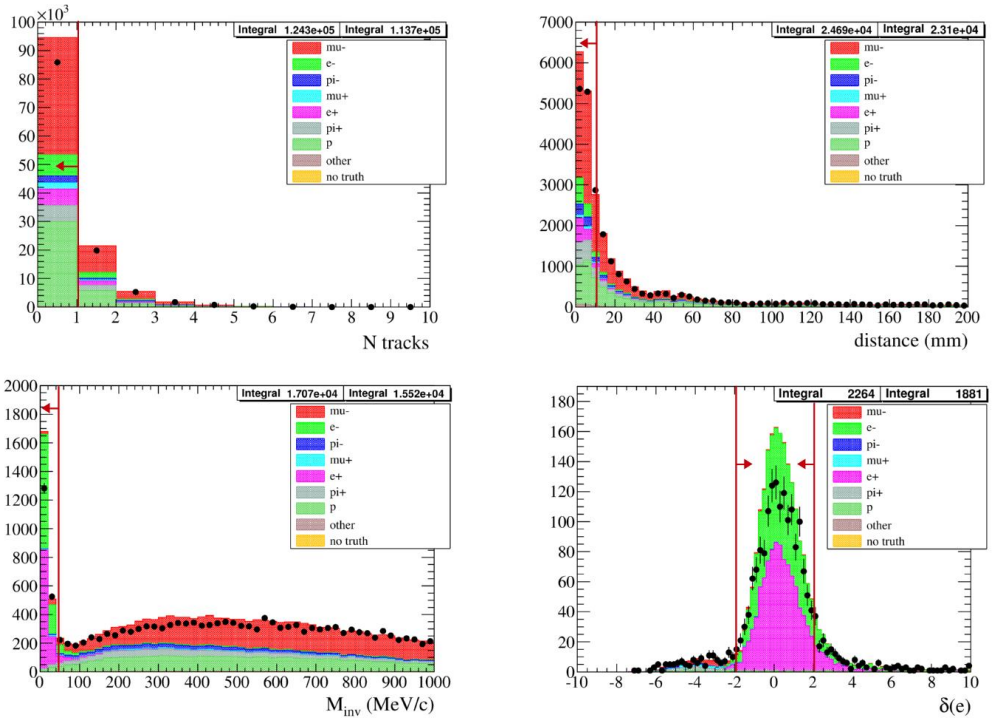

Fig. 7.1: Photon sample selection cuts. From top to bottom and left to right: number of secondary tracks in the event, distance between the main and the closer secondary track, m_{inv} in the photon conversion hypothesis and δ_e of the primary track.

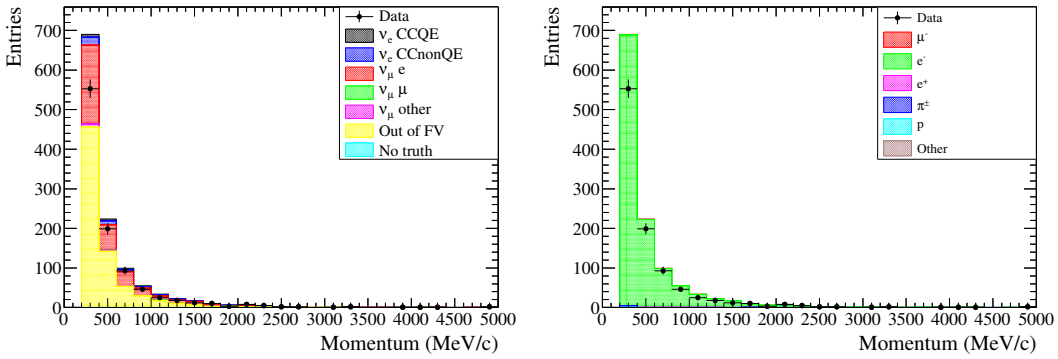

Fig. 7.2: Momentum spectrum for the most energetic track in the final photon selection. The left plot shows the Monte-Carlo broken down by the interaction type, and the right plot shows it broken down by the particle type.

7.1.1 Comparison of the γ background with the γ selection

To assure that it is allowed to use this selection as control sample of the γ background, the γ selection has to be checked to contain events of the same type than the γ background of the ν_eCC selection. As

	# expected events	Purity
ν_eCCQE	24.3	1.9%
ν_eCCnonQE	53.5	4.3%
γ InFV	412.1	32.9%
γ OOFV	760.3	60.7%
Total	1250.3	-
Data	990.0	-

Table 7.1: Purity and number of events for the gamma control sample.

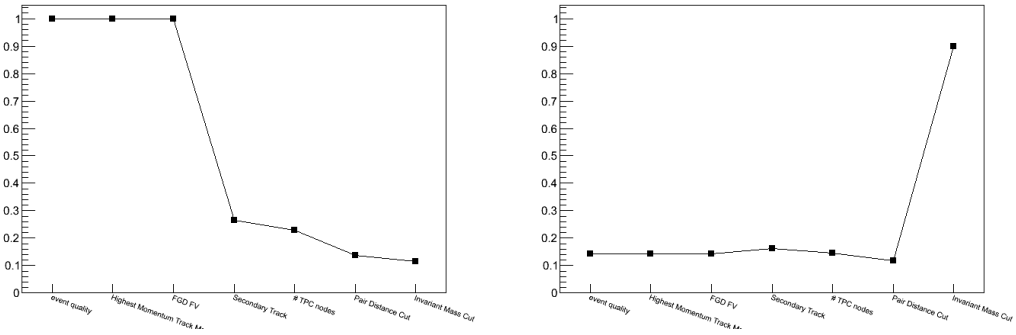

Fig. 7.3: Electron efficiency (left) and purity (right) for gamma selection versus the different cuts.

starting point, whether the samples scan the same phase space of the kinematics of the electron and neutrino is checked. The electron momentum and the Monte-Carlo neutrino energy distributions for both samples are shown in Fig. 7.5 where it is clear that the two samples have a similar distributions. The peak below 1 GeV in neutrino energy is mainly due to NC interactions.

The origin of the selected events in terms of the parent particle, interaction type and target material is presented in Fig. 7.5 and Tab. 7.2 for each sample. First we observe that, indeed, most of the events come from γ conversion. Notice that the difference in the fractions is because in the ν_eCC background we have not only γ conversions, but also some misidentified muons and pions which come directly from a ν interaction. The fraction of interaction type in each sample are very similar. They are mainly dominated by CCDIS and NC events where abundant π^0 production is expected. The γ selection lacks on the OOFV Other component, since it only comes from photon conversion, so it can only control the OOFV$e^+ - e^-$ component of the ν_eCC background. The amount of γOOFV is larger in the γ selection than in the ν_eCC selection. This is because we do not apply the veto cuts in the γ selection. At the bottom of Tab. 7.2 we show that if we do not apply the vetoes to the ν_eCC selection, the fraction on the position of the neutrino interactions are similar in both sets. The material in which the interaction

takes place is important since the systematic uncertainties on the cross-section models depend on the target nuclei. The composition is again similar for the two samples. As conclusion, the γ sample have very similar features with respect to the γ background and hence, it is a good control sample candidate for the ν_e beam analyses.

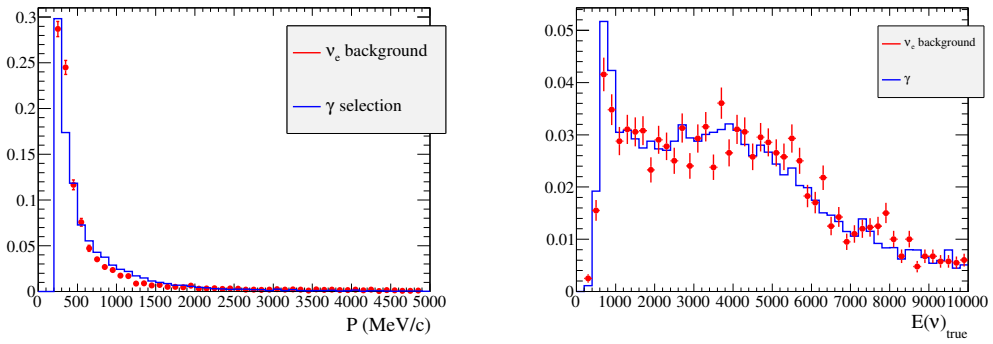

Fig. 7.4: Electron momentum and Monte-Carlo neutrino energy distribution for the background events of the ν_eCC selection and the γ selection.

7.2 Misidentified muons

The $\sim 5\%$ of the ν_eCC sample are muons that pass the PID criteria. We have largely reject the muon background by the 99.8% and the small remainder may be more difficult for the Monte-Carlo to be reproduced. So, we need to cross-check its prediction and a data-driven study is carried out to measure the muon misidentification probability directly from the data.

We select a clean sample of through-going muons requiring: a negative track crossing the three TPCs, compatible with a muon in the upstream TPC ($|\delta_\mu| < 2.5$) and not compatible with an electron ($|\delta_e| > 2$). This TPC is not used in the ν_e analysis. Applying the PID selection described in Section 6.2 we calculate the fraction of muons that passes the conditions. The probability of a muon to enter in either of our selections in function of the momentum is shown in Fig. 7.6. We compare the cases where ECal is and is not applied to show how the muon rejection improves if the ECal is used in the PID criteria. The muon misidentification probability is below 1% in any case. To compute the absolute number of muons entering in our selections, a sample of muons that passes all the ν_eCC criteria, but the PID, is selected. We exclude the electron PID condition, that is replaced by a muon PID condition of $|\delta_\mu| < 2.5$. Multiplying the muon momentum distribution by the misidentified muon probability

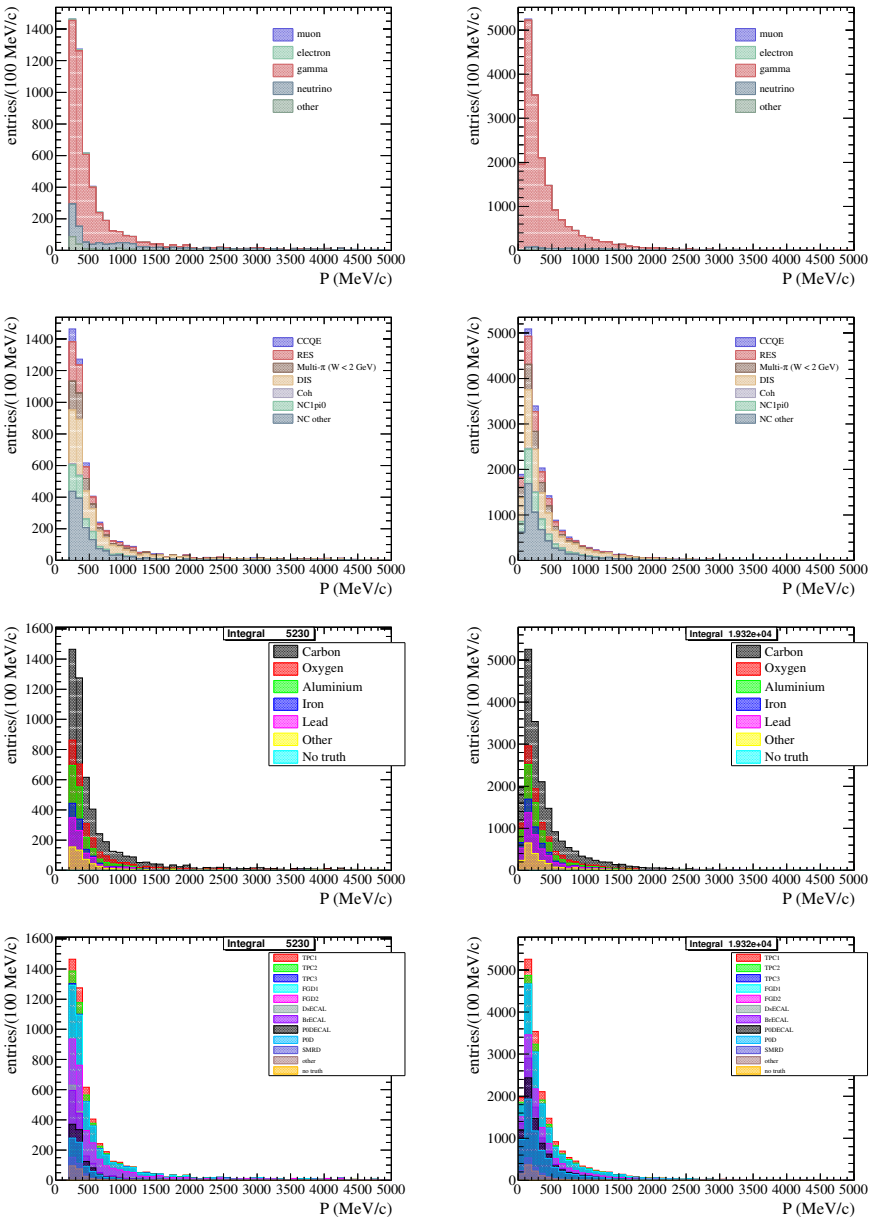

Fig. 7.5: Electron momentum for the background events of the ν_eCC sample (left) and the γ selection (right). The Monte-Carlo is divided in: (from top to bottom) parent particle, interaction, target and detector where the neutrino interaction is produced.

obtained above, we get the misidentified muons component expected in the ν_eCC selection.

The momentum distribution is shown in Fig. 7.6 along with the Monte-Carlo prediction. If we separate both ν_eCC branches, we measure 13.6 ± 3.5 for the ν_eCCQE selection while 10.2 are predicted and 17.4 ± 3.4 for the ν_eCCnonQE selection while 22.9 are predicted. As the agreement is good in both

Particle	γ backg. in ν_e selection (%)	γ selection (%)
e^-	74.8	97.4
μ	10.8	1.3
π	7.2	0.4
p	3.1	0.8
Parent particle		
γ	74.6	95.0
ν	20.4	4.4
other	5.0	0.6
FV		
ν_eInFV	0	6.2
γInFV	51.1	32.9
OOFV$e^+ - e^-$	33.1	60.3
OOFV Other	16.7	0.5
Interaction		
CCQE	4.3	4.1
CC1π	14.2	11.5
CC Multiπ	11.4	10.1
CC DIS	32.1	31.6
CC Coh	0.5	0.4
NC1π^0	8.6	10.9
NC other	28.8	31.4
Target		
Carbon	46.4	49.3
Oxygen	16.5	11.4
Aluminum	13.5	13.3
Iron	4.3	4.2
Lead	9.4	11.4
Other	9.9	10.4
Detector	ν_e background (no vetoes) (%)	
TPC1	7.3	8.0
TPC2	4.9	4.3
TPC3	0.2	0.2
FGD1	26.3	26.3
FGD2	17.5	12.3
DsECAL	0.5	0.0
BrECAL	5.7	6.2
P0DECAL	5.1	7.5
P0D	27.1	27.2
SMRD	1.6	2.2
Other	3.8	5.3

Table 7.2: Fractions of the types of events ν_eCC background and in the γ selection.

samples and also this component is very small, we conclude that we rely on the Monte-Carlo to control the misidentified muons.

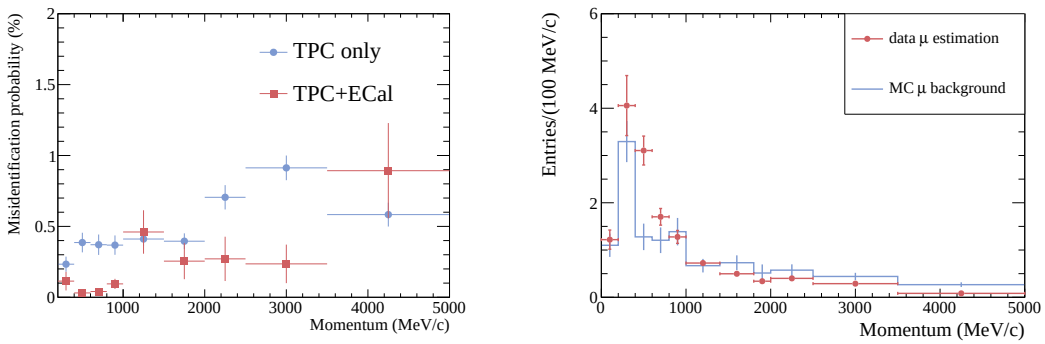

Fig. 7.6: Muon misidentification probability for track with and without ECal object (left), and comparison for the misidentified muons entering in the inclusive ν_eCC (right).

Chapter 8

Systematic uncertainties

There are four different sources of systematic errors that have been considered:

1. Neutrino flux uncertainties
2. Cross-section models uncertainties
3. Neutrino Final State Interactions
4. Detector systematic errors

In the following we introduce and calculate the effect of the systematic errors in the ν_eCCQE, ν_eCCnonQE and γ samples. The systematic errors are correlated each others and these correlations are treated through a covariance matrix. Each systematic error is parametrized in order to be introduced in the analysis and the values of these parameters are summarized in Tab. 8.1. The parametrization adopted for each systematic error is explain in their corresponding sections [Sections 8.1 to 8.4] and a complete summary is presented in Section 8.5. The final covariance matrix we use in our analysis is calculated in Section 8.6 and the effect of the systematic errors in our selections is presented in Section 8.7.

8.1 Flux uncertainties

The flux uncertainties have two main sources, namely: hadron production cross-sections and beam uncertainties. The NA61 experiment [Section 3.4.1] measures the ones corresponding to the hadron production on a Carbon thin target and on a T2K replica target. On the other hand, the T2K beam group calculates the ones coming from the beam uncertainties. In Fig. 3.9 we find the size for each one. The flux uncertainties depend on the Monte-Carlo neutrino energy and on the neutrino flavour. The total neutrino flux uncertainty is parametrized by a set of 25 parameters $\vec{f}_{Flux}$ that drives a specific neutrino flavour and energy range as shown in Tab. 8.2.

Systematic	Before ν_μ fit	After ν_μ fit	# of pars.
ν_μ-flux	$1 \pm [0.10, 0.20]$	$[0.93, 1.05] \pm [0.07, 0.08]$	11
ν_e-flux	$1 \pm [0.11, 0.16]$	$[0.95, 1.02] \pm [0.07, 0.09]$	7
$\bar{\nu}_\mu$-flux	$1 \pm [0.11, 0.17]$	$[0.99, 1.03] \pm [0.09, 0.14]$	5
$\bar{\nu}_e$-flux	$1 \pm [0.14, 0.18]$	$[0.95, 1.01] \pm [0.08, 0.17]$	2
M_A^{QE}[GeV]	1.21 ± 0.45	1.24 ± 0.07	1
M_A^{RES}[GeV]	1.41 ± 0.11	0.96 ± 0.07	1
CC Other Shape [GeV]	0.0 ± 0.4	0.225 ± 0.285	1
Spectral Function (^{12}C&^{16}O)	0 ± 1	0.240 ± 0.129	1
W shape [MeV]	87.7 ± 45.3	–	$1^\dagger$
p_F (^{12}C&^{16}O)[MeVc^{-1}]	217 ± 30	266 ± 11	1
E_b (^{12}C&^{16}O)[MeVc^{-1}]	25 ± 9	30.9 ± 5.2	1
π-less Δ decay [%]	0.2 ± 0.2	0.206 ± 0.085	1
CCQE Norm	1 ± 0.11 1 ± 0.30 1 ± 0.30	0.966 ± 0.076 0.931 ± 0.103 0.852 ± 0.113	3
CC1π Norm	1.15 ± 0.43 1.0 ± 0.40	1.265 ± 0.163 1.122 ± 0.172	2
NC1π^0	0.96 ± 0.43	1.135 ± 0.248	1
NC Other	1.0 ± 0.3	1.410 ± 0.218	1
CCCoh	1.0 ± 1.0	0.449 ± 0.164	1
$\sigma_{\nu_e}/\sigma_{\nu_\mu}$	1 ± 0.03	–	$1^\dagger$
$\sigma_{\bar{\nu}}/\sigma_\nu$	1 ± 0.4	–	1
OutFV $e^+ - e^-$	1 ± 0.3	–	1
OutFV Others	1 ± 0.3	–	1
Detector+FSI	$1 \pm [0.07, 0.19]$	–	17 (10)‡
Total			60 (55)‡

Table 8.1: Summary of all the systematic uncertainties on the analyses. The values before and after the ND280 ν_μ fit are shown being the latter the prior values in our ν_e analyses. The values within brackets are the upper and lower limits for that set of parameters. †Not included in ν_e flux analysis. ‡Number in brackets correspond to the ν_e disappearance analysis. As in that analysis we merge ν_eCCQE and ν_eCCnonQE selections, we have less parameters.

As we learned in Section 5.1, the flux is measured along with the neutrino cross-sections using a sample of ν_μ interactions in ND280. Thanks to this analysis, the uncertainties in the flux are further constrained as it is observed in Fig. 8.1 where we show the error and the central value of the parameters before and after the ν_μ fit. It reduces the flux errors from $\sim 13\%$ to $\sim 8\%$ and also changes the central value of the parameters as is illustrated in Fig. 8.1 and Tab. 8.1. We remit to Section 3.4 for further explanations about the flux features and errors.

Flavor	Binning(GeV)
ν_μ	$[0, 0.4, 0.5, 0.6, 0.7, 1.0, 1.5, 2.5, 3.5, 5.0, 7.0, 30.0]$
ν_e	$[0, 0.5, 0.7, 0.8, 1.5, 2.5, 4.0, 30.0]$
$\bar{\nu}_\mu$	$[0, 0.7, 1.0, 1.5, 2.5, 30.0]$
$\bar{\nu}_e$	$[0, 2.5, 30.0]$

Table 8.2: Neutrino energy binning for flux parameters for the flux systematic errors ν_μ, ν_e, $\bar{\nu}_\mu$ and $\bar{\nu}_e$.

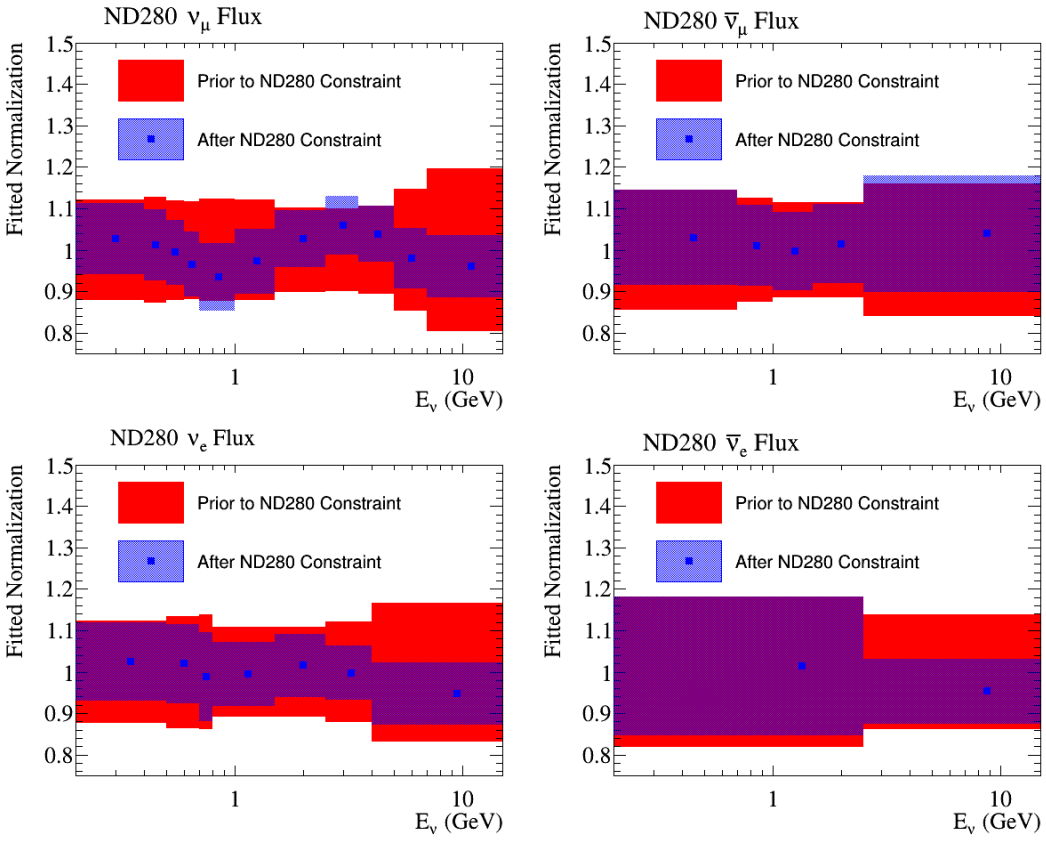

Fig. 8.1: Flux uncertainties before and after the ND280 ν_μ fit.

8.2 Cross-section uncertainties

The cross-section systematic errors come from the uncertainties in the neutrino interaction models. A complete set of cross-section systematic uncertainties are provided by the Neutrino Interaction Working Group of T2K [80]. The MiniBooNE data for the CCQE [66] and CC1π [67] measurements, are fit using the T2K neutrino event generator (NEUT [103]) with a minimal set of parameters that characterize each interaction. In general, the uncertainties in the parameters are taken as the difference of the nominal NEUT parameter and the best fit value for the external data. These uncertainties are set as prior uncertainties and provide a reasonable starting point to the ND280 ν_μ fit.

After the ND280 ν_μ measurement, the cross-section errors get reduced and the improvement is shown in Fig. 8.2, where the final uncertainties are within the range $10-20\%$. The Tab. 8.1 presents the value of each systematic uncertainty before and after the ν_μ fit. Each cross-section systematic error are detailed on the following:

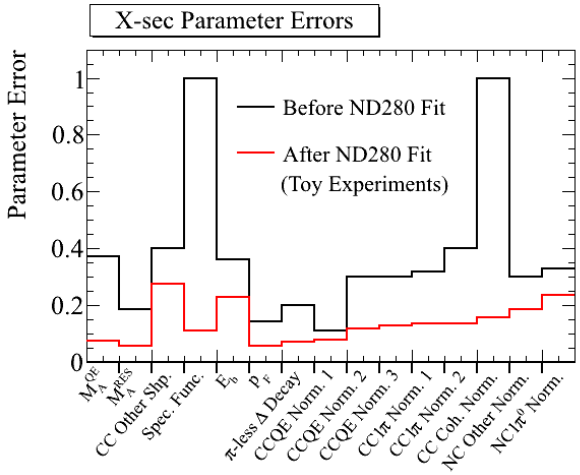

Fig. 8.2: Cross-section uncertainties before and after the ND280 ν_μ fit.

Uncertainties in CCQE

The CCQE cross-section is parametrized by the axial mass M_A^{QE} and three normalization factors. The M_A^{QE} parameter changes the expected momentum shape of the CCQE events while the other three parameters only normalize a given neutrino energy range binned as follows:

$$[0, 1.5, 3.5, 30]\,\text{GeV}$$

For high energy, both the MiniBooNE data and NOMAD [13] data are used to set the uncertainties.

Uncertainties in single charged pion production

Pion production comes from CCRes interactions that are parametrized by the axial mass M_A^{Res} and two more normalization parameters (CC1π) binned as follows:

$$[0, 2.5, 30]\,\text{GeV}$$

For CCCoh interactions we include a simple normalization parameter with a 100% uncertainty as the current data on pion production is compatible with no CCCoh.

Uncertainties in neutral currents

The π^0 production is parametrized with a normalization factor (NC1π^0) with a 30% uncertainty and another parameter called *W-shape*. The latter is an empirical parameter that allows to modify the shape of the momentum of the π^0 produced in NC1π^0 interactions. The error associated to this parameter also come from MiniBooNE studies and it is of 52%. We remark that this systematic error is not included in the ν_e flux validation analysis and we only included in the sterile neutrino analysis in order to be more conservative. The rest of the NC interactions not producing a π^0 (NC Other) are modeled with a normalization parameter with an associated error of 30%.

The NC interactions are poorly measured by the ND280 ν_μ analysis, so after the fit, still a $20-25\%$ uncertainties remain in both parameters. These parameters largely affect to the low energy part of our ν_eCC selection. We rather use the γ control sample, that is rich in NC events ($\sim 30\%$), to constrain this background than rely on external measurements.

Uncertainties in nuclei models

In CCQE cross-sections the target nucleus is described as a Relativistic Fermi Gas (RFG). The nuclear potential is parametrized by the Fermi momentum of the nucleus p_F and the binding energy E_b. A more realistic model of the nuclear potential is called *spectral function* (SF). It is described by a parameter that is 0 when the Relativistic Fermi Gas model is consider and 1 when we use the SF model. We allow

intermediate values even if they have not physical meaning, while values out of the range [0,1] are not allowed.

Uncertainties in ν_e interactions

ν_e cross-section are not precisely measured and according to the models there is a 3% uncertainty in the difference between the CCQE cross-section for electrons σ_{ν_e} and for muons σ_{ν_μ} [79]. A parameter to take this into account is included, but only in the ν_e disappearance analysis. For the beam ν_e measurement, we drop this parameter since we want to allow the study of the sensitivity of the ν_e selections to possible differences between ν_e and ν_μ cross-sections, giving an upper limit.

Uncertainties in other interactions

For the case of multi-pion production, the CC Other Shape parameter modifies the shapes of the different channels: CCDis and CCRes interactions. The prior error that we consider before the ν_μ fit is assumed to be $0.4/E_\nu$ because it is known to be of the order of 0.4 GeV for 1 GeV.

When a neutrino interaction produces a Δ resonance, it might interact before it decays to pions. In this case the topology is identical to a CCQE event. This case is known as π-less Δ decay that is assumed to occur a 20% of the cases. We include an associate systematic error to the uncertainty on this fraction. NEUT simulates by default the 20% of events with π-less Δ decay. We considered as the systematic error the effect that has in the simulation a 0% of π-less Δ decays. This affects to all the interactions with resonances involved. Values of this parameter leading to smaller fraction than 0% are not physical and then they are not considered.

An extra parameter is added to account on the uncertainty in the anti-neutrino cross-section. It is parametrized by a normalization factor applied to the antineutrino component ($\sigma_\nu/\sigma_{\bar{\nu}}$) with a 40% error.

Uncertainties in the out of fiducial volume

As we have shown in the Chapter 6, a sizable fraction of the events that we select comes from OOFV neutrino interactions. The OOFV interactions occur in materials other than Carbon where the neutrino cross-sections are different and are not properly measured by ND280 because the ν_μ selection contains

only a 3% of OOFV. Moreover, it does not contain OOFV events coming from γ conversion, but of other types. We apply an extra systematic error of 30% to account on the ignorance of this component. To parametrize the OOFV component we define two parameters, each of one accounting on one different OOFV component (see Section 6.5.1):

- OOFV $e^+ - e^-$: drives the γOOFV background;
- OOFV Other: affects to the misidentified particles produced in OOFV.

8.3 Final State Interaction systematic uncertainties

Re-interactions of the hadrons produced by neutrino interactions within the nucleus, known as FSI, lead to large uncertainties in neutrino analyses. Since we classify our selection attending to the exiting particles from the nucleus, an event selected as ν_eCCQE can be an actual ν_eCCRes with a pion absorption. So, mismodelling of these effects lead to important systematic errors. We assume FSI for leptons is negligible since they do not interact strongly, and also, FSI are not considered for hadrons produced off unbound protons (like Hydrogen in water) since the neutrino interaction is far from the nuclear medium. The final state of pions is the largest contribution to the errors.

NEUT includes the hadron re-interaction as a semi-classical microscopic cascade model where a set of 6 low-level parameters change the different aspects of the cascade ([124, 103]). Our calculation of their uncertainties is driven by a fit on the MiniBooNE data, as it covers the same phase space of T2K. The dependencies of the 6 low-level parameters are complicated and their correlations are strong. So, we re-parametrize them by effective parameters $\vec{f}_{FSI}$, each of them being applied to a specific neutrino flavour, electron momentum range and selection (ν_eCCQE, ν_eCCnonQE or γ samples). We include 7 parameters for the ν_eCCQE, 7 for the ν_eCCnonQE and 3 for the γ selection according to the momentum ranges in Tab. 8.3.

The ν_e disappearance analysis (Chapter 10) is performed in reconstructed neutrino energy instead of electron momentum, so the parameters refer to a reconstructed neutrino energy range. Another important difference is that we treat together the ν_eCC selections, so in total we only have 7 parameters for the ν_eCC and 3 for the γ selection as it is established in Tab. 8.3.

To calculate the uncertainties in $\vec{f}_{FSI}$ in both of the cases, we built N different distributions (electron momentum for beam ν_e measurement and neutrino energy for ν_e disappearance analysis) for each

selection varying the low-level parameters within their uncertainties. In this way, we calculate the 1σ effect of the FSI uncertainties on each distribution bin. The $\vec{f}_{FSI}$ uncertainties and their correlations are provided by the covariance, defined as:

$$V_{i,j} = \frac{1}{N}\sum_{i}^{N} \frac{\left[n^i_{var} - n^i_{nom}\right] \cdot \left[n^j_{var} - n^j_{nom}\right]}{n^i_{nom} \cdot n^j_{nom}} \tag{8.1}$$

where N is the number of generated distributions, n^i_{nom} is the content of the bin i for the nominal Monte-Carlo and n^i_{var} is the bin content of the varied distribution. This provides a covariance matrix shown in Fig. 8.3 for $\vec{f}_{FSI}$. The squared root of the diagonal terms corresponds to the 1σ uncertainties of $\vec{f}_{FSI}$ and it is shown in Fig. 8.3. The FSI uncertainties are $\sim 4\%$.

			Analysis	
			ν_e beam meas.	ν_e disappearance
Detector+FSI Parameter	ν flavour	Selection	Momentum (GeV)	ν energy (GeV)
$f^1_{FSI+Det}$	ν_e	ν_eCCQE (ν_eCC)	0.2 - 0.6	0.2 - 0.6
$f^2_{FSI+Det}$	ν_e	ν_eCCQE (ν_eCC)	0.6 - 1.2	0.6 - 2.0
$f^3_{FSI+Det}$	ν_e	ν_eCCQE (ν_eCC)	1.2 - 2.5	2.0 - 2.5
$f^4_{FSI+Det}$	ν_e	ν_eCCQE (ν_eCC)	2.5 - 10.0	2.5 - 10.0
$f^5_{FSI+Det}$	ν_μ	ν_eCCQE (ν_eCC)	0.2 - 0.5	0.2 - 0.5
$f^6_{FSI+Det}$	ν_μ	ν_eCCQE (ν_eCC)	0.5 - 1.0	0.5 - 1.0
$f^7_{FSI+Det}$	ν_μ	ν_eCCQE (ν_eCC)	1.0 - 10.0	1.0 - 10.0
$f^8_{FSI+Det}$	ν_e	ν_eCCnonQE	0.2 - 0.6	-
$f^9_{FSI+Det}$	ν_e	ν_eCCnonQE	0.6 - 1.2	-
$f^{10}_{FSI+Det}$	ν_e	ν_eCCnonQE	1.2 - 2.5	-
$f^{11}_{FSI+Det}$	ν_e	ν_eCCnonQE	2.5 - 10.0	-
$f^{12}_{FSI+Det}$	ν_μ	ν_eCCnonQE	0.2 - 0.5	-
$f^{13}_{FSI+Det}$	ν_μ	ν_eCCnonQE	0.5 - 1.0	-
$f^{14}_{FSI+Det}$	ν_μ	ν_eCCnonQE	1.0 - 10.0	-
$f^{15}_{FSI+Det}$	all	γ	0.2 - 0.5	0.2 - 0.5
$f^{16}_{FSI+Det}$	all	γ	0.5 - 1.0	0.5 - 1.0
$f^{17}_{FSI+Det}$	all	γ	1.0 - 10.0	1.0 - 10.0

Table 8.3: Parameters for the FSI and Detector systematic errors. The ν flavour, selection and range where is applied are shown per parameter. Each analysis has its proper set of parameters: the ν_e beam measurement is parametrized in electron momentum, while the ν_e disappearance in ν reconstructed energy. Also, the latter uses the ν_eCC selection as a whole and not separated.

8.4 Detector systematic uncertainties

The systematic uncertainties associated to the detector performances are calculated by different techniques using control samples. In Appendices A.1 and A.2 we include two examples of calculation of

Systematic	Type	Applied to
B-field distortion	Migration	All
FGD mass uncertainty	Weight	All
FGD track efficiency	Weight	Not used for γ
Michel electron eff.	Weight	Not used for γ
Pile-up (TPC1)	Weight	Not used for γ
Pion secondary interactions	Weight	All
TPC-FGD matching eff.	Weight	All
TPC charge confusion	Weight	All
TPC momentum scale	Migration	All
TPC momentum resolution	Migration	All
TPC track eff.	Weight	All
TPC track quality	Weight	All
TPC PID scale ($e^{\pm}$)	Migration	All
TPC PID bias ($e^{\pm}$)	Migration	All
TPC PID scale ($\mu^{\pm}$ and $\pi^{\pm}$)	Migration	All
TPC PID bias ($\mu^{\pm}$ and $\pi^{\pm}$)	Migration	All
TPC PID scale (p)	Migration	All
TPC PID bias (p)	Migration	All
ECal energy resolution	Migration	All
ECal energy scale	Migration	All
ECal PID	Migration	All
Pile-up (P0D)	Weight	Not used for γ
Pile-up (ECal)	Weight	Only for ν_eCCQE
Pile-up (Upstream ECal)	Weight	Only for ν_eCCnonQE
TPC-ECal matching eff.	Migration	All

Table 8.4: List of detector systematic errors implemented in the analysis. The meaning of the *type* of systematic error is explained in the text.

detector systematic errors: the TPC charge misidentification and the electron TPC PID. In Tab. 8.4 we summarize the full list of detector systematic errors calculated for ND280 and propagated in this analysis. The one having the biggest effect is the TPC momentum resolution.

The Monte-Carlo nominal prediction is corrected to include the estimation of the detector systematic errors. In the following chapter we evaluate these differences when we calculate the expected number of events depending on each Monte-Carlo tunning [Section 9.1.2].

The parametrization of the detector systematic error is the same than the FSI [Tab. 8.3]. Each systematic error is driven by a low-level parameter that tune an observable of the event. As including these parameters in our analysis is very difficult and implies too much computation time, they are treated in an effective way. The same $\vec{f}_{FSI}$ defined for the FSI are used for the detector systematic errors and then become $\vec{f}_{FSI+Det}$. The uncertainties on this parameters given by the detector systematic errors are calculated generating throws of the low-level parameters and calculating the covariances Eq. (8.1). There are two types of low-level parameters associated to the detector systematic errors:

- Migration: it causes a selected event to migrate from one momentum bin to another, from one sample to another or being removed from the selection. For instance, the momentum resolution applies a smearing in the reconstructed electron momentum that can migrate within the selection or even put it below 200 MeV, so that it is not selected.

- Reweight: it changes the contribution of the event, so that it does not count as 1 anymore. For instance, this is the case of the TPC charge misidentification.

The detector systematic errors covariance matrix is showed in Fig. 8.3, whose squared root of the diagonal, that provides the uncertainties, are of the order of $\sim 6\%$.

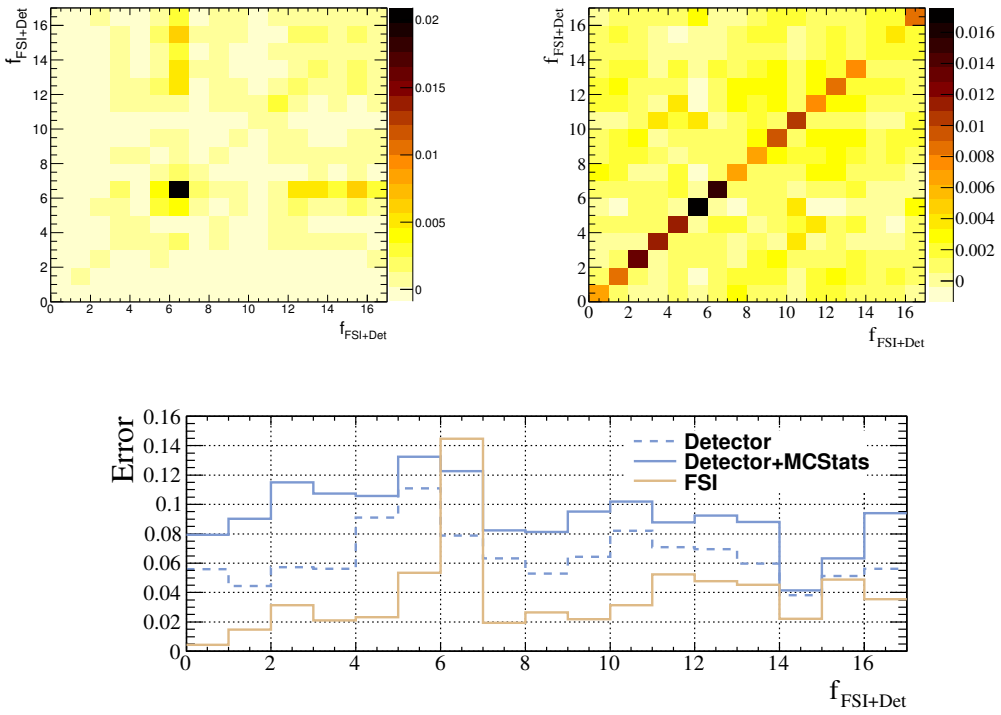

Fig. 8.3: FSI (left) and detector (right) systematic error covariance matrices. The errors on the bottom are calculated as the squared root of the diagonal elements. Each bin corresponds to a different parameter $\vec{f}_{FSI+Det}$ of the list in Tab. 8.3.

8.4.1 Uncertainties due to limited Monte-Carlo statistics

Statistical fluctuations in the Monte-Carlo is treated as another source of detector systematic error. We have an exposure of $\sim$ 10 times the data POT, so we expect the fluctuations to be small. The

statistical fluctuations affect each analysis bin independently and follow a Poisson distribution, so the squared uncertainty σ_i is:

$$\sigma_i{}^2 = (\sqrt{n_i}/n_i)^2 = 1/n_i \tag{8.2}$$

where n_i is the number of events in the bin i-th in one of the selections. In general, the analysis binning b_i (defined in the corresponding analysis chapter) and the binning b'_j of the detector systematic parameters $\vec{f}_{FSI+Det}$ are different. As we want to calculate the uncertainties on $\vec{f}_{FSI+Det}$, we need to perform a re-binning of the uncertainties σ_i. We define the uncertainty in the parameter $f^j_{FSI+Det}$ as the weighted mean of the uncertainties on the bins b_i that are contained in the bin b'_j:

$$\sigma_j{}^2 = \left(\sum_i \frac{\sigma_i \times n_i}{N_j}\right)^2 = \left(\frac{1}{N_j}\sum_i \sqrt{n_i}\right)^2$$

where N_j is the number of events of the Monte-Carlo in b'_j. The uncertainties we obtain are about the 6%, but the effect is smaller than the detector or FSI systematic errors because there are no bins correlations. This uncertainties are added the diagonal of the detector covariance matrix, so that they are considered together. The effect is observed in Fig. 8.3.

8.5 Systematic error parametrization

Each systematic error source is parametrized with one or several parameters as we have seen through this chapter. We have introduced a total of 60 parameters $\vec{f}$ for the beam ν_e measurement while 55 for the ν_e disappearance analysis. In the latter we merge both the ν_eCCQE and ν_eCCnonQE selections, so the number of $\vec{f}_{FSI+Det}$ parameters is reduced from 17 to 10. In addition, to be more conservative in this analysis, we introduce two extra systematic errors that do not appear in the ν_e beam measurement: the difference between the ν_e and ν_μ cross-sections and the *W-shape*. The complete list of the systematic errors and their parameters is given in the Tab. 8.1.

These parameters are simply reweight parameters that change the contribution of the events in the Monte-Carlo. Tunning these parameters changes the total number of predicted events and their spectra. There are three different types of parameters depending on the reweighting strategy adopted:

1. Linear weights that affect E_{True} ranges: the parameters of this class reweight the events in a

given interval of the E_{True}. The value of the parameter and its error is directly proportional to the event weight. In this category we find the complete set of 25 neutrino flux parameters $\vec{f}_{flux}$ and 11 cross-section parameters $\vec{f}_{Xsec(l)}$ (CCQE, CC1π, CCCoh, NC1π^0, NC Other, $\sigma_{\bar{\nu}}/\sigma_{\nu}$ and OOFV's).

2. Response functions weights: the weights have a complicated dependency with the parameters that are modeled by pre-calculated response functions $w(f_{Xsec(rf)})$, where $f_{Xsec(rf)}$ is the corresponding parameter. A total of 7 parameters are included in this category: M_A^{QE}, M_A^{RES}, CC Other Shape, Spectral Function (SF), Fermi momentum (p_F), Binding Energy (E_b), W shape and π-less Δ decay.

3. Linear weights that affect a range of the analyzed distribution: this type of parameter is aim to reweight a specific range on the electron momentum range in the ν_e measurement, or a neutrino reconstructed energy interval in the ν_e disappearance analysis. This is an effective way of treat them as they are so correlated each other that cannot be introduced using the techniques above. We define a set of parameters $f^j_{FSI+Det}$ that account on: FSI, detector and Monte-Carlo limited statistics uncertainties.

Generation of the response functions

The response functions are calculated for each of the Monte-Carlo event and each of the $f_{Xsec(rf)}$ parameters. Provided one specific event and parameter, they are calculated in the following way:

1. The given parameter f is varied by $\pm3\sigma, \pm2\sigma, \pm1\sigma$ and 0σ giving $f_{x\sigma}$, where σ is the uncertainty on that parameter.

2. The weights $w(f_{x\sigma})$ are computed for each of the 7 cases.

3. The response function is provided by the graph built out of the points $\big(f_{x\sigma} : w(f_{x\sigma})\big)$. An example for a given event and the M_A^{QE} parameter is in Fig. 8.4.

4. The weight $w(f)$ for a point in between the $x\sigma$ variations is calculated by linear interpolation

Each response function is particular for a specific event attending to the type and the kinematic of interaction.

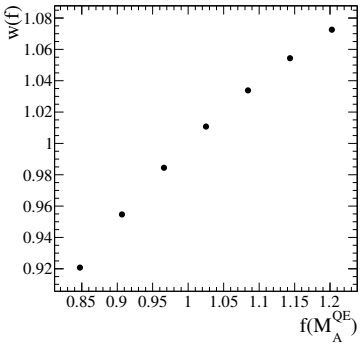

Fig. 8.4: Response function of a single event of the parameter M_A^{QE}. The points correspond to variation of $+3\sigma$, $+2\sigma$, $+1\sigma$, $+0\sigma$, -1σ, -2σ, -3σ of the $f_{M_A^{QE}}$.

8.6 Total covariance matrix

The parameters $\vec{f}$ are in general correlated each other. Correlations between the flux and cross-section parameters exist because the ND280 ν_μ analysis measure both at the same time. The FSI and detector systematic errors are correlated each other [Sections 8.3 and 8.4] but uncorrelated with the flux and cross-section parameters, as they are two independent sets.

We treat the uncertainties on the parameters and their correlations through a covariance matrix. As we have in total 60 systematic error parameters, we have a square and symmetric 60×60 covariance matrix (55×55 in the sterile analysis). The covariance matrix for the neutrino flux and cross-sections is provided by the ND280 ν_μ analysis while the covariance matrix for the FSI and detector systematic errors are calculated in Sections 8.3 and 8.4. As they are driven by the same set of effective parameters $\vec{f}_{FSI+Det}$, the matrices are added each other. Both matrices are treated together in an uncorrelated way.

The total covariance matrix is shown in Fig. 8.5. The non-zero terms out of the diagonal of the flux and cross-section parameters represent the correlations introduced by the ν_μ fit. On the other hand the zero non-diagonal terms between the flux-cross-section matrix and the detector-FSI matrix indicate

that these pieces are not correlated. There are some others systematic errors that are also not correlated with the others as it is the case of the OOFV parameters.

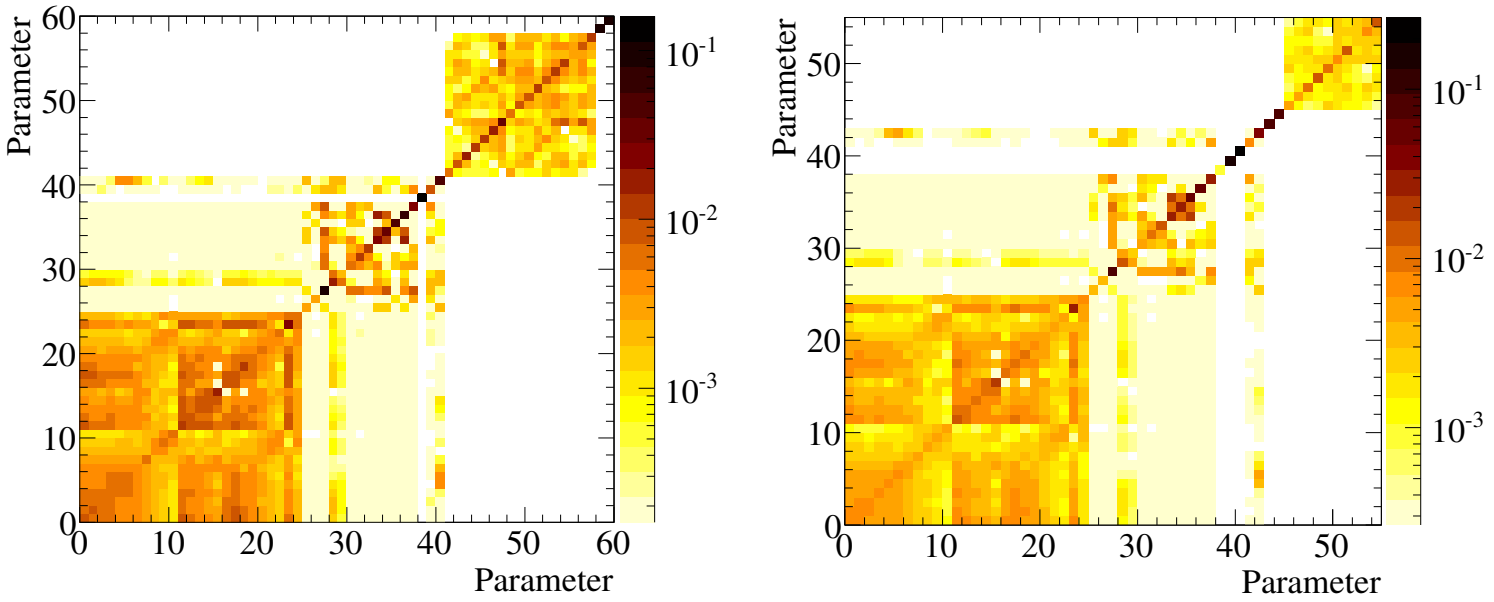

Fig. 8.5: Total covariance matrix for systematic uncertainties parameters. **Left**, beam ν_e measurement: ν_μ-flux (0-10), $\overline{\nu}_\mu$-flux (11-15), ν_e-flux (16-22), $\overline{\nu}_e$-flux (23-24),M_A^{QE} (25), M_A^{RES} (26), CC Other Shape (27), Spectral Function (28), Fermi Momentum (29), CCQE (30-32), CC1π (33-34), NC1π^0 (35), NC Other (36), CCCoh (37), $\sigma_{\overline{\nu}/\nu}$ (38), π-less Δ decay (39), Binding Energy (40), FSI+Det (41-57), Out-FV e^+e^- (58), Out-FV Other (59). **Right**, ν_e disappearance analysis: ν_μ-flux (0-10), $\overline{\nu}_\mu$-flux (11-15), ν_e-flux (16-22), $\overline{\nu}_e$-flux (23-24),M_A^{QE} (25), M_A^{RES} (26), CC Other Shape (27), Spectral Function (28), Fermi Momentum (29), CCQE (30-32), CC1π (33-34), NC1π^0 (35), NC Other (36), CCCoh (37), σ_{ν_e/ν_μ} (38), $\sigma_{\overline{\nu}/\nu}$ (39), W shape (40), π-less Δ decay (41), Binding Energy (42), Out-FV e^+e^- (43), Out-FV Other (44), FSI+Det (45-54).

8.7 Effect of the systematic uncertainties in the selections

The effect of the systematic errors in the momentum distribution is shown in Fig. 8.6 for the uncertainties before and after the ND280 ν_μ measurement. The contributions of the flux and cross-section uncertainties are reduced sensibly and the total systematic uncertainty on the ν_e selection is decreased from $\sim 25\%$ to $\sim 15\%$. At low momentum, the errors are larger and reach the 20% level. The biggest contribution comes from the cross-section uncertainties due to we have most of the γ background that is affected by the large π^0 production and the OOFV systematic errors. At higher momentum, the flux and cross section uncertainties contributions are similar and about 10%. The detector and FSI systematic errors are the smallest contribution, concentrated mainly at low momentum with an effect of 5%.

The overall effect on the distributions for the ν_eCC (ν_eCCQE + ν_eCCnonQE) and the gamma selections is shown in Tab. 8.5 for 1σ variations for each of the systematic error parameters individually. In this way we estimate the impact that each parameter has in our analysis. As far as the ν_e selection is concerned, the OOFV $e^+ - e^-$ systematic error has an effect of 3.2% and it corresponds to the largest one. It is interesting to check which are the dominant systematic errors in the gamma selection as it is a background enriched sample and it gives information about the impact of the background in the ν_e selection. There are two parameters whose effects are specially large: the NCOther with 5.7% and the OOFV $e^+ - e^-$ with 18%. It means that a small variation of this parameters (1σ) can change the total number of expected events for the background dramatically (20%).

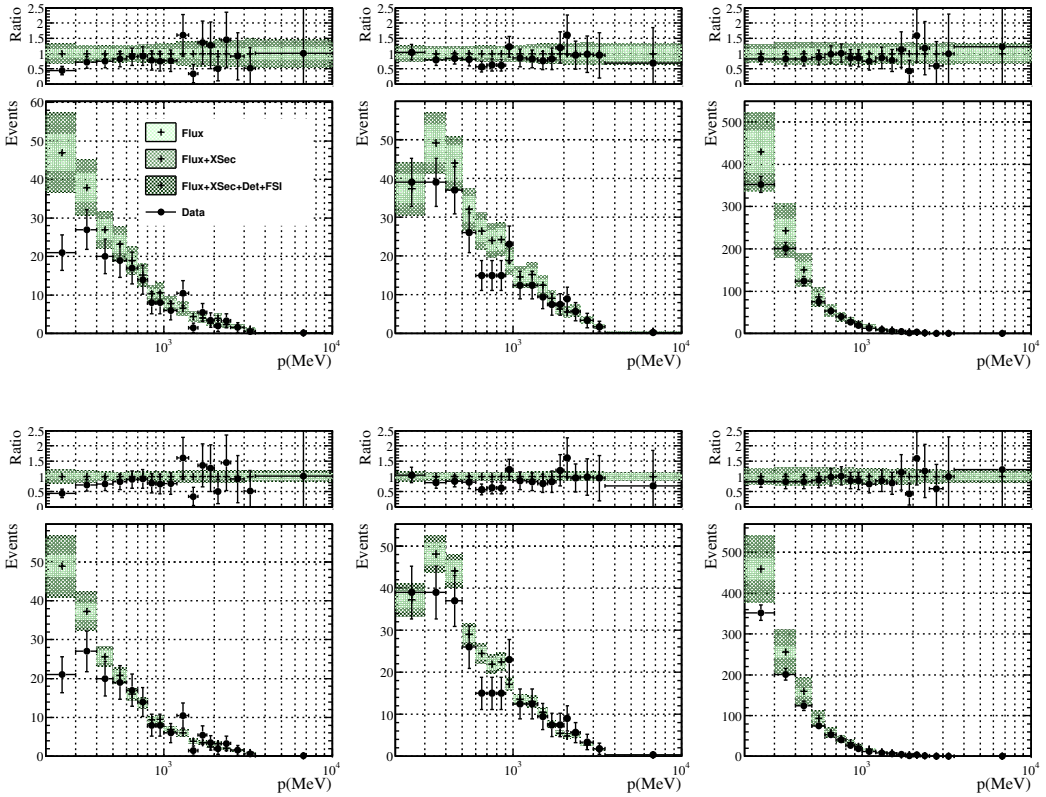

Fig. 8.6: Systematic uncertainties before (top) and after (bottom) the ND280 ν_μ measurement. Electron momentum distributions for (from left to right) ν_eCCQE, ν_eCCnonQE and γ selections. The dots correspond to the data that shows only the statistical error. Above the distributions the ratio respect to the Monte-Carlo are shown.

Parameter	ν_e sel. (%)	γ sel. (%)
ν_μ Flux 1	0.0085	0
ν_μ Flux 2	0.012	0.0013
ν_μ Flux 3	0.043	0.012
ν_μ Flux 4	0.066	0.034
ν_μ Flux 5	0.2	0.13
ν_μ Flux 6	0.2	0.24
ν_μ Flux 7	0.25	0.53
ν_μ Flux 8	0.28	0.79
ν_μ Flux 9	0.48	1.4
ν_μ Flux 10	0.49	1.6
ν_μ Flux 11	0.65	1.9
$\overline{\nu}_\mu$ Flux 1	0.0062	0.0037
$\overline{\nu}_\mu$ Flux 2	0	0.0083
$\overline{\nu}_\mu$ Flux 3	0.01	0.01
$\overline{\nu}_\mu$ Flux 4	0.023	0.044
$\overline{\nu}_\mu$ Flux 5	0.12	0.33
ν_e Flux 1	0.06	0
ν_e Flux 2	0.23	0.011
ν_e Flux 3	0.2	0.012
ν_e Flux 4	0.83	0.055
ν_e Flux 5	1.1	0.093
ν_e Flux 6	1.2	0.11
ν_e Flux 7	1.1	0.13
$\overline{\nu}_e$ Flux 1	0.0064	0.022
$\overline{\nu}_e$ Flux 2	0.013	0.026

Parameter	ν_e sel. (%)	γ sel. (%)
M_A^{QE}	1.2	0.24
M_A^{Res}	2.5	1.9
CC Other Shape	2.2	2.7
Spectral Function	0.017	0.0044
Fermi Momentum	0.049	0.012
CCQE1	0.95	0.07
CCQE2	1.2	0.21
CCQE3	0.51	0.12
CC1π 1	1.7	0.47
CC1π 2	1.7	0.65
NC1π^0	0.54	1.1
NC Other	2.1	5.7
CCCoh	0.49	0.06
σ_{ν_e/ν_μ}	1.9	0.16
$\sigma_{\bar{\nu}/\nu}$	0.37	0.91
W shape	0.4	1.4
π-less Δ decay	0.077	0.98
Binding Energy	0.2	0.03
OOFV Electron	3.2	18
OOFV Other	0.96	0.027

Parameter	ν_e sel (%)	γ sel. (%)
Det-like 1	1	0
Det-like 2	2.4	0
Det-like 3	0.49	0
Det-like 4	1.1	0
Det-like 5	1.8	0
Det-like 6	0.73	0
Det-like 7	1.0	0
Det-like 8	0	3.4
Det-like 9	0	1.9
Det-like 10	0	1.2

Table 8.5: Effect in the selections of 1σ variation of each independent systematic for both ν_e (CCQE + CCnonQE) and γ selections. Correlations between the systematic errors are not taken into account.

Chapter 9

Measurement of the beam ν_e component

In this chapter we present the measurement of the ν_e intrinsic component in the T2K neutrino beam published in [74]. This component is predicted by the simulation of the beam-line, that is controlled by the INGRID monitoring, and by the NA61 measurements of hadron production cross section. It is expected to represent the 1.2% of the total neutrino flux [Section 3.4]. The neutrino flux is further controlled by the ν_μ measurement at ND280 [Section 5.1] that provides the final prediction of the neutrino interaction rates at ND280 and at SK. This is the prediction used to calculate the expected number of signal and background events in the T2K oscillation analyses [Section 5.2]. The aim of the ν_e measurement at ND280 is to compare the ν_e flux prediction after the ν_μ fit with the data at ND280 [Chapter 6], providing a key confirmation to the entire T2K analysis chain. In order to do this, we use the maximum likelihood method applied to the momentum distributions for the ν_e selections and the photon control sample at ND280. The ν_e component is parametrized in different manners and the best fit values for the parameters are calculated. The result on those parameters along with the *goodness-of-fit* test give the level of compatibility of the prediction with the data.

In Section 9.1 we detail how we calculate the expected number of events in each momentum bin used in the binned likelihood [Section 9.2] for the fit and the systematic errors propagation. Before we apply the fit to the data, the algorithm is validated using toys Monte-Carlo in Section 9.3. Finally, we present and discuss the results on the measurements of the beam ν_e component [Section 9.6].

9.1 Electron momentum distributions

The number of expected events in each momentum bin n^i_{exp} is calculated re-weighting event by event the Monte-Carlo prediction taking into account the systematic error parameters.

9.1.1 Binning choice

We perform our analysis in the reconstructed electron momentum p range from 0.2 GeV to 10 GeV. The binned likelihood method used to extract the ν_e signal requires a minimum number of entries per bin to avoid biases induced by Poisson fluctuations. The criteria that we have followed to find the most appropriate binning is:

- fine binning where most of the signal events are selected;
- $\gtrsim 10$ events per bin.

Taking into account this criteria we end up with the following 18 bins for each of the three selections:

`[0.2|0.3|0.4|0.5|0.6|0.7|0.8|0.9|1.0|1.2|1.4|1.6|1.8|2.0|2.2|2.5|3.0|3.5|10.0]` GeV

9.1.2 Expected number of events

The expected number of events is parameterized by several normalization factors $\vec{R}^{\nu_e}$ that are applied to the ν_e component to describe how well the Monte-Carlo reproduces the ν_e event rates at ND280. We explore four different parameterizations for the ν_e signal:

1. Overall scale factor R^{ν_e}: only one free parameter to rescale the ν_e component on the entire momentum range;
2. Energy dependent scale factors: 4 different parameters as a function of the neutrino energy are defined. In this way we study whether the Monte-Carlo reproduces the ν_e properly at different energy ranges;
3. Neutrino parent: ν_e events separated by neutrino parent in ν_e coming from kaons and from muons;
4. Interaction type: fit separately ν_e producing CCQE or CCnonQE interactions.

In addition, the number of events depends on the values of the systematic error parameters $\vec{f}$ [Section 8.5]. The selections presented in Section 6.5 for the ν_e and Section 7.1 for the photon conversion sample correspond to the prediction before the ND280 ν_μ analysis. This prediction needs to be adapted to the ND280 ν_μ measurement. In order to do this, we apply event by event the reweights given by

the parameters $\vec{f}$ defined in Chapter 8 to our momentum distributions. It means that the contribution of each event becomes a number that depends on $\vec{f}$ and in general is different from 1. As described in Chapter 8, we include four sets of parameters: flux weights $\vec{f}_{flux}$, cross-section linear weights $\vec{f}_{Xsec(l)}$, cross-section weights through response functions $\vec{w}(\vec{f}_{Xsec(rf)})$ and detector and FSI weights, $\vec{f}_{FSI+Det}$.

The total weight W given for the systematic errors parameters of a specific event j selected in either of the samples becomes:

$$W^j(\vec{f}) = \vec{f}_{flux}(E^j_{True}) \times \vec{f}_{Xsec(l)}(E^j_{True}) \times \vec{w}^j(\vec{f}_{Xsec(rf)}) \times \vec{f}^j_{FSI+Det}(p^i) \tag{9.1}$$

The predicted number of events in the momentum bin p^i of one of the three selections α (= ν_eCCQE, ν_eCCnonQE, γ) is given by the expression:

$$n^{i,\alpha}_{exp}(\vec{R}^{\nu_e}, \vec{f}) = \frac{N^{data}_{POT}}{N^{MC}_{POT}} \sum_j^{N_i} W^j(\vec{f}) \times \vec{R}^{\nu_e} \tag{9.2}$$

where N_i is the number of events in p^i, and N^{data}_{POT} and N^{MC}_{POT} are the number of POT for data and Monte-Carlo. It is important to notice that the $\vec{R}^{\nu_e}$ parameters only apply to the ν_e events. The weights W are defined for the ν_eCCQE, ν_eCCnonQE and the γ selections separately, but they are modulated by the same parameters. The electron momentum distributions after applying the final flux and cross-section tunning for the different selections are shown in Fig. 9.1, where we divide the Monte-Carlo by ν flavour and interaction.

The Monte-Carlo prediction is tuned by several analyses:

- Flux prediction: using the data from the hadron-production experiment NA61 at CERN and *in situ* T2K beam monitoring at INGRID [Section 3.4];
- Detector systematic errors correction: applied to the Monte-Carlo after the detector systematic errors estimation. It can reweight events as well as migrate them from one bin to another [Section 8.4];
- ν_μ fit at ND280: it correspond to the best knowledge we have for the neutrino fluxes and cross-sections [Section 5.1].

The number of selected events and their momentum distributions change after each step as it is represented in Tab. 9.1. In Fig. 9.2 we show the effect of the different tunings on our selections. The one

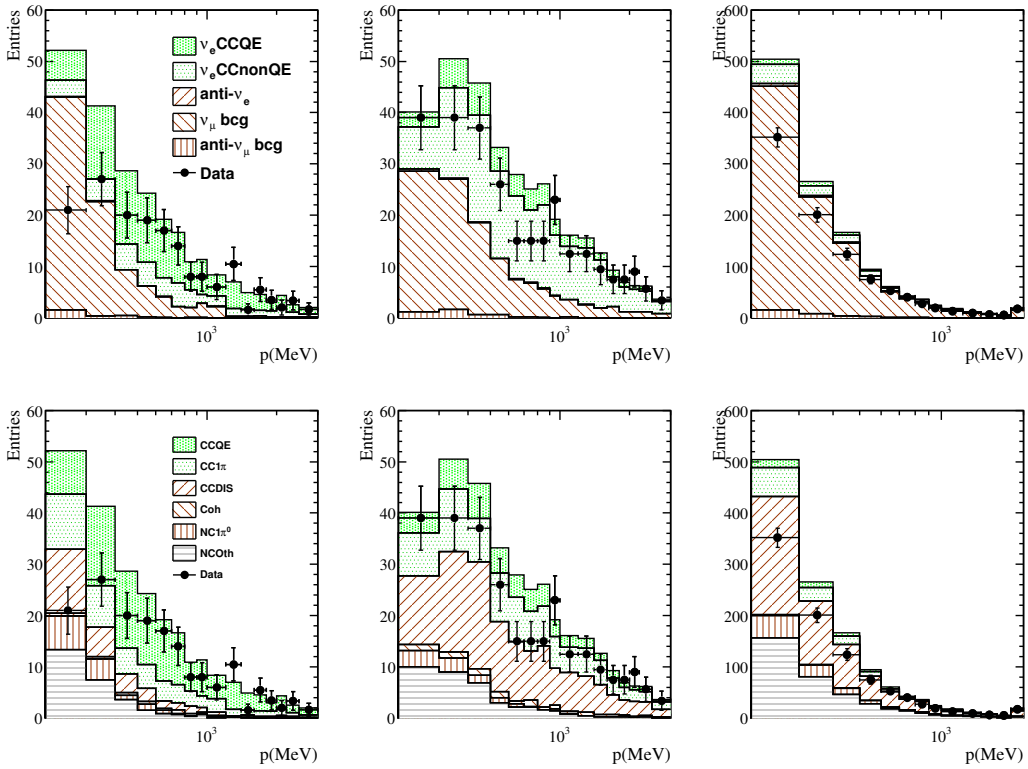

Fig. 9.1: Electron momentum distribution for the different selections: ν_eCCQE on the left, ν_eCCnonQE in the middle and γ at the right. The Monte-Carlo is divided according to the ν flavor (top) and interaction (bottom). The Monte-Carlo distributions are tuned with the prediction of the NA61 experiment and the beam monitoring, and also corrected by the detector systematic errors.

that we use in our final analysis is the green one, resulting from applying all the tunings to the nominal Monte-Carlo.

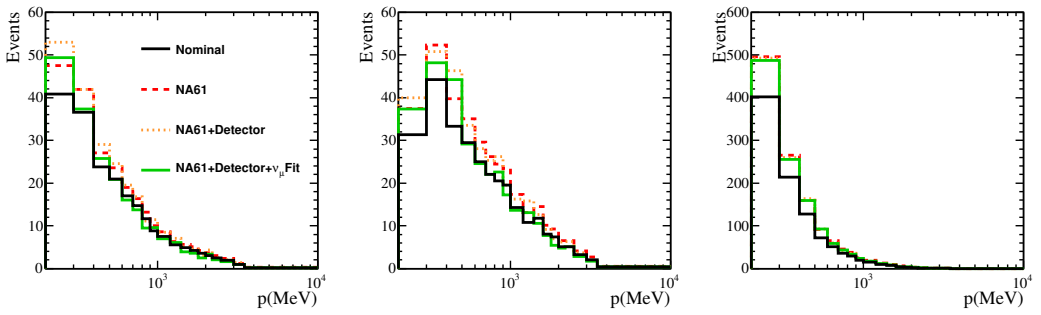

Fig. 9.2: Momentum distributions for the different tunings and selections. ν_eCCQE on the left, ν_eCCnonQE in the middle and gamma on the right.

Selection	Tunning	ν_e CCQE	ν_e CCnonQE	$\overline{\nu}_e$	ν_μ	$\overline{\nu}_\mu$	OOFVe^-e^+	OOFV Other	Total
ν_eCCQE	NEUT	116.1	53.5	0.4	26.8	1.2	37.6	15.5	251.1
	NA61	132.1	62.9	0.4	30.9	1.2	45.6	18.6	291.8
	ν_μ ND280	121.6	49.6	0.4	31.0	1.5	44.3	17.2	265.3
	Detector	113.9	47.1	0.3	29.9	1.5	42.6	24.4	259.7
	DATA	-	-	-	-	-	-	-	225
ν_eCCnonQE	NEUT	49.0	219.8	1.4	96.2	4.7	16.9	6.4	394.4
	NA61	56.2	267.4	1.4	123.0	5.4	21.1	7.9	482.5
	ν_μ ND280	54.5	218.4	1.2	125.4	5.1	21.1	7.2	432.9
	Detector	52.0	203.9	1.1	126.3	4.9	20.6	6.3	415.1
	DATA	-	-	-	-	-	-	-	392
γ	NEUT	21.1	44.0	6.4	312.4	15.1	591.3	4.6	994.9
	NA61	24.3	53.5	6.8	388.7	16.6	754.5	5.8	1250.3
	ν_μ ND280	23.2	46.8	5.9	405.3	17.3	764.7	5.5	1268.7
	Detector	22.8	46.7	5.7	401.0	17.7	751.7	5.4	1251
	DATA	-	-	-	-	-	-	-	990

Table 9.1: Number of events selected in each sample per each Monte-Carlo tunning. NEUT: nominal NEUT Monte-Carlo prediction; NA61: prediction after NA61; ν_μ ND280: prediction after the ν_μ fit at ND280; Detector: after the correction using the central values of the detector systematic uncertainties; DATA: number of real events.

9.2 Method of the maximum likelihood

A frequentist method is used to measure the beam ν_e component. The free parameters $\vec{R}^{\nu_e}$ are extracted maximizing the likelihood function $\mathcal{L}$ [101] that depends on that parameters and the 60 systematic errors parameters $\vec{f}$. Our analysis is binned in momentum and each bin i correspond to an independent experiment whose probability distribution function (*pdf*) λ_i corresponds to a Poisson distribution:

$$\lambda_i(\vec{R}^{\nu_e}, \vec{f}) = \frac{(n^i_{exp})^{n^i_{dt}} e^{-n^i_{exp}}}{n^i_{dt}!}$$

where $n^i_{exp} \equiv n^i_{exp}(\vec{R}^{\nu_e}, \vec{f})$ [Eq. (9.2)] is the expected number of events in the i-th bin of momentum for one of the selections and n^i_{dt} the observed number of events in the same bin.

$\vec{f}$ are not free parameters, but they are constrained by the ND280 ν_μ analysis and our studies in Chapter 8. So, their *pdfs* are multivariate Gaussian distributions $\rho(\vec{f})$ with mean values $\vec{f}_0$ and covariances given by the covariance matrix V [Fig. 8.5]:

$$\rho(\vec{f}) = \frac{1}{(2\pi)^{k/2}|V|^{1/2}} e^{-\frac{1}{2}\Delta\vec{f}^T V^{-1} \Delta\vec{f}}$$

where k is the number of systematic errors parameters and $\Delta\vec{f}$ is the difference between $\vec{f}$ and their prior values

$$\Delta\vec{f} \equiv \vec{f} - \vec{f}_0$$

The likelihood function $\mathcal{L}$ is defined as the product of all the λ_i (18 bins per selection, so 54 in total) and the constraints that we include for the $\vec{f}$ parameters:

$$\mathcal{L}(\vec{R}^{\nu_e}, \vec{f}) = \prod_i \lambda_i(\vec{R}^{\nu_e}, \vec{f})\rho(\vec{f}) \tag{9.3}$$

where i runs over all the bins of the experiment for the three selections. This is the quantity we want to maximize in order to obtain the estimation of $\vec{R}^{\nu_e}$. In practice, it is easier to minimize the $-2\log\mathcal{L}$ that behaves like a χ^2 distribution with dof degrees of freedom [16] equal to:

$$\begin{aligned} dof &= \#\text{bins} - \#\text{parameters} + \#\text{parameter constrains} \\ &= \#\text{bins} - \#\text{free parameters} = 53 \end{aligned} \tag{9.4}$$

Taking the logarithm of Eq. (9.3), the expression that we minimize in our analysis has the form:

$$\chi^2 \equiv -2\log\mathcal{L} = 2\sum^{\alpha}\sum_{i=0}^{18}\left\{n_{exp}^{i,\alpha} - n_{dt}^{i,\alpha} + n_{dt}^{i,\alpha} \times \log\left(\frac{n_{dt}^{i,\alpha}}{n_{exp}^{i,\alpha}}\right)\right\} + \Delta\vec{f}^T V^{-1}\Delta\vec{f}$$

where α runs over the three selections (ν_eCCQE, ν_eCCQE and γ). The first term provides the contribution of our samples to the χ^2 value. The second term is the so-called penalty term that constrain the parameters $\vec{f}$ to their prior values through their covariances calculated in Chapter 8.

We minimize this expression in the electron momentum range $[0.2\,\text{GeV}, 10\,\text{GeV}]$ using the TMinuit package included in the ROOT libraries. To improve the uncertainties calculated by the fit, the HESSE method was implemented after MIGRAD convergence. If the minimization fails, MIGRAD is called again up to 8 times starting from the last values. As far as the systematic error parameters are concerned, we bind them within $\pm5\sigma$ and we require them to be always in the allowed physical region.

9.3 Validations of the fitter

In order to validate the fit mechanism, we performed several tests using *toys Monte-Carlo*. A toy Monte-Carlo (or fake data) is a simulation of the momentum distributions obtained for the three selections we introduced in the fit. They are built using the expression for the number of expected events given in Eq. (9.2) for a given set of parameters $\vec{R}^{\nu_e}$ and $\vec{f}$. Then the toys are fit by the method described in Section 9.2.

9.3.1 Generation of the toys Monte-Carlo

The toys are generated assuming $\vec{R}^{\nu_e} = 1$ and the current statistics of 5.9×10^{20} POT. Statistical fluctuations and variations of the systematic error parameters within the uncertainties presented in Chapter 8 are taken into account. To build a toy with a specific extraction of the systematic errors parameters, we need to generate a properly correlated set of $\vec{f}_{toy}$ to be applied to Eq. (9.2). This is done in the following way:

1. We throw a set of 60 random parameters $\vec{g}$ normal-distributed.
2. We use the Cholesky decomposition [112] to extract a vector $\vec{f}_{toy}$ of correlated parameters according to the covariance matrix V:
   - We find the matrix M that fulfills $V = M^T \times M$
   - Then: $\vec{f}_{toy} = \vec{f}_0 + M\vec{g}$
3. The events in the three selections are reweighted according to $\vec{f}_{toy}$ using Eq. (9.2) and the momentum distributions are filled.
4. Each momentum bin is fluctuated as a Poisson distribution in order to take into account the statistical fluctuations.

If any of the weights given by a parameter is negative, we throw another toy. This is done in order to avoid parameters that lead to negative reweights, as removing events from the distributions would not be physical.

9.3.2 Pull studies

The fit is applied to 5000 toys with different systematic error parameter extractions and statistical fluctuations. We validate the parameterizations with only one R^{ν_e} parameter. The distribution for the the best fit values for R^{ν_e} is shown in Fig. 9.3 and, as expected, the averaged value is compatible with 1, as the toys where built using $R^{\nu_e} = 1$. The width of the Gaussian predicts an uncertainty in the beam ν_e measurement to be $\sim 10\%$. To study a possible bias in our analysis we compare the parameters extracted from the fit with the expected ones defining the pulls of the R^{ν_e} parameter δ_{ν_e}

as:

$$\delta_{\nu_e} = \frac{R^{\nu_e}_{toy} - R^{\nu_e}_{bf}}{\sigma_{R^{\nu_e}}} \tag{9.5}$$

where $R^{\nu_e}_{toy} = 1$ is the value that we use to construct the toys, and $R^{\nu_e}_{bf}$ and $\sigma_{R^{\nu_e}}$ are respectively the best fit parameters and the corresponding uncertainty given by the fit. The pull distribution is expected to behave like a Gaussian distribution centered at 0 and with width 1 if there is no bias. Indeed, this is our case as can be observed in Fig. 9.3. The deviation from zero is $\sim 3.3 \pm 1.4\%$, what is negligible, and the width is 0.98 ± 0.01, very compatible with one.

The pull study is extended to the systematic error parameters. We compare the best fit values with the value of the parameter we extract to build the toy:

$$\delta_f = \frac{f_{toy} - f_{bf}}{\sigma_{f_{bf}}} \tag{9.6}$$

where f_{toy} is the extracted systematic error parameter for each specific toy using the procedure explained in Section 9.3.1. The pull distribution for each parameter is obtained and the mean and the RMS are calculated and represented in Fig. 9.3. The mean is well compatible with zero and the deviations are found to be $\sim 10\%$ at most. The only one that is slightly larger is the parameter that correspond to the Spectral Function. This is because the *pdf* of this parameter is constrained to only the positive region so it turns to be highly non-Gaussian. The widths are rather compatible with 1.

9.4 *Goodness-of-fit* test

The *goodness-of-fit* test provides a measurement of the significance on the discrepancy between the data and a given hypothesis. According to the Wilks theorem [140], under some assumptions (like having enough statistic in each bin), the distribution of the best fit values for a large number of toys Monte-Carlo, follows a χ^2 distribution with the number of degrees of freedom (dof) equal to 53 [Eq. (9.4)].

Firstly, it is interesting to check whether this is fulfilled in our conditions to detect any anomaly in the framework. In order to do this, we minimize 5000 toys experiments and built the distribution of χ^2_{bf} . It is shown in Fig. 9.4 and it adapts to a χ^2 distribution with $dof = 53.14 \pm 0.14$, in perfect agreement with the expectation of $dof = 53$.

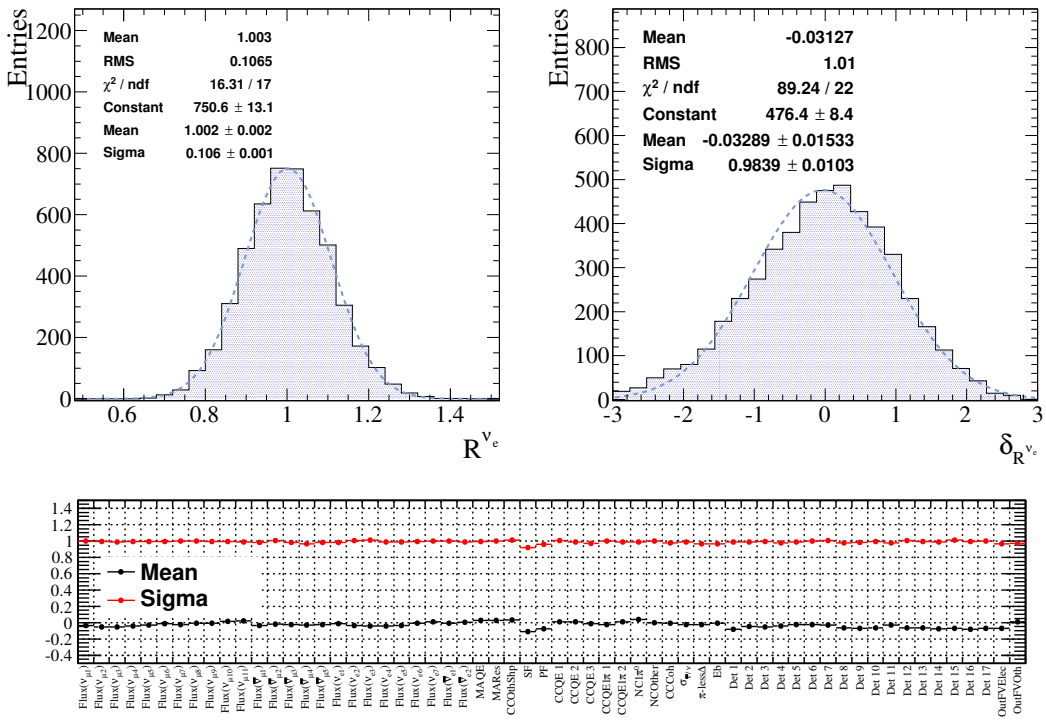

Fig. 9.3: Distribution of the best fit values (left) and of the pulls (right) of the ν_e free parameter for 5000 toys. On the bottom, average and *RMS* of the pull distributions [Eq. (9.6)] for the systematic error parameters.

Applying the fit to the data and comparing its minimum value $\chi^2_{bf,data}$ with this distribution, an estimator of the compatibility can be constructed. The fraction of toys experiments whose values $\chi^2_{bf} > \chi^2_{bf,data}$ defines the *goodness-of-fit*. Mathematically:

$$gof = \frac{1}{N_{toys}} \int_{\chi^2_{bf,data}}^{\infty} d\chi^2_{bf} f(\chi^2_{bf})$$

where f is the *pdf* of the χ^2_{bf} values. Inversely, critical values of the χ^2 can be calculated to provide confidence levels. The critical value χ^2_C that gives the x%CL is defined as:

$$\int_0^{\chi^2_C} d\chi^2_{bf} f(\chi^2_{bf}) = x/100$$

For instance, a confidence interval that it is commonly defined is the 90%CL. So then, for this case

$$\chi^2_C(90\%CL) = 67$$

because the 90% of the χ^2_{bf} values for the toys are below χ^2_C. It means that if $\chi^2_{bf,data} < \chi^2_C$, the hypothesis we are testing is compatible with the data within the 90%CL.

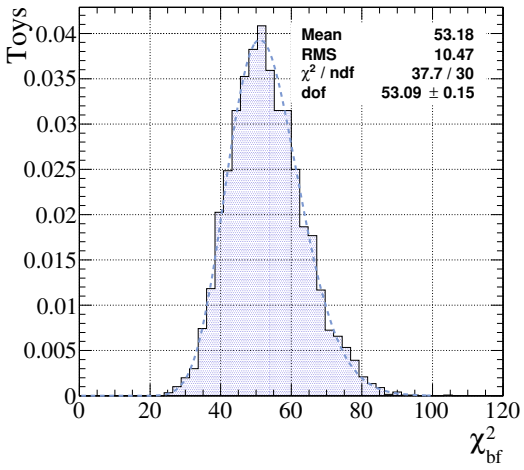

Fig. 9.4: Distribution of χ^2_{bf} for 5000 toys experiments. The distribution is fit with a χ^2 function.

9.5 Expected uncertainty in the beam ν_e measurement

For the current statistics, and provided the systematic errors described in Chapter 8, the expected uncertainty in the ν_e beam measurement is of 10% parameterizing the selected ν_e component with only one parameter (estimated from the width of the $R_{bf}^{\nu_e}$ values distribution, Fig. 9.3).

We made a study of the expected evolution of the precision of the ν_e beam measurement with the POT and with smaller systematic errors. In Fig. 9.5 we show the total relative error versus the POT for the current systematic errors scenario. The uncertainty saturates at $\sim 7\%$ where it becomes independent on the statistics and dominated by the systematics errors. We also assumed a scenario with the current systematics errors reduced a factor of two. This is realistic as we have only reached the 8% of the expected POT goal of T2K and the ND280 ν_μ analysis will measure the neutrino flux and cross-sections more precisely in the future.

In the best case scenario we expect to reach a precision of $\sim 4\%$, so the analysis becomes sensitive to measure cross-section differences between ν_e and ν_μ interactions that is calculated in the theory to be at the 3% level [79].

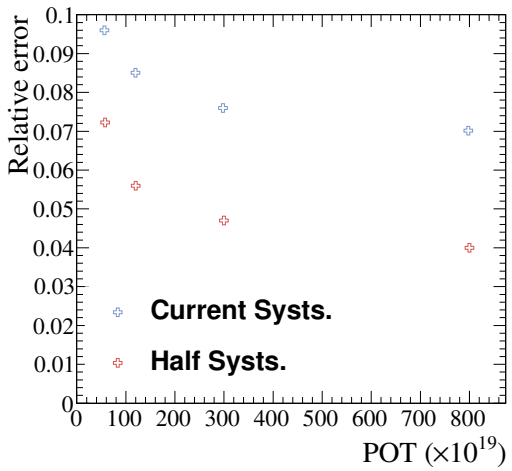

Fig. 9.5: Expected relative errors in the R^{ν_e} measurement versus the POT and for two different cases: current systematic errors (black) and half of the systematic errors (red).

9.6 Results

The ND280 data is fit using the method described above. The different parametrization of the ν_e component are used in different versions of the fit.

9.6.1 Inclusive ν_e: 1 parameter

The parameter R^{ν_e} is measured by applying the fit to our samples getting:

$$R^{\nu_e} = 1.01 \pm 0.06(\text{stat}) \pm 0.07(\text{Flux-XSec}) \pm 0.04(\text{Det-FSI}) = 1.01 \pm 0.10$$

for the free parameter. It indicates that the data is in good agreement with the Monte-Carlo prediction for the beam ν_e. The momentum distributions before and after the fit is shown in Fig. 9.6. The χ^2_{bf} obtained is

$$\chi^2_{bf}/dof = 56.43/53$$

that correspond to a $gof = 33.9\%$. This result indicates that the fit parameters, including $\vec{f}$, are well compatible with the ν_e flux prediction. The statistical and systematics errors have similar impact in the final uncertainty of 10%.

The uncertainties on the systematic errors parameters are practically unchanged as indicates Fig. 9.7. This is because, with the current level of statistics, the ν_eCC's and γ selections are not able to constrain more the systematic errors than the ND280 ν_μ selections. The only exception is the OOFV for electrons coming from photon conversion (OOFV$e^+ - e^-$) whose uncertainty is reduced from 30% to 15%. This component is not controlled by the ND280 ν_μ fit but it is constrained by the photon sample that is rich in this background.

The pulls obtained for the systematic error parameters are shown in Fig. 9.6. Most of them are within 1σ uncertainties. There are some cases (like flux-$\bar{\nu}_\mu$) where the deviation is larger. However, those are parameters with a small impact in the analysis. The two parameters that rule the OOFV events

(OOFV from γ and from other particle) are fit to have smaller values than predicted:

$$f(\text{OOFV } e^+ - e^-) = 0.64 \pm 0.10$$
$$f(\text{OOFV Other}) = 0.83 \pm 0.29$$

Those results are still compatible with the prior uncertainty of 30%, but they clearly indicate that the OOFV component is not well reproduced in our Monte-Carlo and we have to reduce it by $\sim 35\%$ to fit the data. In particular, thanks to this reduction the gamma sample has a very good agreement after the fit while before the fit the prediction overestimated the number of events. It gives confidence that the background is better reproduced after the fit.

9.6.2 ν_e for different true energy bins: 4 parameters

A second test is to fit the ν_e component in different energy bins to check whether the Monte-Carlo correctly reproduces the data as a function of the neutrino energy. We have divided the signal ν_e component in 4 different ranges of Monte-Carlo neutrino energy, according to the following bins:

$$[0|1.2|2.5|3.5|30\,\text{GeV}\ ]$$

This binning has been chosen to have about the same number of events for each sample, in order to get similar errors for the parameters. The contribution to the ν_e signal component for each electron momentum bin is shown in Fig. 9.8, where each color corresponds to a different true energy bin. Using the same fitting scheme but with this new ν_e parametrization we get the momentum distributions in Fig. 9.9 that correspond to the following best fit values:

$$R(\nu_{e1}) = 0.83 \pm 0.21(\text{stat}) \pm 0.12(\text{Flux-XSec}) \pm 0.15(\text{Det-FSI}) = 0.83 \pm 0.29$$
$$R(\nu_{e2}) = 0.92 \pm 0.35(\text{stat}) \pm 0.16(\text{Flux-XSec}) \pm 0.06(\text{Det-FSI}) = 0.92 \pm 0.39$$
$$R(\nu_{e3}) = 0.90 \pm 0.36(\text{stat}) \pm 0.21(\text{Flux-XSec}) \pm 0.06(\text{Det-FSI}) = 0.90 \pm 0.42$$
$$R(\nu_{e4}) = 1.31 \pm 0.29(\text{stat}) \pm 0.12(\text{Flux-XSec}) \pm 0.08(\text{Det-FSI}) = 1.31 \pm 0.33$$

We notice that the errors are higher, as expected, and dominated by the statistical uncertainties. At low energy the ν_e component is slightly overestimated but still the results are compatible with the unity

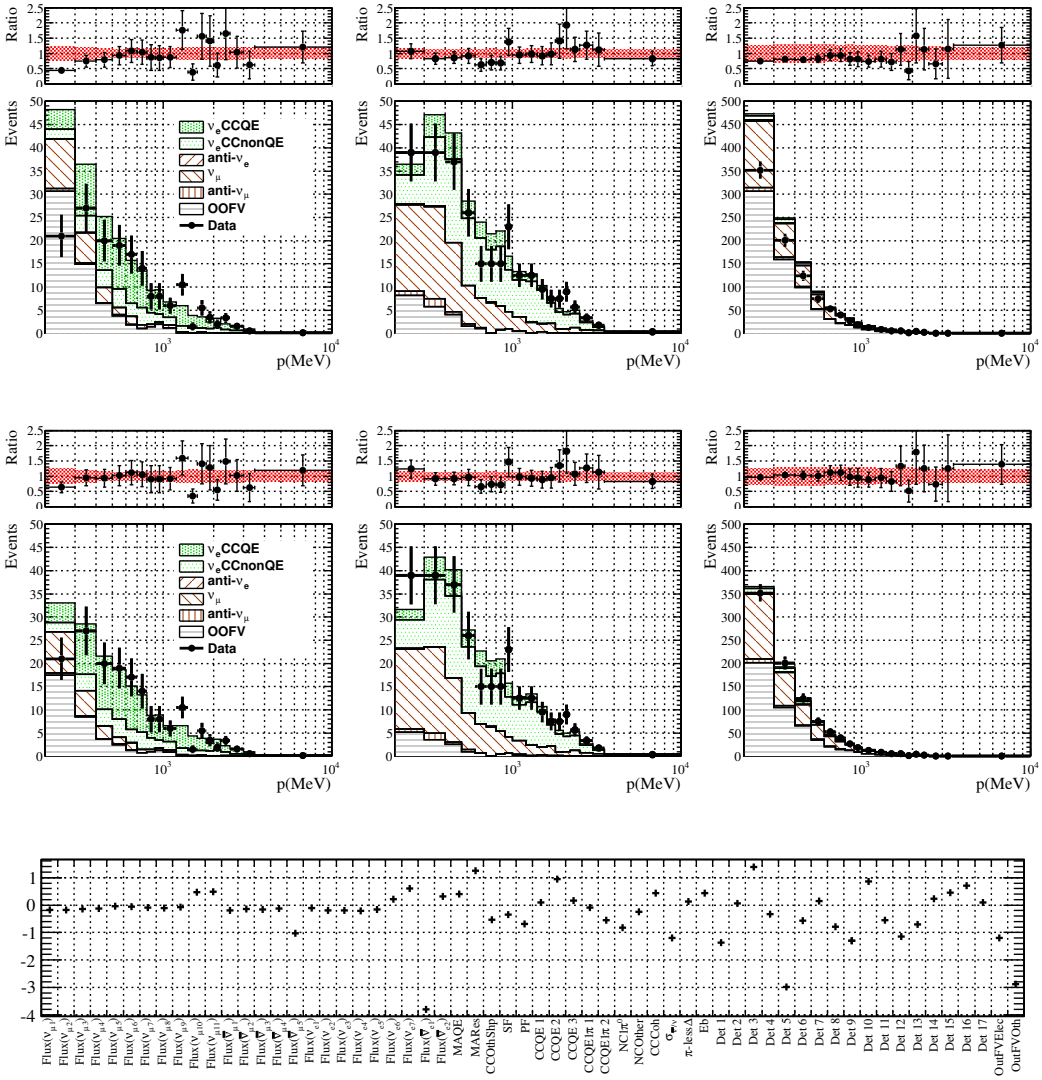

Fig. 9.6: Momentum distributions before (top) and after (middle) the fit with 1 parameter for the ν_e component. From left to right: ν_eCCQE, ν_eCCnonQE and gamma selections. At the bottom the pulls for the systematic error parameters are shown.

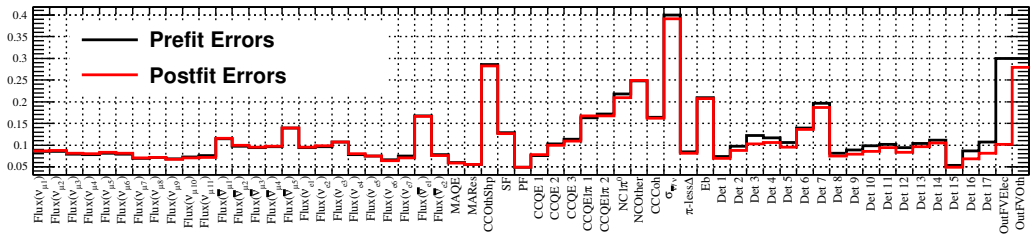

Fig. 9.7: Uncertainties before and after the fit for each systematic error parameter.

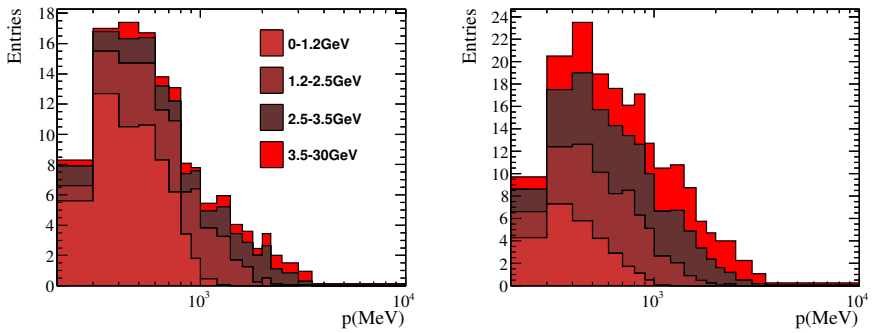

Fig. 9.8: Contribution for the ν_e signal of each of the four neutrino energy bin (left ν_eCCQE and right ν_eCCnonQE).

within $\sim 1\sigma$. The pulls in Fig. 9.9 have the expected behavior and the $\chi^2_{bf}/dof = 54.16/50$ means that the agreement is good. With the current data, the results are dominated by the statistical errors but it is an interesting analysis for the future.

9.6.3 ν_e coming from muons or kaons: 2 parameters

In the neutrino beam the ν_e component comes from the decay of muons and kaons. ν_e from muons mainly populates the low energy region while the ones from kaons dominates the high energy part of the spectrum [Section 3.3.1]. The processes that produce each component are different so it is interesting to measure them separately.

In Fig. 9.10 we show the signal broken down by neutrino parent for both selections. The ν_eCCQE selection turns to be an enhanced selection of neutrinos coming from muons and the same with CCnonQE respect to the kaons. The shapes of each component are quite different and we can fit both component separately without large correlations. The fit results for this approach are [Fig. 9.10]:

$$R(\nu_e^{\mu}) = 0.68 \pm 0.24(\text{stat}) \pm 0.12(\text{Flux-XSec}) \pm 0.14(\text{Det-FSI}) = 0.68 \pm 0.30$$
$$R(\nu_e^{K}) = 1.10 \pm 0.08(\text{stat}) \pm 0.09(\text{Flux-XSec}) \pm 0.06(\text{Det-FSI}) = 1.10 \pm 0.14$$

In the case of the $\nu_e(\mu)$ component, the prediction slightly overestimates the data. Nevertheless, data and Monte-Carlo are compatible around 1σ. The error in the muon component is largely dominated by the low statistics. Its estimation is also difficult since at the low momentum region the detector systematics are larger and the background is more abundant.

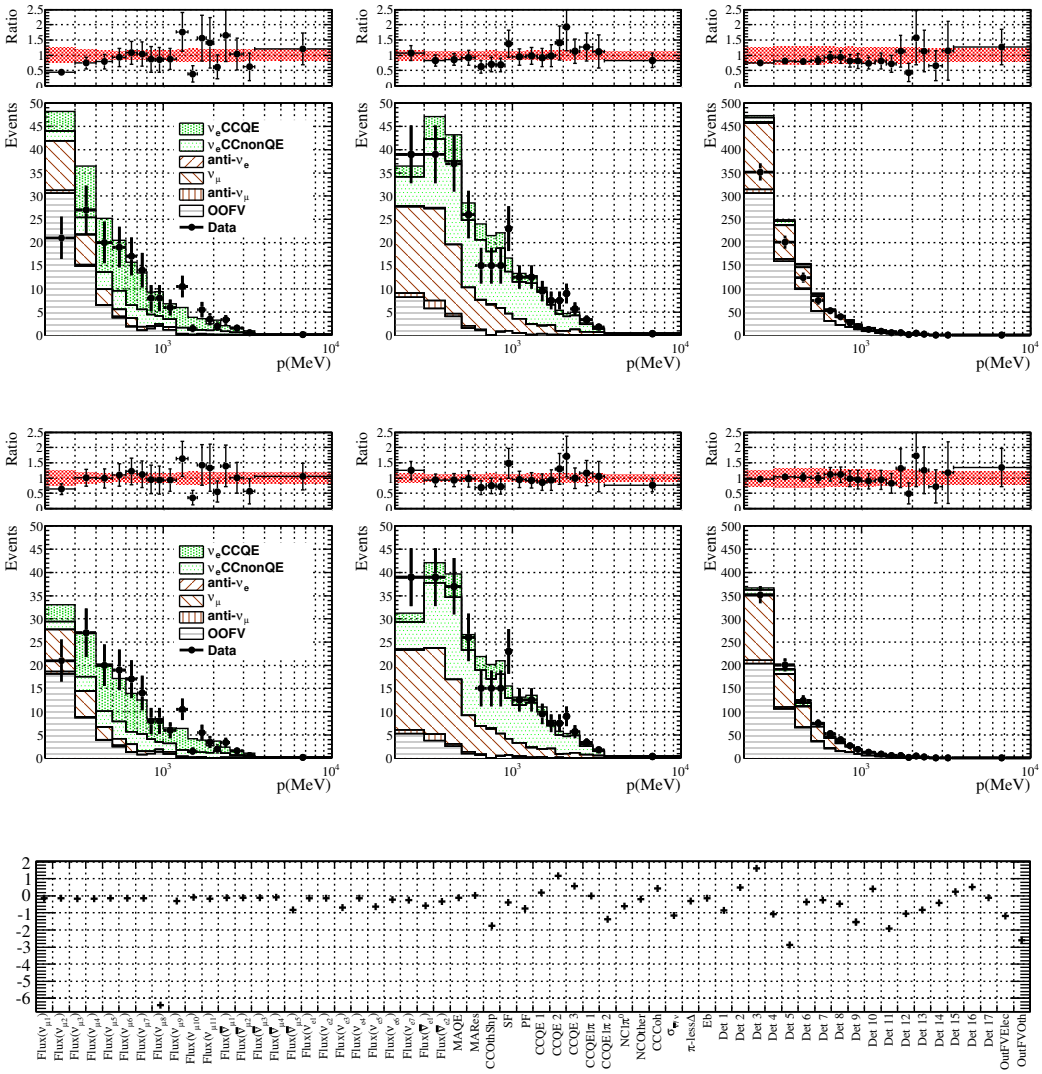

Fig. 9.9: Momentum distributions before (top) and after (middle) the fit with 4 parameters for the ν_e component. From left to right: ν_eCCQE, ν_eCCnonQE and gamma selections. At the bottom the pulls for the systematic error parameters are shown.

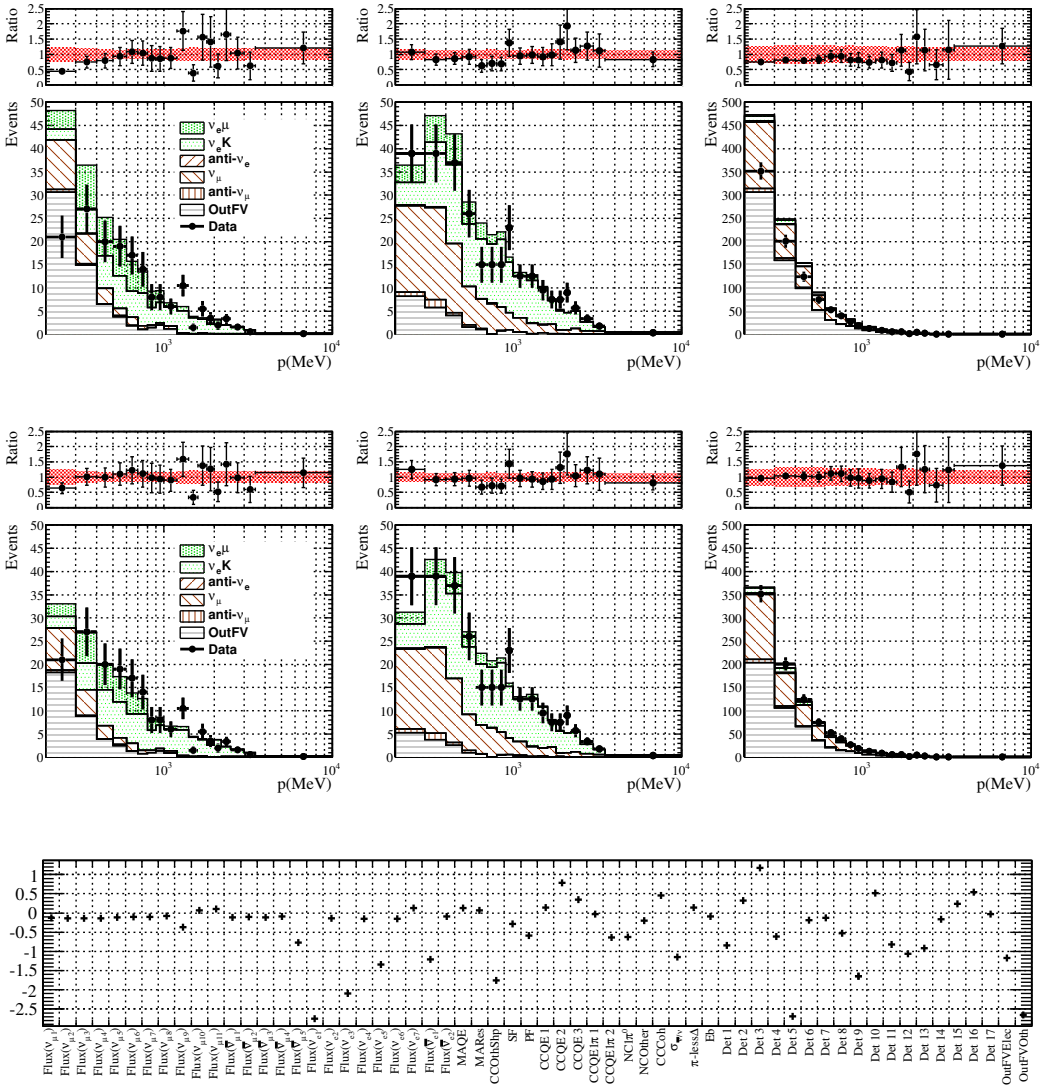

Fig. 9.10: Momentum distributions before (top) and after (middle) the fit with 2 parameters for the different ν_e particle sources. From left to right: ν_eCCQE, ν_eCCnonQE and gamma selections. At the bottom the pulls for the systematic error parameters are shown.

9.6.4 ν_eCCQE or ν_eCCnonQE interactions: 2 parameters

The last approach that we investigated is fitting the ν_eCCQE and ν_eCCnonQE interactions independently. This channel is very useful for cross-section analyses, as we can study the Monte-Carlo performances for the two interaction types. The results:

$$R(\nu_e^{CCQE}) = 1.08 \pm 0.15(\text{stat}) \pm 0.03(\text{Flux-XSec}) \pm 0.09(\text{Det-FSI}) = 1.08 \pm 0.18$$
$$R(\nu_e^{CCnonQE}) = 0.94 \pm 0.11(\text{stat}) \pm 0.12(\text{Flux-XSec}) \pm 0.05(\text{Det-FSI}) = 0.94 \pm 0.17$$

are again compatible with the unity, in good agreement with the prediction, as can be seen in the momentum distributions after the fit shown in Fig. 9.11.

9.7 Conclusion and discussion

The predicted ν_e beam component has been confirmed using a selection of ν_e interactions at ND280. We used several parameterizations to model the ν_e component and each and every of them are compatible with the expectations. We recall that the prediction in the number ν_e interactions at ND280 that we have validated is the one provided by the ND280 ν_μ flux and cross-section measurement and hence, it is the same flux used in the ν_e appearance analysis at SK [55]. Our analysis confirms that the intrinsic ν_e background prediction at SK is correct at the 10% level. This is a necessary and very important check that provides confidence in our understanding of the main source of background in the measurement of θ_{13}.

On the other hand, this analysis also provides a constraint in the differences between the ν_μ and ν_e cross-sections. The ν_e cross-section has never been measured with a good precision and we find current constraints at the 3% level from the theory [79]. Assuming that the flux is precisely predicted, the possible deviations of the data from the prediction can be considered as differences in the ν_e and ν_μ cross-sections represented by R^{ν_e}. As this parameter shows good agreement with the expectation and it is measured at the 10% level, we conclude that the differences between ν_e and ν_μ cross-section cannot be larger than 10%. It will be interesting to repeat this analysis when more data will be available, to test the theoretical predictions for the ν_e and ν_μ cross-section differences.

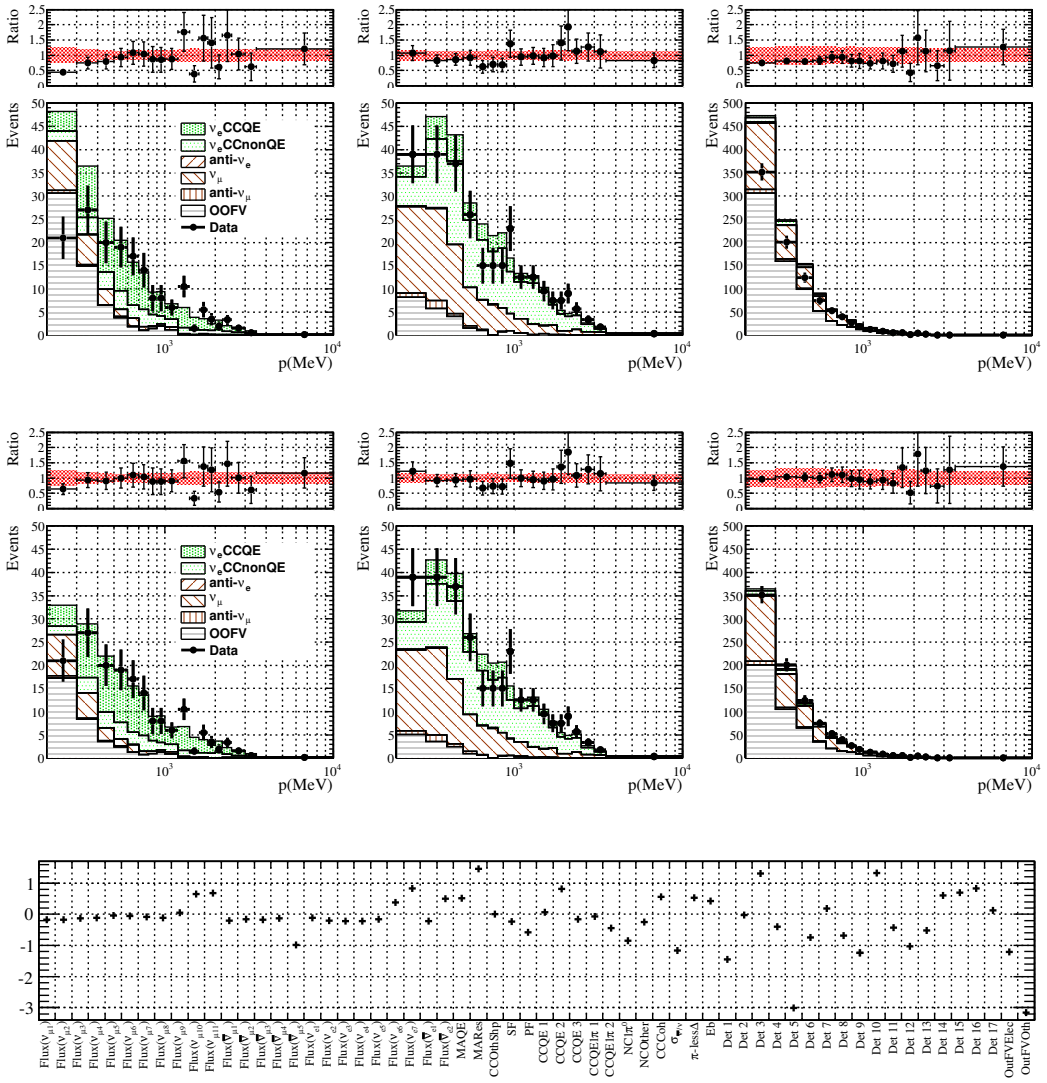

Fig. 9.11: Momentum distributions before (top) and after (middle) the fit with 2 parameters for the different ν_e interaction modes. From left to right: ν_eCCQE, ν_eCCnonQE and gamma selections. At the bottom the pulls for the systematic error parameters are shown.

Chapter 10

ν_e disappearance at short baseline

In this chapter we investigate the ν_e disappearance at short baseline due to mixing with light sterile neutrinos in the 3+1 model. Given the short distance of ND280 from the neutrino source and its energy measurement capabilities, a study on the ν_e event rates allows to test the existence of light sterile neutrinos at the $\Delta m^2_{41} > 1\,eV^2$ scale for some values of the mixing angle.

The survival probability of a ν_e due to mixing with sterile neutrinos was deduced in Section 2.1.1 and we rewrite it here:

$$P_{ee} = P(\nu_e \to \nu_e) = 1 - \sin^2(2\theta_{ee}) \sin^2\left(1.27\,\Delta m^2_{41}[\,eV^2]\frac{L[m]}{E[\,MeV]}\right) \tag{10.1}$$

where $\sin^2(2\theta_{ee})$ and Δm^2_{41} characterize the neutrino oscillation and are free parameters in the model. This expression also depends on the energy of the neutrino E and its flight path L. Both quantities cannot be exactly calculated on the data because we just know the kinematic of the electron and the position of the neutrino interaction. However, the neutrino energy can be estimated making some assumptions and the oscillatory behavior of P_{ee} is manifested in function of the reconstructed neutrino energy. We exploit this option and perform an analysis of the ν_e interaction rates as well as their reconstructed neutrino energy shape (what is called in jargon: rate+shape analysis).

Motivations on the model choice

Within the ND280 precision, an analysis only in the ν_eCC distributions cannot disentangle between 3+1, 3+2 or 1+3+1 models, so we consider the simplest model with only one sterile neutrino (3+1). This decision is also justified by the fact that the global fit described in Section 2.2.4 do not shown any model preference.

The 3+1 model includes two more potential research channels as stressed in Section 2.1.1: ν_μ disappearance and ν_e appearance. In our analysis we do not consider any of them. For the first channel, it is

justified by the fact that it has never been observed and there are strong constraints (see Section 2.2.3). This allows the study of the ND280 ν_μ event rates to reduce the flux and cross-section systematic errors [Section 5.1]. Secondly and to be consistent with the assumption of no $\nu_\mu \to \nu_s$ mixing, we do not consider the ν_e appearance possibility. Essentially, we test the 3+1 model neglecting the mixing matrix element $U_{\mu 4}$.

Overview of the analysis

In this analysis we use the ν_e selections together (see Chapter 6), defining an inclusive ν_eCC selection. In Section 10.1 we start discussing about the ν_e flight path of the selected sample. In Section 10.2 we show the reconstructed neutrino energy of the events selected in Chapter 6. The number of expected events in the presence of oscillations is calculated by introducing P_{ee} [Eq. (10.1)]. The statistical framework is presented in Section 10.3 where the likelihood ratio method is introduced and different methods to calculate the confidence intervals are also discussed, namely the constant $\Delta\chi^2$ and the Feldman-Cousins methods. After validating the minimization technique in Section 10.4 we calculate the sensitivity of ND280 for the study of the ν_e disappearance in Section 10.5. Finally, the results with the ND280 data are presented in Section 10.6 and compared with the literature in Section 10.7.

10.1 Neutrino flight path

P_{ee} depends on the distance L traveled by the neutrino. As the hadrons produced in the Carbon target do not decay immediately, L is in general smaller than the distance between the target and ND280 (280 m). Each particle decay at different points along the 96 m long decay tunnel depending on the mean life τ of the particles. The kaons (K^0 and K^+), with a mean life of $\tau_K \sim 10^{-8}s$, tend to decay promptly while the muons, with $\tau_\mu \sim 10^{-6}$, decay along the whole tunnel. This can be observed in the L patterns for the different ν_e sources in Fig. 10.1. L represents the distance between the production point of the neutrino and the point of its interaction. The kaons have exponential distributions with peaks at the production points while the μ have an almost flat pattern. There are almost no ν_e from pion decay. The average flight path is 244 m and due to this effect, ND280 is sensitive to slightly larger Δm^2_{41} than expected. In addition, the fact that L is not perfectly defined makes the oscillation pattern along the neutrino energy more diffuse.

We remark that it is not possible to measure the flight path with enough precision for the data, so an analysis on the L distribution is not available and we only show the Monte-Carlo distributions for illustration.

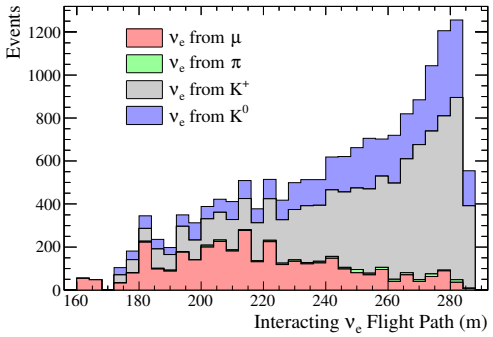

Fig. 10.1: Flight path of the neutrino selected in the ν_eCC sample broken down by neutrino parents.

10.2 Reconstructed neutrino energy

Assuming a ν_eCCQE interaction, we can reconstruct the neutrino energy E_{Rec} using the electron kinematics according to the formula:

$$E_{Rec} = \frac{m_p^2 - (m_n - E_b)^2 - m_e^2 + 2(m_n - E_b)E_e}{2(m_n - E_b - E_e + p_e \cos\theta_e)} \tag{10.2}$$

where m_e, p_e and E_e are the mass, momentum and energy of the reconstructed electron, m_p is the mass of the proton, m_n is the mass of the neutron, θ is the angle between the trajectory of the neutrino and the produced electron, that is the polar angle of the electron considering the neutrino going straight along the z axis and $E_b = 27\,\text{MeV}$ is the binding energy. E_{Rec} contains the momentum and the angle of the outgoing electron so it includes more valuable information than a solely momentum distribution. In addition, E_{Rec} is correlated with the real energy of the neutrino E_{True} so the oscillation pattern of P_{ee} will be more sensitive in the E_{Rec} than in the momentum distributions. This correlation is shown in Fig. 10.2 for different type of neutrino interaction. The correlation between E_{true} and E_{rec} is strong in the CCQE interactions, while in the other cases the majority of the events are below the diagonal due to the fact that part of the energy is carried by the other particles produced in the neutrino interaction that are not taken into account in the approximation of Eq. (10.2). In the case of the γ background there is no correlation between E_{Rec} and E_{True} as the electron is produced by a γ conversion and not

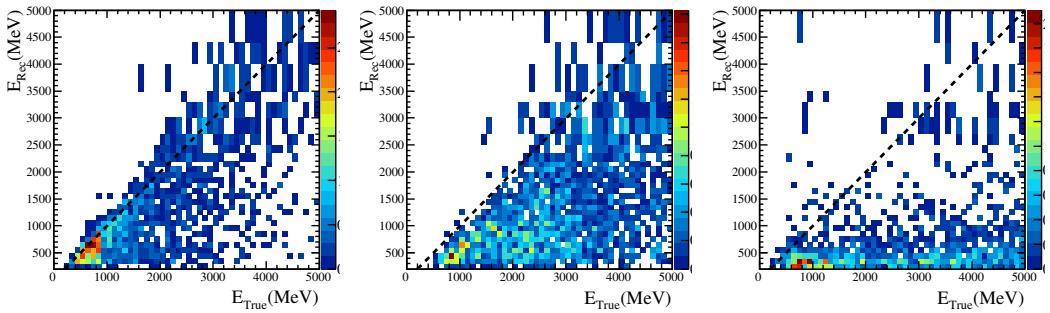

Fig. 10.2: E_{Rec} vs E_{true} for the different components of the ν_eCC selection. From left to right: ν_eCCQE, ν_eCCnonQE and γ background.

by a neutrino interaction. We want to stress that the distributions in Fig. 10.2 are not used in this particular form in the analysis and are only shown to illustrate the performances of E_{Rec}.

The distributions of E_{Rec} are shown in Fig. 10.3 for the ν_eCC selection and the γ control sample for Monte-Carlo and data. The Monte-Carlo is broken down by neutrino flavour and the background shows explicitly the OOFV component.

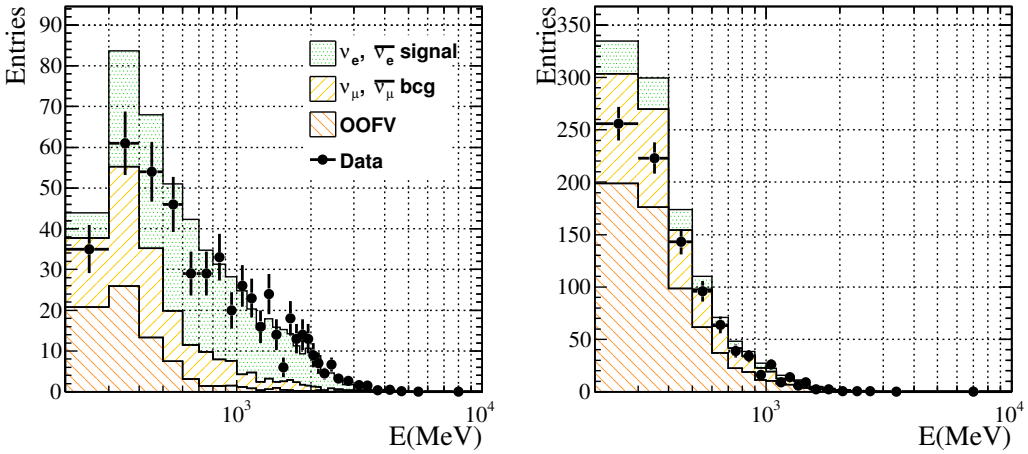

Fig. 10.3: Neutrino reconstructed energy spectrum for selected events for the ν_eCC selection (left) and γ selection (right). The Monte-Carlo is divided in ν flavour and OOFV background.

10.2.1 Binning choice

The range of E_{Rec} for the analysis is from 200 MeV to 10 GeV with a variable binning different from Section 9.1.1 as we need a finer binning to have good resolution for the E_{Rec} shape to have the best

possible precision on Δm^2_{41}. As the γ sample is barely affected by the oscillations (ν_e correspond to less than 10%), we can keep a coarser binning for that selection. The binning is optimized to have 31 E_{Rec} bins for the ν_eCC selection and 20 bins for the γ selection distributed as follows:

$\nu_e =$ [200,300,400,500,600,700,800,900,1000,1100,1200,1300,1400,1500,
1600,1700,1800,1900,2000,2100,2200,2350,2500,2700,3000,3300,3500,4000,
4400,5000,6000,10000]

$\gamma =$ [200,300,400,500,600,700,800,900,1000,1100,1200,1300,1400,1500,
1700,1900,2200,2500,2800,4000,10000]

10.2.2 Expected number of events with oscillations

The short baseline ν_e disappearance is introduced by multiplying the number of ν_e and $\overline{\nu}_e$ events by the survival probability P_{ee} defined in Eq. (10.1). This introduces the dependency of $\sin^2(2\theta_{ee})$ and Δm^2_{41} on the number of expected events. To get the total number of expected events in the i-th E_{Rec} bin entering in one of the two selections including the ν_e oscillation, we use an event by event framework where the weight of each event is given by the systematic errors parameters $\vec{f}$ and P_{ee}. It is defined as:

$$n^{i,\alpha}_{exp}(\sin^2(2\theta_{ee}),\, \Delta m^2_{41}; \vec{f}) = \frac{N^{data}_{POT}}{N^{MC}_{POT}} \sum_{j}^{N_i} W^j(\vec{f}) \times P_{ee}(\sin^2(2\theta_{ee}),\, \Delta m^2_{41}) \tag{10.3}$$

where N_i is the number of events in the i-th E_{Rec} bin, W^j is the weight of the event given by $\vec{f}$ as defined in Eq. (9.1), α runs over the two selections and P_{ee} only applies to ν_e and $\overline{\nu}_e$. The same formula is used for ν_eCC and γ samples, although the latter have a very small ν_e and $\overline{\nu}_e$ components and the effect of the oscillations is negligible.

In Fig. 10.4 we provide the E_{Rec} distributions for the ν_eCC selection under different oscillation hypotheses . The corresponding number of events are shown in Tab. 10.1. Regarding the ratios, we observe how the maximum of the disappearance moves with Δm^2_{41}, indicating the a shape analysis of E_{Rec} is sensitive to Δm^2_{41}. Despite of the fact that we used $\sin^2(2\theta_{ee}) = 0.2$, a 20% disappearance effect is never observed due to the following reasons:

- For low Δm^2_{41} the maximum of P_{ee} sits at low energies where we have most of the γ background coming from ν_μ that do not oscillate;

- for higher Δm^2_{41} the maximum of P_{ee} stands at higher energies where we are dominated by ν_eCCnonQE, for which the neutrino energy is poorly correlated with E_{Rec} (see Fig. 10.2) and the oscillation pattern is more diffuse;

- for very high Δm^2_{41} we enter in the fast oscillation regime [Eq. (1.9)] and the oscillation is averaged to $\sim \sin^2(2\theta_{ee})/2$ giving a disappearance of the $\sim 10\%$ for $\Delta m^2_{41} = 20\,\mathrm{eV}^2$.

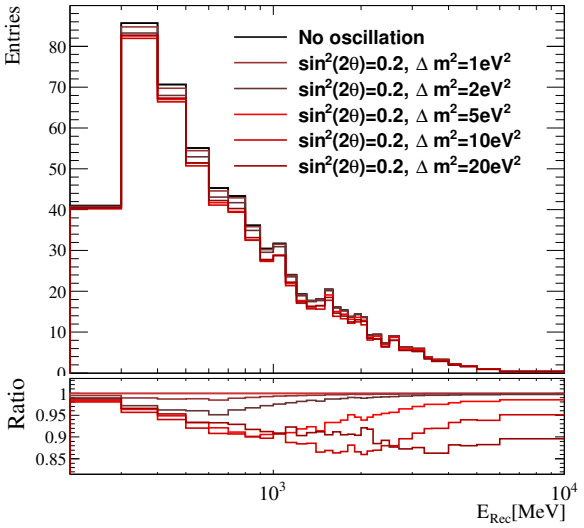

Fig. 10.4: Expected number of events in the case of oscillation for several hypothesis. Top: Expected events in function of the reconstructed neutrino energy; bottom: ratio with respect to the non oscillation prediction.

Hypothesis	ν_e sample		γ sample	
	ν_e Signal	Total	ν_e Signal	Total
No oscillation	414.8	669.7	69.3	1248.7
$\sin^2(2\theta_{ee}) = 0.2,\ \Delta m^2_{41} = 1\,\mathrm{eV}^2$	410.2	665.2	68.9	1248.2
$\sin^2(2\theta_{ee}) = 0.2,\ \Delta m^2_{41} = 2\,\mathrm{eV}^2$	400.2	655.1	67.7	1246.9
$\sin^2(2\theta_{ee}) = 0.2,\ \Delta m^2_{41} = 5\,\mathrm{eV}^2$	378.5	633.4	64.0	1243.0
$\sin^2(2\theta_{ee}) = 0.2,\ \Delta m^2_{41} = 10\,\mathrm{eV}^2$	361.7	616.5	60.6	1239.3
$\sin^2(2\theta_{ee}) = 0.2,\ \Delta m^2_{41} = 20\,\mathrm{eV}^2$	368.6	623.3	61.1	1239.8

Table 10.1: Predicted number of events for different oscillation hypothesis. The final prediction given by the ν_μ ND280 analysis for the Monte-Carlo is used.

10.3 Calculation of the confidence intervals

The purpose of an oscillation analysis is finding which values of $\sin^2(2\theta_{ee})$ and Δm^2_{41} are compatible or excluded by our data. In order to do this, we use a *frequentist* approach. A bi-dimensional parameter space is defined in the physical region:

$$0 < \sin^2(2\theta_{ee}) < 1$$
$$0 < \Delta m^2_{41} < 100$$

where a large upper bound for Δm^2_{41} has been set. A *test statistic* value is calculated per oscillation hypothesis, *i.e.* a value that provides whether an hypothesis for $\sin^2(2\theta_{ee})$ and Δm^2_{41} is accepted or rejected. The *test statistic* that we use is the likelihood ratio. In practice, we define a bi-dimensional 40×50 discrete grid G in the parameter space

$$G_{ij} \equiv (\sin^2(2\theta_{ee})_i, \Delta m^2_{41\,j})$$

and the value of the best fit likelihood ratio is calculated at each point. This provides a map of the likelihood ratio value and hence, the confidence intervals. The grid is defined coarser at large values of Δm^2_{41} where we do not have much resolution in Δm^2_{41} because of the fast oscillations. The binning in each parameter for the grid is:

$\sin^2 2\theta =$ `[0., 0.025, 0.05, 0.075, 0.1, 0.125, 0.15, 0.175, 0.2, 0.225,`
`0.25, 0.275, 0.3, 0.325, 0.35, 0.375, 0.4, 0.425, 0.45, 0.475,`
`0.5, 0.525, 0.55, 0.575, 0.6, 0.625, 0.65, 0.675, 0.7, 0.725,`
`0.75, 0.775, 0.8, 0.825, 0.85, 0.875, 0.9, 0.925,0.95, 0.975, 1]`

$\Delta m^2[\mathrm{eV}^2] =$ `[0., 0.5, 1, 1.5, 2, 2.5, 3, 3.5, 4, 5, 6, 7, 8, 9, 10, 12.5,`
`15, 17.5, 20, 22.5, 25, 27.5, 30, 32.5, 35, 37.5, 40, 42.5, 45,`
`47.5, 50, 52.5, 55, 57.5, 60, 62.5, 65, 67.5, 70, 72.5,`
`75, 77.5, 80, 82.5, 85, 87.5, 90, 92.5, 95, 97.5, 100 ]`

10.3.1 Likelihood ratio definition

The likelihood ratio $\mathcal{L}^r$ at the point of the grid G_{ij} compares the value of the likelihood at that point ($\mathcal{L}_{ij}$) with the value of the likelihood at the point $G_{bf} \equiv (\sin^2(2\theta_{ee})_{bf}, \Delta m^2_{41\,bf})$ where the agreement between data and Monte-Carlo is better (*best fit point*) and the likelihood is maximal ($\mathcal{L}^r_{bf}$). It is defined as the ratio of the two likelihood values:

$$\mathcal{L}^r_{ij} = \frac{\mathcal{L}_{bf}}{\mathcal{L}_{ij}}$$

The quantity that provides the *test statistic* to compute the confidence intervals is

$$\Delta\chi^2_{ij} \equiv -2\log\mathcal{L}^r_{ij} = \chi^2_{ij} - \chi^2_{bf} \tag{10.4}$$

that should follow a χ^2 distribution with $dof = 2$. The likelihood function was deduced in Section 9.2 and we define it for this analysis as:

$$\begin{aligned}\chi^2 \equiv -2\log\mathcal{L} =& 2\sum_{l=0}^{31}\left\{n^{l,\nu_e}_{exp} - n^{l,\nu_e}_{dt} + n^{l,\nu_e}_{dt}\times\log\left(\frac{n^{l,\nu_e}_{dt}}{n^{l,\nu_e}_{exp}}\right)\right\}\\ &+2\sum_{i=0}^{20}\left\{n^{l,\gamma}_{exp} - n^{l,\gamma}_{dt} + n^{l,\gamma}_{dt}\times\log\left(\frac{n^{l,\gamma}_{dt}}{n^{l,\gamma}_{exp}}\right)\right\}\\ &+(\vec{f}-\vec{f}_0)^T V^{-1}(\vec{f}-\vec{f}_0)\end{aligned} \tag{10.5}$$

where $n^{l,\alpha}_{dt}$ and $n^{l,\alpha}_{exp}$ are the expected number of events in the l-th E_{Rec} bin of the α selection (ν_eCC or γ) and $\vec{f}$ are the 55 systematic errors parameters that are constrained by the penalty term using the covariance matrix V (see Chapter 8). In order to build the confidence intervals for the parameter space we calculate the minimal value of the log-likelihood [Eq. (10.5)] at the best fit point χ^2_{bf} and the value at each point of the grid χ^2_{ij}. The calculation of the global minimum χ^2_{bf} suffers from computational issues and it is discussed in Section 10.3.3.

Treatment of the nuisance parameters

The likelihood Eq. (10.5) depends on the oscillation parameters and also on the 55 parameters $\vec{f}$ that include the systematic uncertainties in the analysis. The results of these parameters are not interesting for the analysis so they are called *nuisance parameters*. To build the contours in the bi-dimensional

grid they must be removed. A common way to do that, is by building the *profile likelihood* defined as the minimum value of the log-likelihood fixing the oscillation parameters to the point G_{ij}:

$$\chi^2_{ij} = \chi^2_{ij}(\vec{f}_{bf})$$

where $\vec{f}_{bf}$ is the nuisance parameters vector that minimize the log-likelihood at G_{ij}.

10.3.2 Simple study of the likelihood map on the parameter space

We present a simple analysis of the shape of the likelihood in the parameter space. We calculate the χ^2_{ij} map [Eq. (10.5)] for a toy Monte-Carlo built under some oscillation hypothesis. This toy is not fluctuated according to statistical nor systematic uncertainties, since we want to study solely the effect of the oscillations. We have done two different toy experiments:

- *Set 1*: No oscillations, $\sin^2(2\theta_{ee}) = 0$ and $\Delta m^2_{41} = 0$

- *Set 2*: Oscillations with parameters $\sin^2(2\theta_{ee}) = 0.7$ and $\Delta m^2_{41} = 8\,\mathrm{eV}^2$.

The map of the likelihood in the bi-dimensional oscillation parameter space is shown for each case in Fig. 10.5. A large value indicates that the corresponding region can be excluded with a large confidence level.

In the *Set 1* we observe large values of the likelihood at around $\Delta m^2_{41} = 15\,\mathrm{eV}^2$. This is the region where the effect of the oscillation are stronger since it corresponds to the value of Δm^2_{41} that locates the maximum of the disappearance at the peak of the E_{Erec} distribution. Hence, this is the region where our analysis is more sensitive to $\sin^2(2\theta_{ee})$. For lower values of any of the parameters, the likelihood becomes rather flat since the effect of the oscillations diminish. It implies that a random fluctuation of the data might easily change the position of the global minimum in that region and hence, we are not able to discriminate among the points in that region. A similar feature occurs at high Δm^2_{41}: this region corresponds to the fast oscillations regime where the values of Δm^2_{41} are degenerate because of the flatness of the likelihood with respect to Δm^2_{41}.

For the *Set 2* we observe an important effect to be stressed: the global minimum of the likelihood sits in ($\sin^2(2\theta_{ee}) = 0.7$, $\Delta m^2_{41} = 8\,\mathrm{eV}^2$), but for higher Δm^2_{41} and same $\sin^2(2\theta_{ee})$ we find local minima.

This effect is introduced by the oscillatory behaviour of P_{ee}. Hence, a fluctuation in the data can move the global minimum of the likelihood to a *wrong* solution with higher Δm^2_{41}. This is called a *ghost* point and they are very common in neutrino oscillation analysis.

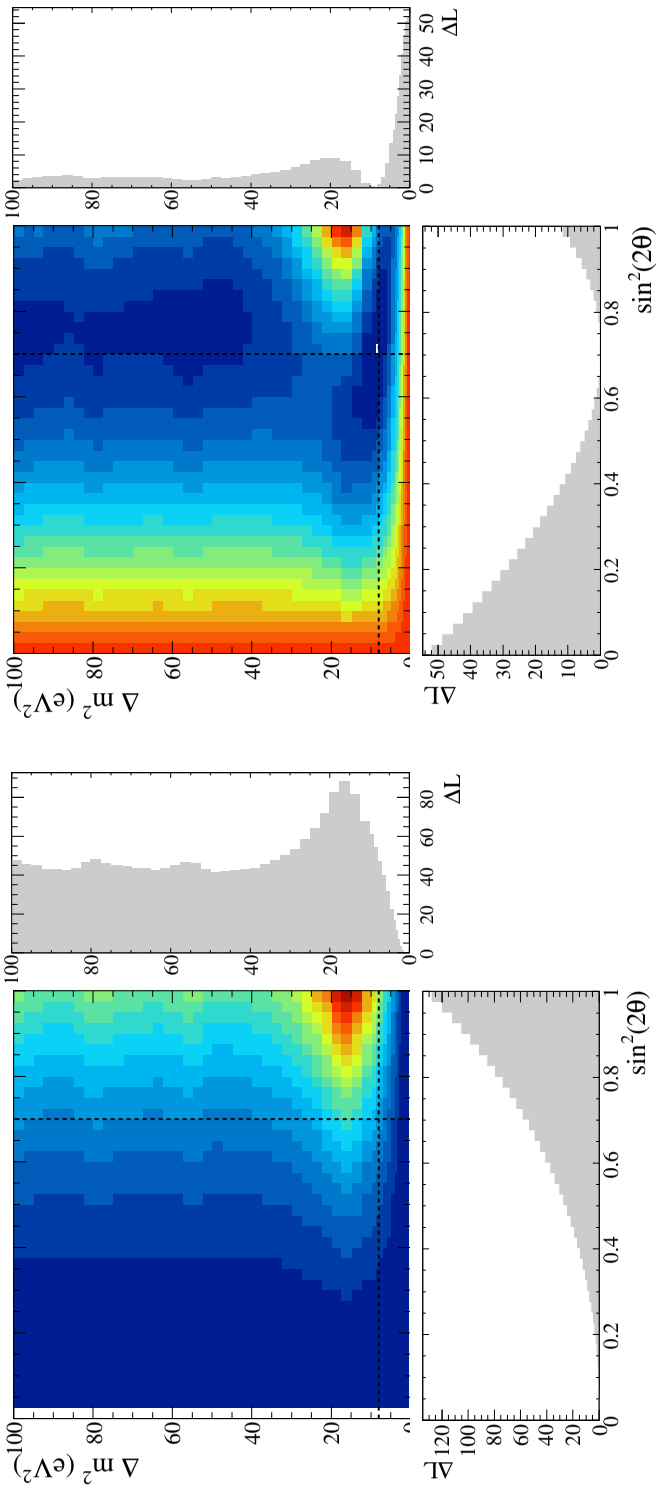

Fig. 10.5: Likelihood value in the bi-dimensional oscillation parameter space ($\sin^2(2\theta_{ee})$, Δm^2_{41}) Left: non oscillations case; right: oscillation with parameters $\sin^2(2\theta_{ee}) = 0.7$, $\Delta m^2_{41} = 8\,\mathrm{eV}^2$. The side plots represent the 1-dimensional shape of the likelihood for fixed parameters at the dotted lines.

10.3.3 Minimization technique

The log-likelihood or χ^2 defined in Eq. (10.5) is minimized using the `TMinuit` library provided by `ROOT` in order to calculate the minimal value at the best fit point χ^2_{bf}. The free oscillation parameters are constrained within the same parameter intervals than the bi-dimensional grid

$$0 < \sin^2(2\theta_{ee}) < 1$$
$$0 < \Delta m^2_{41} < 100$$

where we included an upper constrain in Δm^2_{41} that is large enough not to give boundary problems at high Δm^2_{41}. The minimization presents some purely computational problems that have been extensively studied. Depending on the choice of the starting values for the oscillation parameters $\sin^2(2\theta_{ee})_s$ and $\Delta m^2_{41\,s}$, the fit might not find the correct global minimum. This is a problem because the fitted parameters are not properly estimated and moreover, the value of the χ^2_{bf} is not the minimum one, giving a false confidence interval. We tried several options:

- Fixed at some point far from the boundaries $\sin^2(2\theta_{ee})_s = 0.4$ and $\Delta m^2_{41\,s} = 5\,\mathrm{eV}^2$: in some cases the fit did not find the correct global minimum because it falls in a local minimum
- Random starting values: similarly to the previous case, sometimes the fit falls in a local minimum
- *Multi-fit*: based on performing several fits at different starting points and extract the minimum value of them. This is the most accurate approach and the one we utilize in our analysis.

The two first cases are the fastest approaches, but they turn to be insecure and imprecise. The fit finds in some cases a local minimum instead of the global minimum due to the *multi-modal* nature of the likelihood, since in some regions, it changes rapidly giving many local minima. Further discussion about these methods appear in Appendix B. The third procedure is the one used in present analysis and it is described as follows:

1. A set of 10 starting values for Δm^2_{41} is chosen.
2. For each starting value, the log-likelihood expression [Eq. (10.5)] is minimized.
3. The lowest χ^2_{bf} value is taken as the global minimum.

This receipt is not applied to $\sin^2(2\theta_{ee})$ since the problem is only related to the oscillatory behavior driven by Δm^2_{41}, so then the starting value of $\sin^2(2\theta_{ee})$ is always set to 0.5. The set of initial Δm^2_{41} values is defined as:

$$\Delta m^2_{41_s} = \{5,\ 10,\ 20,\ 30,\ 40,\ 50,\ 60,\ 70,\ 80,\ 90\}\,[\mathrm{eV}^2]$$

10.3.4 *p-value*

The *p-value* is an estimator of the compatibility of the data with a hypothesis, commonly, the null hypothesis. It is equivalent to the *goodness-of-fit* test using $\Delta\chi^2$ instead of χ^2.

We build N_{toys} toys experiments in the non-oscillation hypothesis $\sin^2(2\theta_{ee}) = 0$, $\Delta m^2_{41} = 0$ and are minimized using the method described previously. The value $\Delta\chi^2_{00}$ of best fit is calculated for each of them and also computed for the data $\Delta\chi^2_{00,data}$.

The *p-value* is defined as the fraction of toys experiment for which $\Delta\chi^2_{00} > \Delta\chi^2_{00,data}$. Mathematically:

$$p - value = \frac{1}{N_{toys}} \int_{\Delta\chi^2_{00,data}}^{+\infty} d\Delta\chi^2 f(\Delta\chi^2) \tag{10.6}$$

This value provides the probability that the differences between the null hypothesis and the observed data are due to fluctuations. Thus, a low *p-value* indicates that the data does not favor the null hypothesis.

10.3.5 The constant $\Delta\chi^2$ method

The constant $\Delta\chi^2$ method is a simple method that provides confidence intervals in the oscillation parameter space. To determine whether a given point of the parameter space G_{ij} is rejected or permitted, we calculate the $\Delta\chi^2_{ij}$ value [Eq. (10.4)] and we check whether this value is larger or smaller than a critical value $\Delta\chi^2_{Cij}$ provided in Tab. 10.2 for each confidence level:

- If $\Delta\chi^2_{ij} > \Delta\chi^2_C$: G_{ij} is rejected at some confidence level
- If $\Delta\chi^2_{ij} < \Delta\chi^2_C$: G_{ij} is allowed at some confidence level
- If $\Delta\chi^2_{ij} = \Delta\chi^2_C$: the G_{ij}'s that fulfill this condition define the confidence contour

The $\Delta\chi^2_C$ values are calculated with the *goodness-of-fit* provided by a χ^2 with $dof = 2$.

This method provides a reliable contour in the limit of large statistic (*i.e.* Gaussian *pdfs*) and when the contour is far from the physical boundaries. If any of the conditions are not fulfilled, other methods (like the Feldman-Cousins) must be used. In general, this method is conservative since it provides over-coverage to most of the relevant regions in the parameter space [92].

	1σ	90%CL	95%CL	2σ	3σ
1dof	1.00	2.71	3.84	4.00	9.00
2dof	2.30	4.61	5.99	6.18	11.83

Table 10.2: Critical values of the $\Delta(\chi^2)$ representing each confidence level according to the constant $\Delta\chi^2$ method [101].

10.3.6 The Feldman-Cousins method

An alternative frequentist method to build confidence interval, commonly used in neutrino analyses is the Feldman-Cousins method [92]. This is a more accurate method that the previous constant $\Delta\chi^2$ method, but it is also much more time consuming.

According to the Feldman-Cousins technique, the critical value that provides whether a point in the parameter space G_{ij} is permitted or not, is not constant but depends on G_{ij} itself:

$$\Delta\chi^2_{Cij} \equiv \Delta\chi^2_{Cij}(\sin^2(2\theta_{ee}),\, \Delta m^2_{41})$$

Those values need to be pre-calculated for the whole parameter space in the following way:

1. Choose a point G_{ij} on the oscillation parameter space;

2. Throw N_{toys} toys Monte-Carlo in the oscillation hypothesis $\sin^2(2\theta_{ee})^i$, $\Delta m^2_{41}{}^j$ following the procedure explained in Section 9.3.1;

3. For each toy we calculate $\Delta\chi^2_{ij}$ and build its distribution. We show these distributions for some example G_{ij} in Fig. 10.6;

4. The critical value $\Delta\chi^2_{Cij}$ at the x%CL corresponds to the value that fulfills:

$$\frac{1}{N_{toys}}\int_{\Delta\chi^2_{Cij}}^{\infty} d\Delta\chi^2 f(\Delta\chi^2) = x/100 \tag{10.7}$$

This procedure is repeated for the whole parameter space and, the sensitivity contour is provided in the same way that the constant $\Delta\chi^2$ but using these new critical values $\Delta\chi^2_{Cij}$.

If the distribution of $\Delta\chi^2_{ij}$ values follows a χ^2 distribution with two degrees of freedom, the critical values calculated with Feldman-Cousins coincide with the ones of the constant $\Delta\chi^2$ and both methods converge. In general this is not true, as shown in Fig. 10.6. The critical values generated with Feldman-Cousins using 5000 toys per grid point G_{ij} is shown in Fig. 10.7 for 1σ, 90%CL and 95%CL, respectively. We show the difference between the critical value calculated with Feldman-Cousins and the constant $\Delta\chi^2$ [Tab. 10.2]: a zero value indicates that both methods provide same confidence levels. The dark region indicates over-coverage by the constant $\Delta\chi^2$ and the bright regions means that it is under-covered. Differences between constant $\Delta\chi^2$ and Feldman-Cousins exist due to three reasons:

1. Proximity to the unphysical region: points close to the unphysical region occasionally have best fits in the unphysical region. Since our algorithm restricts fits to the physical region, these fits give a lower $\Delta\chi^2_{Cij}$ value;

2. sinusoidal nature of the oscillation function: for high values of Δm^2_{41}, fluctuations can cause a global minimum in a wrong dip of the function, increasing the value of $\Delta\chi^2_{Cij}$;

3. one-dimensional regions: in some regions of the plane, the $\Delta\chi^2_{Cij}$ distribution acts like a $dof = 1$ rather than $dof = 2$ χ^2 distribution. For instance, at very low values of Δm^2_{41}, where the only relevant quantity is the number of events in the lowest E_{Rec} bin. In these regions, $\Delta\chi^2_{Cij}$ tends to lower values than normal.

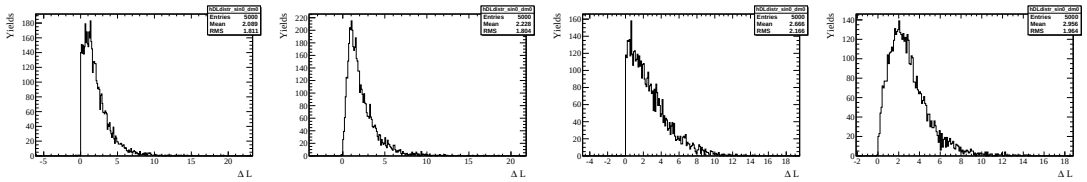

Fig. 10.6: Distributions of $\Delta\chi^2$ for 5000 toys generated with the following oscillation parameters $\left(\sin^2(2\theta_{ee}),\ \Delta m^2_{41}[\mathrm{eV}^2]\right)$ from left to right: $(0.3, 5)$, $(0.3, 90)$, $(0.7, 8)$, $(0.7, 50)$.

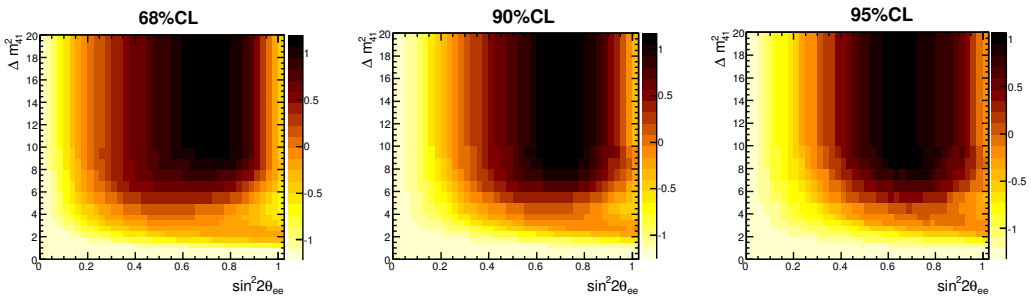

Fig. 10.7: Critical values $\Delta\chi^2_{Cij}$ for each point of the oscillation parameter space P^{ij} provided by Feldman-Cousins. From left to right: 68%CL, 90%CL and 95%CL

10.4 Validation of the fitter with toys Monte-Carlo

The minimization technique is validated using 5000 toys Monte-Carlo generated according to Section 9.3.1. The toys are built under the $\sin^2(2\theta_{ee})_{toy} = 0.7$ and $\Delta m^2_{41\,toy} = 8\,\mathrm{eV}^2$ oscillation hypothesis applying the survival probability P_{ee}. The minimization technique defined in Section 10.3.3 is used to find the best fit values for each of the toys. The distribution of the best fit points G_{bf} in the parameter space is shown in Fig. 10.8. The largest population is around the point where the toys Monte-Carlo were built. Nevertheless, some of the G_{bf} are spread at higher Δm^2_{41}. This is directly related with the degeneracy of the Δm^2_{41} values due to the oscillatory behaviour of the ν_e disappearance (see Section 10.3.2).

As a result, the distributions of $\sin^2(2\theta_{ee})_{bf}$ and $\Delta m^2_{41\,bf}$ showed at the sides of Fig. 10.8 present some features. The oscillation parameter Δm^2_{41} is highly non Gaussian due to its degeneracy with higher Δm^2_{41} values. The parameter $\sin^2(2\theta_{ee})$ is Gaussian distributed, but it is highly correlated with Δm^2_{41} and a large Δm^2_{41} moves $\sin^2(2\theta_{ee})$ to higher values, since there must be a compensation: there are less ν_e events at high E_{Rec}, so a larger ν_e disappearance amplitude is required to mimic the same effect at low Δm^2_{41}. Hence, the average of $\sin^2(2\theta_{ee})_{bf}$ is slightly larger than $\sin^2(2\theta_{ee})_{toy}$ and we find a pile up in $\sin^2(2\theta_{ee})_{bf} = 1$ more prominent than expected due to the asymmetry on the distribution.

The pull distributions for the oscillation parameters defined as:

$$\delta(\sin^2(2\theta_{ee})) = \frac{\sin^2(2\theta_{ee})_{toy} - \sin^2(2\theta_{ee})_{bf}}{\sigma_{\sin^2(2\theta_{ee})}} \qquad \delta(\,\Delta m^2_{41}) = \frac{\Delta m^2_{41\,\mathrm{toy}} - \Delta m^2_{41\,\mathrm{bf}}}{\sigma_{\,\Delta m^2_{41}}}$$

are shown at Fig. 10.9. They are not centered at zero as expected from the discussion above. The peak

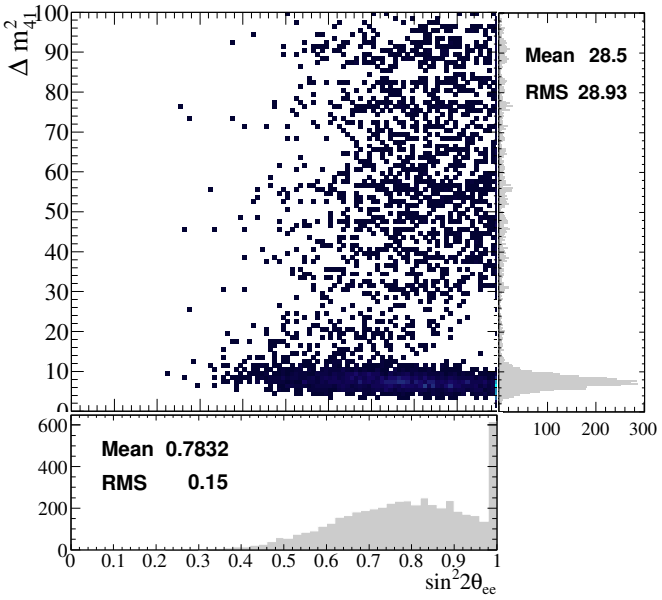

Fig. 10.8: Best fit points distribution in the oscillation parameters space resulting from the minimization of 5000 toys Monte-Carlo oscillated according to $\sin^2(2\theta_{ee}) = 0.7,\ \Delta m^2_{41} = 8\text{eV}^2$. On the sides, the projections on the parameter axes are shown.

at zero of $\delta(\sin^2(2\theta_{ee}))$ correspond to the pile up at $\sin^2(2\theta_{ee})_{bf} = 1$. As they are in the boundary, the error calculated by the minimization is very large making the denominator in $\delta(\sin^2(2\theta_{ee}))$ large and its value small. If we fix $\Delta m^2_{41} = \Delta m^2_{41\,\text{toy}}$ during the minimization and only allow to change $\sin^2(2\theta_{ee})$, the correlations are avoided and a good behavior of $\delta(\sin^2(2\theta_{ee}))$ is expected. The pull distribution is shown in Fig. 10.10 where we observe that the mean decreases to $\langle\delta(\sin^2(2\theta_{ee}))\rangle = 0.04 \pm 0.01$.

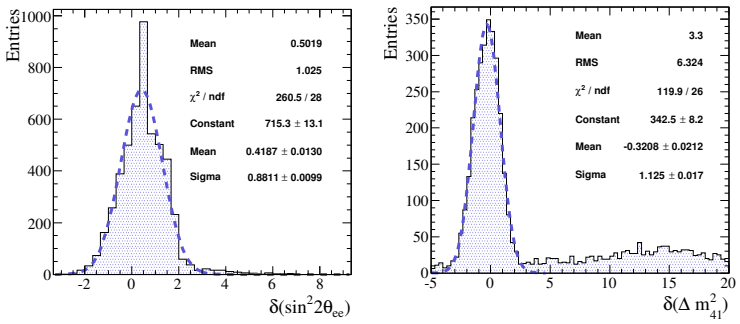

Fig. 10.9: Pulls of the oscillation parameters for 5000 toys with simulated 5.9×10^{20} POT and oscillations in the point $(\sin^2(2\theta_{ee}) = 0.7,\ \Delta m^2_{41} = 8\,\text{eV}^2)$.

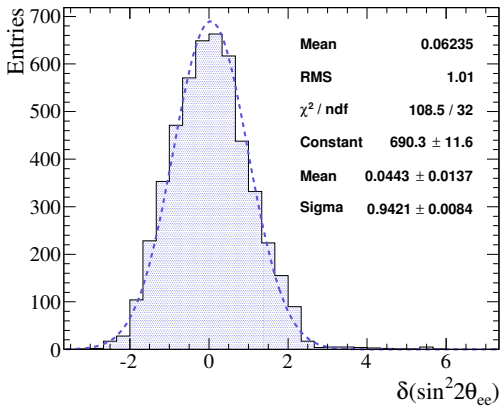

Fig. 10.10: Pull of $\sin^2(2\theta_{ee})$ with Δm^2_{41} fixed to the toy value.

Regarding the bias in Δm^2_{41}, it should be reduced by enlarging the amount of simulated data, as the statistical fluctuations are smaller and the degeneracy of Δm^2_{41} reduced. Thus, toys Monte-Carlo simulated 10 times more statistics (5.9×10^{21}POT) are built. We perform the minimization on 5000 toys and the distribution of the fitted oscillation parameters in Fig. 10.11 shows that the spread on Δm^2_{41} is smaller because the degeneracy of Δm^2_{41} is soften. The distribution of $\delta(\Delta m^2_{41})$ is more centered at zero as can be observed in Fig. 10.12. Concerning $\delta(\sin^2(2\theta_{ee}))$, it is shifted since the determination of $\sin^2(2\theta_{ee})$ does not depend on the statistics but just on the correlations with Δm^2_{41}.

With this discussion we demonstrate that the biases are driven by the *multi-modal* behavior of the likelihood and it is not related with the minimization technique. For the sake of completeness, in Fig. 10.13 we show the nuisance parameters pulls using the definition Eq. (9.6). It demonstrates that the minimization technique gives the correct solution as the mean values are well below 10%. On the other hand, the χ^2_{bf} values for the toys experiments should follow a χ^2 distribution with 49 dof, since we have 51 bins and 2 free parameters [Eq. (9.4)]. In Fig. 10.14 we show the χ^2_{bf} distribution and we conclude that it is very compatible with what we expected, meaning that the framework estimates properly the global minimum.

10.5 Sensitivity analysis

The sensitivity of ND280 to the ν_e disappearance is defined as the intervals in the oscillation parameter space that can be excluded with a certain probability in the case that there is no sterile oscillations.

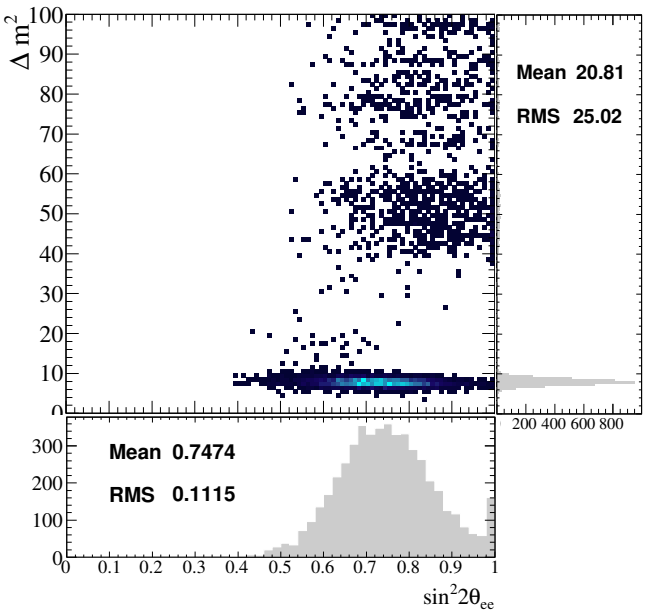

Fig. 10.11: Best fit points distribution in the oscillation parameters space resulting from the minimization of 5000 toys Monte-Carlo oscillated according to $\sin^2(2\theta_{ee}) = 0.7,\ \Delta m^2_{41} = 8\text{eV}^2$ simulating 10 times the current ND280 data exposure. On the sides, the projections on the parameter axes are shown.

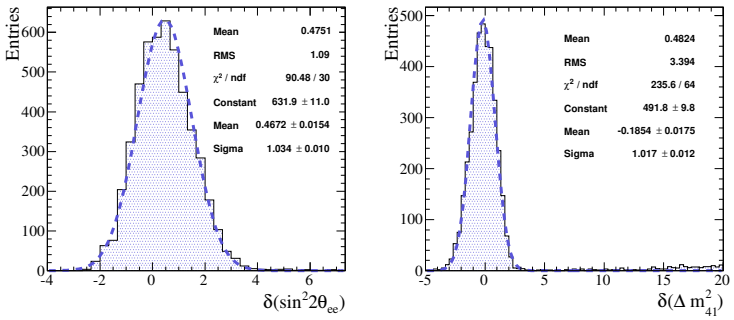

Fig. 10.12: Pull mean and width of the oscillation parameters for 5000 toys at 5.9×10^{21}POT in the point $(\sin^2(2\theta_{ee}) = 0.7,\ \Delta m^2_{41} = 8\,\text{eV}^2)$.

This studies are purely based on Monte-Carlo. We calculate the $\Delta\chi^2_{ij}$ map for a toy Monte-Carlo without oscillations and compare at each point G_{ij} with the critical values given by the constant $\Delta\chi^2$ method or the Feldman-Cousins. As the confidence intervals depend strongly on the statistical and the systematic errors fluctuations, the $\Delta\chi^2_{ij}$ map used to get the sensitivity is obtained as the average of

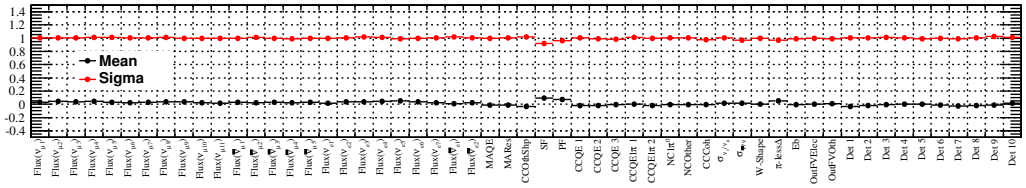

Fig. 10.13: Pull mean and width of the nuisance parameters for 5000 toys built under the oscillation hypothesis $\sin^2(2\theta_{ee}) = 0.7$ and $\Delta m^2_{41} = 8\,\mathrm{eV}^2$. The pulls are calculated using Eq. (9.6).

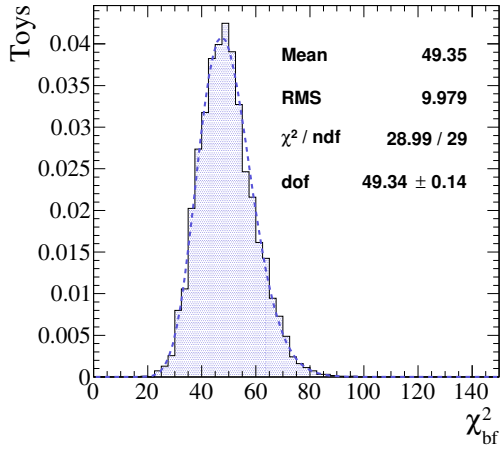

Fig. 10.14: χ^2_{bf} distribution for 5000 toys Monte-Carlo built with oscillation parameters $\sin^2(2\theta_{ee}) = 0.7$ and $\Delta m^2_{41} = 8\mathrm{eV}^2$. The distributions are fitted with a χ^2 function to extract the *dof* parameter.

1000 toys experiments built in the null hypothesis but with different statistical and systematic error fluctuations.

10.5.1 Sensitivity with constant $\Delta\chi^2$

The contours at 1σ, 90%CL and 95%CL cases are shown in Fig. 10.15 for linear and logarithmic scales. The area to the left of the lines are the regions that we expect to reject if the ND280 data is compatible with the Monte-Carlo prediction in the null hypothesis. If, on the contrary, the data presents any signal of ν_e disappearance within that region, our analysis will be able to measure it and discriminate the null hypothesis within the corresponding confidence level.

The bump at low Δm^2_{41} corresponds to the position of the first oscillation maximum over the E_{Rec} peak of the ν_e component selected at the ν_eCC sample. In this region we have the best sensitivity to

$\sin^2(2\theta_{ee})$. When we go to higher Δm^2_{41} region we enter in the fast oscillation regime where we lose the dependency on Δm^2_{41}, so we get a vertical straight line. At this point the ν_e disappearance effect is halved and this is why the sensitivity in $\sin^2(2\theta_{ee})$ becomes worse (see Section 10.3.2).

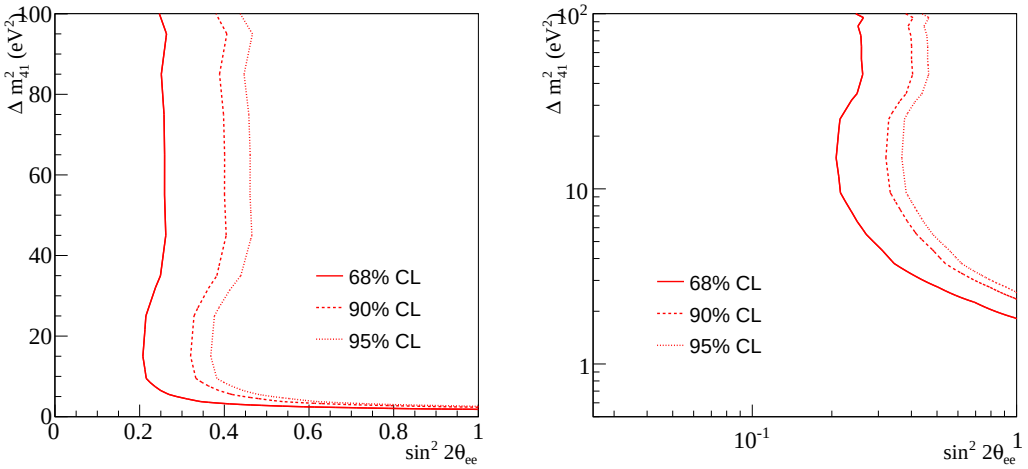

Fig. 10.15: Sensitivities at 68%CL, 90%CL and 95%CL calculated using the constant $\Delta\chi^2$ method applied to an average grid for 1000 toys. Left plot: linear scale, right plot: logarithmic scale.

It is also interesting to study the effect of each systematic uncertainty on the final contour. This can be done by enabling or disabling groups of systematic errors parameters. On the top of Fig. 10.16 we show the sensitivity for only one group of systematic errors at a time[1]. The rest of systematic parameters that are not used are neither thrown in the toys nor fitted during profiling the likelihood. We have separated the systematic errors in three groups: flux, cross-section and detector and FSI systematic errors. The different sources have similar impact on the sensitivity although the cross-section uncertainties are slightly more important.

The evolution of the sensitivity with the amount of data is studied by simulating toys Monte-Carlo with approximately 10 times the current POT (7.8×10^{21}POT, T2K final goal). The result for this sensitivity is shown in the middle of Fig. 10.16. We tested both the exposures with and without systematic errors. Increasing the statistics moves the sensitivity from $\sin^2(2\theta_{ee}) = 0.5$ to $\sin^2(2\theta_{ee}) = 0.35$ (taking as reference the high Δm^2_{41} part) while if we remove the systematic uncertainties it moves up to $\sin^2(2\theta_{ee}) = 0.25$, meaning that we are dominated by the systematic errors with the current POT. For ten times the current statistics and without considering systematic errors, we reach the lower limit for

[1] A coarser binning is used to built the sensitivity grid and save time. In this way the contour slightly moves. This is used just for checks and not for the final results where the fine binning is used.

the ND280 sensitivity of $\sin^2(2\theta_{ee}) = 0.1$.

Finally, we studied the impact of the gamma control sample in the sensitivity by removing the contribution of this selection to the likelihood. The contours are shown at the bottom of Fig. 10.16 where we observe that the sensitivity improves if we include the gamma selection. This is mainly due to the better knowledge of the OOFV background that allows to further constrain the systematic errors on this component.

10.5.2 Sensitivity with Feldman-Cousins

The final results for this analysis will be provided by the Feldman-Cousins technique as it gives more reliable contours than the constant $\Delta\chi^2$. The critical values calculated in Section 10.3.6 for different confidence levels are compared with the averaged $\Delta\chi^2$ map for the toys Monte-Carlo. In Fig. 10.17 we show the sensitivity using this technique. As the contours provided by the constant $\Delta\chi^2$ stand in the region of good coverage [Fig. 10.7], the Feldman-Cousins contours do not differ to much from them.

10.6 Confidence intervals given by the data

We apply the fitting technique to the data and calculate the confidence regions with the methods described in Section 10.3. The minimal value for the χ^2 expression [Eq. (10.5)] that we find for the real data is:

$$\chi^2_{bf}/dof = 43.2/49$$

and corresponds to the point G_{bf} in the parameter space:

$$\sin^2(2\theta_{ee})_{bf} = 1.00 \qquad \Delta m^2_{41\,bf} = 2.14\,\mathrm{eV}^2$$

This values indicate that a non-zero value for the ν_e disappearance is preferred by the data set. Nevertheless, G_{bf} is in a region outside the sensitivity region [Fig. 10.17] and hence, the position of the best fit point is not relevant. What really matters are the confidence intervals that are presented below. In Fig. 10.18 the reconstructed neutrino energy distributions for the ν_e and gamma selections are shown for the data and the Monte-Carlo before and after the fit. The deficit of the data observed in Fig. 10.18

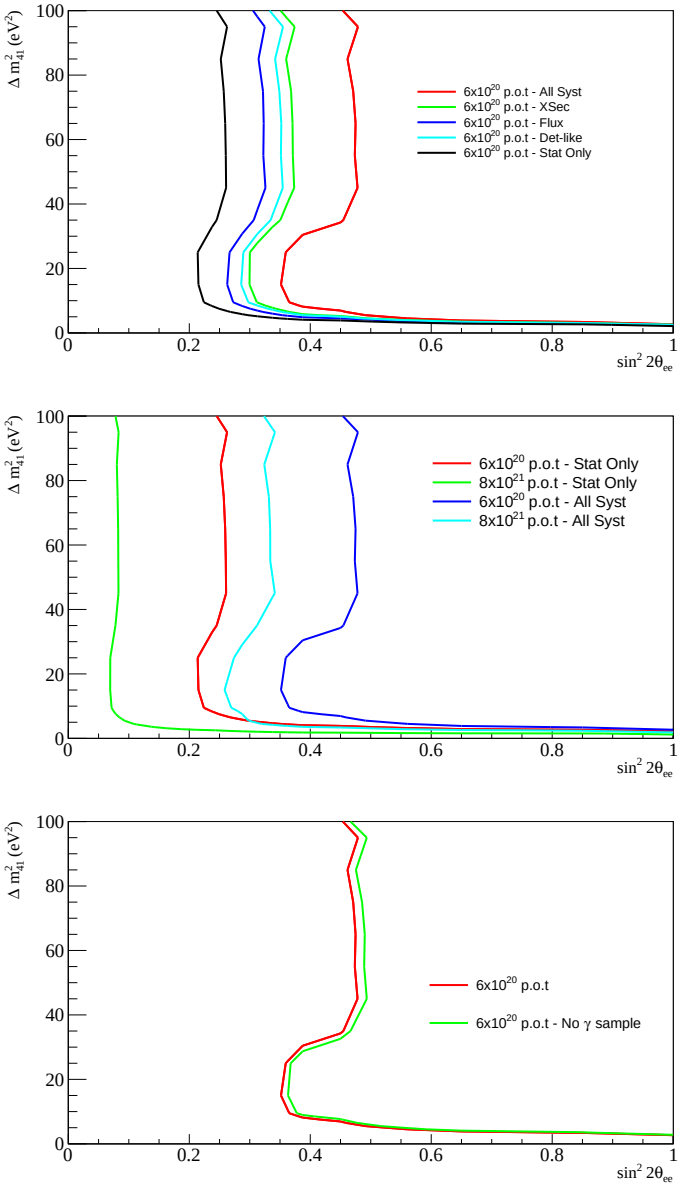

Fig. 10.16: 90%CL exclusion regions averaged over 1000 toys in the non oscillation hypothesis. Top: shows the contributions of each uncertainty for the case with $6.0 \cdot 10^{20}$ POT; middle: dependency of the sensitivity with the POT; bottom: impact of the photon sample in the sensitivity.

for the nominal Monte-Carlo disappear after the fit and the *goodness-of-fit* is $gof = 70\%$, indicating a good agreement. The fact that the deficit at low E_{Rec} is observed in both, the ν_eCC and the γ samples indicates that it comes partially from an overestimation of our backgrounds. This fact emphasizes the importance of including the gamma control sample in the ν_e disappearance analysis.

It is interesting to check which systematic parameter have been tunned by the fit, comparing them

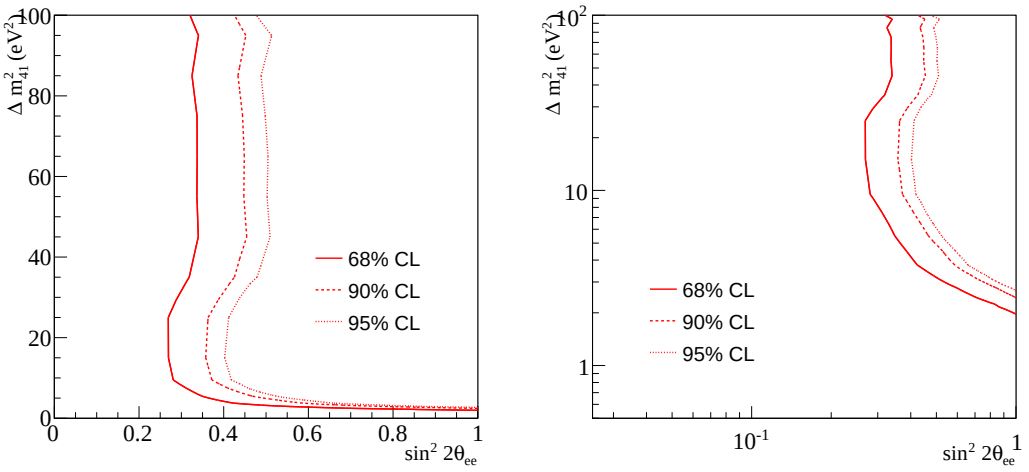

Fig. 10.17: Sensitivities at 68%CL, 90%CL and 95%CL calculated using the Feldman-Cousins method applied to an average $\Delta\chi^2$ grid for 1000 toys. Left plot: linear scale, right plot: logarithmic scale.

before $\vec{f}_0$ and after $\vec{f}_{bf}$ using the pull definition:

$$\delta_f = \frac{f_0 - f_{bf}}{\sigma_{f_0}}$$

They are shown for each parameter in Fig. 10.18. Essentially, the pulls are around 1σ, being the largest variation of about -2σ for the NC interactions without a π^0 (NC Other). It means that all the parameters are compatible with their prior errors and there are no tensions in our results with the ND280 ν_μ analysis. Also in this case, as well as in the ν_e beam measurement [Section 9.6], the OOFV coming from photon conversion is reduced by $\sim 30\%$ (1σ) what largely affects to the low E_{Rec} region. This is what mainly drives the reduction at low E_{Rec} for both the γ and the ν_eCC selections.

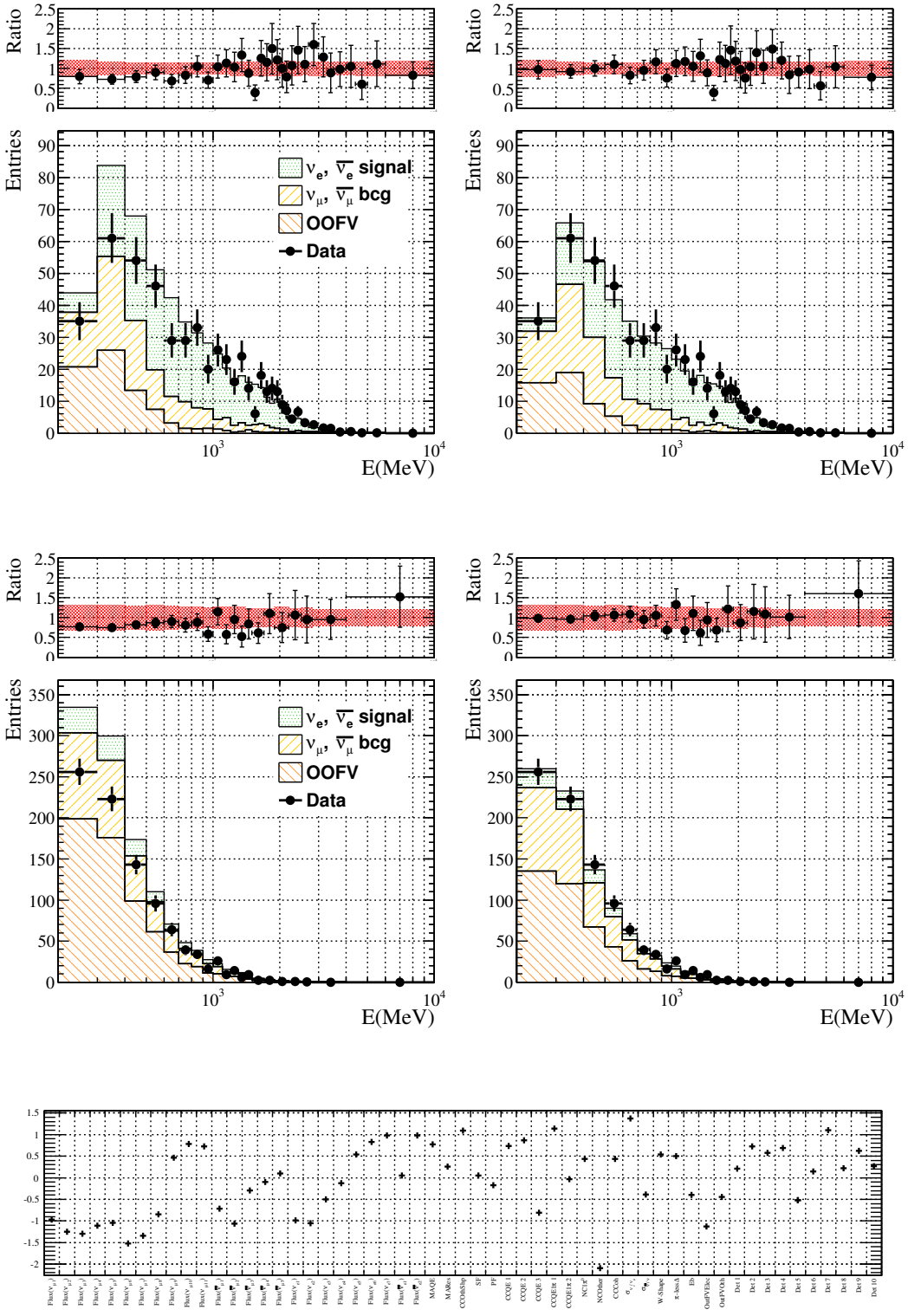

Fig. 10.18: Reconstructed energy distributions and ratios for the ν_eCC (top) and gamma (middle) selections. The left plots show the nominal distributions before the fit and the right plots the Monte-Carlo distribution tuned with the post-fit results together with the real data. The boxes on the top of each distribution show the ratio of the data respect to the Monte-Carlo before the fit with the systematic uncertainties in red. At the bottom we show the pulls of the systematic error parameters.

10.6.1 Results fixing the oscillation parameters

To further clarify and justify the discrepancies at low energies between the expectation and the real data, we study the compatibility between the Monte-Carlo in the null hypothesis and the data. The nuisance parameters are profiled as usual. In this way we study if only systematic errors variations are able to fully reproduce the behaviour of the data. Essentially, this analysis provides the χ^2_{00} value in the point of the parameter space G_{00} ($\sin^2(2\theta_{ee}) = 0$, $\Delta m^2_{41} = 0$). The best fit value $\chi^2_{00,data}$ if no ν_e disappearance is introduced corresponds to:

$$\chi^2_{00,data} = 47.6$$

meaning a *goodness-of-fit* of 62%, smaller than in the case in which we allow ν_e disappearance.

The ratio between data and Monte-Carlo are presented in Fig. 10.19 for the ν_eCC and gamma samples. There are the ratio between the data and the nominal Monte-Carlo compared with the ratio of the best fit Monte-Carlo without fitting ν_e disappearance and fitting ν_e disappearance. In those figures, we appreciate how the fit without oscillations is able to accommodate the discrepancy between data and Monte-Carlo in the γ sample. As this sample is not affected by the oscillations the ratios with and without oscillation parameters are basically identical. Regarding the ν_eCC selection, there is still a small deficit on the data between 600 MeV and 800 MeV that is better reproduced including the ν_e disappearance.

10.6.2 *p-value*

The estimator of the *p-value*, according to Section 10.3.4, is:

$$\Delta\chi^2_{00,data} = \chi^2_{00,data} - \chi^2_{bf,data} = 4.4$$

This value is compared with the $\Delta\chi^2_{00}$ distribution for 5000 toys Monte-Carlo in the non oscillation hypothesis and the *p-value* is given by:

$$p - value = \int_{4.4}^{+\infty} dx \Delta\chi(x) = 0.061$$

meaning that our data are compatible with the non oscillation hypothesis at the 6.1% level. This

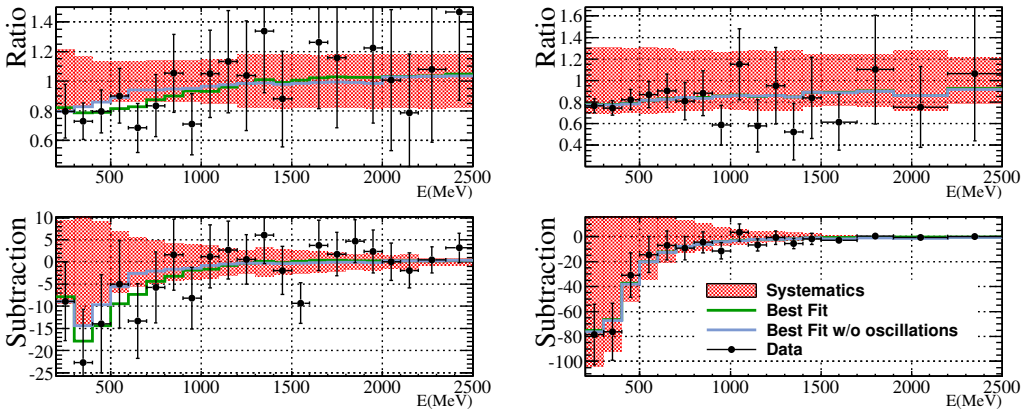

Fig. 10.19: Ratio (top) and subtraction (bottom) of the E_{Rec} distributions for the data and the nominal Monte-Carlo in the case of the ν_eCC sample on the left and photon sample on the right. The differences between the Monte-Carlo after the fit (with or without oscillations) and before the fit are shown as well. The data (dots) only show the statistical uncertainties while the red shadowed regions show the systematic uncertainties.

is shown in Fig. 10.20 where the critical value for the 90%CL is shown in red for reference and it corresponds to $\Delta\chi^2_C(90\%CL) = 3.4$.

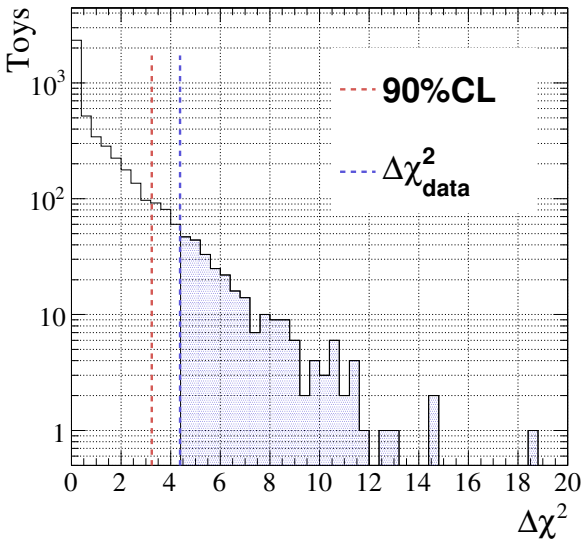

Fig. 10.20: p-value of the null hypothesis given by the data. The distribution correspond to the $\Delta\chi^2_{00}$ from 5000 toys Monte-Carlo without oscillations. The critical value for the 90%CL is shown for reference.

10.6.3 Exclusion regions with the constant $\Delta\chi^2$ method

Confidence intervals are built for the data using the constant $\Delta\chi^2$ method described in Section 10.5.1. The $\Delta\chi^2_{ij}$ map [Eq. (10.4)] is calculated for the data and shown in Fig. 10.21. The contours are located by comparing this map with the critical values in Tab. 10.2 for different confidence levels (1σ, 90%CL and 95%CL). They are shown in Fig. 10.22. According to this method, the null hypothesis is excluded at the 1σ level. On the other hand, for high $\Delta m^2_{41} > 5\,\mathrm{eV}^2$ our analysis set constrains for $\sin^2(2\theta_{ee}) > 0.1$ at the 90%CL and $\sin^2(2\theta_{ee}) > 0.3$ at the 95%CL, reaching a maximum of $\sin^2(2\theta_{ee}) > 0.05$ for $\Delta m^2_{41} \sim 11\,\mathrm{eV}^2$ at the 90%CL.

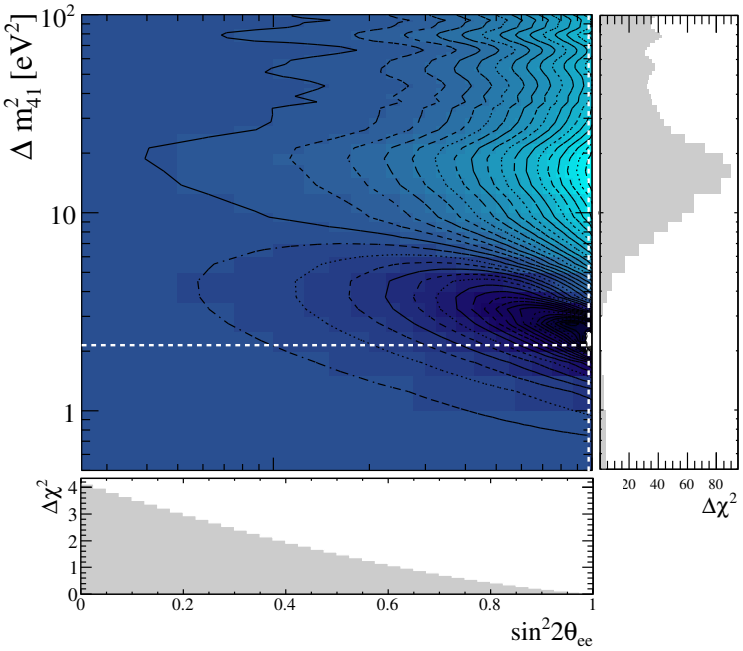

Fig. 10.21: $\Delta\chi^2$ map on the parameter space for the data. On the sides we show the profile of the $\Delta\chi^2$ on the coordinates of the best fit point. Several contours are marked to show to gradients.

10.6.4 Exclusion region with the Feldman-Cousins method

Confidence intervals using the Feldman-Cousins method are built by comparing the $\Delta\chi^2$ map for the data [Fig. 10.21] with the critical values calculated and shown in Fig. 10.7. At the bottom of

Fig. 10.22 the contours for the 1σ, 90%CL and 95%CL are shown. The 95%CL contour is similar to the one obtained with the constant $\Delta\chi^2$ method because it sits on the region of good coverage. On the contrary, the exclusion regions at 1σ and 90%CL are noticeably different since they are out of this region. The Feldman-Cousins intervals are more restrictive since the constant $\Delta\chi^2$ over-covers the zones near the boundaries [Section 10.3.6]. The non oscillation hypothesis is excluded at the 90%CL as the *p-value* indicated. All the high $\Delta m^2_{41} > 7\,eV^2$ is excluded at the 90%CL and $\sin^2(2\theta_{ee}) > 0.2$ is also excluded at the 95%CL.

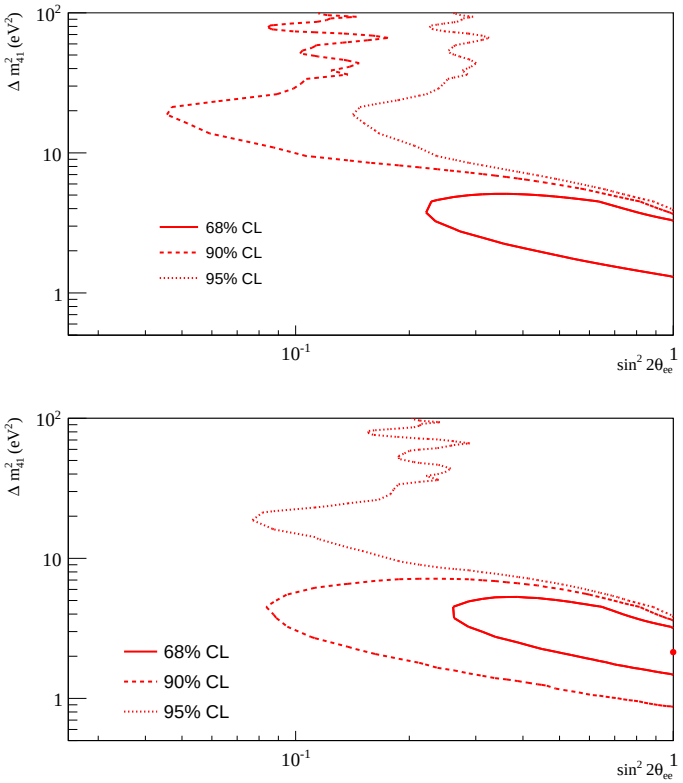

Fig. 10.22: 68%CL, 90%CL and 95%CL exclusion regions calculated using the constant $\Delta\chi^2$ method (top), and the Feldman-Cousins method (bottom).

10.6.5 Discrepancies between the expected sensitivity and the exclusion regions

The confidence contours obtained from the data and the expected sensitivity [Fig. 10.17] have different features. In Fig. 10.23 we compare the confidence interval of the data at the 95%CL with the predicted sensitivity including the 1σ envelope where we expect to have the confidence contours.

For low Δm^2_{41}, the contour set by the data is contained within the 1σ envelope, while for $\Delta m^2_{41} > 10\,eV^2$, the data excludes more than expected. This has its origin in a positive fluctuation of the background (*lucky exclusion*). We find slightly more events than predicted at high E_{Rec} as can be seen in the ratio of the ν_eCC [Fig. 10.19] and hence we are more sensitive than expected. On the other hand, at low E_{Rec} we see a deficit in the ν_e sample partially covered by the systematic uncertainties (specially the OOFV backgrounds as previously discussed) that justifies the low *p-value* obtained.

To better clarify this, we simply count the events at low energy ($0 \leq E_{Rec} \leq 1.5\,GeV$) and high energy ($1.5 \leq E_{Rec} \leq 10\,GeV$) for several toys Monte-Carlo and compare the distributions on the number of events with the data. For the toys experiments we have include a 30% reduction in the OOFV parameter. In Fig. 10.24 we see that, indeed, for low E_{Rec} the data is below the averaged predicted value and only $\sim 10\%$ of the toys have less events than the data, while at high E_{Rec} the data is above the mean and the $\sim 80\%$ of the toys have less events than the data.

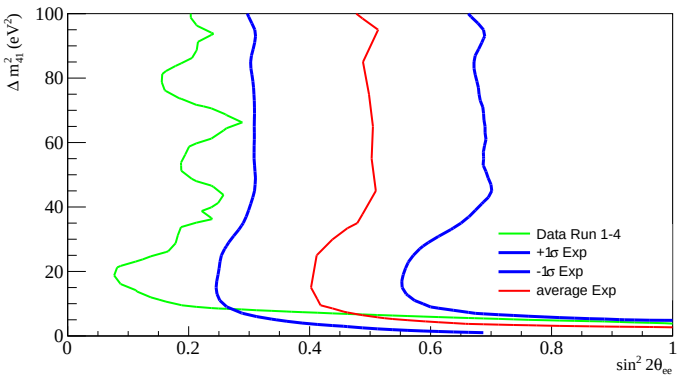

Fig. 10.23: Comparison for the predicted sensitivity (red) and the confidence contours calculated with the data (green) using Feldman-Cousins at the 95%CL. The blue curves provides the $\pm 1\sigma$ variations of the contours.

10.7 Conclusion and discussion

The contours at 68%CL and 90%CL exclude the non-oscillation hypothesis and it is interesting discuss the compatibility of our result with the literature. We chose the ν_e disappearance experiments presented in Section 2.2, namely:

- Reactor neutrino experiments (*Reactor anomaly*).

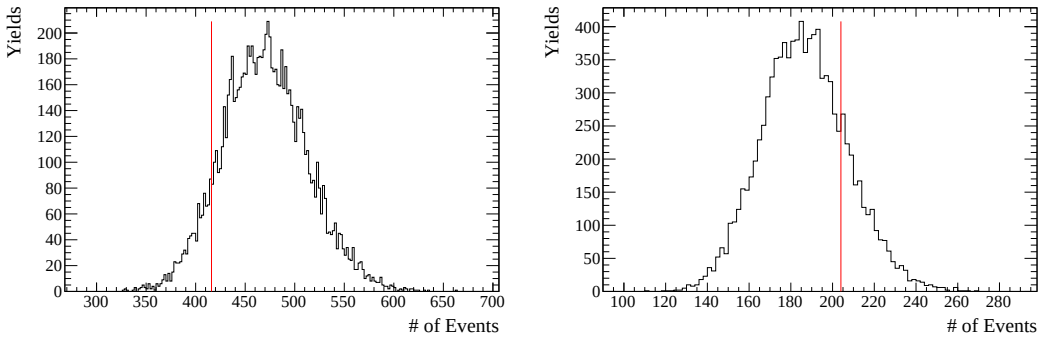

Fig. 10.24: Number of events in the range $0 \leq E_{reco} \leq 1.5\,\text{GeV}$ (left) and $1.5 \leq E_{reco} \leq 10\,\text{GeV}$ (right) obtained from 10000 toys experiments varying the systematic errors parameters. The red lines correspond to the number of events in the corresponding range in the data sample.

- Experiments in gallium with radioactive sources (*Gallium anomaly*).
- Solar neutrino experiment and KamLAND experiment using the measurements of Daya Bay and RENO on $\sin^2(2\theta_{13})$.
- Measurements on ν_e-Carbon scattering at LSND and KARMEN.
- Combined analysis of the experiments above [96].

In Fig. 10.25 we show the confidence contours found by those experiments in comparison with ours for the 90%CL and the 95%CL.

At the 90%CL the allowed region by the ND280 data encompasses the best fit point of the *gallium anomaly* and agrees with the *reactor anomaly* and the combined analysis. The high Δm^2_{41} part of the allowed regions of the ν_e-Carbon experiments are largely excluded by our data. As well as the rest of the experiments, our results are slightly in tension with the Solar neutrino constrains.

At 95%CL a small part of parameter space is rejected including the high $\Delta m^2_{41} > 10\,\text{eV}^2$ part of the *gallium anomaly* and the region delimited by $\sin^2(2\theta_{ee}) > 0.1$ and $\Delta m^2_{41} = 10 - 30\,\text{eV}^2$ of the *reactor anomaly*. The ν_e-Carbon best fit point is still excluded and there is no tension with the solar neutrino experiments.

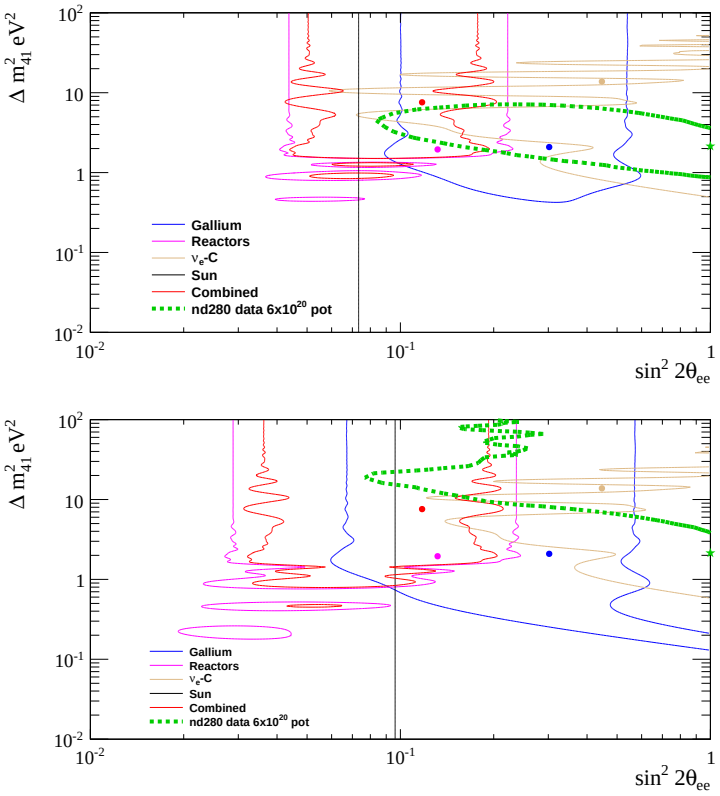

Fig. 10.25: 90%CL (top) and 95%CL (bottom) confidence contours for different experiments: ND280 using Feldman-Cousins (green), *gallium anomaly* (blue), *reactor anomaly* (pink), solar neutrino experiments (black), ν_e-Carbon cross-section experiments (brown) and the combined result of the previous experiments except ND280 (red) [96]. The star and the dots correspond to the position of the global minimum for the different experiments.

Chapter 11

Summary and outlook

The neutrino flux and cross sections for the T2K analyses at both, ND280 and SK, are measured from the selection of ν_μCC interactions at ND280. Specifically the intrinsic beam ν_e component, that constitute the main background to the T2K ν_e appearance analysis, is predicted by this procedure. The only direct confirmation of this prediction is given by the measurement of the ν_e event rates at ND280. With the analysis described in this thesis we performed this measurement, confirming the prediction with a 10% uncertainty, being the ratio between the measured and expected ν_e component:

$$R^{\nu_e} = 1.01 \pm 0.06(\text{stat}) \pm 0.07(\text{Flux-XSec}) \pm 0.04(\text{Det-FSI}) = 1.01 \pm 0.10$$

It reinforces our understanding of the intrinsic ν_e background component in the ν_e appearance analysis at SK. It is the most important background and our validation establishes that the measurement of the last mixing angle $\sin^2(2\theta_{13})$ has not to be corrected. This analysis was possible thanks to a clean selection of ν_eCC events at ND280, combining the TPC and the ECal PID to select electrons, and an exhaustive study of our backgrounds, estimating the misidentified muons in the selected sample and including a photon conversion control sample in the fit. In the future with 10 times more data (up to now we have only collected the 8% of the final POT goal), we will be sensitive to differences between the ν_e and ν_μ cross sections up to the 4% level, being a very promising analysis.

The ν_e interaction rates along with the reconstructed neutrino energy information have been used to search for $\nu_e \to \nu_s$ oscillations (ν_e disappearance) at short base-line in the 3+1 model. The *reactor and gallium anomalies* measure some deficit in their ν_e event rates compatible with ν_e SBL disappearance at the $\Delta m^2_{41} \sim 1\,\text{eV}^2$ scale. Indeed, we are able to investigate at ND280 mass differences of that order. This is the first time that this channel is studied by a standalone neutrino beam experiment at the GeV scale. Our results are compatible with the null hypothesis at the 6.1% level according to the *p-value* test, and we are able to reject the parameter region above $\Delta m^2_{41} = 10\,\text{eV}^2$ and $\sin^2(2\theta_{ee}) = 0.1$ at the 95%CL. A repetition of this analysis in the future with more statistic is foreseen as it will set stringent

constraints in the parameter space. In addition, this analysis is intended to be the first step in a more complex fit including the remaining channels: ν_e appearance and ν_μ disappearance. Furthermore, with the anti-neutrino data that is been collected at this moment (2014), we might be sensitive to differences between neutrino and anti-neutrino samples and hence, CPV at SBL. It will be interesting to separately test neutrinos and anti-neutrinos mixing with steriles allowing to disentangle between the 3+1 model and models with more that one light sterile neutrino where CPV is allowed.

Part IV

Appendices

Appendix A

Systematic errors calculation

A.1 Charge misidentification systematic error

This corresponds to a summary on the work developed and reported in the T2K internal paper [29].

The charge of the particles is measured by the TPCs reconstructing the curvature of the tracks due to the magnetic field. The charge misidentification associated to the TPC is calculated using a statistical approach by comparing the reconstructed charges in the different TPCs.

A clean sample of through-going muons are selected by requiring a track crossing the three TPCs with more than 18 clusters per TPC segment. This sample lacks of backward-going tracks and also tracks whose TPC segments belong to different particles due to reconstruction mismatches. This allows to study the charge misidentified purely by the TPC detectors. The charge confusion is calculated as a function of the momentum in a variable binning that we have optimized. The probability of a wrong charge reconstruction p_{cm} is related with the probability of obtaining different charges p_{same} in the TPCs by

$$p_{same} = (1 - p^1_{cm})(1 - p^2_{cm})(1 - p^3_{cm}) + p^1_{cm}p^2_{cm}p^3_{cm} \tag{A.1}$$

where the first piece is the probability that the three TPC charges are properly reconstructed and the second is the probability that the reconstruction fails in calculating each of them. The indexes refer to the different TPCs. This is exact only under the assumption that each of the TPC segment belongs to the same particle, i.e. there is no mismatch. As we explained above, this is very accurate for the through-going muons sample. Making the approximation of considering the systematic error equal in the three TPCs

$$p^1_{cm} = p^2_{cm} = p^3_{cm} \tag{A.2}$$

we get, developing the former expression, the following formula for the charge misidentification as a function of p_{same}, that is a quantity we can measure in both data and Monte-Carlo

$$p_{cm} = \frac{1}{2}(1 - \sqrt{1/3(4p_{same} - 1)}) \tag{A.3}$$

To check the performances of the statistical approach, a parallel pure Monte-Carlo study has been done by comparing directly the reconstructed charge with the real charge that has that particle in the simulation (*true charge*). In summary we present two results:

- Statistical calculation: calculated both for data and Monte-Carlo and taken as the *multi-fit* results.
- Monte-Carlo truth validation: direct comparison of the reconstructed and true charges to cross-check the above results.

Fig. A.1 shows the results for the charge confusion given by the two methods for data and Monte-Carlo. An increase of the charge confusion probability with the momentum is observed, since the reconstruction of the curvature is more difficult for the very straight tracks. The low energy region is populated mainly by low quality reconstructed tracks, short tracks, mismatches of the global reconstruction and also backward-going tracks. This explains the worsening of the charge confusion at lower energies. In addition, the first bins has low statistics due to the requirement of 3 TPC segments. Then, the error in the charge confusion is also quite large. Because of this, the Monte-Carlo truth method shows discrepancies with the statistical calculation. Essentially, the former predicts a larger charge misidentification.

The final systematic error is given by the absolute difference between data and Monte-Carlo (Fig. A.1). The final numbers propagated to the ν_e analysis depend on the momentum and number of reconstructed hits in the TPC and are given in Tab. A.1.

A.2 Electron TPC PID systematic error

This corresponds to a summary on the work developed and reported in the T2K internal paper [27].

The sample of γ conversions can be used to estimate the TPC PID systematics for electrons as it provides a clean sample of electrons and positrons without using the TPC PID. Here we will use the same

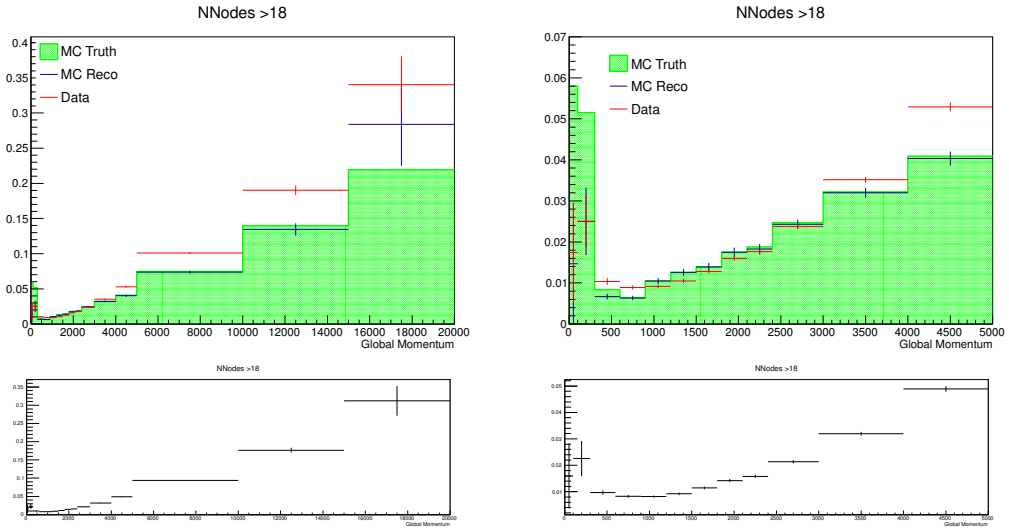

Fig. A.1: Top: Fraction of charge mis-identification (p_{cm}, see text for definition) as function of global momentum. The Monte-Carlo truth method is shown in green. Black and red lines show the statistical method results for Monte-Carlo and data respectively (zoomed on the right) Bottom: Absolute difference between data and MC of the fraction of charge mis-identification (zoomed on the right).

Momentum (GeV)	data	MC	data-MC	MC Truth
0-0.1	2.63 ± 1.84	1.5 ± 1.5	1.17 ± 2.62	5.80
0.1-0.3	2.47 ± 0.74	2.5 ± 1.0	0.03 ± 1.11	5.15
0.3-0.6	0.98 ± 0.09	0.67 ± 0.07	0.31 ± 3.27	0.84
0.6-1.0	0.88 ± 0.05	0.70 ± 0.05	0.18 ± 0.20	0.71
1.0-1.5	1.02 ± 0.04	1.20 ± 0.06	0.18 ± 0.19	1.20
1.5-3.0	1.85 ± 0.03	1.89 ± 0.06	0.04 ± 0.08	1.92
3.0-5.0	4.29 ± 0.07	3.52 ± 0.10	0.78 ± 0.78	3.55
5.0-20.0	11.0 ± 1.6	7.95 ± 0.20	3.10 ± 3.11	8.11

Table A.1: Summary table with the charge misidentification (%) results for data and Monte-Carlo propagated in the ν_e analysis.

sample described in Chapter 7 but without using the cut on the electron pull, as that is the systematic that we want to evaluate.

In Fig. A.2 we show the pull in the electron hypothesis for the most energetic track and the secondary track in the γ conversion sample, divided in 5 momenta bins

$$[0, 300\,\text{MeV}]; [300\,\text{MeV}, 600\,\text{MeV}]; [600\,\text{MeV}, 1\,\text{GeV}], [1\,\text{GeV}, 1.5\,\text{GeV}], [1.5\,\text{GeV}, 3\,\text{GeV}] \tag{A.4}$$

Combining together primary and secondary tracks we obtain the distributions shown in Fig. A.2: as

we can see data and MC are compatible for the whole momentum range.

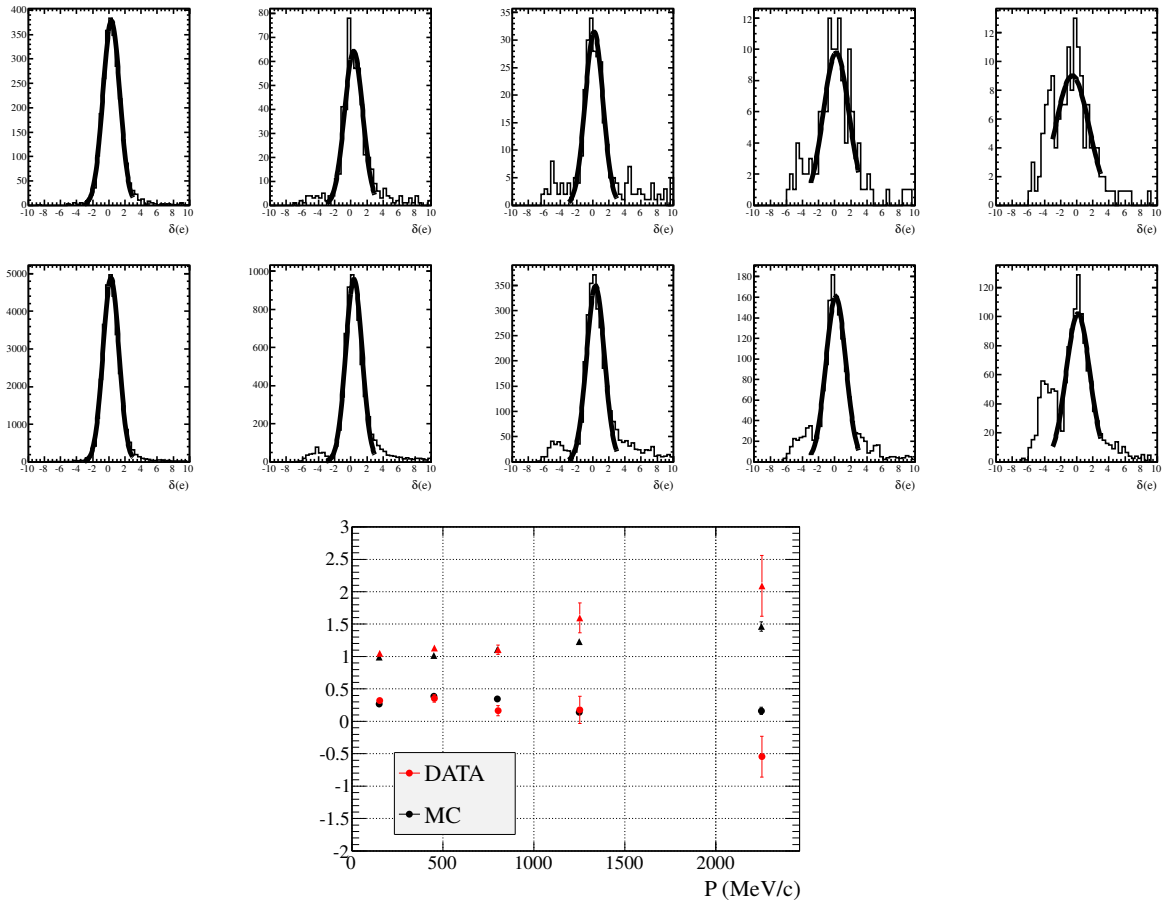

Fig. A.2: TPC pull in the electron hypothesis for different momenta bins for all the electron like tracks in the γ conversion sample for data (top) and MC (middle). The bottom plot shows the mean (circles) and the σ (triangles) of the above Gaussian fits.

By combining all the momenta together we obtain the pull distribution shown in Fig. A.3 for data and MC. The mean values are compatible while the width in the MC is slightly narrower than the one in the data. For the systematics, the shift on the mean come from the statistical error on the mean position in the data, while to account for different widths we compute a smearing factor on the width given by:

$$s = \sqrt{\sigma_{DT}^2 - \sigma_{MC}^2} = \sqrt{1.11^2 - 1.02^2} = 0.44 \tag{A.5}$$

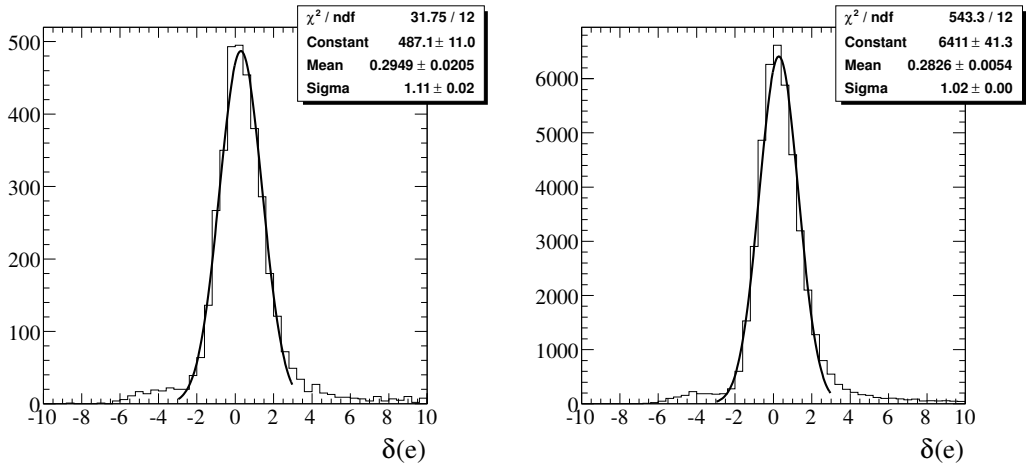

Fig. A.3: Electron pull distribution in data (left) and MC (right) for the γ conversion sample integrated from 0 to 3 GeV.

Appendix B

Further fit validations for the ν_e disappearance analysis

Apart from the official minimization of the analysis (*multi-fit*) presented in Chapter 10, three more techniques were tested. These are similar and they are all based on a standard fit using the `MIGRAD` minimization of the `TMinuit` library of `ROOT`. The only difference is the starting values $G^s \equiv (\sin^2(2\theta_{ee})_s, \Delta m^2_{41\,s})$ of the oscillation parameters from where the fit is released:

- *Standard values*: defined in a point of the grid far from the boundaries $\sin^2(2\theta_{ee})_s = 0.4$ and $\Delta m^2_{41\,s} = 5\,\mathrm{eV}^2$
- *Toy values*: set the same values of the toy Monte-Carlo. We did not present this in the main body of the analysis because it cannot be applied to the real data. However, it helps to understand the problem.
- *Random values*: minimize the toys from a different random value each time. It present the same features that the first case, so we do not show this method here.

B.1 Pull studies

Two sets of 5000 toys experiment built under two different oscillation hypotheses are minimized:

$\sin^2(2\theta_{ee}) = 0.7$ and $\Delta m^2_{41} = 8\,\mathrm{eV}^2$

For the *standard values*, the distribution of the best fit value in the parameter space is shown in Fig. B.1. The peak of the distribution is around the expected values of the parameters while there are some toys that are away from this point.

As can be seen in Fig. B.2, the distributions of the fitted oscillation parameters have Gaussian distributions centered around the expected values.

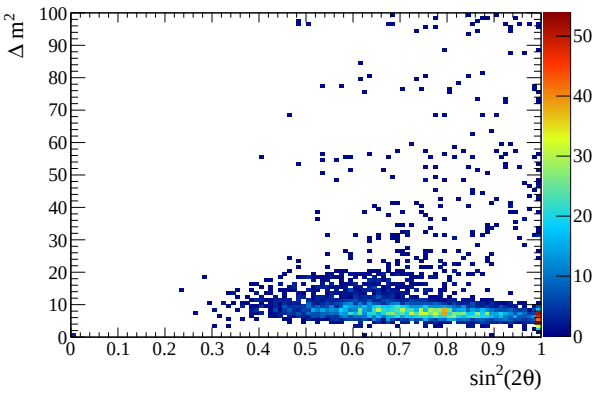

Fig. B.1: Best fit point in the parameter space for 5000 toys and 5.9×10^{20}POT in the $\sin^2(2\theta_{ee}) = 0.7$, $\Delta m^2_{41} = 8\text{eV}^2$ hypothesis.

$\sin^2(2\theta_{ee}) = 0.7$ and $\Delta m^2_{41} = 50\,\text{eV}^2$

In this case the Δm^2_{41} is large to study the degeneracy of Δm^2_{41} in the fast oscillation regime. For the standard values, shown in the left plot of Fig. B.3, a large fraction of the toys fall in and incorrect point with average in $\sin^2(2\theta_{ee}) = 0.64$, $\Delta m^2_{41} = 11.9\,\text{eV}^2$. If instead we use the *toy values* as starting points, the distribution changes and get closer to the oscillation parameter of the toys. This illustrates clearly the risk of using only one global fit, since we demonstrate that the results are strongly dependent on the starting values.

B.2 $\Delta\chi^2$ distributions

For the 5000 with $\sin^2(2\theta_{ee}) = 0.7$, $\Delta m^2_{41} = 8\,\text{eV}^2$ we calculate the best fit value χ^2_{bf} using each of the methods including the official one. The distributions are shown in Fig. B.4 where we have fit a χ^2 function.

The first two cases correspond to χ^2 distributions with $dof \sim 50$ while we expect $dof = 49$. This slight disagreement indicates that the minimum the fit is calculating is not the global one, but a local minimum where the fit got stuck. The *multi-fit* minimization does not show this feature and the χ^2

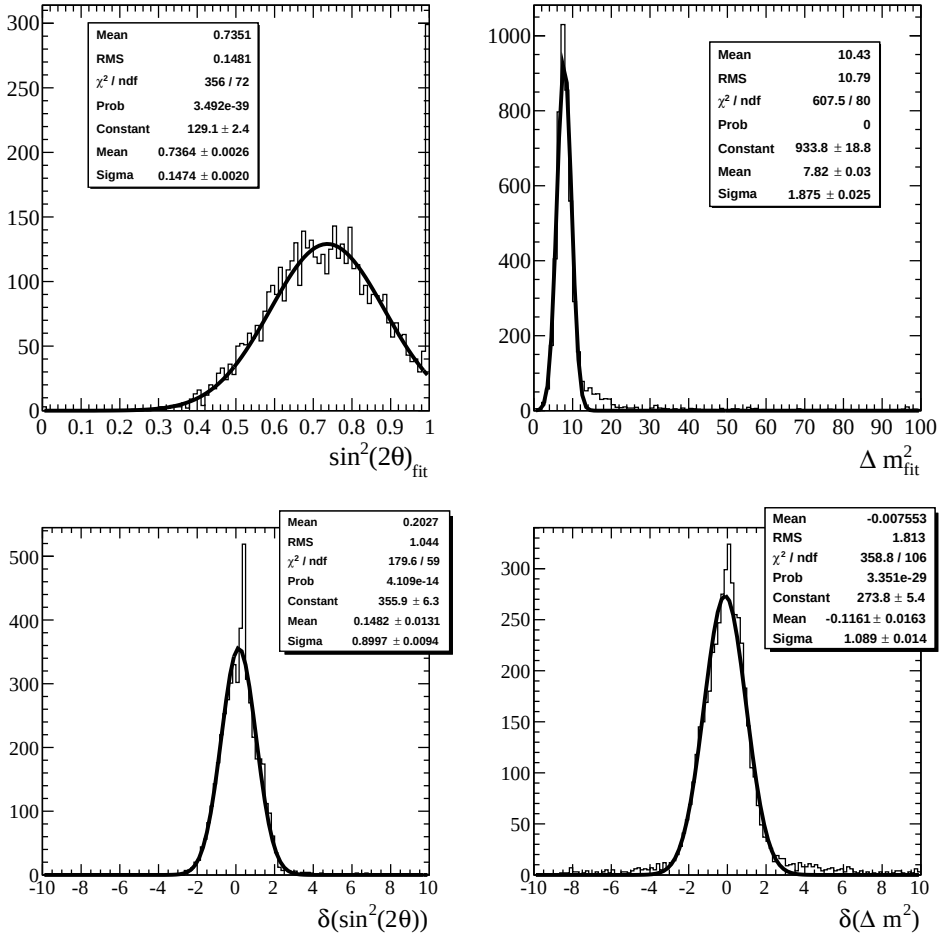

Fig. B.2: Fitted values (top) and pulls (bottom) of oscillation parameters for 5000 toys at 5.9×10^{20} POT corresponding to the true values $\sin^2(2\theta_{ee}) = 0.7$, $\Delta m^2_{41} = 8\,\mathrm{eV}^2$. The starting values for the fit are set to the *default* (see text) ones.

distribution is compatible with $dof = 49$.

Now we calculate:

$$\Delta\chi^2_{00} = \chi^2_{00} - \chi^2_{bf} \tag{B.1}$$

The first term is computed using the *likelihood profile* and removing the nuisance parameters. As the oscillation parameters are fixed, this number does not depend on the minimization approach we take. The second term was extracted above for each of the cases. The distributions are shown in Fig. B.5.

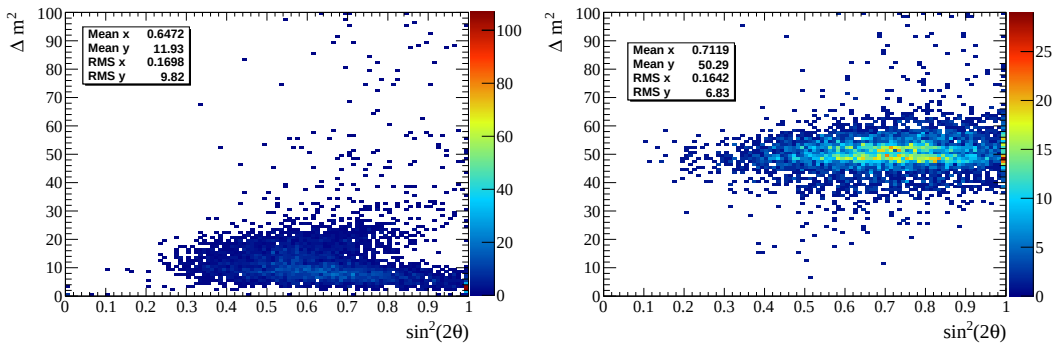

Fig. B.3: Fitted values of oscillation parameters for 5000 toys at 5.9×10^{20}POT corresponding to the true values $\sin^2(2\theta_{ee}) = 0.7,\ \Delta m^2_{41} = 50\,\mathrm{eV}^2$. Left: starting values of the oscillation parameters are set to the *default* values. Right: Starting values of the oscillation parameters are set to the *true* values.

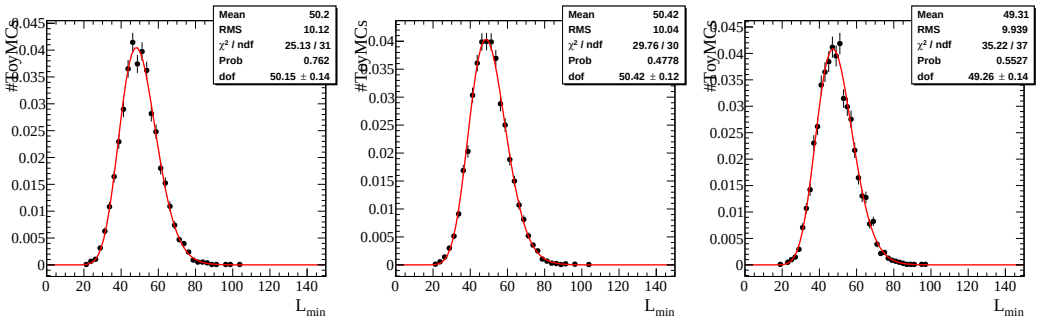

Fig. B.4: χ^2_{bf} distributions for 5000 toys generated for $\sin^2(2\theta_{ee}) = 0.7,\ \Delta m^2_{41} = 8\,\mathrm{eV}^2$. The distributions are fitted with a χ^2 function. Left: *default* fit; middle: *default* fit with starting values set to the true values; and right: *multi-fit* method.

We observe that using the *standard values* there are some cases with $\Delta\chi^2_{00} < 0 \Rightarrow \chi^2_{bf} > \chi^2_{00}$, meaning that χ^2_{bf} is not the minimal value on the parameter space. This pathological behaviour needs to be overcome as this distribution is not a good distribution for goodness-of-fit tests and for calculation of the confidence intervals.

Setting the starting values to the *toy values* the problem is solved. This indicates again that the problem arises due to a local minimum created by a fluctuation on the toy experiment. Finally, we show that for the *multi-fit* technique the distribution of $\Delta\chi^2$ has not a negative tail and furthermore is broader than the previous case, indicating that the global minimum is better estimated.

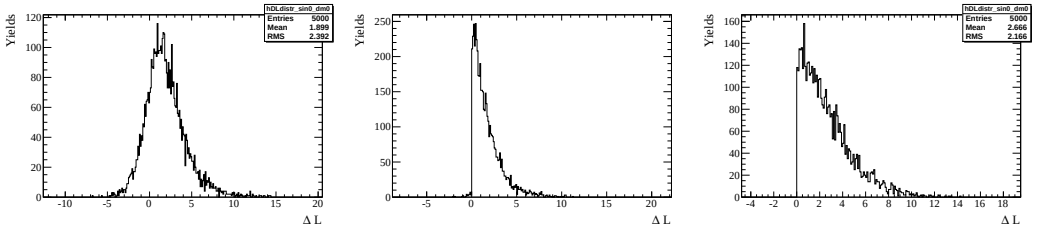

Fig. B.5: Distribution of $\Delta\chi^2_{00}$ obtained from 5000 toys generated for $\sin^2(2\theta_{ee}) = 0.7$ and $\Delta m^2_{41} = 8\,\mathrm{eV}^2$. Left: *default* fit; middle: *default* fit with starting values set to the true values; and right: *multi-fit* method.

Bibliography

[1] *UA1 central detector.* CERN-OBJ-DE-015. 62

[2] A.A.Aguilar-Arévalo et al. Phys.Rev.Let. 98, 231801 http://prl.aps.org/pdf/PRL/v98/i23/e231801, 2007. 37

[3] A.A.Aguilar-Arévalo et al. Phys.Rev.Let. 105, 181801 http://prl.aps.org/pdf/PRL/v105/i18/e181801, 2010. 37

[4] [LSND Collaboration] A.Aguilar et al. *Evidence for Neutrino Oscillations from the Observation of ν_e Appearance in a ν_μ Beam.* http://arxiv.org/pdf/hep-ex/0104049v3.pdf, 2001. 36

[5] [T2K Collaboration] K. Abe et al. Nucl. Instrum. Meth. A659, 106, 2011. 45

[6] [T2K Collaboration] K. Abe et al. Phys. Rev. D 87, 012001, 2013. 56

[7] N. Abgrall et al. *NA61/SHINE facility at the CERN SPS: beams and detector system.* CERN-PH-EP-2014-003, 2014. 56

[8] A. Afonin et al. JETP Lett. 93, 1, 1988. 31

[9] S. Agostinelli et al. Nucl. Instrum. Meth. A506 250-303, 2003. 88

[10] ALEPH, DELPHI, L3, OPAL, SLD, and LEP Collaborations. Phys.Rept.427, 257-454 http://arxiv.org/pdf/hep-ph/0610064v2.pdf, 2006. 8, 25

[11] T. Araki et al. Phys. Rev. Lett. 94 081801, 2005. xv, 21, 33, 34

[12] B. Armbruster et al. Phys. Rev. D 65 112001, 2002. 37

[13] P. Astier et al. Phys. Lett. B 570 19, 2003. 62, 127

[14] [LSND Collaboration] C. Athanassopoulos et al. Nucl.Instrum.Meth. A388, 149 arXiv:nucl-ex/9605002, 1997. 35, 36

[15] J. Bahcall et al. *Solar Models: current epoch and time dependences, neutrinos, and helioseismological properties.* Astrophys. J. 555, 990-1012 http://arxiv.org/pdf/astro-ph/0010346v2.pdf, 2001. 8

[16] S. Barker and R. Cousins. Nucl. Instrum. Methods 221, 437, 1984. 146

[17] M. Bass et al. *Future Sensitivity Task Force Summary report.* T2K Technical Note 187 http://www.t2k.org/docs/technotes/173, 2013. 83

[18] D. Beavis et al. *P889: Long Baseline Neutrino Oscillation Experiment at the AGS.* Report No. BNL-52459, 1995. 51

[19] Carlo Bemporad, Giorgio Gratta, , and Petr Vogel. *Reactor-based neutrino oscillation experiments.* Rev.Mod.Phys. 74 2 297 rmp.aps.org/pdf/RMP/v74/i2/p297_1, 2002. 30

[20] A. H. Bequerel. *On radioactivity, a new property of matter.* http://www.nobelprize.org/nobel_prizes/physics/laureates/1903/becquerel-lecture.pdf, 1903. 5

[21] N. Abgrall B. Andrieu P. Baron P. Bene V. Berardi et al. Nucl. Instrum. Meth. A637 25-46, 2011. 64

[22] H. Bethe and R. Peierls. *The Neutrino.* Nature 133, 532, 1934. 6

[23] F. Boehm et al. *Final results from the Palo Verde neutrino oscillation experiment.* Phys. Rev. D 64, 112001, 2001. xv, 33, 35

[24] R. Brun, F. Carminati, and S. Giani. CERN-W5013, 1994. 55

[25] R. Brun and F. Rademakers. Nucl. Instrum. Meth. A389 81-86, 1997. 88

[26] B.Smith. *Measurement of the ν_eCC Inclusive Cross-section on Carbon Using Data From Runs 1-4.* T2K Technical Note 187 http://www.t2k.org/docs/technotes/187/v1r3, 2014. 83

[27] J. Caravaca et al. *Measurement of the electron neutrino beam component in the ND280 Tracker for 2013 analyses.* T2K Internal Note 149: http://www.t2k.org/docs/technotes/149. 198

[28] J. Caravaca et al. *Study of electron neutrino disappearance with the ND280 tracker.* T2K Internal Note 158: http://www.t2k.org/docs/technotes/158. 87

[29] J. Caravaca et al. *Charge Misidentification in local and global reconstruction in the 2010/2011 data.* T2K Internal Note 048: http://www.t2k.org/docs/technotes/048/v2, 2011. 197

[30] J. Chadwick. *Possible existence of a Neutron.* Nature 129, 312 http://www.nature.com/nature/journal/v129/n3252/pdf/129312a0.pdf, 1932. 6

[31] G. Cheng, W. Huelsnitz, et al. http://arxiv.org/pdf/1208.0322v2.pdf, 2012. 39

[32] J.H. Christenson et al. Phys. Rev. Lett., 13, 138-140, 1964. 8

[33] B. T. Cleveland et al. *Measurement of the solar electron neutrino flux with the Homestake chlorine detector.* Astrophys. J. 496 505-526, 1998. 34

[34] [Daya Bay Collab.], F.P. An, et al. Phys. Rev. Lett. 108, 171803, 2012. 21, 22, 76

[35] [Daya Bay Collab.], F.P. An, et al. Chinese Phys. C37, 011001, 2013. xv, 22, 33, 35

[36] [RENO Collab.], J.K. Ahn, et al. Phys. Rev. Lett. 108, 191802, 2012. 22, 35

[37] [T2K Collab.], K. Abe, et al. Phys. Rev. Lett. 107, 041801, 2011. 22

[38] Borexino Collaboration, G. Bellini, et al. *Precision measurement of the 7Be solar neutrino interaction rate in Borexino.* Phys.Rev.Lett. 107 141302, 2011. 34

[39] [DOUBLE-CHOOZ Collaboration], Y. Abe, et al. *Indication for the disappearance of reactor electron antineutrinos in the Double Chooz experiment.* arXiv:1112.6353, 2011. xv, 22, 31, 33, 35

[40] MINOS Collaboration. *Search for sterile neutrino mixing in the MINOS long baseline experiment.* Phys.Rev. D 81 052004, 2010. 39

[41] [NA61/SHINE Collaboration], N. Abgrall, et al. Phys.Rev. C 84, 034604, 2011. 56

[42] [NA61/SHINE Collaboration], N. Abgrall, et al. Phys.Rev. C 85, 035210, 2012. 56

[43] [NA61/SHINE Collaboration], N. Abgrall, et al. Nucl. Instr. Meth. A 701 99, 2013. 56

[44] [SAGE collaboration], J. N. Abdurashitov, et al. Phys. Rev. C 59, 2246 arXiv.org/abs/hep-ph/9803418, 1999. 9, 32

[45] [SAGE collaboration], J. N. Abdurashitov, et al. Phys. Rev. C 73, 045805 arXiv.org/abs/nucl-ex/0512041, 2006. 32, 34

[46] [SAGE collaboration], J. N. Abdurashitov, et al. Phys. Rev. C 80, 015807 arxiv.org/abs/0901.2200v3, 2009. 33

[47] Super-Kamiokande Collaboration, K. Abe, et al. *Solar neutrino results in Super-Kamiokande-III.* Phys.Rev. D83 052010, 2011. 34

[48] [Super-Kamiokande Collaboration], Y. Ashie, et al. Phys. Rev. D 71, 112005, 2005. 69

[49] [T2K Collaboration], K. Abe, et al. http://arxiv.org/pdf/1403.3140v1.pdf. 83

[50] [T2K Collaboration], K. Abe, et al. Phys.Rev.Lett. 107, 041801, 2011. 77

[51] [T2K Collaboration], K. Abe, et al. Phys.Rev. D 88, 032002, 2013. 77

[52] [T2K Collaboration], K. Abe, et al. Phys. Rev. Lett. 111, 211803, 2013. 81

[53] [T2K Collaboration], K. Abe, et al. Phys. Rev. D 87, 092003, 2013. 83

[54] [T2K Collaboration], K. Abe, et al. Phys. Rev. Lett. 112, 181801, 2014. 21, 81

[55] [T2K Collaboration], K. Abe, et al. Phys. Rev. Lett. 112, 061802, 2014. 77, 158

[56] The ATLAS Collaboration. Phys.Lett. B716 1-29, 2012. 12

[57] The ATLAS Collaboration. *Observation of a new particle in the search for the Standard Model Higgs boson with the ATLAS detector at the LHC.* http://arxiv.org/abs/1207.7214, 2012. 10

[58] The CHOOZ Collaboration. *Search for neutrino oscillations on a long base-line at the CHOOZ nuclear power station.* European Physical Journal C, 27, 3, 331-374, 2003. xv, 33, 35

[59] The CMS Collaboration. Phys. Lett. B 716, 30, 2012. 12

[60] The CMS Collaboration. *Observation of a new boson at a mass of* 125 GeV *with the CMS experiment at the LHC.* http://arxiv.org/pdf/1207.7235.pdf, 2012. 10

[61] The DONUT Collaboration. *Observation of tau neutrino interactions.* Phys. Lett. B, 504, 3, 218, 2000. 7

[62] The HyperKamiokande Collaboration. *Letter of Intent: The Hyper-Kamiokande Experiment.* http://arxiv.org/pdf/1109.3262v1.pdf. 24

[63] The K2K Collaboration. *Improved Search for $\nu_\mu \rightarrow \nu_e$ Oscillation in a Long-Baseline Accelerator Experiment.* Phys. Rev. Lett. 96, 181801, 2006. 21

[64] The LBNE Collaboration. *The Long-Baseline Neutrino Experiment. Exploring the fundamental symmetries of the Universe.* https://sharepoint.fnal.gov/project/lbne/LBNE$%$20at$%$20Work/science$%$20doc%20pdfs/lbne-sci-opp-optim.pdf. 24

[65] The LBNO Collaboration. *The mass-hierarchy and CP-violation discovery reach of the LBNO long-baseline neutrino experiment.* http://arxiv.org/pdf/1312.6520v3.pdf. 24

[66] The MiniBooNE Collaboration. *First measurement of the muon neutrino charged current quasielastic double differential cross sectio.* Phys. Rev. D 81, 092005, 2010. 126

[67] The MiniBooNE Collaboration. *Measurement of neutrino-induced charged-current charged pion production cross sections on mineral oil at 1* GeV. Phys. Rev. D 83, 052007, 2011. 126

[68] The MINOS Collaboration. *Measurement of Neutrino Oscillations with the MINOS Detectors in the NuMI Beam.* Phys. Rev. Lett. 101, 131802, 2008. 21

[69] The NOνA Collaboration. *NuMI Off-Axis ν_e Appearance Experiment, Technical Design Report.* http://www-nova.fnal.gov/nova_cd2_review/tdr_oct_23/tdr.htm. 24

[70] The Planck Collaboration. *Planck 2013 results. XVI. Cosmological parameters.* http://arxiv.org/pdf/1303.5076v3.pdf, 2013. 41

[71] The T2K Collaboration. *The elecSim Library.* http://nngroup.physics.sunysb.edu/~mcgrew/t2k/elecSim/v5r0/dox/index.html#elecSim. 88

[72] The T2K Collaboration. *HighLand.* http://www.hep.lancs.ac.uk/nd280Doc/devel/invariant/highLevelAnalysis/index.html. 88

[73] The T2K Collaboration. *oaAnalysis.* http://nngroup.physics.sunysb.edu/~mcgrew/t2k/oaAnalysis/v3r12/dox/index.html. 88

[74] The T2K Collaboration. *Measurement of the intrinsic electron neutrino component in the T2K neutrino beam with the ND280 detector.* Phys. Rev. D 89, 092003, 2014. 87, 141

[75] Japan Proton Accelerator Research Complex. J-PARC TDR, KEK-Report 2002-13 and JAERI-Tech 2003-044, http://hadron.kek.jp/ accelerator/TDA/tdr2003/index2.html„ 2003. 48

[76] C.L. Cowan and F. Reines. *The Neutrino.* Nature 178, 446, 1956. 6

[77] G. Danby et al. *Observation of High-Energy Neutrino Reactions and the Existence of Two Kinds of Neutrinos.* Phys. Rev. Lett. 9 36, 1962. 7

[78] R. Davis et al. Rev. Mod. Phys. 75 985 http://journals.aps.org/rmp/pdf/10.1103/RevModPhys.75.985, 2003. 8

[79] M. Day et al. *Differences in quasielastic cross sections of muon and electron neutrinos.* Phys. Rev. D 86, 053003, 2012. 75, 128, 151, 158

[80] Patrick de Perio et al. *Cross section parameters for the 2012a oscillation analysis.* T2K Internal Note 166: http://www.t2k.org/docs/technotes/108, 2013. 126

[81] Y. Declais et al. *Study of reactor anti-neutrino interaction with proton at Bugey nuclear power plant.* Phys.Lett. B 338 383-389, 1994. 30

[82] Y. Declais et al. Nucl. Phys. B 434, 503, 1995. 31

[83] F. Dydak et al. Phys. Lett. B134 281 http://www.sciencedirect.com/science/article/pii/0370269384906889, 1984. 39

[84] F. Von Feilitzsch, A. Hahn, and K. Schreckenbach. Phys.Lett. B118, 162, 1982. 30

[85] E. Fermi. *Zeitschrift für Physik (English translation).* Am. J. Phys. 36, 1150, 1968. 6

[86] A. Ferrari, P. R. Sala, A. Fasso, and J. Ranft. CERN-2005-010, SLAC-R-773, INFN-TC-05-11. 55

[87] G.L. Fogli et al. Phys. Rev. D86, 013012, 2012. xxiii, 22, 23

[88] J.A. Formaggio and G.P. Zeller. *From eV to EeV: Neutrino Cross Sections Across Energy Scales.* Rev.Mod.Phys. 84 1307, 2012. 14

[89] Y. Fukuda et al. Phys.Rev.Lett. 82 2430-2434, 1999. 9, 70

[90] R.L. Garwin, L.M. Lederman, and M. Weinrich. *Observation of failure of conservation of parity and charge conjugation in mesons decays: the magnetic moment of the free muon.* Phys. Rev. 105 1415, 1957. 7

[91] H. Gemmeke et al. Nucl. Instrum. Meth. A289, 490, 1990. 35, 37

[92] G.Feldman and R.Cousins. Phys. Rev. D 57, 3873, 1998. xvii, 81, 174

[93] C. Giganti et al. *Particle Identification with the T2K TPC.* T2K Internal Note 001: http://www.t2k.org/docs/technotes/001. 94

[94] C. Giganti et al. *The TPC beam test: PID studies.* T2K Internal Note 003: http://www.t2k.org/docs/technotes/003. 94

[95] I. Giomataris et al. Nucl. Instrum. Meth. A560 405-408, 2006. 64, 65

[96] C. Giunti et al. *Update of Short-Baseline Electron Neutrino and Antineutrino Disappearance.* http://arxiv.org/pdf/1210.5715.pdf. xxii, 191, 192

[97] C. Giunti and M. Laveder. Phys.Rev. C83, 065504 arxiv.org/abs/1006.3244, 2011. xvi, 34

[98] M. Goldhaber, L. Grodzins, and A. W. Sunyarand. *Helicity of Neutrinos.* Phys. Rev. 109 1015, 1957. 7

[99] Z. Greenwood, W. Kropp, M. Mandelkern, S. Nakamura, E. Pasierb-Love, et al. Phys.Rev. D 53, 6054, 1996. 31

[100] V. Grivov and B. Pontecorvo. Phys. Lett. B, 28, 7, 493-496, 1969. 8

[101] [Particle Data Group], J. Beringer, et al. Phys.Rev. D 86, 010001, 2012. xvii, xxiv, 79, 81, 145, 174

[102] F.J. Hasert et al. *Search for elastic muon neutrino electron scattering.* Phys. Lett. B46 121, 1973. 7

[103] Y. Hayato. Acta Phys.Polon. B40, 2477, 2009. 83, 88, 126, 129

[104] Y. Hayato et al. Phys.Rev.Lett. 83 1529-1533, 1999. 70

[105] A. Hoummada, S. Lazrak Mikou, M. Avenier, et al. Appl. Rad. Isot. Vol. 46, No. 6/7, p. 449, 1995. 31

[106] J.V. Jelley. *Cerenkov radiation and its applications.* British Journal of Applied Physics 6, pp. 227-232, 1955. 70, 72

[107] F. Kaether, W. Hampel, G. Heusser, J. Kiko, , and T. Kirsten. *Reanalysis of the GALLEX solar neutrino flux and source experiments.* Phys. Lett. B 685, 47 arxiv.org/abs/1001.2731v1, 2010. 9, 32

[108] F. Kaether, W. Hampel, G. Heusser, J. Kiko, and T. Kirsten. *Reanalysis of the GALLEX solar neutrino flux and source experiments.* Phys.Lett. B685 47-54, 2010. 34

[109] M. Kobayashi and T. Maskawa. *CP-Violation in the Renormalizable Theory of Weak Interaction.* Progress of Theoretical Physics, Vol. 49, No. 2, pp. 652-657, 1973. 16

[110] J. Kopp et al. *Sterile neutrino oscillations: the global picture.* http://arxiv.org/pdf/1303.3011.pdf. xvi, 32, 38, 40, 41

[111] S. Kopp. Phys. Rept. 439 101, 2007. 52

[112] A. Krishnamoorthy and D. Menon. *Matrix Inversion Using Cholesky Decomposition.* http://arxiv.org/abs/1111.4144, 2011. 147

[113] V. Kuvshinnikov et al. JETP Lett. 59, 390, 1994. 31

[114] J. G. Learned. Phys.Rev.D78 071302, 2008. 24

[115] K. B. M. Mahn et al. Phys. Rew. D 85, 032007 http://prd.aps.org/pdf/PRD/v85/i3/e032007, 2012. 39

[116] Z. Maki, M. Nakagawa, and S. Sakata. *Remarks on the unified model of elementary particles.* Progress of Theoretical Physics, vol. 28, no. 5, pp. 870-880, 1962. 8, 16

[117] K. Matsuoka et al. Nucl. Instrum. Meth. A623 385-387, 2010. 51

[118] K. Matsuoka et al. Nucl. Instrum. Meth. A624 591-600, 2010. 51

[119] G. Mention, M. Fechner, T. Lasserre, T. Mueller, D. Lhuillier, and others arXiv:1101.2755. Phys.Rev. D 83, 073006, 2011. 31

[120] R. N. Mohapatra and G. Senjanovic. Phys. Rev. Lett. 44 912 http://journals.aps.org/prl/pdf/10.1103/PhysRevLett.44.912, 1980. 13

[121] F. Moreau et al. Nucl. Instrum. Meth. A613 46-53, 2010. 61

[122] T. Mueller, D. Lhuillier, M. Fallot, A. Letourneau, S. Cormon, et al. Phys.Rev. C 83, 054615 arXiv:1101.2663, 2011. xv, 31

[123] H. Nishino et al. Phys.Rev.Lett. 83 1529-1533, 2009. 70

[124] E. Oset et al. *A Theoretical Approach to Pion Nuclear Reactions in the Resonance Region.* Phys.Lett. B165, 1985. 129

[125] R. B. Palmer. Presented at Informal Conference on Experimental Neutrino Physics, CERN, Geneva, Switzerland, 20-22 Jan 1965 (C.Franzinetti, (Ed.), CERN-65-32, pp. 141-146, 1965. 50

[126] W. Pauli. *Pauli's letter.* http://microboone-docdb.fnal.gov/cgi-bin/RetrieveFile?docid=953;filename=pauli%20letter1930.pdf, 1930. 6

[127] M.L. Perl et al. *Evidence for Anomalous Lepton Production in electron-positron Annihilation.* Phys. Rev. Lett. 35, 1489, 1975. 7

[128] B. Pontecorvo. Chalk River Laboratory Report PD-205, 1946. 6, 8

[129] B. Pontecorvo. *Neutrino experiments and the question of leptonic-charge conservation.* Soviet Physics-JETP, vol. 26, p. 984, 1968. 25

[130] Ahmad Q. R. et al. Phys. Rev. Lett. 87, 071301, 2001. 9

[131] Ahmad Q. R. et al. Phys. Rev. Lett. 89, 011301, 2002. 9, 34

[132] D. Renker and E. Lorenz. JINST 4 P04004, 2009. 61

[133] Hirata. K. S., , et al. Phys. Rev. Lett. 65, 1297-1300, 1990. 9

[134] M. Schwartz. *Feasibility of Using High-Energy Neutrinos to Study the Weak Interactions.* Phys. Rev. Lett. 4 306, 1960. 7

[135] M. Shiozawa et al. Phys.Rev.Lett. 81 3319-3323, 1998. 70

[136] I. Stockdale et al. Phys. Rev. Lett. 52 1384 http://prl.aps.org/pdf/PRL/v52/i16/p1384_1, 1984. 39

[137] I. Stockdale, others F. Dydak, et al. Phys. C27 53, 1985. 39

[138] A. Suzuki et al. Nucl. Instr. and Meth. A 329 299, 1993. xvii, 70, 71

[139] S. van der Meer. CERN-61-07, 1961. 50

[140] S. S. Wilks. *The Large-Sample Distribution of the Likelihood Ratio for Testing Composite Hypotheses.* The Annals of Mathematical Statistics, Vol. 9, No. 1, pp. 60-62, 1938. 148

[141] L. Wolfenstein. Phys. Rev. D 17, 2369-2374, 1978. 9, 20

[142] C.S. Wu et al. *Experimental test of parity conservation in beta decay.* Phys. Rev. 105 1413, 1957. 7

[143] Fukuda Y. et al. Phys. Rev. Lett. 81, 1562-1567, 1998. 9, 21, 70

[144] M. Yokoyama et al. Nucl. Instrum. Meth. A622 567-573, 2010. 61

[145] [CALTECH-SIN-TUM COLLABORATION] G. Zacek et al. Phys.Rev. D34, 2621, 1986. 31

[146] C. Zeitnitz and T. Gabriel. *Calorimetry in high energy physics.* Corpus Christi 394-404, 1992. 56

Glossary

BrECal	Barrel electromagnetic calorimeter	68
CC	Charged Current	7
CCCoh	Charged current with coherent pion production	13
CCDis	Charged current deep inelastic scattering	14
CCQE	Charged current quasi-elastic	13
CCRes	Charged current resonant	13
DsECal	Downstream electromagnetic calorimeter	68
ECAL	Electromagnetic Calorimeter	61
ES	Elastic scattering	14
FGD	Fine Grained Detectors	61
FSI	Neutrino Final State Interactions	14
FV	Fiducial volume	93
IBD	Inverse Beta Decay	6
LINAC	Linear accelerator	47
MIP	Minimal ionizing particle	68
MPPC	Multi-Pixel Photon Counter	61
MUMON	Muon monitor	51

NC	Neutral Current	7
NCπ^0	Neutral current that produces a π^0	14
NCOther	Neutral current that does not produce a π^0	14
NCQE	Neutral current quasi-elastic	83
P0D	π^0 Detector	61
PID	Particle Identification	66
PMT	Photo-multipliers tube	70
POT	Protons on target	88
RFG	Relativistic Fermi gas	127
SK	SuperKamiokande detector	20
SM	Standard Model	5
SMRD	Side Muon Range Detector	61
SSM	Solar Standard Model	8
TPC	Time Projection Chamber	61
WLS	Wavelength shifter	61